UNIVERSITÉ DE LILLE

UNITÉ DE MÉCANIQUE DE LILLE - J. BOUSSINESQ ULR 7512

MÉMOIRE RÉDIGÉ EN VUE DE L'OBTENTION DU DIPLÔME
D'HABILITATION À DIRIGER DES RECHERCHES

PRESENTÉE PAR

ENRICO CALZAVARINI

IN THE FLOW: PARTICLES AND FIELDS IN FLUID SYSTEMS

LE 16/10/2026

JURY

ERIC CLIMENT, CNRS - Imperial College, UK	Rapporteur
CRISTIAN MARCHIOLI, Università di Udine, IT	Rapporteur
ANNE SERGENT, Sorbonne Université	Rapporteur
FRANÇOIS G. SCHMITT , CNRS - Université de Lille	Examinateur
GILMAR MOMPEAN, Université de Lille	Garant

Contents

Abstract **v**

1 *Preface* **1**

2 Particle laden turbulent flows: A primer **5**
2.1 Descriptions of fluid motion: Lagrange *vs.* Euler . . . 5
2.2 Turbulence . . . 7
2.3 The motions of material particles . . . 8
2.4 Particle-laden flows . . . 9
2.5 Research Objectives . . . 11

3 Accelerations of inertial particles in turbulence **13**
3.1 Inertial particles accelerations statistics . . . 13
3.2 Simulations of finite-size spheroids in turbulence . . . 19
3.2.1 Methodology and study protocols . . . 19
3.2.2 Accelerations of finite-size neutral particles . . . 21
3.2.3 Accelerations of finite-size non-spherical particles . . . 23
3.2.4 Accelerations of finite size non-neutrally buoyant particles . . . 27
3.3 Conclusions and Perspectives . . . 31

4 Rotations and orientations of anisotropic particles in turbulent flows **33**
4.1 Rotation of finite-sized inertial particles . . . 35
4.2 Rotation of anisotropic particles in convective turbulence . . . 39
4.2.1 Anisotropic particles in 2D convective turbulence . . . 40
4.2.2 Anisotropic particles in 3D Rayleigh–Bénard turbulence . . . 42
4.3 Conclusions and Perspectives . . . 48

5 Settling and buoyant particles in turbulence **49**
5.1 The role of gravity in particle laden flows . . . 49
5.2 Accelerations of settling/buoyant particles in turbulence . . . 50
5.3 Settling of particles in turbulent convecting flows . . . 53
5.3.1 Analysis of Particles Residence Times . . . 55
5.3.2 Spatial distribution of settled particles . . . 59
5.4 Recent Developments and Future Perspectives . . . 63

6 Microorganisms in turbulence as motile particles **65**
6.1 Planktonic Copepods: The Basics . . . 66
6.2 The Lagrangian Copepod Model . . . 69
6.3 Clustering and Patchiness . . . 74
6.4 Encounter Rates . . . 77

6.5 Experimental Investigations . . . 81
6.6 Conclusions and Perspectives . . . 82

7 Introduction to freezing and melting in the presence of flows 85
7.1 Motivation . . . 85
7.2 My path through Phase-change coupled to Natural Convection . . . 87

8 Convection with a melting boundary 91
8.1 Basal melting driven by thermal convection . . . 91
8.1.1 Scaling of global quantities . . . 94
8.1.2 Effect of Stefan number . . . 96
8.1.3 Morphology of the phase-change interface . . . 97
8.2 A glimpse into the evolution of multiple ice melt ponds . . . 99
8.2.1 A model of melt pond topography evolution . . . 99
8.2.2 Sensitivity to turbulent heat flux scaling . . . 101
8.2.3 Robustness of pond geometry . . . 102

9 Convective Freezing & Melting in Water 105
9.1 Convective freezing in freshwater . . . 106
9.1.1 Equilibrium ice thickness . . . 107
9.2 Effects of inclination and container aspect ratio . . . 112
9.2.1 Ice front shaping by upward convective current . . . 112
9.2.2 Effects of aspect ratio . . . 114
9.2.3 Bistability . . . 115

10 Freezing Modes and Ice Aging in Salty Water 119
10.1 Convective freezing in salty water . . . 120
10.1.1 Mushy ice and its growth dynamics . . . 120
10.1.2 Global properties of the equilibrium state . . . 122
10.1.3 Multi-layer 1D heat flux model . . . 123
10.2 Sea ice aging by diffusion-driven desalination . . . 126
10.2.1 Dynamics of ice aging . . . 128
10.3 Conclusions and Future perspectives . . . 130

Bibliography 133

***ANNEXES* 148**

A Code Infrastructure the CH4-PROJECT 149

B Complete publications list 151

Abstract

Transport phenomena and the coupling between moving fluids and embedded entities represent a broad research field involving a wide range of physical systems. These entities may be discrete, such as finite-inertia particles, or extended, such as fields with distinct physical properties. My research explores these interactions in canonical flow configurations, simple in geometry but rich in dynamics, including fully developed turbulence and buoyancy-driven convection. It combines advanced computational fluid dynamics with collaborations involving experimental investigations.

The first part focuses on the dynamics of inertial particles in turbulent and convective flows, examining how particle properties, including density, size, and shape, influence their statistical behavior through quantities such as acceleration, rotation, preferential concentration, and settling velocity. This work is further extended to the modelling of planktonic organisms using active-particle approaches.

The second part addresses phase-change phenomena coupled with fluid motion, with the aim of improving our understanding of environmental ice dynamics. It investigates melting and solidification processes in convective systems, including pure substances, freshwater, and saline solutions. Although studied in idealized configurations, such as convective cells with varying sizes, inclinations, and temperature differences, the resulting phenomenology is remarkably rich and still calls for a comprehensive and predictive theoretical description.

Chapter 1

Preface

This document aims to provide an overview of the research work I carried out during my tenure as a Maître de Conférences at the University of Lille, a period that spans from September 2010 to the present. It represents a selection and synthesis of the themes on which I have worked most consistently over these years, supervising intern master students and doctoral theses, collaborating with colleagues either locally or abroad.

All these studies share a common objective: to understand transport phenomena and interactions involving a moving fluid and either localized entities with finite inertia, hereafter referred to as *particles*, or extended entities with negligible inertia but distinct physical properties, termed *fields*. The fluid motion under consideration is often, though not exclusively, turbulent and typically takes place in canonical systems—that is, idealized configurations with simple geometries and boundary conditions, such as homogeneous isotropic turbulence in periodic domains or natural convection in closed systems (e.g. the Rayleigh–Bénard model system).

This manuscript is organized into two main parts. The first part (Chapters 2–6) is devoted to *Particles*. It presents my studies on the dynamics of inertial particles in both fully developed turbulent flows and thermally convecting fluids. The primary focus is on understanding how observables, such as particle acceleration, rotation, and settling velocity, depend - in a statistical sense - on the physical properties of the particles (e.g., density, size, and shape). The final chapter of this part also provides a brief overview of my work on the modeling of planktonic organisms using an active-particle approach.

The second part (Chapters 7–10) is devoted to *Fields*. It focuses on a topic to which I have devoted considerable attention in recent years: the melting and solidification of substances interacting with a fluid in convective motion. Within this broad topic, I have investigated a variety of phase-change problems, including the melting and solidification of pure substances, the melting of ice ponds, the freezing of fresh water and saline solutions, and the aging of porous ice resulting from desalination.

The first appendix briefly presents the computational fluid dynamics (CFD) code that I developed and that became my *computational research laboratory*. Its ability to simulate the transport of both particles and fields within a variety of fluid flows made it the primary computational tool for the research presented in this thesis. The second appendix contains the complete list of my publications together with open-access links to their full texts.

These research themes were advanced through several funded projects and the work of many committed students.
The initial development of the computational code described in Appendix A, was enabled by an industrial contract with the Innocold (Dunkerque-LNG) consortium, which also supported **Kalyan Sherestha**'s PhD thesis (defended in 2015, co-advised with G. Mompean). **Hamidreza Ardeshiri**'s PhD on zooplankton modelling (defended in 2016, co-advised with F. G. Schmitt *CNRS, LOG Wimereux*) was funded by a University of Lille President Scholarship. A French National Research Agency Young Researcher Grant ANR JCJC (ANR-13-JS09-0010) made possible our first exploratory work on thermal convection coupled with phase change in **Babak Rabbanipour Esfahani**'s thesis (defended in 2018, co-advised with S. C. Hirata & N. Ouarzazi). Finally, the ongoing collaboration with C. Sun's group at Tsinghua University in Beijing, providing access to experimental approaches in fluid-dynamics and allowing me to co-mentor the PhD thesis of **Linfeng Jiang**, **Ziqi Wang** (both defended in 2022) & **Yhong Du** (ongoing), was supported in part by the Cai Yuanpei French-Chinese Grant.

For conciseness, I will not mention in this habilitation thesis the research done with some of the doctoral students I have had the opportunity to co-supervise. Specifically, this includes:

- The work of **Himani Garg** on particle transport in diluted solutions of polymers in the regime of elastic turbulence (PhD obtained in 2019, co-supervised with S. Berti & G. Mompean) (Garg et al., 2021, 2018). Himani is now Assistant Professor at Lund University, and we continue to collaborate on the topic.
- The studies of **Wenwei Wu** on the transport of reactive fields in turbulent flows (PhD in 2021, co-supervised with F. G. Schmitt & L. Wang *Shanghai Jiao Tong Univ.*) (Wu et al., 2020, 2021, 2022).
- The work with **Vinicius Beltram Tergolina** and **Alice Jaccod** (PhD both in 2022 and co-supervised respectively with S. Berti, G. Mompean and S. Berti, S. Chibbaro *Sorbonne Univ.*) on phytoplankton dynamics in flows modelled as a reactive field (Jaccod et al., 2021, 2022; Tergolina et al., 2021, 2022).
- The currently ongoing work on thermoconvective onset in the RB system with particles carried on by **Saad Raza** (defended in 2025, coadvised with S. C. Hirata) (Raza et al., 2025, 2024, 2026), now continuing with **Ousman Daouda Ali** (PhD started in 2025 also coadvised with S. C. Hirata).
- The ongoing work of **Luz Andrea Silva Torres** (Silva Torres et al., 2026) (who will defend in 2027, PhD co-supervised with S. Berti) on particle dispersion in stratified fluids.

All the work accomplished on this variety of themes would not have been possible without a professional framework that guarantees academic freedom, a balance between teaching duties, administrative responsibilities and research, along with a pleasant working environment. For this reason, despite the many areas still open to improvement and the emerging challenges brought about by budgetary pressures, I wish to express my sincere gratitude to the French university system and to the Université de Lille, which welcomed me among its members some years ago.

I wish to acknowledge my fellow travellers—Silvia, Stefano, Gilmar, Najib, Moussa, and François—with whom I have shared many professional adventures and countless enriching discussions over the years. I have been also fortunate to develop a rich network of scientific collaborations, many of which have grown into lasting friendships. I am deeply indebted to many colleagues for their continuous support and encouragement throughout the years, and especially during the preparation of this HDR thesis, whose writing I repeatedly postponed as I was carried along by the excitement of ongoing projects. I am particularly grateful to Chao Sun for his enthusiasm, generosity, and warm hospitality during my many visits to his research group.

Chapter 2

Particle laden turbulent flows: A primer

This chapter provides a brief introduction to particle-laden turbulent fluid flows, namely the transport of dispersed bodies by a turbulent flow. This is a broad and multifaceted subject, not defined by a single central problem but rather encompassing a wide range of phenomena, applications, and research areas. We outline the general physical and mechanical setting in which these phenomena should be understood, introducing the fundamental concepts underlying their modelling and the basic terminology used throughout this document.

2.1 Descriptions of fluid motion: Lagrange *vs.* Euler

While the perception of fluid motion is familiar to us from everyday experience, it is less obvious how to talk about it, or to describe it, let alone quantify it. This is a question to which at least two physically sound and, in a certain sense, complementary answers can be given: the Lagrangian and Eulerian descriptions of fluid motion. It is useful to briefly review them here.

A first approach is to imagine a fluid as composed of a collection of distinct fluid parcels (or particles), with positions $\boldsymbol{x}_f$ at the initial time t_0 which evolve over time t: we use the notation $\boldsymbol{x}_f(t;t_0)$. Based on this definition - known as the **Lagrangian** or material description - it is straightforward to define the velocity $\boldsymbol{u}$ of a particle at time t or its acceleration $\boldsymbol{a}$, through derivatives in time:

$$\frac{d}{dt}\boldsymbol{x}_f(t;t_0) = \boldsymbol{u}(t;t_0) \tag{2.1}$$

$$\frac{d^2}{dt^2}\boldsymbol{x}_f(t;t_0) = \boldsymbol{a}(t;t_0). \tag{2.2}$$

The incompressibility of the fluid—as it is reasonable to assume in the case of liquids and as we will do throughout this thesis—implies that two or more particles cannot occupy the same position simultaneously, and therefore their trajectories cannot intersect at a given moment in time. The motion of a fluid is hence described by the set of trajectories of the fluid parcels that compose it.

However, we shall note that this Lagrangian point of view does not take us very far in terms of quantitative description. How does a fluid move? This depends on the externally applied forces to the parcels as well as on the internal ones which stem from how fluid particles interact with one another. While it is possible, in principle, to model frictional forces between neighboring fluid particles in Lagrangian terms, it is much harder to express in a mathematically tractable form the effect of the pressure, which arises also from long-range interactions involving all particles simultaneously. The path of a quantitative Lagrangian description of an incompressible fluid thus quickly proves to be impractical.

A second approach is to describe the motion of a fluid by assuming that its velocity can be described by vectors located at any position in the space occupied by the fluid, such vectors may depend on time, in other words one introduces a time dependent vector field $\boldsymbol{u}(\boldsymbol{x}, t)$. Its evolution at a fixed location in space (**Eulerian** or spatial description) is ruled by the Navier-Stokes (NS) equation:

$$\partial_t \boldsymbol{u} + (\boldsymbol{u} \cdot \boldsymbol{\nabla})\boldsymbol{u} = -\frac{1}{\rho_f}\boldsymbol{\nabla} p + \nu \boldsymbol{\Delta} \boldsymbol{u} + \boldsymbol{f}_e. \tag{2.3}$$

This equation expresses Newton's second principle of dynamics, $\boldsymbol{a} = \boldsymbol{F}/m$, for an incompressible continuum medium with linear internal friction forces (Newtonian fluid) and external force per unit mass (i.e. acceleration) $\boldsymbol{f}_e$, e.g., gravity. The left-hand-side terms represent nothing else than the fluid acceleration $\boldsymbol{a}_f = \frac{D}{Dt}\boldsymbol{u}$, the symbol $\frac{D}{Dt} = \partial_t + (\boldsymbol{u} \cdot \boldsymbol{\nabla})$ denotes the so called fluid material (or convective) derivative. It shows that the acceleration of a fluid in any given spatial position may be the result both of a local temporal variation of the velocity or of the transport by the velocity itself of velocity gradients from nearby regions. Let us note *en passant* that this term is quadratic in $\boldsymbol{u}$, a fact that lies at the root of the complexity of fluid mechanics.
The NS equation written above assumes that the fluid is identified by two constant material parameters the mass density ρ_f and the kinematic viscosity ν, and that is incompressible, all these hypothesis are valid for fluid flows characterised by small velocity amplitudes (much smaller than the speed of sound in the same medium) and which are isothermal. The pressure scalar field $p(\boldsymbol{x}, t)$, the fourth scalar unknown in the equations (besides the three velocity components), can be determined by means of the incompressibility constraint (or continuity or mass-conservation equation: $\boldsymbol{\nabla} \cdot \boldsymbol{u} = 0$).

While the field-based Eulerian approach is naturally suited to describe temporal measurements at fixed locations—such as those performed at meteorological weather stations—the fluid parcel Lagrangian perspective is more intuitive and suitable when addressing problems involving spatial transport, such as the release from a source of pollutant substance in a flow. The Eulerian framework is more convenient for analytical treatments, though it remains exceptionally challenging: the NS equation admits analytical solutions only in a few simplified scenarios (none of which capture the complexity of turbulent flows). On the other hand, as we have discussed the Lagrangian approach is inherently not closed—calculating the trajectory of a single Lagrangian particle requires knowledge of fluid velocity gradients and pressure, which in turn depend on the global configuration of all other particles in the flow. As such, these quantities cannot be determined from local information alone, limiting the practical use of a fully Lagrangian description. However, the formal link between these two description, Eulerian and Lagrangian, is straightforward,

and can be expressed as:

$$\frac{d}{dt}\boldsymbol{x}_f(t;t_0) = \boldsymbol{u}(t;t_0) \equiv \boldsymbol{u}(\boldsymbol{x},t)|_{\boldsymbol{x}=\boldsymbol{x}_f(t)} \tag{2.4}$$

$$\frac{d^2}{dt^2}\boldsymbol{x}_f(t;t_0) = \boldsymbol{a}(t;t_0) \equiv \frac{D}{Dt}\boldsymbol{u}(\boldsymbol{x},t)|_{\boldsymbol{x}} = \boldsymbol{x}_f(t). \tag{2.5}$$

Such a connection can be used to switch from one vision of the system to the other, depending on the problem.

2.2 Turbulence

When a fluid is set into motion with a velocity amplitude beyond a critical value, which depends on the system, the fluid movement can acquire a spatially and temporally disordered state that we call *turbulence*. Such a phenomenon is certainly familiar to every reader as turbulent flows are encountered everyday in life. We see or sense fluid turbulence effects when we vigorously mix coffee in a cup, when we boil water in a pot for cooking, while biking on a windy day or when on a plane we experience a bumpy fly.

More precisely, when the NS equation is complemented with a geometrical domain and boundary conditions, a dimensionless quantity, the Reynolds number, $Re = UL/\nu$, where U and L are problem dependent velocity and space scale, can be introduced. Re parametrizes the global state of the system. Turbulence is characterized by large values of the Reynolds number, which is understood as the regime of the flow where the non linear term in $\boldsymbol{u}$ in NS prevails with respect to the dissipative one. In the Lagrangian frame this correspond to the fact that the fluid acceleration is dominated by the pressure gradient rather than by the viscous friction.
The nonlinear character of NS equation makes it extremely hard to study this problem with analytical techniques, on the other hand the chaotic and unpredictable character of the flow suggests that a suitable approach for a description of turbulence shall be in statistical terms. The *problem of turbulence*, has been defined over time in different ways. As pointed out by the historian M. Eckert (Eckert, 2019), it has indicated through the years and in different scientific communities either the transition to turbulence or the closure problem, or the complete statistical description of its scaling properties (see also the recent (Sreenivasan and Schumacher, 2025)). In this text, we will refer to the latter meaning. In the Eulerian frame the statistical properties of turbulence are highlighted by looking at velocity difference across different spatial locations at equal times. The most commonly studied observables are two-point quantities called Structure functions

$$S_p(\ell) = \langle(\delta_\ell u)^p\rangle, \qquad \delta_\ell u = (\boldsymbol{u}(\boldsymbol{x}+\boldsymbol{r},t) - \boldsymbol{u}(\boldsymbol{x},t)) \cdot \frac{\boldsymbol{\ell}}{|\boldsymbol{\ell}|} \tag{2.6}$$

that are momenta of longitudinal velocity differences, where the average is taken over ensemble or homogeneity directions of the studied system.
Although some exact results for low-order structure functions (second and third order) can be derived from the Navier–Stokes equations under the assumption of statistically homogeneous turbulence (through the Kármán–Howarth equation), there is still no general theory based solely on the NS equations that can predict the form of structure functions of

all orders p. However, various phenomenological models are available (based on assumptions inspired by observational data) that can predict the behaviour of the structure functions within certain limits. Here, we just mention the similarity theory of Kolmogorov and Obhukhov proposed in 1941 (K41 so in the following) , its subsequent refinement in 1962, and, more recently, the multifractal model, see (Frisch, 1995) and (Alexakis and Biferale, 2018) for more recent descriptions of the topic. We also note that the description of the statistical properties of turbulence in Lagrangian terms (along fluid particle trajectories) is more problematic than the Eulerian one, precisely because it lacks independent dynamical equations. However, a great deal of research in recent years has been devoted to understanding the links between the two descriptions in statistical terms, see for a recent account (Toschi and Bodenschatz, 2009).

2.3 The motions of material particles

As we have seen, the concept of Lagrangian fluid parcels and their trajectories, is useful for thinking about the dispersion and the transport by a fluid flow. However, to some extent, this remains an idealized representation. In reality, any material body immersed in a fluid possesses its own inertia determined by its mass, as well as a finite size. Such a material body (from now on called particle) does not exactly and permanently follow the trajectory of a fluid particle. Therefore, the transport of a material particle does not coincide with the one of the surrounding fluid parcels. It is thus legitimate to ask — and this has been a classical question in fluid dynamics — how is an inertial particle transported in a fluid flow?

The equation describing the dynamics of a tiny spherical particle in a flow is nowadays refereed as the Maxey-Riley and Gatignol (MRG) equation, who re-derived them in a modern form (Gatignol, 1983; Maxey and Riley, 1983), even though it is the result of the contributions of studies by many authors (among others Stokes (1851), Boussinesq (1851) Basset (1888), Oseen (1927), Faxén (1922), Tchen (1947), Corrsin-Lumley (1956) to cite only the most noticeable works). The equation for a sphere of of radius r_p and mass m_p, reads:

$$m_p \frac{d\mathbf{v}}{dt} = 6\pi\mu r_p(\mathbf{u}-\mathbf{v}) + m_f \frac{D\mathbf{u}}{Dt} + \frac{m_f}{2}\frac{d(\mathbf{u}-\mathbf{v})}{dt} + 6r_p^2\sqrt{\pi\rho_f\mu}\int_0^t \frac{d(\mathbf{u}-\mathbf{v})}{d\tau}\frac{d\tau}{\sqrt{t-\tau}} + (m_p - m_f)\mathbf{g} \tag{2.7}$$

where $\mathbf{v}(t) \equiv \frac{d}{dt}\boldsymbol{x}_p(t)$ indicates now the velocity of the particle, while $\mathbf{u}(x_p(t), t)$ denotes the unperturbed fluid velocity at the particle position (meaning the velocity that the fluid flow would have at that position in a identical flow where the particle was not present) and m_f the mass of a spherical equivalent volume of fluid. Such an equation is derived from a linearization of NS equation, i.e. the time-dependent Stokes equation, as such it relies on the hypothesis that the particle velocity is small with respect to the fluid one. In dimensionless terms this amount to assuming that the particle Reynolds number based on the slip velocity with respect to the fluid, is vanishing

$$Re_p = \frac{||\mathbf{u}-\mathbf{v}||(2r_p)}{\nu} \ll 1. \tag{2.8}$$

The above equation (2.7) also does not assume the variation of the flow field at the scale of

the particle. When instead weak variations of the flow are allowed, expressed in terms of a vanishing shear Reynolds number

$$Re_s = \frac{||\boldsymbol{\nabla}\mathbf{u}||(2r_p)^2}{\nu} \ll 1 \tag{2.9}$$

the equation can be modified by the addition of the so called Faxén's corrections, which amount to replacing in eq. (2.7) the unperturbed fluid velocity with appropriate spherical surface and volume averages respectively in dissipative forces and inertial ones. To the leading order this corresponds to the following changes:

$$\mathbf{u} \rightarrow [\mathbf{u}]_S \simeq \mathbf{u} + \frac{r_p^2}{6}\Delta\mathbf{u} \tag{2.10}$$

$$\mathbf{u} \rightarrow [\mathbf{u}]_V \simeq \mathbf{u} + \frac{r_p^2}{10}\Delta\mathbf{u}. \tag{2.11}$$

Two other corrections at least deserve to be mentioned here. When the particle Reynolds number Re_p is not small, the for-aft symmetry of the flow around the particle is broken and a wake forms behind the particle. Mathematically this corresponds to the come into play of non-linear terms of the NS equation and to an increased drag force on the particle. This can be accounted for an empirical correction to the linear drag (also called Stokes drag) proposed by Shiller and Neumann (Schiller and Naumann, 1935):

$$6\pi\mu r_p \rightarrow 6\pi\mu r_p(0.15\ Re_p^{0.687})\ , \text{ if } Re_p \lesssim 10^3. \tag{2.12}$$

While the drag force is, by definition, a force opposite to the relative motion of a body moving with respect to a surrounding fluid, the lift force is perpendicular to it. A lift can be generated around a spherical particle if a vortical motion is present in the surrounding fluid flow. In such case the inviscid calculation by Auton (1987), leads to the following expression

$$\mathbf{f}_{lift} = \frac{m_f}{2}(\mathbf{u} - \mathbf{v}) \times (\nabla \times \mathbf{u}) \tag{2.13}$$

We observe that due to the proportionality to m_f, such a force is negligible for particles whose density is much larger than the one of the fluid $\rho_p \gg \rho_f$, like sand in air, while it is important in the opposite case, e.g. for air bubbles in water.

2.4 Particle-laden flows

In the previous section, we discussed which equation of motion can best describe the trajectory of a single material particle transported by a fluid flow. However, we did not address the situation in which many particles are present in the fluid environment. This is the case of the so-called particle-laden flows, or dispersed phase flows (i.e., a particulate phase and a continuous fluid phase). These kind of physical system is very common in nature as well as in industrial applications. Examples include sands in ocean turbidity currents (Meiburg and Kneller, 2010), planktonic organisms in marine ecosystems (Guasto et al., 2012), ice crystals and droplets in clouds (Falkovich et al., 2002; Heymsfield, 1977), atmospheric particles causing smog (Sabban and Hout, 2011). Industrially, particle-laden flows are found in papermaking (Lundell et al., 2011), fluidized beds (Tavoulareas, 1991), and ore flotation

(Meyer and Deglon, 2011). Their understanding in realistic conditions (often involving turbulent flows) is essential for the optimization of productive processes.

The complexity of these phenomena stems primarily from two factors. First, hydrodynamic turbulence—as also observed in single-phase fluids—is an inherently nonlinear phenomenon, characterized by a large number of degrees of freedom, which manifests in the emergence of multiple temporal and spatial scales; thus, in principle, only a statistical approach to its analysis proves feasible. Second, the dispersed particles, defined by their physical properties (such as size, shape, mass density, volume concentration, etc.), introduce additional degrees of freedom into the system, giving rise to novel physical effects as their coupling with the carrier fluid becomes increasingly significant.

Particle laden flows are thus classified in terms of the level of coupling between the two constituent phases (Balachandar and Eaton, 2010; Elghobashi, 1994). A common terminology is the following:

- **One-way coupled** systems: When particles are smaller or close to the smallest active fluid motion scale and their total volume fraction Φ_v is low ($< 10^{-6}$), the particle dynamics does not affect the flow and the dispersed phase is solely transported by it.
- **Two-way coupled**: Larger particles or higher Φ_v (conventionally $\leq 10^{-3}$) cause changes in the fluid velocity field that may alter the overall characteristics of the flow (e.g. weakening or enhancing turbulence).
- **Four-way coupled**: At even higher Φ_v, particle-particle collisions and interactions become important and can affect further the behaviour of the system leading to collective effects on the particulate phase.

Even restricting the study to the first situation, namely the case in which the particles do not influence the dynamics of the fluid, the occurring phenomena can be extremely diverse. This is because, alongside the Reynolds numbers of the fluid flow (Re) and those of the particles (Re_p, Re_s) mentioned before, other parameters to define the problem come into play. These are, the Stokes number (St), which characterizes the effect of the viscous relaxation time of the particle with respect to the typical variation time of the flow. In the simple case of a particle whose size $2r_p$ (diameter) is smaller than any other active scale in the fluid flow, hence the dissipative scale η in the case of turbulence, then $St = \tau_p/\tau_\eta$, where $\tau_p = r_p^2(1 + 2\rho_p/\rho_f)/(9\nu)$ from MRG eq, and $\tau_\eta = \eta^2/\nu$ follows from the K41 dimensional theory of turbulence. A second key parameter is the density ratio between particle and fluid (ρ_p/ρ_f), which parametrizes the relative effects of the inertia of the two phases; and the Froude number (Fr), which measures the importance of the Archimedes buoyancy force relative to the acceleration of the fluid.

This set of three parameters gives rise to phenomena such as the preferential sampling by particles of fluid regions, particle clustering, the demixing (also called segregation) of polydisperse particulate suspensions (Fessler et al., 1994; Maxey, 1987). These are topics on which I worked on extensively prior to my arrival at the University of Lille (Calzavarini et al., 2008a,b), see Figures 2.1 and 2.2. The two phenomena mentioned above are mainly controlled by the Stokes number (St) and the density ratio. Clustering occurring maximally when $St \simeq 1$. When the Froude number (Fr) comes into play, particle sedimentation

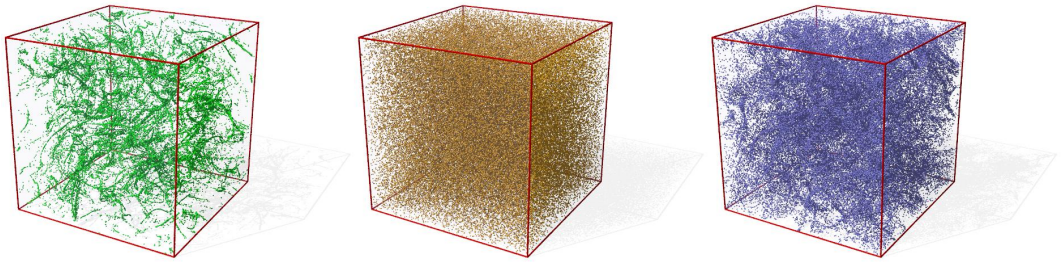


FIGURE 2.1: Illustration of inertial particle distributions in a turbulent from: (from left to right) bubbles, fluid tracers; heavier than the fluid particles, all with $\mathrm{St} = 0.6$. From Calzavarini et al., 2008b.

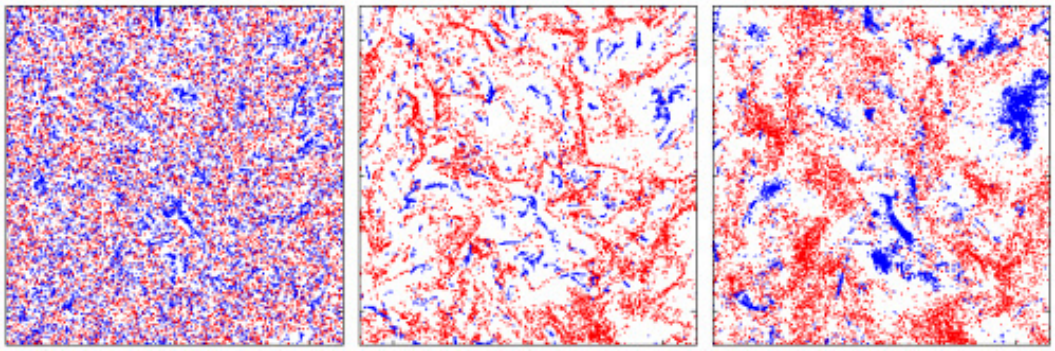


FIGURE 2.2: Illustration of the segregation phenomenon, particle heavier than the fluid are in red while light ones are in blue color. The St number increases from left to right. The maximal segregation occurs for $St \simeq 1$, in the middle. From Calzavarini et al., 2008a.

appears to. The way in which the buoyancy force interacts with turbulence, either accelerating or slowing down the sedimentation of particles compared to the case of a suspension in a fluid at rest is a classical and still challenging subject of study (Petersen et al., 2019; Wang and Maxey, 1993).

The quantitative characterization of the statistical properties of inertial particles transported by turbulent flows has, in recent decades, relied not only on the most advanced visualization and tracking techniques, but also on state-of-the-art numerical simulations using high-performance computing, together with a wide range of theoretical tools (Bec et al., 2024; Brandt and Coletti, 2022; Toschi and Bodenschatz, 2009).

2.5 Research Objectives

My more recent research in the field of dispersed-phase fluids has focused on several specific problems, which can be formulated as the following questions:

1. What are the statistical properties of the **acceleration** of inertial spherical particles in fully developed turbulent flows? How do these properties depend on the particle mass density and on their size?

2. In the case of non-spherical particles, their **rotational dynamics** are influenced not only by the fluid vorticity but also by strain. Furthermore, since spherical symmetry

is broken, preferential alignment effects may arise. What are these effects, and how do they depend on the particle size or on the flow characteristics?

3. When the contribution of gravitational acceleration becomes comparable to or greater than that of the flow-induced acceleration, **sedimentation** effects become significant. What are the mechanisms of interaction between turbulent flow and buoyancy forces in this regime?

4. Certain marine organisms, such as plankton, have characteristic sizes comparable to the smallest turbulent scales and densities close to that of seawater. They can therefore be approximated as weakly inertial particles advected by a flow. Some of these organisms—*copepods*, for example—have developed, through natural evolution, non-trivial **motility** strategies that enable them to survive, reach nutrient sources, and reproduce in environments dominated by highly energetic ocean currents. Is it possible to test hypotheses on the behavior of such organisms by means of Lagrangian modeling, treating them as *active particles*?

The following chapters will be devoted to presenting my researches addressing the above questions, though in some cases the questions remain only partially resolved.

Chapter 3

Accelerations of inertial particles in turbulence

Contents

2.1 Descriptions of fluid motion: Lagrange *vs.* Euler 5
2.2 Turbulence 7
2.3 The motions of material particles 8
2.4 Particle-laden flows 9
2.5 Research Objectives 11

3.1 Inertial particles accelerations statistics

In the last decades the study of the acceleration of inertial particles in turbulent flows, and more specifically the statistical characterization of this observable in fully developed turbulence, has stirred up considerable interest. The problem is central to the investigation of turbulent flows both from the practical and from the fundamental perspective.
First, from the applicative point of view one can observe that all modern non invasive techniques of flow imaging are essentially based on the principle of particle tracking, this is the case of the widely employed Particle Image Velocimetry (PIV) technique which is based on image correlations of particles or the Particle Tracking Velocimetry (PTV) based on the particle trajectory reconstruction. The accuracy of such techniques relies on the precise characterization of the relation between the acceleration of the tiny particles seeding the flow (for PIV/PTV in water typically neutrally buoyant polystyrene particles are used) and the 'true' local fluid acceleration that the flow would have at the same positions without the presence of the particle probes.
Second, on a more fundamental level, it is evident that if the mass of the particles is known, the knowledge of their accelerations is equivalent to the information on the local hydrodynamic forces acting on specific position in a turbulent flow. This allows to precisely probe and investigate the characteristics of the smallest scale structures of turbulent flows.

This chapter is based on:

1. *Dynamics of finite-size spheroids in turbulent flow: the roles of flow structures and particle boundary layers*, Lin-Feng Jiang, Cheng Wang, Shuang Liu, Chao Sun, Enrico Calzavarini, [http://arxiv.org/abs/2202.03937] J. Fluid Mech 939 , A22 (2022) [PDF]

2. *Accelerations of large particles in turbulence*, Yaning Fan, Cheng Wang, Linfeng Jiang, Chao Sun and Enrico Calzavarini, EPL – Europhys. Lett.,145 (4), pp.43001 (2024) [PDF]

The pioneering experiments performed in Bodenshatz group (La Porta et al., 2001) in early 2000 have first clearly highlighted the strong fluctuations characterizing the accelerations of tiny particles in turbulence (see Fig. 3.1). In the these works three main observations were

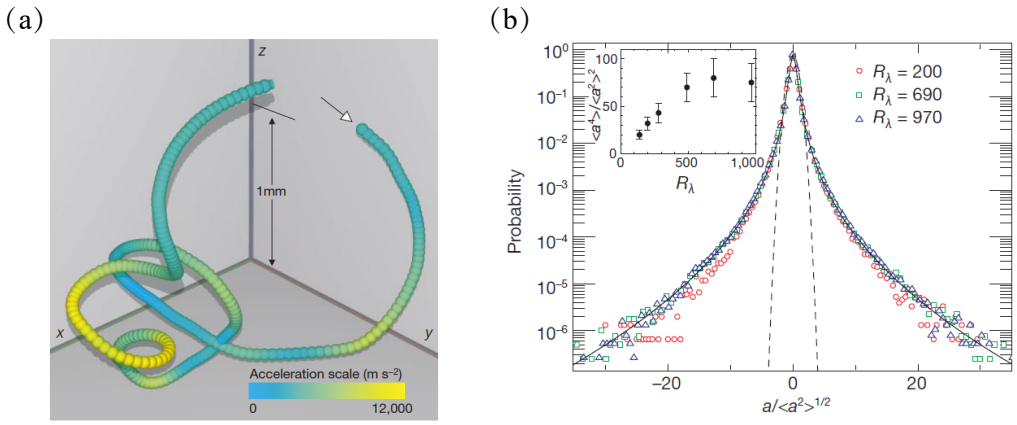


FIGURE 3.1: (a) Experimental tracer particle trajectory at Taylor Reynolds number 970 colored by acceleration magnitude. (b) Probability density function of acceleration fluctuations; inset showing flatness dependence. Adapted from La Porta et al., 2001.

put forward: i) The probability density function of the instantaneous acceleration (any of its cartesian components) along a trajectory is non-Gaussian, with events often surpassing several times the gravitational acceleration. ii) The magnitude of the acceleration intensity is of the order of the fluid acceleration at the dissipative scale, $a_\eta = \eta/\tau_\eta^2$, however with a remaining weak but non-negligible Reynolds number dependence. In other words the so called Heisenberg-Yaglom 'constant' (a_0), which is defined from the acceleration variance $\langle a_i^2 \rangle$ (summation non implied):

$$a_0 \equiv \frac{\langle a_i^2 \rangle}{a_\eta^2}, \tag{3.1}$$

is not a constant but possibly a weakly increasing function with the flow Reynolds number (which in turbulence is defined as the Taylor-scale based Reynolds number Re_λ). Finally, iii) the acceleration dynamics is extremely rapid, the temporal correlation of the a_i cartesian components of the acceleration is of the order of the dissipative time (τ_η).

These intriguing experimental results stimulated the development of numerical studies through high-resolution simulations of fluid tracers and particles in turbulent flows. Simulations revealed that the above described acceleration properties are due to the existence of recurring turbulent flow structures. The most evident ones are denoted as vortex filaments (Biferale et al., 2004a), they produce huge centrifugal accelerations along fluid tracer trajectories, see Figure 3.2.

In this context, my research has focused on understanding two aspects related to the dynamics of accelerations of inertial particles: the effects of virtual or added mass, which is related to the relative density between the particle and the fluid, and the effect of the size of the particle.

The case of a neutrally buoyant particle ($\rho_p = \rho_f$) is clearly the simplest, although still non-trivial. When the size of such a particle is small enough and its shape spherical (isotropic)

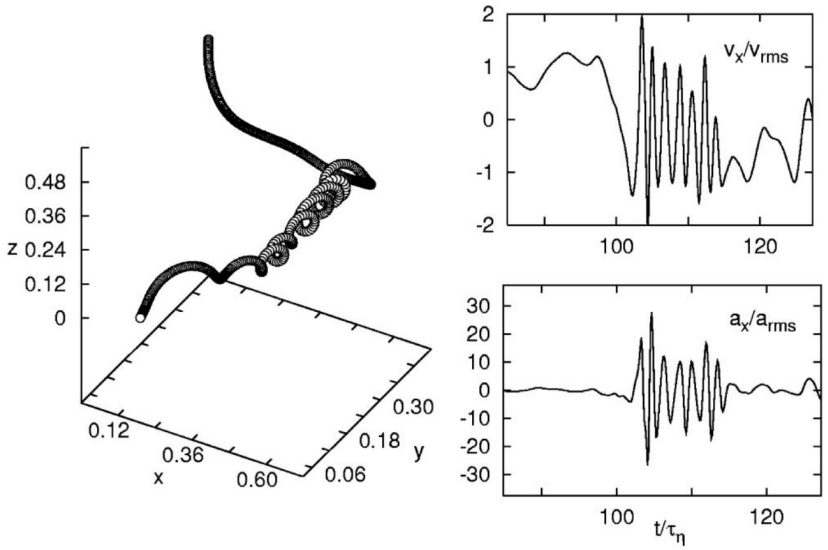


FIGURE 3.2: Trajectory and time series. Left panel: 3D trajectory of a trapping event in vortex filament. Acceleration and velocity fluctuations here reach about 30 and 2 r.m.s. values, respectively. Reproduced from Biferale et al., 2004a

it is natural to expect that the inertial effects can be neglected and that its trajectory reproduces without biasses the one of an ideal fluid tracer. On the other hand when the particle is larger - e.g. of the order of the dissipative scale of turbulence - inertia can play a double role. In first place the effect of hydrodynamics drag is to filter in time the fluctuations of the fluid velocity that occurs on a shorter time-scale than τ_p, this leads to reduced accelerations. Secondly the particle trajectory could depart from the fluid one and sample different regions of the flow in a biassed way. The latter phenomenon is known as preferential sampling.

The case of non-neutrally buoyant particles ($\rho_p \neq \rho_f$) calls into play a further effect, the extra acceleration due to the inertia of the displaced fluid when the particle move. Such an inertia can be important in the case of particles that are much lighter than the fluid, while it is negligible for heavy ones (ballistic limit). This purely inertial effect (as opposed to dissipative ones like for the drag) denoted with the name of added mass has been shown to be responsible for a strong phenomenon of particle preferential concentration. The added mass term contributes to the accumulation of particles lighter than the fluid inside vortical structures. Such preferential sampling and concentration effect are reflected in different acceleration properties.

I first addressed these phenomena in 2008 in a work in collaboration with the group at École Normale Supérieure (ENS) Lyon which combined numerical and experimental work (Volk et al., 2008). The modelling approach undertook in that study consisted in a strong simplification of the MRG equation that considered uniquely the Stokes drag and the added mass effect, as follows:

β-St model

$$\frac{d\mathbf{V}}{dt} = \frac{1}{St}(\mathbf{U} - \mathbf{V}) + \beta \frac{D\mathbf{U}}{Dt}. \tag{3.2}$$

This model has just two dimensionless parameters, the modified density ratio $\beta = 3\rho_f/(\rho_f + 2\rho_p)$ and the Stokes number, for this reason is sometime dubbed the β-St model. The variance of the acceleration in this two-dimensional parameter space for particles in a

moderately developed turbulent flow ($Re_\lambda = 75$) from our numerical simulations is shown in figure 3.3. Two important features could be underlined: the mean acceleration intensity

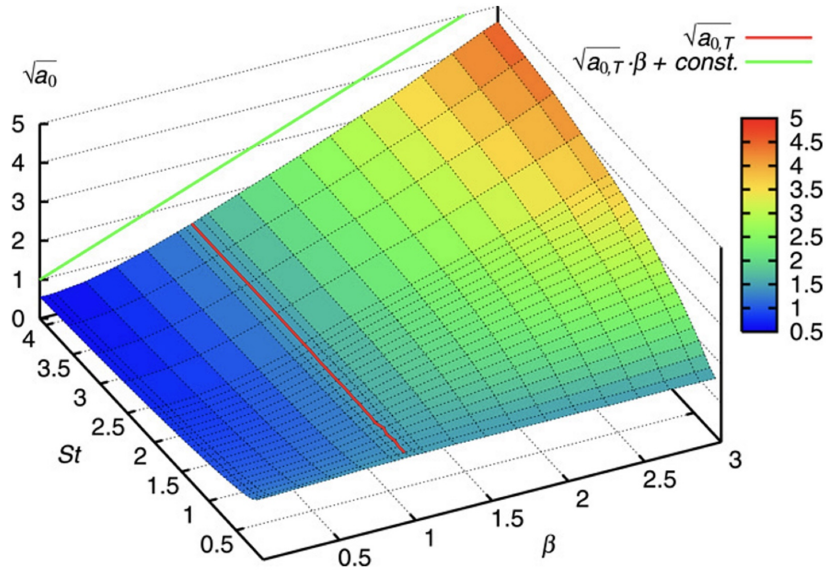


FIGURE 3.3: Dimensionless acceleration variance ($\sqrt{a_0}$) versus β and St according to the β-St model.From Volk et al., 2008.

increases with β, it coincides with the fluid acceleration intensity $D\mathbf{u}/Dt$ for neutral particles, while it is larger for light ones and smaller for heavy ones. The differences tend to vanish when St is small, while their are maxima for large St values, because the effect of viscous drag ($\propto St^{-1}$) tends to vanish and so the acceleration amplitude tends to coincide with the one of the inertial added mass term $\beta D\mathbf{u}/Dt$. Remarkably the St parameter seems to have no effect on neutral particles. However, in Volk et al., 2008 we observed that while the trends with respect to β detected in the numerical simulations of (3.2) were corroborated by the experimental measurements, the trend with St was not supported by them. In particular the experiments observed a marked decrease in the typical acceleration of large neutrally buoyant particles as compared to small ones and fluid tracers. Similar partial agreements were observed in the temporal correlation function of the acceleration. Bubbles displayed shorter correlations than tracer while the opposite was true for heavy particles, this both in experiments and simulations. However, in the experiments an increase of the temporal correlation was also observed for large neutral particles as compared to tracers, while this was absent in the simulations with the β-St model.

This study clearly indicated that the adopted particle dynamics modelization, while satisfactory in the description of the effects mediated by particle density, was incomplete for what concerned the effect of particle spatial-size. The particle diameter indeed in this model affects only the amplitude of the particle response time ($\tau_p = D^2/(12\nu\beta)$). In other words the β-St is a point-particle model, which only accounts for the effect of temporal filtering of fluid fluctuations by the viscous Stokes time and disregards the effect of spatial filtering due to the finite size of the particles. As mentioned in Chapter 2 the effect of spatial extension of the particle can be taken into account in the particle equation of motion by means of the Faxén corrections , which correspond to specially defined spatial averages (either surface or volume averages, see eq. (2.10-2.11). This is a suitable approximation as

long as the size of the particle is of the order (or smaller) than the typical radius of curvature of the fluid velocity field, that in turbulent flow corresponds to the Taylor microscale (λ). Including this ingredient in the minimalistic β-St model leads to:

Faxén β-Stokes model

$$\frac{d\mathbf{V}}{dt} = \frac{1}{St}([\mathbf{U}]_S - \mathbf{V}) + \beta \left[\frac{D\mathbf{U}}{Dt}\right]_V, \tag{3.3}$$

where the square brackets indicate the mentioned averages. In the vanishing particle size limit these terms amount to introduce corrections proportional to the laplacian of the velocity field times the squared particle diameter. However, the model (3.3) can be implemented numerically in a more efficient way by approximating the averages over a spherical domain with averages over a three-dimensional Gaussian envelope. This was indeed the approach we proposed in a work where we studied the impact of spatial finite size on the accelerations properties (Calzavarini et al., 2009). As shown in figure 3.4 the Faxén-β-St model was capable to reproduce two main effects highlighted in the previous experiments, namely the reduction of the variance of the fluid acceleration and the increase in the temporal correlation time with the particle size. Furthermore, an additional effect was brought up by the model, the reduction of extreme events in the acceleration distribution of larger particles. This can be visualized by comparing the probability density functions (pdf) of the accelerations, normalized by their standard deviations, for particles of different size. Or alternatively by computing the evolution of the flatness factor of the acceleration as a function of the particle diameter (see again figure 3.4). However, such a feature seemed to be not present in the available experimental measurements, in 2009. In a further numerical

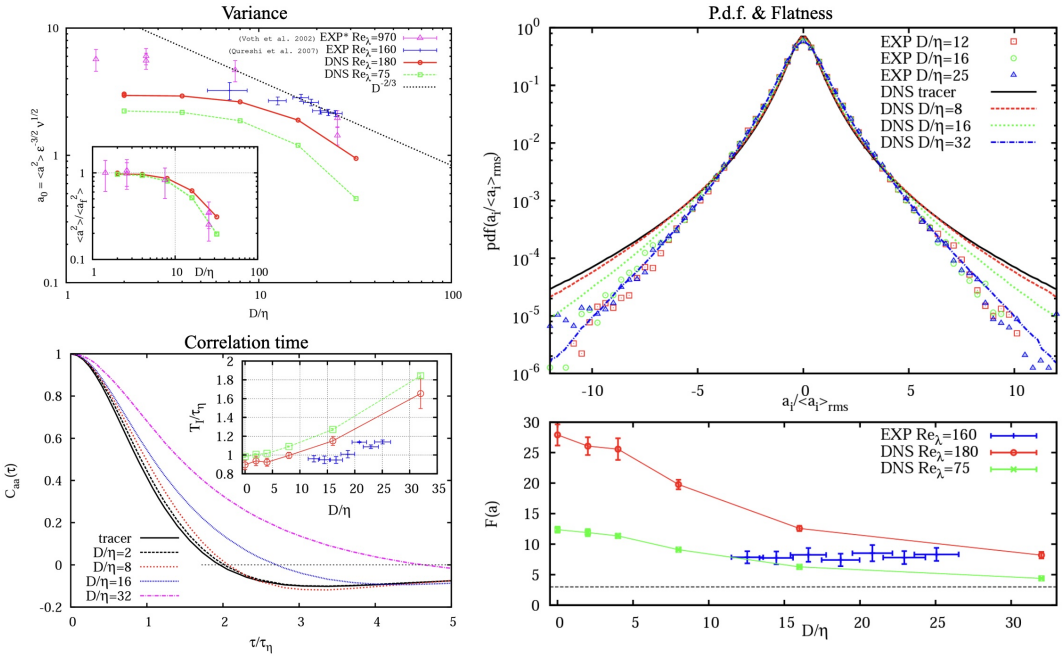


FIGURE 3.4: Trends of acceleration variance, correlation time, *pdf* and flatness versus the particle size for neutrally buoyant particles according to the β-St model and experiments. From Calzavarini et al., 2009.

study, we confirmed that, for neutral particles, the inclusion of the unsteady drag force (i.e.

history force) and the non-linear drag force (wake drag) which had been previously neglected do not affect significantly the statistical acceleration properties even if they modify the velocity fluctuations (Calzavarini et al., 2012).

We shall mention here the available theoretical predictions for the behaviour of the above described quantities, which are scarce and solely based on dimensional reasoning. The motion of neutrally buoyant finite-size material particles in a turbulent flow is typically regarded as the result of turbulent flow fluctuations occurring at the scale of the particle. In other words, the particles are seen as probes of a coarse-grained turbulent field. This implies that the scaling trends in the fluctuations of accelerations as a function of the particle size are interpreted in terms of the known scaling of structure functions of turbulence. For that, the scaling laws given by the Kolmogorov (K41) phenomenology and its refinements can be adopted. This interpretation assumes that neutrally buoyant material particles are only weakly coupled to the flow, so that the feedback effects (i.e. the two-way coupling) stemming from the formation of boundary layers and wakes around the particle do not play a significant role, at least in statistical terms. This implies respectively that the typical intensity, temporal correlation and flatness for the acceleration of a particle of size $D = 2r_p$ is expected to follow:

$$a(D) \sim \frac{\delta_D p}{D} \sim \frac{(\delta_D u)^2}{D} \sim D^{-1/3} \tag{3.4}$$

$$\tau_a(D) \sim \frac{D}{\delta_D u} \sim D^{2/3} \tag{3.5}$$

$$\mathcal{F}_a(D) \sim \frac{\langle a(D)^4 \rangle}{\langle a(D)^2 \rangle^2} \sim D^{\zeta_4 - 2\zeta_2} \tag{3.6}$$

where ζ_p is the scaling exponent of the p-order structure function $\langle (\delta_\ell u)^p \rangle \sim \ell^{\zeta_p}$.

The experimental study by Volk et al., 2011, in which I was involved, confirmed all the trends highlighted in the Faxén β-St model, including the ones on the reduction of the acceleration variance and increasing of the temporal correlation, and for the first time in an experiment, the sensible reduction with respect to tracers of the acceleration flatness for larger spheres.

Although the comparison between experiments, simulations, and theoretical models gave encouraging results, the problem was far from solved in general terms. Both the simulations and the theory focused only on relatively large particles, but still small enough that the fluid velocity field could be treated as smooth (approximately $D \simeq 10\eta$). What happens instead when particles are so large that their size falls within the inertial range of turbulence? The inertial range is the regime in which the dynamics of the energy cascade —from the larger vortical structures to the smaller ones—is dominated by the nonlinear couplings present in the NS equations, and where the effects of viscosity are negligible. However, this is true for the fluid flow not strictly for the particles, around which viscous boundary layers can form.

Studying this regime of large particles requires more advanced tools, especially on the numerical and theoretical side. The MRG equation is no longer adequate to describe inertial-scale particles. As a result, it is not possible to rely on the same approaches used earlier, such as the Eulerian–Lagrangian modelizations with one-way coupling. Instead, one must use simulations that fully resolve the hydrodynamic scales of the problem—that is, the

fluid flow around the particle, including characteristic structures such as boundary layers and wakes. It took roughly a decade before these fully resolved numerical methods became widely adopted in this domain of research (Homann and Bec, 2010; Ten Cate et al., 2004; Uhlmann, 2005). I also pursued this approach starting from 2020 in collaboration with a research team at Tsinghua University (Beijing, China), where we codeveloped a CFD code for fully resolved particle simulations. Our study focused on large neutrally buoyant particles, considering both spheres and spheroids, and later on non-neutral particles. In the following, I will briefly outline both the methodologies and main findings of these relatively recent studies.

3.2 Simulations of finite-size spheroids in turbulence

3.2.1 Methodology and study protocols

The numerical experiment conducted in our study (Jiang et al., 2022) consisted of evolving a set of particles within a cubic, triperiodic spatial domain, where a statistically stationary, homogeneous, and isotropic turbulent flow is simulated. At difference from previously discussed studies, the key distinction here is that particle dynamics are governed directly by the rigid-body equations, rather than by perturbative models (such as the MRG) or approximate ones (such as the one for finite-sized particle discussed in the previous section). This approach removes the need for small Reynolds number approximations (Re_p, Re_s), allowing the numerical simulation to remain physically consistent without such constraints. Its main drawback, however, is the significantly higher demand for memory and computational resources, along with the increased complexity of numerical implementations (particularly when addressing code parallelization and scalability challenges).

The translation and rotation of rigid-body material particle is governed by the Newton-Euler equations (NEE):

$$m_p \frac{\mathrm{d}\mathbf{v}}{\mathrm{d}t} = \mathbf{F} + \mathbf{F}_c, \tag{3.7}$$

$$\frac{\mathrm{d}\boldsymbol{\mathcal{I}}\boldsymbol{\Omega}}{\mathrm{d}t} = \mathbf{T} + \mathbf{T}_c, \tag{3.8}$$

where $\mathbf{v}(t) = d\mathbf{x}_p/dt$ and $\boldsymbol{\Omega}(t)$ are the velocity and angular velocity vectors of a particle at position $\mathbf{x}_p(t)$ with mass $m_p = \rho_p V_p$, ρ_p is a uniform density, and $\boldsymbol{\mathcal{I}}$ the moment of inertia tensor. $\mathbf{F}$ and $\mathbf{T}$ in (3.7)-(3.8) denote the hydrodynamic force and torque acting on the particle, which are formally written as:

$$\mathbf{F} = \oint_{S_p} \boldsymbol{\sigma} \cdot \mathbf{n}\, dS \tag{3.9}$$

$$\mathbf{T} = \oint_{S_p} (\mathbf{x} - \mathbf{x}_p) \times (\boldsymbol{\sigma} \cdot \mathbf{n})\, dS, \tag{3.10}$$

where $\boldsymbol{\sigma} = -p\boldsymbol{I} + \rho\nu(\nabla\mathbf{u} + \nabla\mathbf{u}^T)$ is the fluid stress tensor, $\mathbf{x} - \mathbf{x}_p$ the position vector relative to the particle center and $\mathbf{n}$ the outward-pointing normal to the particle surface S_p. For simplicity we neglect here the effect of gravity, assuming either that the particle is neutrally buoyant $\rho_p = \rho$ or that the buoyant acceleration is negligible over turbulent one. The coupling between the fluid and the particles (two-way coupling) is provided by the

requirement of no-slip boundary condition on the particle surfaces. This is achieved by the immersed boundary (IB) method (Luo et al., 2007; Mittal and Iaccarino, 2005; Peskin, 2002; Uhlmann, 2005), which consist in applying an iteratively adjusted fictitious localized force at the particle–fluid interface to enforce the physical boundary condition.

In (3.7)-(3.8) $\mathbf{F}_c$ and $\mathbf{T}_c$ are the additional impulsive forces and torques related to the particle-particle collisions (the four-way interaction). In the simulations, these particle-particle interactions can be enforced by means of soft-sphere collision forces (Costa et al., 2015) with lubrication corrections (Ardekani et al., 2016; Brenner, 1961; Cooley and O'Neill, 1969; Costa et al., 2015). These forces clearly might have an impact on the statistical properties of the particle acceleration and must be properly excluded from the analysis when the research question - as in the present case - concerns the dynamics of isolated particles. In our simulations, in order to limit the effect of the pair interactions on the statistics of particle dynamics, the concentration of particles was kept very low (the maximal volume fraction is 1%) and only up to 4 particles are included in the simulation and only for the smallest particle sizes. All inter-particle collision events were removed from the data sets employed for the statistical analysis performed in our studies. To achieve this, the particle trajectory data around the collisions are removed by a time window whose width is of the order of the correlation time of the particle acceleration (i.e. $\gtrsim \tau_\eta$). Thus, the effect of four-way interactions is negligible.
The IB method allows to simulate particles in a flow that are not only large, i.e. well in the inertial range of turbulence, but also not necessarily spherical. In Jiang et al., 2022 we considered axisymmetric spheroidal particles: prolate spheroids ($\alpha = 2, 4$), spherical ($\alpha = 1$) and oblate ($\alpha = 0.5$). See Fig. 3.5 to illustrate the range of particle parameters explored.

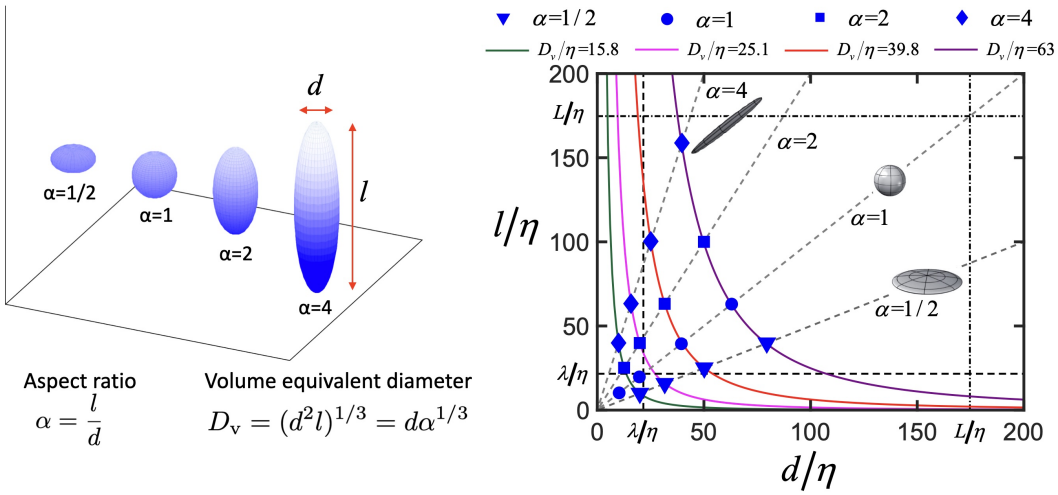


FIGURE 3.5: (a) Visualization of the particle shapes simulated in our study as well as (b) their size in comparison to the relevant scales of turbulent fluid flow: η, λ, L indicate respectively the dissipative, Taylor, and large scale. From Jiang et al., 2022.

The HIT flow in the simulation was governed, similarly to my past studies, by the NS equation sustained by random volume forcing acting at the largest scales. The particle-free turbulent flow intensity was therefore identified by a single dimensionless parameter, the

Reynolds number based on the Taylor microscale, $Re_\lambda = \lambda u'/\nu$ [1]. To fully resolve turbulent dynamics, the required spatial resolution must be of the order of the dissipative scale. In our simulations, which are implemented with a lattice Boltzmann (LB) method–based code (Calzavarini, 2019), the chosen setup is such that $\Delta x \geq 1.5\eta$, while $\Delta t \sim O(10^{-2})\tau_\eta$. Particular attention must also be paid to the spatial resolution of the particles too. For all considered cases, the minimal linear size of the particle, either d or l, is $> 15\Delta x$ (grid units). Such choice guarantees a reasonable resolution of the particle boundary layers whose inner (or viscous) thickness is expected to be of order η (although it might become thinner for particles with equivalent diameter $D_\nu \gg \eta$ as pointed out in Cisse et al., 2013). The particle Stokes number, defined as the ratio of the particle viscous response time ($\tau_p = D_\nu^2/(12\nu)$) with respect to the characteristic flow scale at the particle scale (here the turbulent eddy-turnover time $\tau_\ell = \ell^{2/3}/\epsilon^{1/3}$), can be expressed as $St_\ell = \frac{1}{12}(\frac{D_\nu}{\eta})^{4/3}$ (Fiabane et al., 2012; Xu and Bodenschatz, 2008). In our study it varied in the range 1.8 to 20.9.

3.2.2 Accelerations of finite-size neutral particles

Validation in weak turbulence

In order to validate the numerical results, we carried out simulations first at $Re_\lambda = 32$ for spheres only, in the same condition as in a previous numerical study (Homann and Bec, 2010). Figure 3.6a shows the single-cartesian-component acceleration variance, $\langle a_i^2 \rangle$, normalized by the acceleration variance of tracers, $\langle a_i^2 \rangle^{tracer}$, as a function of normalized particle diameter D/η. Our simulation results shows good agreement with the previous study (Homann and Bec, 2010) and scale as $(D/\eta)^{-4/3}$. At low Re_λ, the scaling exponent is much smaller than -2/3 which is the exponent value expected in HIT with high Re_λ. The dashed-dot line represents the prediction of the Faxén correction based on point-particle simulation under the same Re_λ. We note that when the particle is small ($D/\eta < 4$), the acceleration variance is well captured by the Faxén corrections. However, Faxén model cannot account for the scaling behaviour of the acceleration variance when $D/\eta > 7$. The inset shows the PDFs of the acceleration component for the variant size of spheres. The effect of particle size on the PDF of acceleration is very weak, which is also consistent with previous studies(Brown et al., 2009; Homann and Bec, 2010; Xu et al., 2007). This is even better highlighted in the trend of the flatness (F) versus the particle size Figure 3.6c. Figure 3.6b shows the normalized integral time of the temporal correlation function for particle acceleration, T_I/τ_η, as a function D/η. The time T_I is defined as the integral of the autocorrelation function from time zero to its first zero-crossing time T_0

$$T_I \equiv \int_0^{T_0} C(\tau)d\tau, \quad C(\tau) \equiv \frac{\langle a_i(t+\tau)a_i(t)\rangle}{\langle (a_i(t))^2 \rangle} \tag{3.11}$$

Again the comparison with with the corresponding correlation time measured in Ref. (Homann and Bec, 2010) is satisfactory and it displays the expected power-law behaviour $T_I \sim (D)^{2/3}$. The inset shows the autocorrelation functions for various sizes of spheres, illustrating the increasing autocorrelation time as the size of the sphere increases.

[1] where $u' = \sqrt{\langle u_i u_i \rangle^{v,t}/3}$ is the root-mean-square (r.m.s.) velocity of the turbulent flow ($\langle \ldots \rangle^{v,t}$ denotes here volume and time average), $\lambda = \sqrt{15\nu u'^2/\epsilon}$ is the Taylor length scale and $\epsilon = (\nu/2)\Sigma_{i,j}\langle(\nabla_i u_j + \nabla_j u_i)^2\rangle^{v,t}$ is the mean global energy dissipation rate

In conclusion, the acceleration statistics of our simulation show good agreement with the previous study (Homann and Bec, 2010), which validates our simulations.

$Re_\lambda = 32$

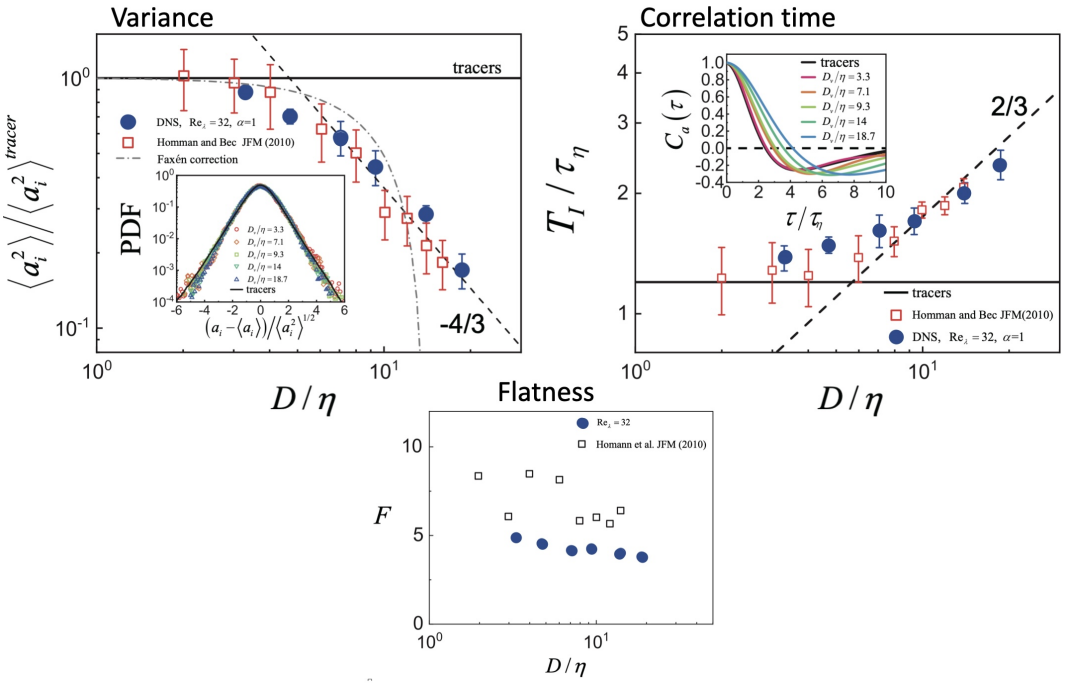


FIGURE 3.6: a). Normalized single cartesian component of the acceleration variance $\langle a_i^2 \rangle / \langle a_i^2 \rangle^{tracer}$ as a function of the normalized particle size D/η at $Re_\lambda = 32$. Squares denote the results in Ref. (Homann and Bec, 2010) at the same Re_λ. The dashed-dot line denotes the Faxén correction (Calzavarini et al., 2012). The inset shows the PDFs of acceleration at different sizes. b). Normalized correlation time of acceleration, T_I/τ_η, as a function of the normalized particle size D/η. Squares denote the correlation time in (Homann and Bec, 2010) at the same Re_λ. The inset shows the autocorrelation function of a single cartesian acceleration component. c) Acceleration Flatness normalized with respect to the Flatness of fluid tracers as a function of D/η.

Measurements in developed turbulence

How do these scaling behaviours change when the level of turbulence is increased? Shall one expect a better agreement with the theoretical predictions based on the scaling laws for turbulence without particles? Or on the contrary one must expect that these prediction are satisfied only in some asymptotics limit and only for particles whose size is well into the inertial range?

In order to reply to this question we conducted simulations at higher resolution, on a 512^3 grid cube (vs. previous 128^3) corresponding to a Reynolds number $Re_\lambda \simeq 120$ for which turbulence is more developed and scale separations are more evident. The overall computational cost of these calculations does not come solely from the spatial resolution but also from their temporal duration. In fact in order to access statistical properties up to the fourth order moments for the acceleration (as it is required by the flatness) one need to simulate a sufficient number of eddy-turnover times, therefore computational costs grows approximately with the eddy-turnover time corresponding to the particle size, $\tau_{eddy} \sim D/\delta_D u \sim D^{2/3}$. We remark that the ensemble averaging, i.e. the averaging over

different particle trajectories, that is normally adopted in one-way coupled particle simulations cannot be adopted in this case. In fact, increasing the number of particles would perturb the carrier flow leading to biassed measures. For this reason we limited our simulations to maximum 4 particles in the domain and we excluded from the analysis the data relative at the close interactions and collisions between these particles.

Since direct numerical measurements were not available at the new higher Reynolds number, we compared our results with the experimental data of Volk et al., 2011, obtained in turbulent von Kármán flow at Taylor Reynolds numbers roughly 4–9 times higher. In Fig. 3.7a we observe that the particle acceleration variance now scales approximately as D^{-1}, which is less steep than at lower Reynolds numbers. By contrast, the experiments display a scaling closer to the predicted $D^{-2/3}$. Taken together, these observations suggest that the dimensional scaling $D^{-2/3}$ may indeed hold asymptotically at high Reynolds numbers—values currently accessible to experiments (Volk et al., 2011) but not yet reached in simulations.

Additional support for this interpretation comes from the behavior of the acceleration flatness as a function of particle size. In Fig. 3.7(c), we report the particle acceleration flatness normalized by the flow acceleration flatness. Both experiments and simulations exhibit a decreasing trend consistent with $D^{-0.4}$, in line with the general expectation of a power-law $D^{\zeta_4-2\zeta_2}$. This supports the idea that larger particles suppress extreme acceleration events through spatial filtering, consistent with the coarse-graining hypothesis.

The situation becomes more puzzling, however, when examining the temporal correlation, see Fig. 3.7b. In experiments, the correlation time increases as D^1, more steeply than the expected $D^{2/3}$, whereas in simulations it remains closer to the predicted scaling, though still slightly below it. The origin of this discrepancy in temporal correlation still remains an open question.

3.2.3 Accelerations of finite-size non-spherical particles

A next step in our investigation was to examine how the particle's shape affects the statistical properties of its acceleration. As mentioned above we used for this the simulation spheroidal particles with shape ratio, length over diameter, α, variant between $1/2$ and 4 , i.e., from oblate disk-like particles to prolate rod-like ones.

We also carry out several auxiliary numerical simulations of 'artificial' particles, i.e., toy-models lacking certain characteristics typical of a real particle. These are obtained by deactivating either the boundary conditions defining the particle-fluid problem or part of the governing equations of motion. The configuration of each numerical experiment is listed in Tab.3.1 and visually represented in Fig. 3.8.

The first numerical experiment involves the calculations of trajectories of real particles (RP) that follow the complete model system introduced in the previous section. The second involves just spheroidal volume averages (VA) of the flow field, obtained by averaging the fluid acceleration and vorticity over N spheroids with the same diameter D_v and aspect ratio α as those used for RP. These averages are used to contrast the properties of RP particles and to test coarse-graining hypothesis. In the third experiment, we introduce so called virtual particles (VP). These particles evolve according to the NEE, however without taking into account any boundary condition between the fluid and the particle. In practice here the

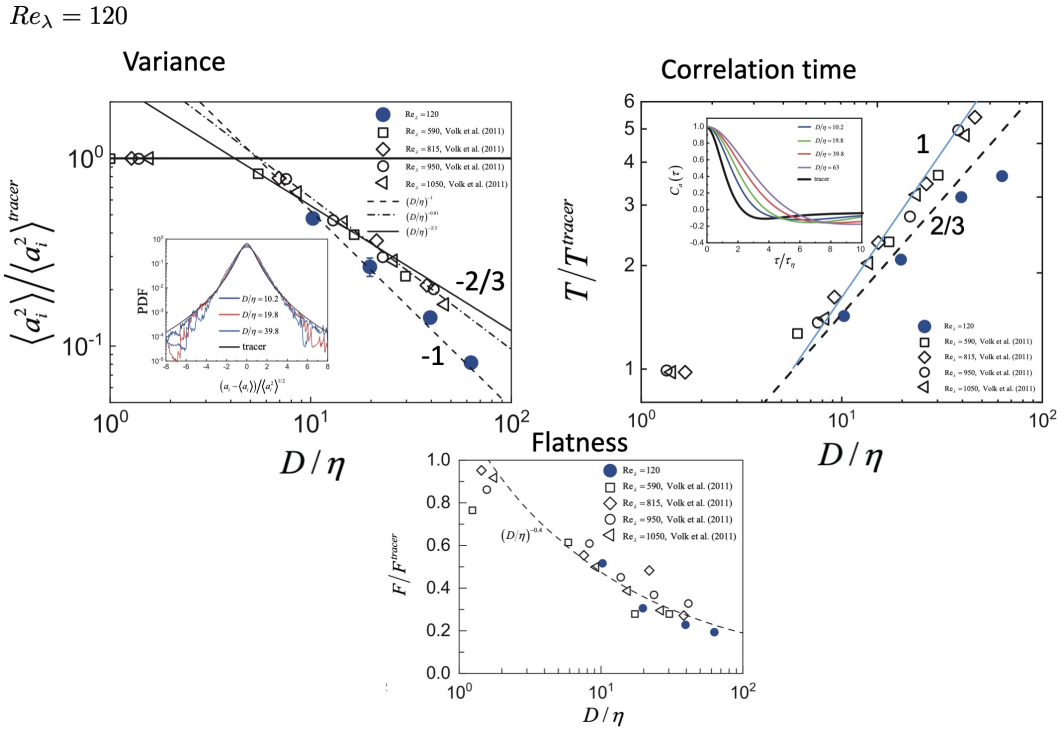


FIGURE 3.7: a). Normalized single cartesian component of the acceleration variance $\langle a_i^2 \rangle / \langle a_i^2 \rangle^{tracer}$ as a function of the normalized particle size d/η at $Re_\lambda = 120$. Empty symbols denote the results in Ref. (Volk et al., 2011) at larger Re_λ. The dashed and dotted lines indicate several power-law fits . The inset shows the PDFs of acceleration at different sizes. b). Normalized correlation time of acceleration, T_I/τ_η, as a function of the normalized particle size D_v/η for the same data sets. The inset shows the autocorrelation function of a single cartesian acceleration component. c) Acceleration Flatness normalized with respect to the Flatness of fluid tracers as a function of D/η.

IBM algorithm is disabled, and the particles exert no feedback on the flow, i.e. $\mathbf{f}_p = 0$ (see Tab.3.1). The fourth experiment considers real particles with fixed locations (RPFL): their positions remain static while their rotation evolves according to Eq. (3.8). Similarly, the fifth setup examines virtual particles with fixed locations (VPFL). These virtual are held stationary in the turbulence, and their rotation—again governed by Eq. (3.8)—is driven solely by the time derivative of the angular momentum of the surrounding fluid. No flow feedback is here included. Finally, to contrast the finite-size particle dynamics with sub-Kolmogorov-scale behaviour, the sixth experiment tracks inertialess point-like spheroids, whose center of mass perfectly follow the flluid flow while their orientation evolves according to Jeffery's equation. In this latter case the particle angular velocity is given by

$$\boldsymbol{\omega}_p = \frac{\boldsymbol{\omega}}{2} + \frac{\alpha^2 - 1}{\alpha^2 + 1} \boldsymbol{p} \wedge \mathcal{S}\boldsymbol{p} \tag{3.12}$$

where $\boldsymbol{\omega}$ and $\mathcal{S}$ are respectively the fluid vorticity and the rate-of-strain tensor.

The shape of each particle is identified by two parameters: the axial length and the diameter. However, in order to better compare the measurements with the case of spherical particles, it is convenient to use as characteristic parameters the aspect ratio α and the diameter of the sphere of equivalent volume, $D_v = (d^2 l)^{1/3} = d\alpha^{1/3}$. This choice is not

n.	Numerical Experiments	Model Equations
1	Real Particles (RP)	NSE + NEE + IBM
2	Volume Averages (VA)	NSE
3	Virtual Particles (VP)	NSE + NEE
4	Real Particles with Fixed Locations (RPFL)	NSE + EE + IBM
5	Virtual Particles with Fixed Locations (VPFL)	NSE + EE
6	Jeffery Fluid Tracers (JFT)	NSE + tracer eq.+ Jeffery eq.

TABLE 3.1: Summary of the six performed numerical experiments with the corresponding involved dynamical equations: Navier-Stokes equation (NSE), Newton-Euler equation (NEE) (3.7)-(3.8); Euler equation (EE) (3.8) meaning only rotation for particles with a fixed location; No-slip boundary conditions (i.e. two-way coupling) at particle-fluid interface implemented via the immersed boundary method (IBM); inertialess translation (tracer eq.) and rotation (Jeffery eq.).

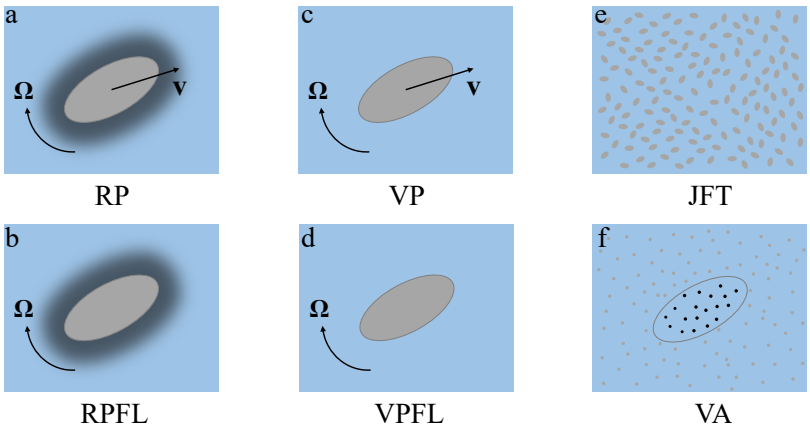


FIGURE 3.8: Sketches of the six numerical experiments performed: (a) real particles RP, (b) real particles with fixed locations RPFL, (c) virtual particles VP, (d) virtual particles with fixed locations VPFL, (e) Jeffery fluid tracers JFT, and (f) volume average of Jeffery fluid tracers VA . The light blue region denotes the fluid. The black shaded areas in panels (a) and (b) represent the two-way coupling region. The points in panels (e) and (f) represent the Jeffery fluid tracers. The tracers marked in black in panel (f) are used to calculate the volume averages.

unique, but we have found that it is the one that best allows to collapse the measured data for different aspect ratios.

Figure 3.10(a) presents the mean single-component acceleration variance $\langle a_i^2 \rangle$ of real particles (RP), normalized by that of fluid tracers $\langle a_i^2 \rangle^{tracer}$, as a function of the equivalent diameter in dissipative scale units D_v/η. Two key observations can be drawn. First, the acceleration variance decreases with increasing spheroid size, exhibiting a power law $\sim (D_v/\eta)^{-1.0\pm0.1}$ for $D_v/\eta \in [10, 63]$ and $Re_\lambda = 120$. Second, data for various aspect ratios ($\alpha = [1/2, 1, 2, 4]$) collapse onto a single curve, indicating that the translational hydrodynamic forces on large neutrally buoyant spheroids are primarily set by their volume, while it is independent of their shape. To further support these findings, Figure 3.10(a,b) (empty symbols) shows acceleration variances for fluid volume averages (VA) and virtual particles (VP). Both VA and VP exhibit similar inertial-range scaling, but their magnitudes differ: VP acceleration fluctuations are closer to those of real particles (RP), as seen in the insets where their ratios are plotted. VA and VP represent volume-averaged fluid acceleration in the stationary (Eulerian) and advected (Lagrangian) frames, respectively. We can infer that

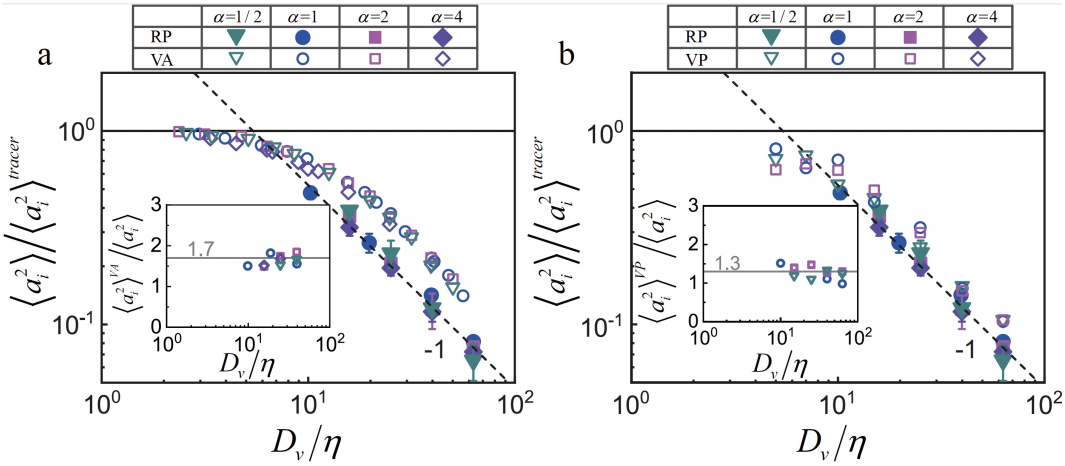


FIGURE 3.9: (a) Normalized single-component acceleration variance vs. D_v/η at $Re_\lambda = 120$ for real particles (RP, solid) and volume averages (VA, open). Dashed lines: fits for RP spheres (-1.0 ± 0.1). Inset: ratio $\langle a_i^2\rangle^{VA}/\langle a_i^2\rangle^{RP}$ vs. D_v/η. (b) Same as (a) for RP (solid) and virtual particles (VP, open), with inset showing $\langle a_i^2\rangle^{VP}/\langle a_i^2\rangle^{RP}$.

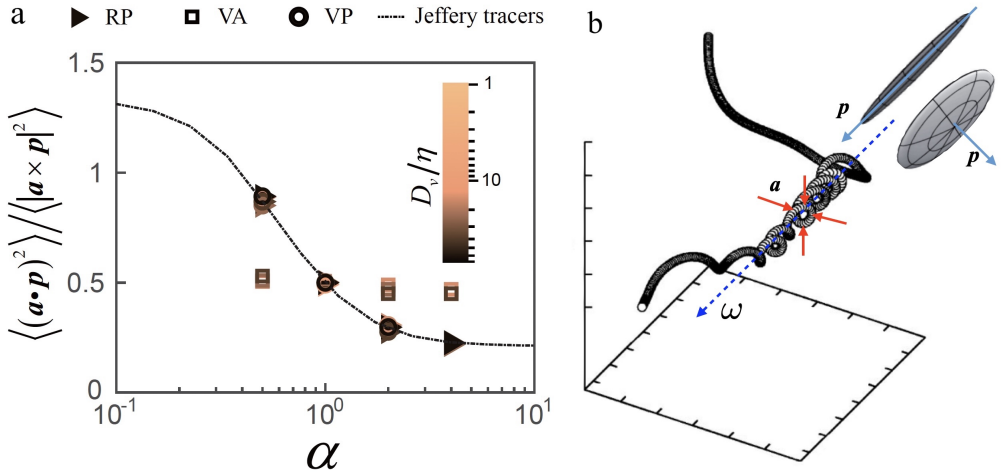


FIGURE 3.10: (a) Ratio of axial to lateral acceleration variance, $\langle(\mathbf{a}\cdot\mathbf{p})^2\rangle/\langle|\mathbf{a}\times\mathbf{p}|^2\rangle$, vs. aspect ratio at $Re_\lambda = 120$ for RP (triangles), VA (squares), and VP (circles). Black dash-dot: Jeffery tracers. Color indicates normalized size D_v/η (log scale). (b) Sketch of particle alignement in a filamentary vortex. ω and $\mathbf{a}$ indicate the fluid vorticity and acceleration, $\mathbf{p}$ the symmetry axis of the particle.

the observed scaling of translational dynamics is governed mainly by volume averaging, rather than by surface forces such as drag. Interestingly, VP more closely match RP statistics than VA. This could result from preferential sampling of flow structures along Lagrangian paths (though particle clustering is not observed in our simulations) or from preferential orientation present in RP and VP but absent in VA. This challenges the expectation that inertial-range particles should become randomly oriented due to the spatial averaging of turbulence.

Therefore, in order to assess correlations between particle acceleration and orientation, we then consider the ratio of axial to lateral acceleration variance, $\langle(\mathbf{a}\cdot\mathbf{p})^2\rangle/\langle|\mathbf{a}\times\mathbf{p}|^2\rangle$, versus aspect ratio (Fig. 3.10(a). For spheres ($\alpha = 1$), this ratio is 0.5 for all sizes, indicating no preferential alignment due to symmetry. Ratios deviating from 0.5 for non-spherical particles indicate preferential orientation between $\mathbf{a}$ and $\mathbf{p}$. It is interesting here to note that the

trend observed for RP is different from the one observed for the VA and VP sets. The latter collapse on the 0.5 line, meaning that any preferential alignment is missing. Interestingly, the real particle (RP) agrees well with the trend observed for the tiny inertialess Jeffery tracers. How can this fact be rationalized?

First of all, we should note that it is well known that axisymmetric particles, neutrally buoyant in terms of density and with a size within the dissipative range, tend to align with the vorticity if they have a prolate shape (Pumir and Wilkinson, 2011). Conversely, they tend to be perpendicular to the vorticity if they have a disk-like shape (Parsa et al., 2012). It is also known that filamentary vortical structures generate strong centripetal accelerations in fluid tracers (Biferale et al., 2004a). These accelerations are oriented in the radial direction of the vortical filament, i.e., perpendicular to its vorticity. It is therefore clear that fiber-like (prolate) particles, which preferentially tend to align with the vortex, will experience strong radial accelerations, much larger than the axial ones (see the illustration in Fig. 3.10(b)). This phenomenon leads to $\frac{\langle(\mathbf{a}\cdot\mathbf{p})^2\rangle}{\langle|\mathbf{a}\times\mathbf{p}|^2\rangle} < 0.5$. The opposite occurs for oblate particles, which explains the trend of the solid line in Fig. 3.10(a).

Quite surprisingly, our fully resolved simulations indicate that the preferential alignment phenomenon described for inertialess spheroidal tracers (JFT) also happens for very large particles RP whose size lies within the inertial range. We can speculate that the dynamics of these particles is affected by inertial-range coherent flow structures present in turbulence, with effects similar to those produced by dissipative-scale turbulent structures on small particles. This is a key new observation made possible through our fully resolved numerical simulation that, to my knowledge, still awaits experimental verification.

3.2.4 Accelerations of finite size non-neutrally buoyant particles

This section tackles an issue that in the present discussion has so far remained unexamined: the statistical properties of finite-size particle acceleration not of the same mass density with respect to the fluid, i.e., $\beta \neq 1$.
For sufficiently large particles, it is reasonable to expect that the drag response time becomes long, so the drag force can be considered small and negligible. In the absence of gravity, this suggests that it is the inertia — represented by the term $\beta\langle D_t\boldsymbol{u}\rangle_V$ in (3.3)— dominates the acceleration properties of large particles.

In Fan et al., 2024 I have attempted to test this hypothesis by means of numerics. We simulated spherical particles whose size is in the range $D/\eta = [6.5, 18.7]$, with densities $\beta = [0.14, 1.67]$, corresponding to $\rho_p/\rho_f = [0.4, 10]$ in turbulent flow at $Re_\lambda = 32$. The computed acceleration variance shows that the particle acceleration grows with β. In order to contrast the density-ratio and the particle-size effect we also trace on Fig.3.11(a) the results for point-like particles (solid lines). As we have already discussed the β-St or point-particle (PP) model (3.2) includes the added mass but does not account for the spatial filtering. While in the limit of small particles the PP model departs weakly from the fluid acceleration value, in the large size limit it converges to $\langle a^2\rangle \simeq \beta^2\langle(D_t u_i)^2\rangle$ (as already observed in (Calzavarini et al., 2009)). This is better evidenced in Fig.3.11(b), where the acceleration variances are normalized by $\beta^2\langle(D_t u_i)^2\rangle$ and all the PP data converge to the same plateau. Conversely, the fully resolved simulation results tend to vanish in the asymptotic limit due to the progressively enhanced smoothing by filtering of turbulent fluctuations.

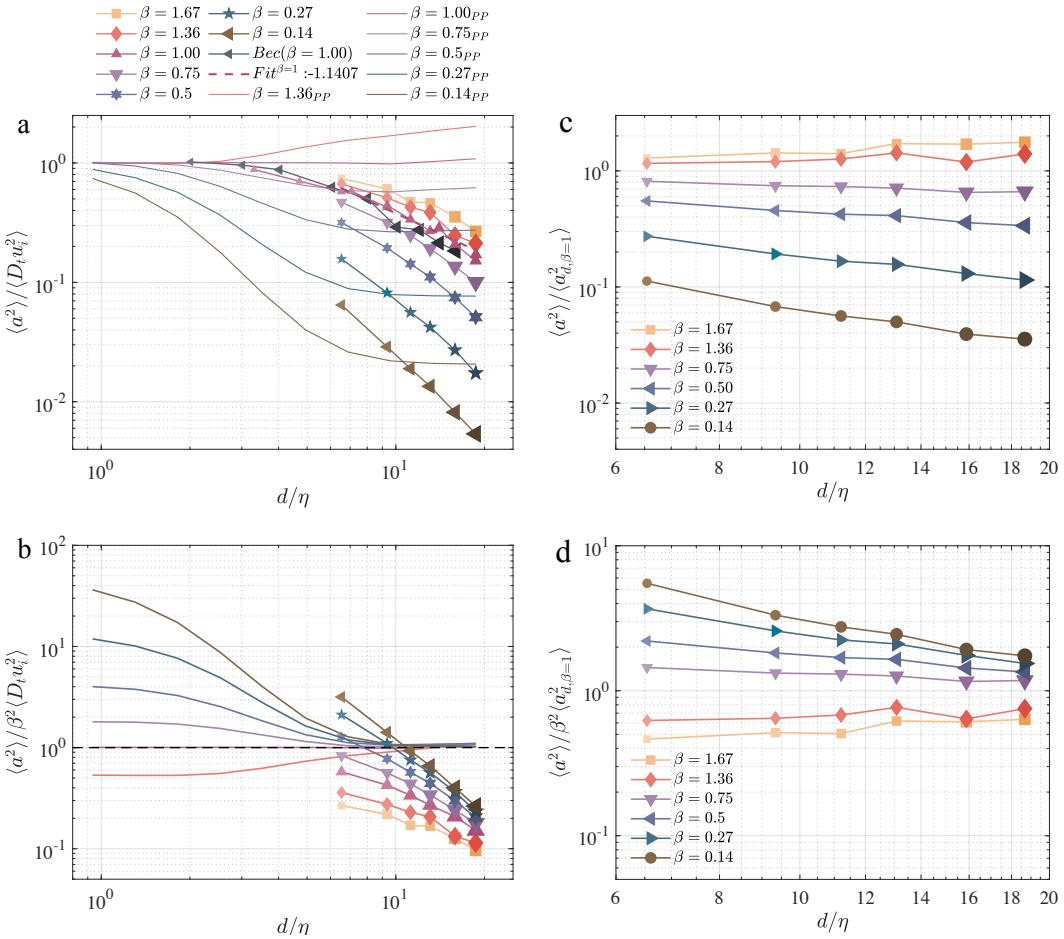


FIGURE 3.11: (a) Particle acceleration variance normalized by fluid-tracer acceleration variance as a function of the particle diameter (d) in dissipative units η. Data for density ratios β are displayed. The corresponding results for the point-point particle (PP) model are reported (solid line). Bec ($\beta = 1$) indicates numerical measurements from Homann and Bec, 2010. (b) Same data with the normalization $\beta^2\langle(D_t u_i)^2\rangle$ for the acceleration variance, this way the PP model tends asymptotically to the unit value. Note that the fully-resolved data with different β do not overlap. (c) Particle acceleration variance normalized by the acceleration variance of the neutrally buoyant particle of the corresponding size $\langle a^2_{d,\beta=1}\rangle$ as a function of the particle diameter (d) in dissipative units η. (d) Same data with the normalization $\langle a^2_{d,\beta=1}\rangle$ for the acceleration variance. Although curves get closer, they do not collapse on each other.

The effect of fluid-to-particle density ratio on the acceleration variance $\langle a^2 \rangle$ can be examined by dividing it by the acceleration variance of the neutral particle of the corresponding size $\langle a^2_{d,\beta=1}\rangle$. This is shown in Fig. 3.11(c), where one can notice that the data still depend on the values of β. It is therefore worth testing also the hypothesis,

$$\langle a_d^2 \rangle \simeq \beta^2 \langle a^2_{d,\beta=1} \rangle. \tag{3.13}$$

This is done in Fig.3.11(d). Although the trend suggests that the curves might overlap for very large-particles, beyond the integral scale of turbulence, $L \simeq 24\eta$, the lack of collapse of the curves can be interpreted as an evidence of the non-multiplicative effect of the added mass and spatial filtering on inertial-scale particles. We note that this multiplicative effect was instead true in the Faxen-corrected (FC) model (3.3), studied in (Calzavarini et al., 2009)

(see in particular their Fig. 1(a) where with a similar rescaling all data collapse for large particle diameters). The origin of this discrepancy with respect to the FC model remains to be understood. In particular it would be interesting to check if it is due to other effect such as the occurence non-linear drag (see (Fan et al., 2024) for a more complete discussion). The

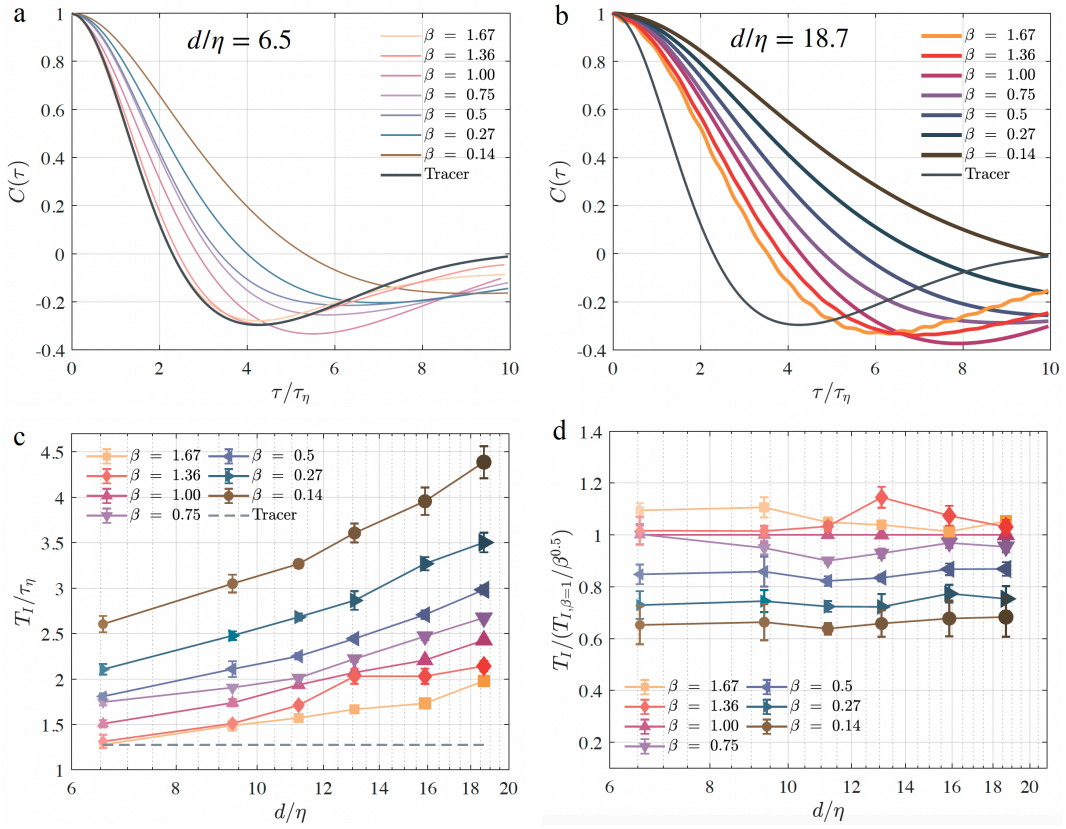


FIGURE 3.12: Single component correlation function acceleration variance for particles diameter (a) $d/\eta = 6.5$ and (b) $d/\eta = 18.7$. (c) Integral correlation time of the particle acceleration versus the particle size, both expressed in dissipative units, for different β families. (d) Integral correlation time divided by $T_{I,\beta=1}/\sqrt{\beta}$ versus the particle size.

study of the temporal correlation functions of the acceleration allows to further reinforce the observations made for the instantaneous acceleration variance. Figure 3.12(a,b) shows the $C(\tau)$ correlation functions for the two small/large particle limiting case in this study, i.e. for (a) $d/\eta = 6.5$ and (b) $d/\eta = 18.7$.

The integral correlation times, T_I, computed from these curves grow with the particle size and decreases with β, see Fig. 3.12(c). The first trend as we have discussed is usually rationalized in term of the coarse-graining hypothesis (Qureshi et al., 2007). However, the same argument cannot be straightforwardly extended to non-neutral particles. A possible approximate adaptation that we proposed in (Fan et al., 2024) goes as follows. We indicate with $X_a = \frac{1}{2}\langle D_t u^2\rangle^{1/2}\tau_a^2$ the length spanned by a fluid particle over the time (τ_a) during which the acceleration is correlated (and so approximately constant). Such a length can be travelled by a finite sized inertial particle over a time $\tau_d = \sqrt{2X_a/\langle a_d^2\rangle^{1/2}}$. Now using the hypothesis (3.13) one obtains

$$\tau_d = \frac{\tau_{d,\beta=1}}{\sqrt{\beta}} \sim \frac{d^{2/3}}{\sqrt{\beta}}. \tag{3.14}$$

This prediction is tested in Fig. 3.12(d), we observe that while the size dependency of the correlation time for any particle seems to be properly normalized by the neutral case (i.e. the coarse graining hypothesis holds true), the density dependence is only approximately explained in terms of the above scaling. The collapse is better for the case of light particles where the above argument is more fitting.

Last we considered statistical properties beyond the second order. This can be done by examining the trends in the shape of the probability density functions (PDF) of the acceleration normalized by its standard deviation. These functions are reported in Figure 3.13; panel (a) shows the curves for the smallest particles, while (b) for the largest particles explored in this study. It is clear the trend towards a Gaussianization of the accelerations when the particle size is increased, this feature was also predicted by the FC model simulations Calzavarini et al., 2009. A similar tendency is observed at increasing the particle mass density: PDF of heavy particles have shorter tails than neutral particles of the same size, on the contrary light particles tend to have extreme accelerations. This trend is evident for the smallest particles, and agrees with former results from PP model simulations Volk et al., 2008, while it appears here negligible for the largest particles.
More robust conclusions can be drawn from the flatness of the acceleration, $F(a_d) = \langle a_d^4 \rangle / \langle a_d^2 \rangle^2$. As mentioned above theoretical considerations suggests that $\langle a_d^4 \rangle / \langle a_d^2 \rangle^2 \sim \langle (\delta_d u)^8 \rangle / \langle (\delta_d u)^4 \rangle^2 \sim d^{\zeta_8 - 2\zeta_4 < 0}$, where ζ_p indicates the scaling exponent of the velocity structure functions of order p, i.e., $\langle (\delta_d u)^p \rangle \sim d^{\zeta_p}$. The value of the exponent $F(a_d) \sim d^{\phi}$ can be estimated in various ways, it is $\phi \simeq -0.44$ from Kolmogorov-Obukhov 1962 model (Kolmogorov, 1962) and $\phi \simeq -0.56$ with She-Lévêque parametrization (She and Leveque, 1994). Measuring a scaling behaviour for $F(a_d)$ is delicate as it requires large datasets. Furthermore, similar to the acceleration variance, large Reynolds numbers are needed in order to establish a wide inertial-range. Although some experiments and simulations did not observe any scaling trend ($\phi = 0$) (Brown et al., 2009; Homann and Bec, 2010; Qureshi et al., 2007; Xu and Bodenschatz, 2008), there are recently increasing evidences towards a reduction of the flatness with size, Volk et al., 2011 measured $\phi \simeq -0.5 \pm 0.1$ for inertial range neutrally buoyant particles, Prakash et al., 2012 observed it for bubbles in turbulence. This trend is also supported by the FC model. The reduction of flatness with particle size increase is confirmed by the present fully resolved simulations (see Figure 3.13 panel (c)). Furthermore, we observe a weak but detectable flatness amplification with β. This was previously observed only for dissipative scale particles both in experiments and simulations (Volk et al., 2008). Its physical interpretation lies in the phenomenon of preferential sampling: light particles explore preferentially vortex cores where the fluid centripetal acceleration is large, while heavy particles sample the outside of vortices which are calmer regions as far as acceleration is concerned, and this is reflected on their normalized accelerations PDF (Bec et al., 2006; Calzavarini et al., 2008b; Tagawa et al., 2012). This points to the fact that preferential sampling is a small but non vanishing effect for inertial-scale particles.

In summary our study on non-neutral finite-sized particles confirms all the tendencies predicted by the coarse graining picture, namely the fact that both the acceleration variance and its flatness decrease with the particle size and the opposite for the acceleration correlation time. Given the limited extension of the inertial range at the present Reynolds number ($Re_\lambda = 32$) it is difficult to estimate reliable scaling laws as a function of the particle diameter d. However, it seems that the observed behaviours deviate systematically from the

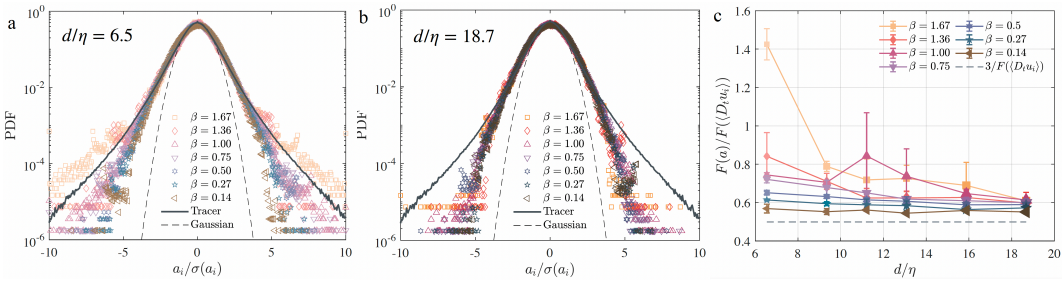


FIGURE 3.13: PDF of particle acceleration normalized by their standard deviation for (a) $d/\eta = 6.5$ and (b) $d/\eta = 18.7$. PDF of fluid tracers acceleration (bold solid line) and Gaussian distribution (dashed). (c) Flatness of the acceleration of particles versus their size. Data are normalized by the fluid acceleration flatness, $F(D_t u_i) \simeq 6$. The dashed line corresponds to the Gaussian value. Error bars estimated from the semidifference of the flatness factors computed from two subsamples of the full dataset.

expected scaling laws derived from the values of the velocity structure function exponents ζ_p. This point is delicate and requires further attention. It might be that the scaling laws derived from ζ_p only holds asymptotically in Re_λ, or it could be that systematic subleading deviations are present due to the influence of other hydrodynamics effects (such as the drag).

Looking at the particle density dependence, we have tried to assess the hypothesis $a_d \sim \beta \langle D_t u_i \rangle_V$. Even if the particle acceleration increases with β, the observed trends can not be interpreted as the simple multiplicative combination of the two dominant terms: the spatial filtering of fluid accelerations and the β fluid-to-particle density ratio. A similar mismatch is observed in the dependence of the correlation time with β, for which we provided a simple model. The study of the acceleration flatness indicates that light particles are more intermittent than heavy ones and this also when their size is large. These features suggest a role of preferential sampling of the flow by the particles. This interpretation shall be put under scrutiny in further studies, in fact in the context of inertial-scale particles the evidences of preferential sampling and the related preferential clustering are at present not univocal (Fiabane et al., 2012; Uhlmann and Chouippe, 2017).

3.3 Conclusions and Perspectives

In this chapter, I have presented a number of results concerning the statistical properties of the acceleration of inertial particles transported by a fully developed turbulent flow. This is certainly an idealized configuration (e.g., a dilute suspension, an unconfined flow, and turbulence sufficiently intense that gravitational effects can be neglected), nevertheless, as we have seen, it is far from being a trivial problem.

Approximately a decade elapsed between the earliest and the most recent studies discussed here, a period during which increasingly sophisticated and realistic numerical simulations became possible. In particular, the field has progressed from point-particle simulations based on MRG-type models to fully resolved particle simulations. It is now routine to perform particle-resolved simulations involving up to 10^5 particles (Chiarini and Rosti, 2024) in turbulent flows with $Re_\lambda \simeq O(10^2)$.

Particle-resolved simulations provide access to quantities that remain difficult to obtain

experimentally (such as the fluid gradient or the local pressure) and allow theoretical interpretations and hypotheses to be tested directly, as illustrated in the study presented earlier in this chapter. The physical understanding gained from such investigations can then be distilled into reduced-order models that are computationally more efficient while retaining a high level of accuracy.

Despite these advances, much work remains to be done. In the immediate future, for example, it will be interesting to perform simulations at larger Reynolds number and in larger domain size in order reduce the impact of finite inertial-range and finite-domain effects present in our simulations. It will also be interesting to develop new analysis techniques for the detection of preferential sampling by inertial-scale particles in turbulent flows. Furthermore, the statistical relevance for large particles in turbulence of forces such as history (Jaganathan et al., 2023) or lift (Mazzitelli and Lohse, 2004), remains to be clearly assessed.

These results may help in developing effective models for the dynamics of large particles in different context where particles are large with respect to the typical variation scale in the flow, such drifters and floaters in the ocean (Beron-Vera, 2021) or rock crystals in magmatic chambers and primordial magma oceans (Patočka et al., 2022).

Chapter 4

Rotations and orientations of anisotropic particles in turbulent flows

Contents

3.1 Inertial particles accelerations statistics 13
3.2 Simulations of finite-size spheroids in turbulence 19
3.2.1 Methodology and study protocols 19
3.2.2 Accelerations of finite-size neutral particles 21
3.2.3 Accelerations of finite-size non-spherical particles 23
3.2.4 Accelerations of finite size non-neutrally buoyant particles 27
3.3 Conclusions and Perspectives 31

In the previous chapter, which was entirely focused on the properties of inertial particle accelerations, we briefly mentioned effects related to the particle shape. In particular we observed that non-spherical particles can preferentially align with certain structures of the fluid flow. For example, axisymmetric prolate particles tend to align their axis with that of the vortices they encounter, and this produces statistical signatures in the acceleration when it is decomposed into an axial and a transverse component (see Sec. 3.2.3).

A comprehension of the phenomena of rotation and alignment of inertial particles, particularly in turbulent flows, proves to be just as challenging as that of acceleration, and it is certainly for this reason that so many experimental and numerical studies have been devoted to it in recent years (for a recent review see Voth and Soldati, 2017). The interest in particle rotations is not motivated solely by scientific curiosity but also by possible applications. In the context of flow visualization and velocimetry techniques, it would be

This chapter is based on:

1. *Rotation rate of rods in turbulent fluid flow*, S. Parsa, E. Calzavarini, F. Toschi, G. A. Voth, Phys. Rev. Lett. 109, 134501 (2012) [PDF].
2. *Dynamics of finite-size spheroids in turbulent flow: the roles of flow structures and particle boundary layers*, Lin-Feng Jiang, Cheng Wang, Shuang Liu, Chao Sun, Enrico Calzavarini, J. Fluid Mech 939 , A22 (2022) [PDF].
3. *Anisotropic particles in two-dimensional convective turbulence*, E. Calzavarini, L. Jiang, and C. Sun, Phys. Fluids 32, 023305 (2020) [PDF].
4. *Rotation of anisotropic particles in Rayleigh-Bénard turbulence*, L. Jiang, E. Calzavarini, and C.Sun, J. Fluid Mech. vol. 901, A8 (2020) [PDF].

valuable to exploit measurements of particle rotation and orientation in order to infer the fluid vorticity or the local rate of kinetic energy dissipation. This is probably the primary motivation that has driven laboratory experiments in this field, using particles of the most diverse types and shapes. The technological challenge is considerable, as it goes beyond the usual trajectory reconstruction techniques (PTV), since it requires distinguishing orientation—something that can be achieved, for example, by drawing patterns on the particle surfaces (Zimmermann et al., 2011) or engineering them to have special shapes (such as slightly curved fibers (Giurgiu et al., 2024). Secondly, the study of the dynamics of non-spherical particles is important for a wide range of situations, from natural contexts (transport of pollens in the air, microplastics or microorganisms in the ocean) to industrial ones, such as papermaking or the production of composite materials.

My first encounter with this subject dates back to 2011, when I attended a brilliant talk by G. Voth (Wesleyan University, USA) at a conference in Potsdam (D). The presentation was about an experimental study in which his team managed, using a system of cameras, to reconstruct the trajectories of a set of non-spherical particles carried by a turbulent flow. I realized that, through the time series of the velocity-gradient tensor along the trajectories of fluid tracers—which I could generate with numerical simulations—we would be able to measure the same observables in a numerical experiment. A comparison between experiment and simulation could lead to a validation of the dynamical models used in the simulations, as well as to a better understanding of the phenomenon.
That is precisely what we did in the collaborative work we started immediately afterwards and which was then distilled in the paper (Parsa et al., 2012). Some of our results are reproduced in figure 4.2. The first panel (a) shows a reconstruction of the experimentally measured motion of a an axisymmetric cylindrical rod, of aspect ration $\alpha = \ell/d = 5$, in a turbulent flow. In panel (b) and (c) we show the comparison between experiments and simulations of the variance (over time and the particle ensemble) of the quantity $\dot{\boldsymbol{p}}$, which is known as the the tumbling rotation rate (Fig. 4.1). The simulations are based on the Jeffery equation, which is suitable to describe the rotation inertialess particles. The center of mass of these particles is assumed to follow the trajectory of a fluid tracer, while the orientation of their symmetry axis evolves according to (Jeffery, 1922):

$$\dot{\boldsymbol{p}} = \boldsymbol{W}\boldsymbol{p} + \frac{\alpha^2 - 1}{\alpha^2 + 1}\left(\boldsymbol{S}\boldsymbol{p} - (\boldsymbol{p}\cdot\boldsymbol{S}\boldsymbol{p})\boldsymbol{p}\right), \tag{4.1}$$

where $\boldsymbol{S}$ and $\boldsymbol{W}$ are the symmetric and antisymmetric parts of the velocity gradient tensor $\boldsymbol{\nabla u}$. Another way to express the above equation is:

$$\dot{\boldsymbol{p}} = \boldsymbol{\Omega}_J \wedge \boldsymbol{p} \tag{4.2}$$

$$\boldsymbol{\Omega}_J = \frac{\boldsymbol{\omega}}{2} + \frac{\alpha^2 - 1}{\alpha^2 + 1}\boldsymbol{p} \wedge \boldsymbol{S}\boldsymbol{p}, \tag{4.3}$$

where $\boldsymbol{\omega}$ is the fluid vorticity, and $\boldsymbol{\Omega}_J$ is the particle angular velocity. We note that for spherical particles ($\alpha = 1$) the angular velocity is directed as the local flow vorticity, with half of its intensity. Furthermore for the vector $\boldsymbol{\Omega}_J$ can be decomposed into a normal component with respect to $\boldsymbol{p}$, called tumbling $\dot{\boldsymbol{p}}$ and a longitudinal one, called spinning $\boldsymbol{\Omega}_s = (\boldsymbol{\Omega}\cdot\boldsymbol{p})$, see also Fig. 4.1 (Byron et al., 2015; Ni et al., 2015; Zhao et al., 2015) .

The agreement between the numerical simulations that we conducted and experiments confirmed that the squared tumbling rate of particles in turbulence is dominated by rare,

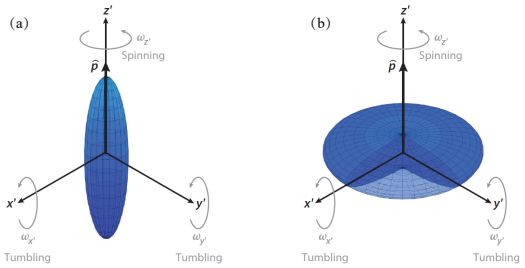


FIGURE 4.1: Ellipsoidal particles in turbulence: (a) Prolate ($\alpha > 1$), (b) Oblate ($\alpha < 1$). From Voth and Soldati, 2017.

extremely intense events, with values reaching up to 60 times the average at $Re_\lambda = O(10^2)$. Simulations further reveal that this mean value depends in a non-trivial way on the particle aspect ratio. In particular, disk-like particles (oblate, $\alpha < 1$) tumble significantly faster than rod-like ones (prolate, $\alpha > 1$), due to the development of strong correlations with the velocity gradients of the surrounding turbulent flow.

This line of research has been carried forward by many groups. On the experimental side, progresses have made it possible to measure not only how particles tumble but also how they spin (Byron et al., 2015; Giurgiu et al., 2024). Researchers have also managed to track particles with inertia (Marchioli and Soldati, 2013; Rosén et al., 2015) and finite size ones (Bounoua et al., 2018; Oehmke et al., 2021; Parsa and Voth, 2014), moving beyond the idealized tracer limit, or with non axisymmetric shapes (e.g. chiral particles Kramel et al., 2016). On the numerical side, more advanced methods have been developed, including fully resolved simulations that capture the complete hydrodynamic problem, and studies of turbulent flows more complex than the classical homogeneous and isotropic case, such as channel turbulence (Marchioli et al., 2010; Zhao et al., 2015). Finally, theoretical approaches based on statistical models of turbulence have provided predictions for the statistics of particle rotations, taking into account the correlations between particle orientation and the local velocity gradients (Gustavsson et al., 2014a; Leppin and Wilczek, 2020; Ni et al., 2015; Pumir and Wilkinson, 2011).

In this context, my activities have mainly focused on two issues:

(i) the study of the effect of the particle size on the rotation properties of neutrally buoyant inertial particles

(ii) the investigation of particle rotations in a non-ideal turbulent flow such as Rayleigh–Bénard convection.

In the remaining of this chapter I will focus on these works in more detail.

4.1 Rotation of finite-sized inertial particles

The study of the rotation of finite-size particles described here is connected to the study of acceleration presented in Section 3.2 of the previous chapter. In fact, it employs the same methods and the same database. As with acceleration, the first question we pose is whether the statistics of particle rotation can be explained in terms of spatial averages of the fluid field. In this case, we consider as the quantity of interest the angular velocity of the particle, in the following denoted by Ω. In the case of small particles (without inertia), this quantity

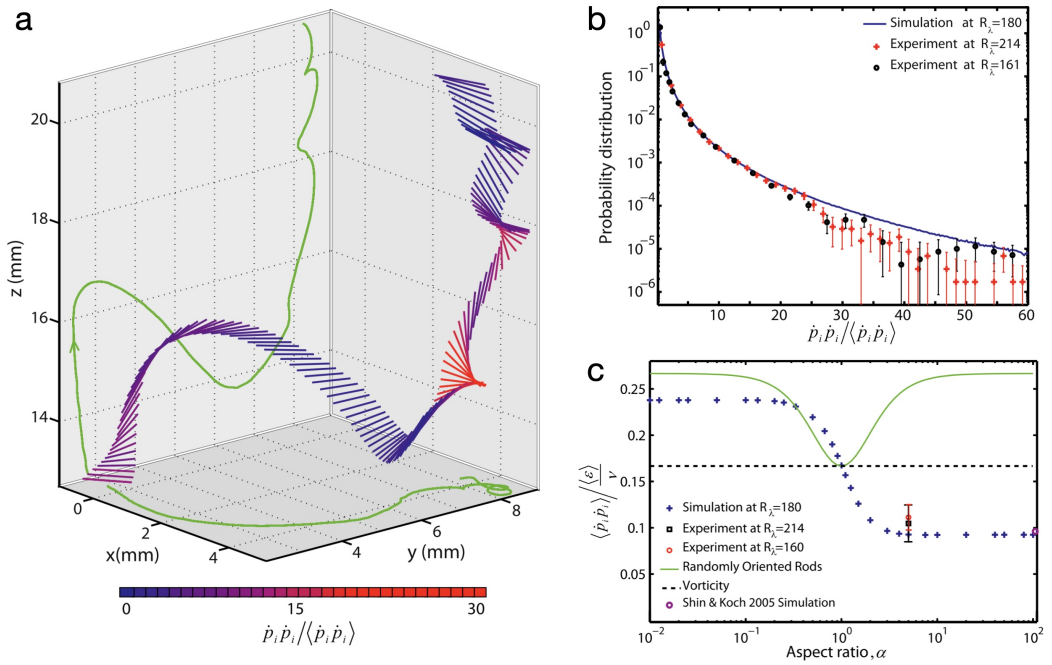


FIGURE 4.2: (a) Three-dimensional view of a rod trajectory with a large rotation rate from the experiment at $Re_\lambda = 214$. The colour of the rod represents the rotation rate. This rod is tracked for 284 ms. The green lines show the projection of the center of the rod onto the y-z and x-y planes. The rod is a circular cylinder with length 1 mm and diameter 0.2 mm. (b) The PDF of rotation rate squared of rods. (a) Comparison of simulation (blue line, $Re_\lambda = 180$) with experiment (black circle, $Re_\lambda = 160$; red plus, $Re_\lambda = 214$) for aspect ratio .... Error bars represent both random uncertainty and the systematic uncertainty produced by measuring rotation rates from experimental orientation data over a time interval. (b) Comparison of the PDF of rotation rate squared for rods at $\alpha = 5$ (blue plus) and spheres at $\alpha = 1$ (black circle) with PDFs of enstrophy (green square) and energy dissipation rate (red triangle) for the simulation at $Re_\lambda = 180$. One symbol is displayed for every twenty bins. (c) Mean square rotation rate as a function of aspect ratio. (a) Blue plus is the DNS at $Re_\lambda = 180$. Black open square is the experiment at $Re_\lambda = 214$. Red open circle is the experiment at $Re_\lambda = 160$. The error bars on the experimental points represent systematic error due to extrapolation from the finite fit time required to measure the rotation rate. The purple open circle shows the result for infinite aspect ratio rods from simulations by Shin and Koch at $Re_\lambda = 53.3$. The green line is the analytic prediction for randomly oriented rods from Eq. (2). The dashed line indicates the rotation due to vorticity.

follows Jeffery's dynamics. Its variance is given by the square of relation (4.3) and it has been shown that in a turbulent flow it is nearly independent of the particle's aspect ratio (Byron et al., 2015).

What happens in the case of a neutrally buoyant particle of finite size? One can assume that only vortices whose sizes are comparable to the particle size are responsible for its rotational motion. As for translational acceleration, the particle would act as a finite-size filter of fluid fluctuations, responding primarily to flow structures at its own scale. Since Ω has the dimensions of the inverse of a time, its magnitude can therefore be estimated as $D_\nu/\delta_{D_\nu}u$ (where D_ν is the diameter of the sphere of equivalent volume), which making use of Kolmogorov (K41) scaling suggests for the variance the behaviour (Bordoloi and

Variano, 2017; Bounoua et al., 2018; Parsa and Voth, 2014; Pujara et al., 2018):

$$\langle \Omega^2 \rangle \sim \left(\frac{D_\nu}{\delta_{D_\nu} u} \right)^2 \sim D_\nu^{-4/3}, \tag{4.4}$$

i.e., the rotation intensity decreases with the particle size. We tested this relation against our numerical simulation datasets. Figure 4.3 shows the mean square angular velocity of what we called real particles (RP), normalized by that of point-like Jeffery fluid tracers (JFT) as a function of the particle equivalent diameter D_ν normalized by the Kolmogorov scale. For sufficiently large particle we clearly observe $\langle \Omega_i \Omega_i \rangle \sim (D_\nu/\eta)^{-4/3}$ for $D_\nu \geq 10\eta$. Despite an offset between spheres and spheroids, prolate and oblate particle data collapse well when plotted against D_ν, confirming it as a relevant scale for rotational dynamics. The observed $-4/3$ scaling matches dimensional predictions from the K41 theory.

The VA (Volume Averages) and VP (Virtual Particles) numerical experiments (refer to Tab. 3.1 in previous chapter for their precise definitions) show a similar decreasing trend in the mean squared angular velocity with D_ν, consistent with a $-4/3$ power law . However, VA and VP values are both larger than those of real particles (RP) (see Figure 4.3a,b), indicating that while volume filtering governs the scaling, other effects influence the intensity of the rotation. Insets reveal that discrepancies in angular velocity variance between VA or VP and RP exceed those seen in acceleration variance (see for comparison Fig. 3.10). Thus, VP, i.e., particles without solid boundaries and no slip boundary conditions attached to them cannot reliably approximate the real particle (RP) angular velocity. This discrepancy becomes even more important when comparing axial versus lateral rotational velocity components (i.e. tumbling versus spinning rates), as discussed next.

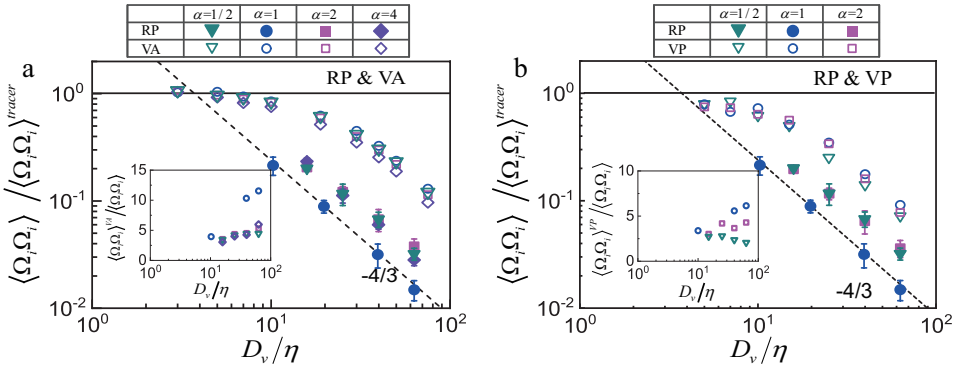


FIGURE 4.3: (a) Mean squared angular velocity normalized by Jeffery tracers at $Re_\lambda = 120$ versus D_ν/η. Open symbols: VA results for spheres. Dashed line: sphere fit with slope $-4/3$. Inset: ratio $\langle \Omega_i \Omega_i \rangle^{VA} / \langle \Omega_i \Omega_i \rangle^{RP}$ versus D_ν/η for spheres. (b) Same as (a) for VP (open symbols) with corresponding inset ratio $\langle \Omega_i \Omega_i \rangle^{VP} / \langle \Omega_i \Omega_i \rangle^{RP}$.

Figure 4.4(a) shows the ratio of the variances of spinning and tumbling, $\langle \Omega_i^s \Omega_i^s \rangle / \langle \dot{p}_i \dot{p}_i \rangle$, versus aspect ratio α for particles of various sizes. For sub-Kolmogorov particles described by Jeffery's equation, assuming isotropic orientation for $\mathbf{p}$ uncorrelated with velocity gradients, time and ensemble averaging yields a relation of the following form (Byron et al., 2015; Parsa et al., 2012):

$$\frac{\langle \Omega_i^s \Omega_i^s \rangle}{\langle \dot{p}_i \dot{p}_i \rangle} = \frac{\frac{1}{12}\langle \omega^2 \rangle}{\frac{1}{6}\langle \omega^2 \rangle + \frac{1}{5}\Lambda^2 \langle \mathcal{S} : \mathcal{S} \rangle} = \frac{5}{10 + 6\Lambda^2}, \tag{4.5}$$

where one assumes $\frac{1}{2}\langle\omega^2\rangle = 2\langle\mathcal{S}:\mathcal{S}\rangle = \epsilon/\nu$ for the HIT flow. This predicts a mild variation of the spinning-to-tumbling ratio across α (blue solid curve in Fig. 4.4a). However, strong correlations between the orientations of small axisymmetric particles and velocity gradients cause significant deviations from such a prediction, as shown by our Jeffery model simulations (circular symbols) and in agreement with prior results at higher $Re_\lambda = 433$ (Byron et al., 2015) (dashed line). Clearly spherical particles maintain isotropic angular velocity and so a near $1/2$ ratio. In contrast, oblate spheroids primarily tumble intensely, while prolate ones are spin-dominated, aligning with vorticity (Parsa et al., 2012; Voth and Soldati, 2017). Both behaviors saturate for not so large aspect ratios : $\alpha \lesssim 1/4$ for oblate and $\alpha \gtrsim 4$ for prolate particles.

For finite-size particles, a naive K41 prediction suggests tumbling scales with the particle length, $\langle\dot{p}_i\dot{p}_i\rangle \sim l^{-4/3}$, and spinning with its diameter, $\langle\Omega_i^s\Omega_i^s\rangle \sim 0.5\, d^{-4/3}$, with the value 0.5 matching the spherical case, this yield:

$$\frac{\langle\Omega_i^s\Omega_i^s\rangle}{\langle\dot{p}_i\dot{p}_i\rangle} \sim \frac{\alpha^{4/3}}{2}. \tag{4.6}$$

We note that, despite our use of l and d in its derivation, the above prediction does not involve the particle size, just its shape. However, simulations (Fig. 4.4a,b) reveal a pronounced decrease of this ratio with particle size $D_\mathcal{V}$: larger particles tend to spin less and tumble more for all aspect ratios except spheres (Fig. 4.4d). As noted by (Oehmke et al., 2021), dimensional arguments overlook the decorrelation of velocity gradients along the particle surface. Since rotation rates arise from integrals of velocity gradients over the particle, spinning can be strongly attenuated in elongated particles ($\alpha \gg 1$). This integral effect grows important when both particle length and diameter exceed the dissipation scale, causing deviations from simple K41 scalings and making the spinning-to-tumbling ratio depend on particle size. Figure 4.4b shows the ratio $\langle\Omega_i^s\Omega_i^s\rangle/\langle\dot{p}_i\dot{p}_i\rangle$ versus the normalized particle size $D_\mathcal{V}/\eta$, exhibiting a scaling $\sim (D_\mathcal{V}/\eta)^{-0.6}$ across all shapes. Although the robustness of this scaling is uncertain, it implies that tumbling and spinning rates cannot both scale as $-4/3$. Currently, no model captures this behavior.
In summary, finite-size particles tend to tumble significantly more than they spin (illustrated in Figure 4.4c). We add that Volume Averages (VA) and Virtual Particles (VP) data differ: VA remains close to the Jeffery random orientation prediction (this is expected as the volume averages are fixed in their orientation), while VP roughly follow the simple K41 scaling of eq. (4.6) (red line in Figure 4.4d), without showing this tumbling dominance. The fact that RP and VP behave differently in their repartition of spinning over tumbling, suggests that the solid wall (no-slip) boundary conditions at the particle surface shall play an important role.

To better understand the latter observations, we used the particle simulations to make detailed fluid observations in the vicinity of the particle surfaces. These measurements helped us characterise how particle feedback affects the surrounding flow. We analyzed the fluid vorticity $\boldsymbol{\omega}$ and the rate-of-strain tensor $\mathcal{S}$ in the boundary layer around particles by computing the variance ratio $\frac{1}{4}\overline{\boldsymbol{\omega}^2}/\overline{\mathcal{S}:\mathcal{S}}$, averaged over time, ensemble, and azimuthally for maximal statistical convergence. In particle-free homogeneous isotropic turbulence, this ratio equals unity. Around particles, however, a thin near-surface region exhibits values slightly above one, indicating vorticity-dominated dynamics. At intermediate distances

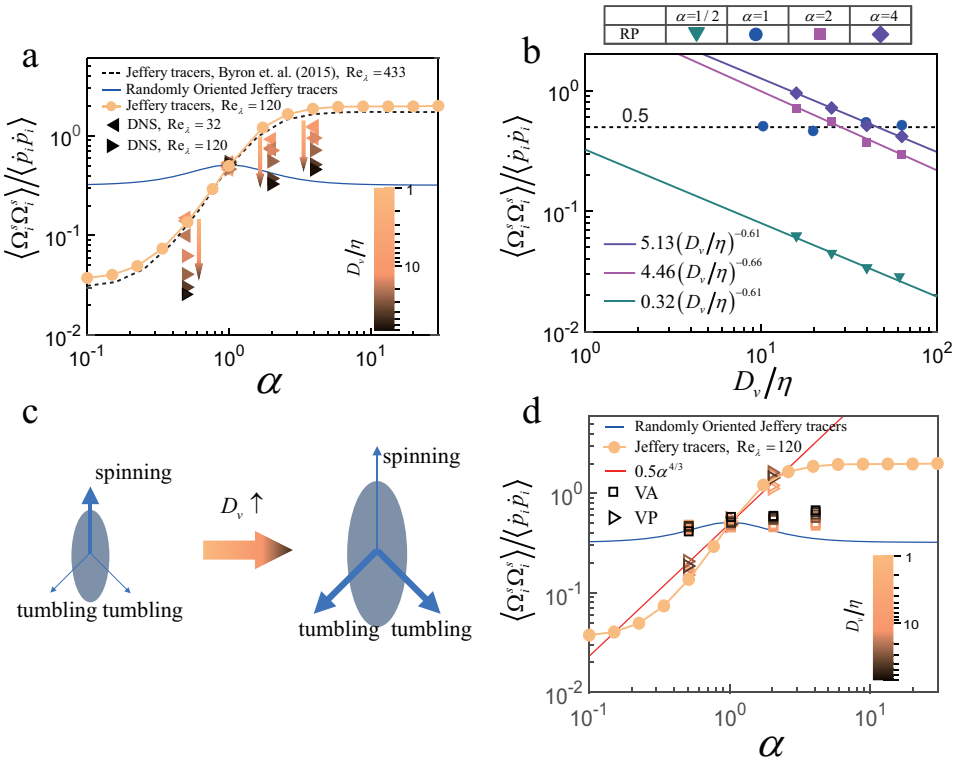


FIGURE 4.4: (a) Ratio of mean squared spinning to tumbling rates, $\langle\Omega_i^s\Omega_i^s\rangle/\langle\dot{p}_i\dot{p}_i\rangle$, versus aspect ratio α for RP. Colors indicate normalized size D_v/η (log scale). Spheres: Jeffery tracers; left/right triangles: $Re_\lambda = 32/120$; arrows show increasing size; dashed line: tracers at $Re_\lambda = 433$ Byron et al., 2015. (b) Same ratio versus size D_v/η. (c) Cartoon illustrating increased tumbling dominance with size for prolate spheroids. (d) Ratio versus α for VA and VP; color bar as in (a).

the ratio falls below one, signalling strain-dominated flow, and it gradually returns to unity farther away. When averaged over a volume extending up to $1.5D_v$, the results consistently show a net reduction of vorticity relative to strain across different aspect ratios and particle sizes. This observation suggests that the reduction of spinning compared to tumbling is due to an effect of fluid–particle coupling, rather than a coarse-graining effect of the fluid fields. The presence of no-slip boundary conditions at the wall leads to the formation of boundary layers where the strain rate is increased relative to the vorticity, which favours a tumbling-type motion. This is a hypothesis that will certainly need to be validated in the future through further numerical and experimental studies. At the moment, the experiments by Oehmke et al., 2021 point similarly to a reduction of spinning as compared to tumbling when the size of the particle is increased and it is in the inertial range; however, a simultaneous characterisation of the flow field around the particles is still missing.

4.2 Rotation of anisotropic particles in convective turbulence

Up to this point in this document, we have discussed physical phenomena of fluid transport taking place in developed turbulence, more precisely in statistically steady, homogeneous, and isotropic flows (HIT in short). This setting is of great importance because it

is considered to be omnipresent in nature, that is to say "universal", as it manifests sufficiently far from the boundaries in any type of vigorously forced Newtonian incompressible fluid. There are, however, in nature many turbulent flows that depart from the HIT prototype. One of them is turbulence generated by natural thermal convection. In this case, the buoyancy force is responsible for breaking the statistical isotropy of the flow (Biferale et al., 2004b), and also to generate peculiar coherent structures, such as thermal plumes and large circulation rolls which appear in the flow. It is therefore interesting to ask how the observations made before on particle rotation and orientation specialise in this and other flow cases.

To keep things simple we just considered small (point-like, or sub-Kolmogorov scale) particles of spheroidal form. This section investigates the rotational dynamics of tiny inertialess anisotropic particles, in turbulent convective flows, that are realized in the Rayleigh-Bénard (RB) model system. In particular I focussed on addressing the following research questions:

i) How is the orientation and the rotation of rods affected by the vertical non-homogeneity of the turbulent convective flow? And what is the effect of coherent flow structures such as the boundary layer (BL), the thermal plumes and the large-scale circulation (LSC)?

ii) What are the trends at varying the particle shape aspect ratio and the turbulence intensity (controlled by the Rayleigh number)?

iii) Finally, in which respect does the phenomenology depend on the system dimensionality (2D vs. 3D)?

4.2.1 Anisotropic particles in 2D convective turbulence

My investigation began with a highly simplified model system (a toy model): the dynamics of inertialess rods in a two-dimensional Rayleigh–Bénard (RB) flow setup (Calzavarini et al., 2020b). The rods are advected in a vertical plane and can rotate only about a horizontal axis through their centre, perpendicular to the plane, thereby restricting their rotational dynamics to tumbling motions. Even this purely hypothetical system is complex enough to make it difficult to predict its statistical properties, particularly those of particle orientation and angular velocity.
To tackle the question the approach was numerical, solving the Boussinesq equations:

$$\partial_t \mathbf{u} + \mathbf{u}\cdot\boldsymbol{\partial}\mathbf{u} = -\boldsymbol{\partial} p/\rho_0 + \nu\,\partial^2\mathbf{u} + \beta g(T-T_0)\hat{\mathbf{y}} \tag{4.7}$$

$$\boldsymbol{\partial}\cdot\mathbf{u} = 0 \tag{4.8}$$

$$\partial_t T + \mathbf{u}\cdot\boldsymbol{\partial} T = \kappa\,\partial^2 T, \tag{4.9}$$

in a 2D rectangular domain of vertical size H and horizontal size $L = 2H$. Boundary conditions were no-slip and isothermal ($T = T_0 \pm \Delta T/2$) on top and bottom horizontal boundaries, and laterally periodic in order to maintain statistical homogeneity along x. In the above equations $\mathbf{u}(\mathbf{x}, t)$ and $T(\mathbf{x}, t)$ are velocity and temperature fields, while $\nu, \kappa, \rho_0, T_0, \beta$, and g are respectively the fluid kinematic viscosity, thermal diffusivity, reference density, reference temperature and volumetric thermal expansion coefficient.

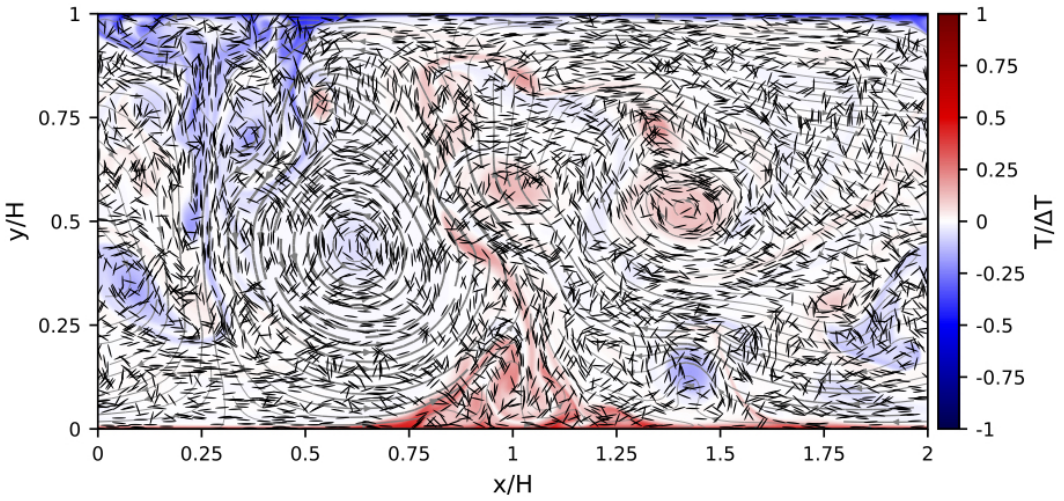
The flow carries point-like anisotropic particles with position $\mathbf{r}(t)$ and orientation $\mathbf{p}(t)$. While the particle center of mass is a perfect fluid tracer the orientation evolves according to (Jeffery, 1922). In 2D eq. (4.1) can be simplified introducing the orientation angle θ by $\mathbf{p} = (\cos\theta, \sin\theta)$, leading to:

$$\dot{\theta} = \frac{1}{2}\omega - \frac{\alpha^2 - 1}{\alpha^2 + 1}[S_{xx}\sin(2\theta) - S_{xy}\cos(2\theta)]. \tag{4.10}$$

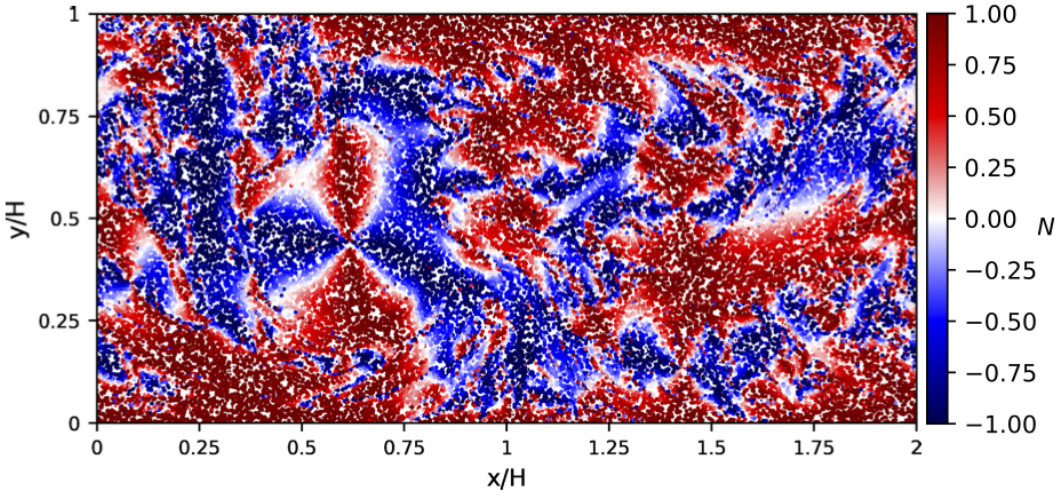
Here α is an aspect ratio that can take only values $\alpha \geq 1$, so ranging from isotropic particles to rods (the usual 3D disks are not possible in our 2D system) The problem then simplifies to the understanding of the statistical properties of such an angle θ and of its temporal derivative $\dot{\theta}$, but all this in a flow that differently from HIT, has lost the isotropy property as well as the homogeneity (as the flow changes going away from the horizontal walls). A visualization of the resulting simulations in such a model system, for the case of very elongated rods ($\alpha = 100$ fibers), is reported in figure 4.5(a). Among the apparent randomness of the fibres' orientations, one can appreciate some sort of order, typically near to the walls where they seem to be preferentially horizontal, or in the thermal plumes where they are mostly vertical.

Gupta et al., 2014 studied a similar system of rods advected by 2D HIT flow. These authors focussed on observables such as the nematic order parameter, $N \equiv 2(\mathbf{p}\cdot\hat{\mathbf{x}})^2 - 1 = 2(\cos\theta)^2 - 1$, and average quadratic tumbling rate $\langle\dot{\theta}^2\rangle$.

In the RB case we adopted the same approach, in figure 4.5(b), I show for illustration a representation of the instantaneous N field corresponding to the snapshot in panel (a) of the same figure. Through this analysis it was possible to show that very elongated particles align preferentially with the direction of the fluid flow, i.e., horizontally close to the isothermal walls and dominantly vertically in the bulk. This behaviour is due to the large-scale circulation flow structure, which induces strong shear at wall boundaries and in up/downwelling regions. In shear-dominated regions, the particles perform Jeffery orbits in the plane and therefore their quadratic rotation rate, $\langle\dot{\theta}^2\rangle$, slows down for orientations parallel to the flow (and orthogonal to the sheared direction). The near-wall horizontal alignment of rods persists at increasing the Rayleigh number (we explored the interval $Ra = 10^5$-10^10, while the vertical orientation in the bulk is progressively weakened by the corresponding increase of turbulence intensity.
Furthermore, we showed that very elongated particles are nearly orthogonal to the orientation of the temperature gradient, an alignment independent of the system dimensionality (as we will see this persists even in 3D systems) and which becomes exact in the limit of infinite Prandtl numbers.
Tumbling rates are extremely vigorous adjacent to the walls, in particular for nearly isotropic particles (short fibers). In the turbulent bulk, the situation reverses, and rods tumble slightly faster than isotropic particles, in agreement with earlier observations in two-dimensional turbulence (Gupta et al., 2014). Most importantly, rods in the bulk do not show any sign of preferential alignment; therefore, as a consequence their tumbling dynamics at the centre of the system can be used to asses the level of local statistical isotropy of the flow. This latter aspect is peculiar to 2D system, in fact as we have seen in 3D turbulent flow the preferential orientation of anisotropic particles is a key dynamical feature(Calzavarini et al., 2020b).



(a)



(b)

FIGURE 4.5: (a) Visualisation of anisotropic particles with aspect ratio $\alpha = 100$ in the Rayleigh-Bénard convective flow at $Ra = 10^9$ and $Pr = 1$. The size of the particle is arbitrary. The color maps the temperature value, while the grey curves represents the instantaneous flow streamlines. (b) visualisation of the corresponding nematic order parameter N. The value 1 (red) indicates horizontal alignment, while -1 (blue) indicates the vertical alignment.

This study persuaded me that the next step to take was to explore a more realistic system in three dimensions.

4.2.2 Anisotropic particles in 3D Rayleigh–Bénard turbulence

A collaboration offered me the possibility to conduct a more comprehensive study. This involved combining experimental investigations with realistic 3D numerical simulations. Linfeng Jiang from Tsinghua University in Beijing, whom I co-mentored during his PhD, was a key driving force behind this work. In this section I present a selection of our findings.

The experiments were conducted in a cubic Rayleigh-Bénard cell of side $H = 24$ cm.

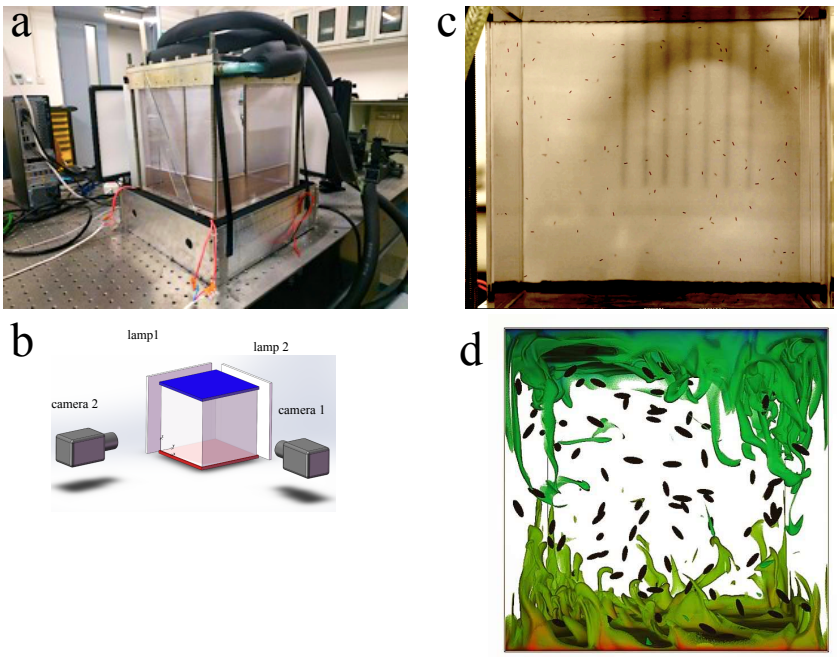


FIGURE 4.6: Picture of the experimental setup (a) and of the cameras positions (b) of the fibers in the cell (their estimated concentration is here $(13\eta)^3$). (c) an illustration from the simulations depicting two temperatures isosurfaces near the horizontal boundaries (particles not on scale).

The system dynamics depend on the Rayleigh number, $Ra = \beta g \Delta T H^3/\nu\kappa$, and Prandtl number, $Pr = \nu/\kappa$. The working fluid was a 55% glycerol solution at mean temperature $T_0 = 40°$C, yielding $Pr \approx 37$. The imposed temperature difference $\Delta T = 17.4$ K corresponded to $Ra = 4 \times 10^9$, satisfying the Boussinesq conditions. The cell had acrylic sides that allowed visual inspection and thick horizontal copper plates. The top plate temperature was controlled by a refrigerated bath, and the bottom plate by a constant heat flux power supply (see Fig.4.6(a)).

Neutrally buoyant polyamide particles (density $\rho = 1.13$ g/cm^3) of cylindrical shape seeded the flow: rods of diameter 0.45 mm, aspect ratio $\alpha = 6$, and disks of diameter 3 mm, aspect ratio $\alpha = 1/6$. Particle concentration was kept very diluted, about one particle per $(13\eta)^3$. Here η denotes the global Kolmogorov scale, which can be estimated thorugh the Nusslet number n, via the relation for the dissipation rate $\bar{\epsilon} = Ra\, Pr^{-2}(Nu - 1)\nu^3/H^4$ Shraiman and Siggia, 1990. The dissipative scales resulted to be $\eta = (\nu^3/\bar{\epsilon})^{1/4} = 1.9$ mm and $\tau_\eta = (\nu/\bar{\epsilon})^{1/2} = 1.1$ s.

The estimated particle response times were $\sim 10^{-2}\tau_\eta$, allowing inertia effects to be neglected. Three-dimensional particle tracking used two orthogonal horizontal cameras covering 89% of the volume, reaching within 4.5 mm of the walls (see Fig.4.6(b,c)). This setup captures both kinetic boundary layers of thickness $\delta_{BL} = H/\sqrt{Re} \approx 10$ mm (with $Re = u_{\rm rms}H/\nu \approx 545$) and the large-scale circulation. Trajectories were reconstructed following Mathai et al., 2016, and orientations from Parsa et al., 2012. Typical trajectory durations spanned $\mathcal{O}(10)$ large eddy turnover times $T = H/u_{\rm rms} = 26.3$ s.

In order to better understand the specificity of particle rotational dynamics in turbulent RB convection as compared to HIT, we perform two series of simulations of anisotropic particles advected by a flow. i) The first set concerns particles that are evolving in a

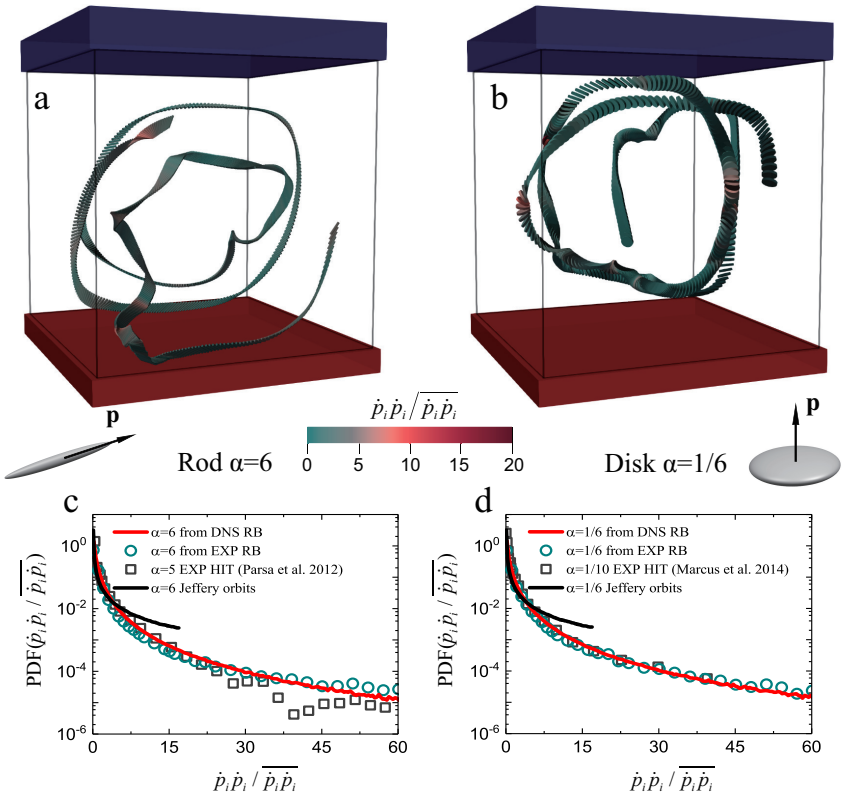


FIGURE 4.7: Visualisation of two trajectories of prolate (a) and oblate (b) particle from experiments. Their duration is $215\tau_\eta$ for $\alpha = 6$ (rod) and $183\tau_\eta$ for $\alpha = 1/6$ (disk). PDF of the square tumbling rate for rods (c) and disks (d): RB experiments (empty circles), DNS results (red line), Jeffery orbits in a steady plane shear flow (black line). For comparison experimental results in HIT from Ref. Parsa et al., 2012 at $\alpha = 5, Re_\lambda = 161$ (c) and Ref. Marcus et al., 2014 at $\alpha = 1/10, Re_\lambda = 91$ (d) are shown.

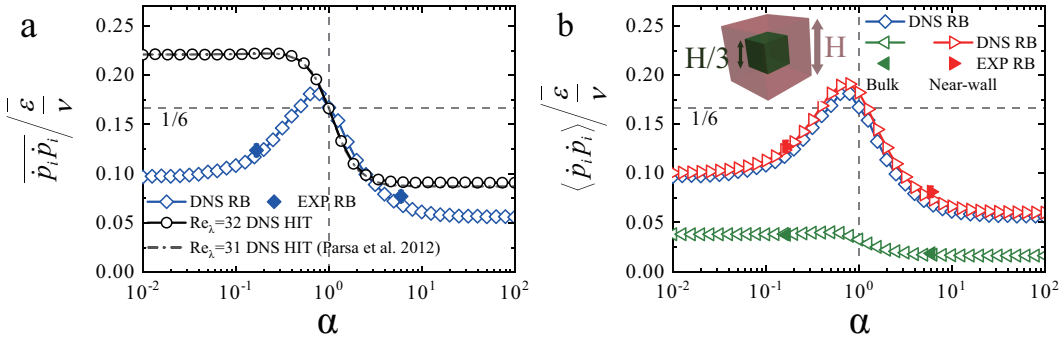


FIGURE 4.8: Mean squared tumbling rate as a function of aspect ratio α. a) With global energy dissipation rate $\bar{\epsilon}$ as normalisation scale: shows RB DNS at $Ra = 10^9$ and $Pr = 40$ (blue diamond), HIT DNS at $Re_\lambda = 32$ (black circles), and for comparison HIT DNS at $Re_\lambda = 31$ from Ref.(Parsa et al., 2012) (grey dashed-dotted line). Filled symbols are experimental measurements in RB for $\alpha = 6$ and $1/6$. b) Measurements in bulk and near-wall subdomains with the same normalisation as in panel a).

Rayleigh-Bénard flow with similar geometrical and physical parameters as the experiments, $Ra = 10^9$, $Pr = 40$ (see Fig.4.6(d) for an illustration); ii) The second set is for particles in a statistically homogeneous and isotropic turbulent flow at Taylor-Reynolds

number $Re_\lambda = 32$, *i.e.*, close to the one estimated in the center of the RB system. As before we adopt an Eulerian-Lagrangian approach, meaning that we describe the flow evolution by means of fluid dynamics equations, while the particle trajectories (i.e. the evolution of their position and orientation) are described in a co-moving frame by ordinary differential equations. Furthermore, we assume that only the evolution of the fluid affects the dynamics of the particles, i.e., we adopt a so called one-way coupling approximation. A numerical resolution of 512^3 equally spaced grid-points is used for the RB flow at $Ra = 10^9$, $Pr = 40$, while 256^3 points are used for the HIT flow at $Re_\lambda = 32$. In all simulations the anisotropic particles cover a wide range of aspect ratios from thin disks to slender fibers, $\alpha \in \left[10^{-2}, 10^2\right]$.

Figure 4.7(a-b) shows typical experimental trajectories of prolate and oblate particles in RB. Visually they appear to follow the large-scale circulation existing in the Rayleigh-Bénard cell. The particle orientation vector $\mathbf{p}(t)$ evolves smoothly in the bulk and changes more abruptly near top and bottom regions, despite the fact that particle-wall collisions are absent. Quantitative analysis via PDFs of the instantaneous quadratic tumbling rate $\dot{p}_i\dot{p}_i$ (normalized by its standard deviation), Fig. 4.7(c-d), reveals fluctuations up to 60 times the mean. For comparison, PDFs for Jeffery orbits, i.e. the ones of randomly oriented particles in steady planar shear, have much shorter tails and finite support. These PDFs agree with prior experiments (Marcus et al., 2014; Parsa et al., 2012) in HIT, agree with the accompanying DNS in RB and curiously do show clear aspect ratio dependence when e.g. we compare fibers with disks.
If the overall distribution of tumbling fluctuations appears to be consistent with what we know from HIT, it is not the case for their intensity in particular the tumbling rate variance $\langle \dot{p}_i\dot{p}_i \rangle$. Figure 4.8(a) presents such a quantity averaged over volume and time, versus aspect ratio $\alpha \in [10^{-2}, 10^2]$. Experimental and numerical data agree and exhibit systematically slower tumbling than in homogeneous isotropic turbulence (HIT) at comparable Re_λ. This indicates either a stronger preferential alignment or a reduced velocity gradient variability in RB flows.

Considering the characteristic RB flow inhomogeneity, we separate the domain into a central bulk volume ($H/3$ side) and a near-wall region (see Fig. 4.8(b)) and perform local averages of the tumbling rates of particles to the regions where they are located. This procedure highlight that tumbling near-wall is nearly twice stronger than in the bulk and that distinct trends appears as a function of the aspect ratio α. Furthermore when we normalize the variance of tumbling rate by the local energy dissipation rates in each region (Fig. 4.9) we reveal that the behaviour in the bulk is nearly perfectly consistent with the one measured in HIT. Clearly this stems from the fact that velocity gradient statistics in the core of the RB cell and in HIT are very similar. On the other hand the near-wall tumbling normalized by local dissipation is lower than in the bulk. Its trend as a function of α shows a local maximum for particles shapes close to spheres, but it contrast with the simple symmetric behaviour of tumbling in a steady planar shear flow (i.e. Jeffery orbits, see solid line in Fig. 4.9). This observation suggests near-wall tumbling might be a superposition of turbulence and steady shear. Indeed a fit resulting from a linear combination of HIT and Jeffery orbit behaviors approaches well the numerical data (Fig. 4.9) and even capture the local maximum near $\alpha \lesssim 1$.

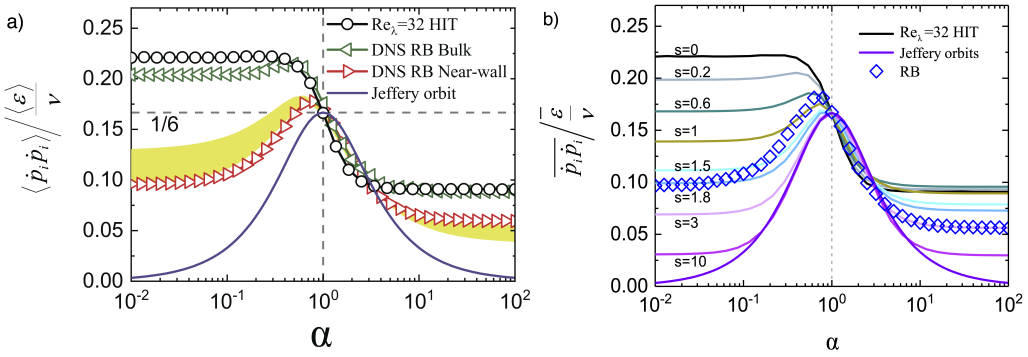


FIGURE 4.9: (a) Local measurements of mean squared tumbling rate in bulk and near-wall regions with the respective local energy dissipation rates normalizations ($\langle\epsilon\rangle$ standing here either for $\langle\epsilon\rangle_{\text{bulk}}$ or $\langle\epsilon\rangle_{\text{near-wall}}$) as a function of aspect ratio α. For comparison we show HIT DNS at $Re_\lambda = 32$ (black circles), Jeffery orbits (violet line) and a best fit of the linear-combination of the two latter curves: $a \times \text{HIT} + (1-a) \times \text{Jeffery}$ with coefficient $a = 0.5 \pm 0.08$. (b) Mean quadratic tumbling rate versus the particle aspect ratio as obtained evolving a particle ensemble with (4.11) where the intensity of the background shear field is s times the average intensity of the HIT velocity gradient fluctuations. The pure HIT case $s = 0$ (black line), and the pure shear case, Jeffery orbits $s = \infty$ (violet line) and the measurements in RB from DNS (diamonds).

To further test the validity of this shear-turbulence superposition hypothesis, we construct a synthetic velocity gradient tensor of the form:

$$\nabla \mathbf{u}_s(t) = \frac{1}{\sqrt{1+s^2}} \left(\nabla \mathbf{u}(t) + \begin{pmatrix} 0 & s\,\tau_\eta^{-1} & 0 \\ 0 & 0 & 0 \\ 0 & 0 & 0 \end{pmatrix} \right), \tag{4.11}$$

where $\nabla \mathbf{u}(t)$ is a signal along a Lagrangian trajectory taken from DNS HIT data, and s controls shear intensity relative to turbulence (the normalization is chosen to preserve the dissipative timescale τ_η). The Jeffery equations are then integrated using the synthetic gradient signal $\nabla \mathbf{u}_s(t)$ as an input and the corresponding average tumbling rates are calculated as a function of the parameter s. In Figure 4.9(b) we show the mean quadratic tumbling versus α for various s, reproducing features observed in RB. The best fit yields $s^* = 2 \pm 0.3$, implying a shear timescale $\tau_s = \tau_\eta \sqrt{1+s^{*2}}/s^* \approx 1.1 \pm 0.1\,\tau_\eta$. This is much shorter than the large-scale circulation turnover time $T \approx 24\,\tau_\eta$ but comparable to the kinetic boundary layer timescale $\tau_{BL} \approx 1.6\,\tau_\eta$. Dimensionally, the relative shear intensity is estimated as $s^* \sim Re^{-1/2}$ (since $Re \sim Ra^{1/2}$ Grossmann and Lohse, 2000; Shraiman and Siggia, 1990), indicating that as Ra increases, the shear influence diminishes compared to turbulence. The ratio $(\tau_s/\tau_\eta)^2$ grows with Ra, reinforcing this trend. However, these estimates remain to be checked in higher-Ra experiments or simulations.

Another observation supports the interpretation that the reduction in tumbling with respect to HIT is due to the wall shear. This is the analysis of the mean alignments of particle with the fluid velocity. Figure 4.10(a)) shows rods ($\alpha = 6$) are preferentially parallel to the local velocity near the walls, while disks ($\alpha = 1/6$) align orthogonally; on the contrary in the bulk particles show no preferential orientation. This agrees with the physics of Jeffery orbits Jeffery, 1922 and is consistent with near-wall dynamics of anisotropic particles observed in simulations in turbulent channel flows (Challabotla et al., 2015; Marchioli et al., 2010).

Additionally we look also at how particles align with the temperature gradient ∇T. Figure 4.10(b) shows clearly that disk-like particles strongly align with it, while rods are weakly but preferentially orthogonal, both in bulk and near-wall regions. This stems from the similarity between particle orientation dynamics and scalar gradient evolution (Calzavarini et al., 2020a).

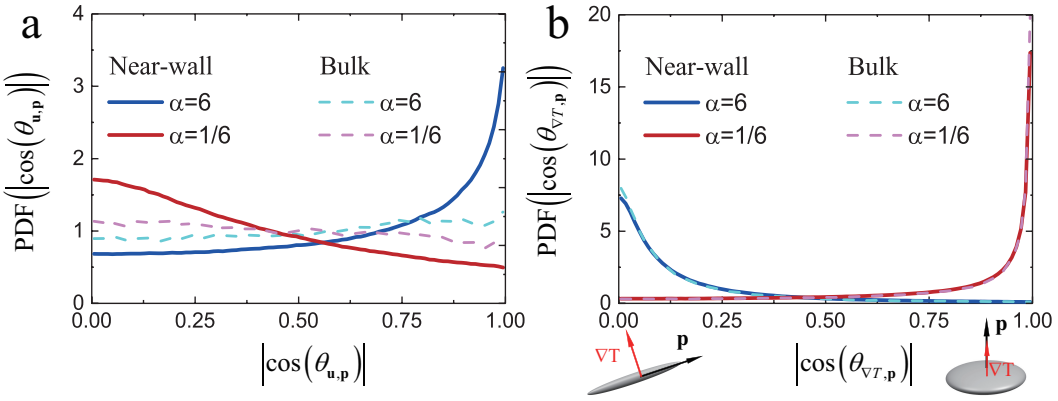


FIGURE 4.10: (a) PDF of the absolute value of the cosine of the angle of particle orientation with the fluid velocity, $|\cos\theta_{\mathbf{u},\mathbf{p}}| = |\mathbf{p}\cdot\mathbf{u}|/||\mathbf{u}||$; (b) the same for the temperature gradient, $|\cos\theta_{\nabla T,\mathbf{p}}| = |\mathbf{p}\cdot\nabla T|/||\nabla T||$. These PDFs use the absolute cosine of the angle for symmetry due to particle fore-aft symmetry.

In fact the orientation $\mathbf{p}(t)$ can be expressed via a non-unit vector $\mathbf{q}(t)$ evolving as (Szeri, 1993):

$$\mathbf{p}(t) = \frac{\mathbf{q}(t)}{\|\mathbf{q}(t)\|}, \quad \dot{\mathbf{q}}(t) = \left(\mathbf{\Omega} + \frac{\alpha^2-1}{\alpha^2+1}\boldsymbol{\mathcal{S}}\right)\mathbf{q}. \tag{4.12}$$

In the thin-disk limit $\alpha \to 0$, this reads

$$\dot{\mathbf{q}}_{\alpha=0} = -\nabla\mathbf{u}^T\mathbf{q}_{\alpha=0}. \tag{4.13}$$

One can now note that the form of this equation matches the evolution equation for a scalar gradient (and so temperature):

$$\dot{\nabla T} = -\nabla\mathbf{u}^T\nabla T + \kappa\Delta\nabla T, \tag{4.14}$$

provided that the diffusion effect is negligible. This explains the observed alignment trend between disks and the gradient of temperature, which becomes particularly pronounced for high Prandtl numbers where thermal diffusivity effects are negligible. We also note that this effect is independent of the dimensionality of the system and explains our earlier specular observation in the 2D RB.

We note that conversely, in the rod limit $\alpha \to \infty$ a similar analogy exists with the vorticity equation (Pumir and Wilkinson, 2011):

$$\dot{\mathbf{q}}_{\alpha=\infty} = \nabla\mathbf{u}\mathbf{q}_{\alpha=\infty}, \quad vs. \quad \dot{\boldsymbol{\omega}} = \nabla\mathbf{u}\boldsymbol{\omega} + \nu\Delta\boldsymbol{\omega}. \tag{4.15}$$

Such an analogy is used to invoke the alignment between fibres and vortices.

In summary, in this work we demonstrated that the orientation dynamics of inertialess anisotropic particles advected by Rayleigh–Bénard turbulent convection exhibit distinctive features compared to those observed in homogeneous isotropic turbulence (HIT). The

heavy-tailed distributions of the tumbling rate indicate that Rayleigh–Bénard flow sustains extreme small-scale fluctuations similar to those found in HIT, despite differences in Reynolds number (which is typicallly smaller in RB as compared to mechanically stirred systems). In contrast, the dependence of the mean tumbling rate on particle aspect ratio reveals a maximum for weakly oblate particles ($\alpha \lesssim 1$), rather than the universal monotonic decrease characteristic of HIT. Moreover, the mean tumbling rate is strongly inhomogeneous across the domain: it is enhanced in the outer regions and reduced in the bulk, where, notably, both its magnitude and its dependence on α recover the behavior typical of HIT. We have shown that the non-monotonic trend observed in the Rayleigh–Bénard system arises from the combined influence of turbulent fluctuations and a persistent mean shear component. This interpretation is supported by the preferential alignment of prolate (oblate) particles parallel (orthogonal) to the local fluid velocity, consistent with Jeffery orbits in steady planar shear flows. These findings might have broader implications for particle rotational dynamics in shear-dominated turbulent flows (such as channel flow) providing an approach to interpret existing measurements. Additionally, the observed preferential alignment with velocity and temperature gradients may inform models of aspherical organisms transported in such environments, both with and without thermal effects (Borgnino et al., 2019; Guasto et al., 2012).

4.3 Conclusions and Perspectives

The work presented in this chapter represents only a small subset of the results achieved in recent years in the field of modeling the rotational dynamics of anisotropic particles. Nevertheless, it highlights two important aspects.

First, as discussed in the latter part of this chapter, it is evident that rotational dynamics strongly depend on the nature of the flow. Properties such as flow statistical isotropy, homogeneity, and, undoubtedly, stationarity influence the fluctuations of particle orientations and alignments. Consequently, observations and measurements obtained in homogeneous isotropic turbulence (HIT) do not necessarily carry over to channel flows, convective systems, or more complex flow configurations. Caution is therefore required when attempting to extrapolate results obtained in idealized systems to more realistic settings, such as the one encountered in natural environments or industrial flows.

Second, the dynamics of real particles can be considerably more complex than those investigated so far. As discussed in the first part of this chapter, the effect of finite particle size alone is not straightforward to rationalize and still requires further clarification. Particles may be non-neutrally buoyant and therefore subject to buoyancy forces, which can significantly affect their rotational behavior. One example is provided by ice crystals in clouds, whose dynamics have been recently thoroughly investigated(Jucha et al., 2018; Pumir et al., 2026). Furthermore, there is a clear need to explore the dynamics of particles with less idealized shapes. A research direction that has developed along these lines concerns the motion of particles with chiral geometries, as investigated, for example in (Huseby et al., 2025; Kramel et al., 2016). Another possible, still to be explored direction concerns particles with irregular shapes, such as volcanic ash particles, microplastics debris, porous dusts. In such cases, the coupling between translational and rotational motion can give rise to complex dynamical behaviors and affect their spreading properties.

Chapter 5

Settling and buoyant particles in turbulence

Contents

4.1 Rotation of finite-sized inertial particles 35
4.2 Rotation of anisotropic particles in convective turbulence 39
4.2.1 Anisotropic particles in 2D convective turbulence 40
4.2.2 Anisotropic particles in 3D Rayleigh–Bénard turbulence 42
4.3 Conclusions and Perspectives 48

5.1 The role of gravity in particle laden flows

The studies presented in the previous chapters have neglected the effect of gravity on the particles considering that the accelerations induced by the carrier fluid are much larger than the ones induced by the gravity. Such an assumption is for instance reasonable for dissipative-scale material particles moving in vigorously turbulent flows generated in laboratory experiments, with Reynolds numbers $Re_\lambda \simeq O(10^2 - 10^3)$. However, this is not necessarily the case in many natural settings, such as for bubbles in oceanic waters (where turbulence is on average milder than the one in a stirred device such as the turbulent Von-Karman flow) or droplets in the atmospheric clouds (where the mass density ratio much in favour of particles). In such situations, the ratio g/a_η, where $a_\eta = \eta/\tau_\eta^2$ is the acceleration at the Kolmogorov scale, can take values of order 10^2 or larger (Devenish et al., 2012). And the particle density contrast with the carrier flow can further enhance the importance of gravity.

In these cases, the Archimedes' buoyancy force cannot be neglected, and the dynamics of dissipative-scale inertial particles are better described by a β-Stokes-Froude model:

$$\frac{d\boldsymbol{v}}{dt} = \beta\frac{D\boldsymbol{u}}{Dt} + \frac{1}{\mathrm{St}}(\boldsymbol{u} - \boldsymbol{v}) + \frac{1}{\mathrm{Fr}}\hat{\boldsymbol{e}_z}, \tag{5.1}$$

This chapter is based on:

1. *Micro-bubbles and micro-particles are not faithful tracers of turbulent acceleration*, Varghese Mathai, Enrico Calzavarini, Jon Brons, Chao Sun and Detlef Lohse, Phys. Rev. Lett. 117, 024501 (2016) [PDF].
2. *Settling of inertial particles in turbulent Rayleigh-Bénard convection*, Vojtěch Patočka, Enrico Calzavarini, and Nicola Tosi, Phys. Rev. Fluids 5, 114304 (2020) [PDF].
3. *Residence time of inertial particles in 3D thermal convection: implications for magma reservoirs*, Vojtvech Patočka, Nicola Tosi, Enrico Calzavarini, Earth and Planetary Sci. Lett. 591, 117622 (2022) [PDF].

where the new dimensionless number, Froude (Fr), that appears here has the following definition Fr $\equiv a_\eta/((\beta-1)g)$.

Buoyancy can have nontrivial effects on particle dynamics, altering their velocity and, consequently, their trajectories and spatial dispersion properties. The combined action of turbulence and gravity creates correlations between particle positions and regions of downward fluid motion. This is the *fast tracking* mechanism, probably first clearly highlighted by Wang and Maxey, 1993 and more recently analyzed in (Bec et al., 2014). Such effects can influence particle clustering (Gustavsson et al., 2014b; Petersen et al., 2019) and the collision rate between particles in less dilute suspensions. Therefore these phenomena are of great applied interest—for instance, in the context of describing the onset of rain formation vapour dense clouds (Falkovich et al., 2002).

For larger particles, as one might expect, the physics becomes more complex. These particles possess higher slip velocities relative to the fluid, therefore their motion is characterised by large Reynolds numbers that call into play non-linear interactions, which manifest in the formation of wakes attached to the particles. In such cases, the so-called *loitering* effect has been observed, whereby particles settle in turbulence at lower speeds than the velocity they would attain in a quiescent fluid (Reartes and Mininni, 2021).

Also for this broad research topic, my contribution focused on a number of specific questions. These were selected either because of their affinity and continuity with my previous studies or, as often happens, because of opportunities that arose during my work, such as encounters with colleagues and the possibility of fruitful collaborations. In the following, I will present two distinct lines of research.

The first is clearly rooted in my previous studies and investigates how gravity influences the statistical properties of the acceleration of particles in a turbulent flow. The focus was here on sub-Kolmogorov inertial particles, but with densities varying in a wide range from bubbles to massive particles. This study was carried out in collaboration with the Physics of Fluids Group at Twente University (Mathai et al., 2016).

The second research topic addresses the problem of the sedimentation of inertial particles in a confined convective turbulent flow (again using the Rayleigh–Bénard system as a prototypical model). My interest in this topic arose from interactions with planetary scientists at the University of Berlin, in particular with N. Tosi and his research group.

5.2 Accelerations of settling/buoyant particles in turbulence

From a theoretical perspective it is possible to show that in the limit of small particles, i.e. $St \to 0$, and finite Fr number, from (5.1) one obtains that the particle velocity goes as $\boldsymbol{v} \simeq \boldsymbol{u} + \frac{St}{Fr}\hat{\boldsymbol{e}}_z$, where $\frac{St}{Fr}\hat{\boldsymbol{e}}_z$ represents the particle settling terminal velocity (i.e. the Stokes velocity) in dimensionless units. This implies for the acceleration,

$$\boldsymbol{a} \simeq D_t\boldsymbol{u} + \frac{\mathrm{St}}{\mathrm{Fr}}\partial_z\boldsymbol{u}. \tag{5.2}$$

Assuming statistical independence between $D_t u_i$ and $\partial_z u_i$, and making use of the statistical relation for the gradients of the velocity field in a statistically stationary, homogeneous and isotropic turbulent flow (Pope, 2000), one arrives at the following relations for the variances of the horizontal and vertical accelerations of a particle

$$\frac{\langle a_x^2 \rangle}{\langle (D_t u_i)^2 \rangle} \simeq 1 + \frac{2}{15 a_0} \left(\frac{\mathrm{St}}{\mathrm{Fr}} \right)^2, \tag{5.3}$$

$$\frac{\langle a_z^2 \rangle}{\langle (D_t u_i)^2 \rangle} \simeq 1 + \frac{1}{15 a_0} \left(\frac{\mathrm{St}}{\mathrm{Fr}} \right)^2, \tag{5.4}$$

where the $\langle (D_t u_i)^2 \rangle$ represent the variance of the fluid acceleration (single component, i.e. summation over i not implied). This relation, first proposed in our work (Mathai et al., 2016), is a remarkable prediction without any adjustable parameter, provided that the fluid acceleration is known. The latter can be measured either through Lagrangian fluid tracers or in Eulerian manner with a fixed probe. Furthermore it is applicable to both heavy (St/Fr < 1) and light (St/Fr > 1) particles of any density. It says that as gravity is more important the acceleration variance increases quadratically in g and with a larger coefficient (the double) for the component transverse to the gravity (x) as compared to the one aligned with it (z).

We tested this prediction using numerical simulations based on point particles and equation (5.1) for HIT flows. The result, see figure 5.1, are in reasonable agreement with the prediction at least till $St/Fr \leq 20$. Experiments involving tiny air bubbles dispersed in a turbulent water tunnel flow also confirmed the prediction. However, we note that for heavy-particles, the prediction still remains to be experimentally verified.

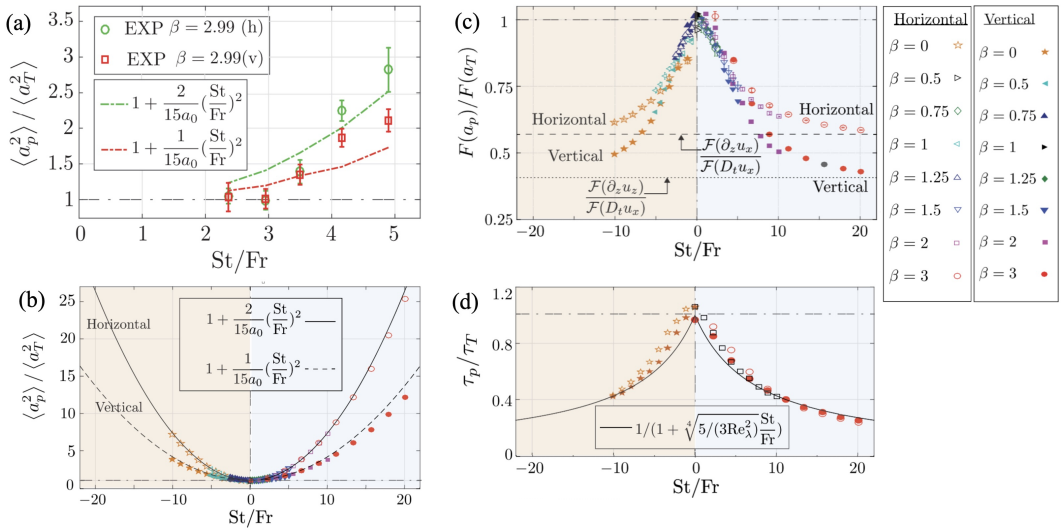


FIGURE 5.1: (a) Normalized acceleration variance in horizontal (h) and vertical (v) directions*vs.* St/Fr for bubbles from experiments. (b,c,d) DNS results: (b) normalized acceleration variance, (c) normalized flatness factor, (d) normalized correlation time *vs.* St/Fr for buoyant and heavy particles. Solid and dashed curves in (a) show our theory predictions based on (5.3) and (5.4) for horizontal and vertical accelerations. The black curve in (d) shows the theoretical prediction for correlation time (5.7).

A corollary of the above prediction concerns the trends for the acceleration flatness of the

components of the acceleration, $\mathcal{F}(a_i) \equiv \langle a_i^4 \rangle / \langle a_i^2 \rangle^2$ Under the same statistical assumptions as above we obtain the trend for the flatness of the particle acceleration normalized by the corresponding quantity for a fluid tracer, i.e. $\mathcal{F}(a_i)/\mathcal{F}(D_t u_i)$. Clearly this quantity must tend to 1 for $St \to 0$, while when St/Fr is large it asymptotically approach the limits

$$\frac{\mathcal{F}(a_x)}{\mathcal{F}(D_t u_i)} \simeq \frac{\mathcal{F}(\partial_z u_x)}{\mathcal{F}(D_t u_i)}, \tag{5.5}$$

$$\frac{\mathcal{F}(a_z)}{\mathcal{F}(D_t u_i)} \simeq \frac{\mathcal{F}(\partial_z u_z)}{\mathcal{F}(D_t u_i)}. \tag{5.6}$$

Since it is verified that $\mathcal{F}(\partial_z u_z) < \mathcal{F}(\partial_z u_x) < \mathcal{F}(D_t u_x)$ (Ishihara et al., 2007), this leads to the prediction $\mathcal{F}(a_z) < \mathcal{F}(a_x)$. In other words, the vertical acceleration of particle is less intermittent than the horizontal one and all less intermittent than the one of fluid tracer in the same flow. This prediction could be verified in the simulations, see figure 5.1(c).

We have seen that gravity increases the variance of acceleration while at the same time reducing its intermittency. What, then, is its effect on the correlation time?

Clearly, the drifting of a buoyant or heavy particle through the flow influences the correlation time of its acceleration. To model this, we consider the case of a particle drifting through the flow with its terminal velocity v_r. In the absence of particle drift, it is well established that the decorrelation time is close to τ_η (Yeung and Pope, 1989). For buoyant or settling particles, however, the correlation time is shortened by the additional drift velocity. The resulting correlation time may be approximated as $\tau_p \simeq \frac{\tau_\eta}{1+v_r/u_{rms}}$. In homogeneous and isotropic turbulence, u_{rms} can be expressed in terms of the Reynolds number, Re_λ, and the Kolmogorov velocity scale, u_η. This leads to the expression

$$\frac{\tau_p}{\tau_\eta} \simeq \frac{1}{1 + \left(\frac{5}{3Re_\lambda^2}\right)^{\frac{1}{4}} \frac{St}{Fr}} \tag{5.7}$$

This prediction is again in reasonable agreement with our numerical observations, Fig. 5.1(c).

This study showed that, in the limit of small inertial particles, it is possible to derive simple yet non-trivial predictions for the behavior of acceleration statistics in fully developed turbulence. These predictions were validated both numerically, for any particle density, and experimentally in the case of bubbles. It is clear that, for larger particles and consequently for larger values of $|St/Fr|$, deviations from these predictions are expected to occur. The problem then becomes more complex, since the simple linear Stokes drag model is no longer sufficient to describe the particle dynamics accurately. Additionally spatial filtering effects due to the particle finite size may appear. To the best of my knowledge, such studies has not yet been systematically carried out, and it would be interesting to pursue them in the future.

5.3 Settling of particles in turbulent convecting flows

It is not surprising that the dynamics of inertial particles and their sedimentation in convective flows are of relevance across many domains of the natural sciences. In fact, atmospheric phenomena, oceanic currents, and planetary cooling are all governed by convective motions, and in each of these contexts one encounters small suspended bodies that can be effectively modelled as inertial particles. Examples include sand and dust transported in the atmosphere (Schwaiger et al., 2012), ashes in volcanic clouds, the drifting and settling of marine snow and microplastics in the ocean and lakes (Ruiz et al., 2004; Squires and Yamazaki, 1995), or the deposition of solid rock crystals embedded in solidifying heterogeneous magmas (Breuer et al., 2015; Jones, 2015).

My interest in this subject began with an encounter with Nicola Tosi of the DLR Institute of Space Research in Berlin, a planetologist. He introduced me to open questions in planet formation studies that could benefit from a fluid-dynamicist approach. One key problem is the crystallisation mechanism of primordial *magma oceans* during planet formation. I will describe this in more detail below.

Planetary-scale volumes of liquid silicates (i.e. magma oceans) are thought to form during the accretion and differentiation of terrestrial bodies like the Earth, Mercury, Venus, Mars and the Moon (e.g., Safronov, 1969; Tonks and Melosh, 1992, 1993). The way magma oceans solidify is of primary importance for the long-term thermo-chemical evolution of the interior of planets (e.g., Tosi and Padovan, 2020). One proposed mechanism is the one of fractional crystallization, i.e. the process by which different minerals crystallize from a cooling magma at different temperatures, and the crystals are physically separated from the remaining liquid, causing the composition of the residual melt to evolve over time. Whether newly formed crystals settle or remain suspended by turbulent flow determines the composition of the silicate mantle (e.g., Elkins-Tanton, 2012). This is a complex problem that depends on the density contrast between crystals and melt, the melt viscosity, the size of the crystals and the convective dynamics of the system. If dense crystals are efficiently maintained in suspension, a magma ocean undergoes equilibrium (or *batch*) crystallization, which leads to a largely homogeneous composition of the rocky mantle. By contrast, if crystals tend to settle and crystal-melt separation is efficient, *fractional* crystallization takes place. Residual melts are progressively enriched in so-called incompatible elements such as iron-oxides and heat-producing elements. This process ultimately leads to a compositionally-stratified mantle whose long-term evolution can be dramatically different from that of a homogeneous one (e.g., Ballmer et al., 2017; Maurice et al., 2017; Plesa et al., 2014; Tosi et al., 2013). Similar processes occurs in Magma chambers that are small-scale analogs of magma oceans. Upon cooling and solidification these typically undergo strong fractionation, which is often attributed to crystal settling (e.g., Koyaguchi et al., 1990; Marsh and Maxey, 1985; Martin and Nokes, 1988; Martin and Nokes, 1989). In summary the differentiation of a cooling magma is a competitive process between generation, sedimentation, advective transport and re-entrainment of crystals in a often vigourously convecting environment. In order to have accurate predictive models it is in principle necessary to understand each of these processes.

This scientific challenge motivated a collaboration within which we conceived an idealized numerical experiment aimed at focussing on the sedimentation properties of crystals

in a convecting fluid enclosed between two boundaries. Specifically, we adopted the classical Rayleigh–Bénard system in the regime of developed turbulent convection in a fluid at high Prandtl numbers (as expected for melted rocks) and considered tiny inertial particles advected by this flow. According to our crude simplifying hypothesis, the particle are homogeneously seeded in the volume containing the fluid, like solid crystal or volatile bubbles that nucleates in a heterogeneous liquid medium. We pose the question of determining the characteristic timescale required for particles within such a flow to sediment, namely, to reach either the lower (or upper if lighter) boundary of the system. Although this is a simplified model that neglects many crucial aspects of crystal dynamics, such as for instance the re-entrainement phenomenon, the resulting phenomenology is far from trivial.

For better clarity we provide the complete set of the equation that compose the model system. The fluid flow is governed by the already presented set of Boussinesq equations which describe the evolution of the velocity $\mathbf{u}$ and temperature θ fields, here below in dimensionless form:

$$\partial_t \mathbf{u} + (\mathbf{u}\cdot\nabla)\mathbf{u} = -\nabla p + \sqrt{\frac{Pr}{Ra}}\nabla^2\mathbf{u} + \theta\,\hat{\mathbf{z}} \tag{5.8}$$

$$\nabla\cdot\mathbf{u} = 0 \tag{5.9}$$

$$\partial_\tau \theta + (\mathbf{u}\cdot\nabla)\theta = \frac{1}{\sqrt{PrRa}}\nabla^2\theta. \tag{5.10}$$

The system is here made dimensionless by means the convective scales: the height of the domain H, the characteristic free-fall velocity $u^* := \sqrt{\alpha g \Delta T H}$, the reference density ρ_0, and the thermal gap ΔT between top and bottom boundaries. The Rayleigh and Prandtl number that control the flow state takes the usual form: $Ra := \frac{\alpha g \Delta T H^3}{\nu\kappa}$, $Pr := \frac{\nu}{\kappa}$. In principle, in magma oceans and chambers, there might also be some volumetric heating due to the decay of radiogenic material; this is neglected in our study. The fluid carries inertial particles, whose trajectory is governed by the equation (5.1), that in the current dimensionless terms reads:

$$\frac{d\mathbf{v}}{dt} = \beta\frac{D\mathbf{u}}{Dt} + \frac{1}{St_H}(\mathbf{u}-\mathbf{v}) + \Lambda\,\hat{\mathbf{z}}, \tag{5.11}$$

The three non-dimensional parameters which control the particle dynamics are now:

$$\beta = \frac{3\rho_\mathrm{f}}{\rho_\mathrm{f}+2\rho_\mathrm{p}}; \quad St_H = \frac{r_c^2\sqrt{\alpha g\Delta T}}{3\nu\beta\sqrt{H}}; \quad \Lambda = \frac{\beta-1}{\alpha\Delta T}. \tag{5.12}$$

The Stokes number, St_H, stands here for the particle viscous response time $\tau_d = r_c^2/(3\nu\beta)$ in units of the characteristic free-fall convective time $T_H = H/u^*$ (it is different , typically much smaller, from the Stokes number based on Kolomogorov scale that encountered before). The parameter Λ (hereafter buoyancy ratio) expresses the relative importance of particle buoyancy with respect to the thermally induced buoyancy of the fluid, and it represents an inverse Froude number for convective flows (note that gravity does not explicitly appear in it, as it simplifies appearing both in the numerator and denominator). In our study we did not consider any feedback mechanism of particles on the flow assuming that the crystal distribution remains diluted.

In turbulent flow conditions, the adopted particle model is appropriate as long as the particle size, $d = 2r_c$ (resp. d/H in dimensionless units) is up to the same order of magnitude as the spatial dissipative scale of turbulence, η. In Rayleigh-Bénard flow the global value of such scale goes as $\eta/H = Pr^{1/2}(Ra(Nu-1))^{-1/4}$ (e.g. Shraiman and Siggia, 1990), meaning that it decreases at increasing the thermal forcing Ra (and so the Nusselt number Nu) but increases at increasing the Prandtl number Pr. Our simulation parameters where chosen in such a way that the condition was always satisfied.

Equations (5.8-5.10) were solved in 2D and some 3D boxes with periodic side walls and in domains with aspect ratio (width/widths over height) $\Gamma \equiv L/H = 2$. No-slip conditions were assumed on the top and bottom boundaries, which are isothermal, with a constant temperature difference driving thermal convection. We simulated convective flows in a statistically steady state up to $Ra = 10^{12}$ and $Pr = [1, 10, 100]$ (the high Prandtl number being of interest for molten rocks). Furthermore, we systematically varied the particle-fluid density ratio, $\rho_\mathrm{p}/\rho_\mathrm{f}$, assuming that it is constant for each particle throughout the simulation. This assumption does not necessarily neglect the density variations of material: in view of the Boussinesq approximation $\rho_\mathrm{f} = \rho_0[1-\alpha(T-T_0)]$, employed in Eq. (5.8), the assumption means that each particle is always at the same temperature as the surrounding fluid and has the same thermal expansivity (for effects resulting from keeping the particles at a different temperature than the fluid, see Gan et al., 2003). The particle response time $\tau_d = r_c^2/(3\nu\beta)$ depends quadratically on the particle radius r_c, which we also vary systematically. The simulations were seeded with $O(10^6)$ particles of $O(10^2)$ different types obtained by evenly sampling $\rho_\mathrm{f}/\rho_\mathrm{p}$ and r_c^2. We note that for particles suspended in a fluid at rest, i.e. with $\boldsymbol{u} \equiv 0$, Eq. (5.11) can be solved analytically, yielding:

$$\tilde{\mathbf{v}}(\boldsymbol{x}, t) = \mathbf{v}_0(\boldsymbol{x}) \, \exp\left(\frac{-t}{St_H}\right) + St_H \, \Lambda \, \hat{\boldsymbol{z}}. \tag{5.13}$$

In the limit $t \to \infty$, the so-called terminal (or Stokes) velocity $v_t = -St\,\Lambda$ is reached (note that we take v_t positive for settling particles).
Particles with $v_t > 0$ ($\Leftrightarrow \Lambda < 0 \Leftrightarrow \beta < 1$), i.e. those denser than the fluid are simply labeled as *heavy*, on the opposite $v_t < 0$ ($\Leftrightarrow \Lambda > 0 \Leftrightarrow \beta > 1$, are denoted as *light*. Initially, all particles are distributed uniformly across the domain and their velocity is set equal to the local velocity of the fluid. A flow visualization of particles suspended in 2D RB turbulence, performed with our Eulerian-Lagrangian code (appendix A), is reported in figure 5.2.

5.3.1 Analysis of Particles Residence Times

The main observable on which we focused on is the time, t_{res}, it takes for a particle to settle at a horizontal wall (at the bottom for heavy particles at the top for light ones). Such a quantity obviously depends on the particle initial position. Therefore, in order address the particle population as a whole we consider the mean residence time of particles of the same type (same β and St_H). The quantity is simply defined as $\overline{t_{res}} = \int_0^\infty N(t)\,\mathrm{d}t/N_0$ where $N(t)$ is the number of suspended particles in the system at a given time and N_0 its initial value. It is convenient to normalize this time by the mean residence time that would be obtained for particles of the same family settling in a quiescent fluid, which can be written has $0.5\,H/|v_t|$. This dimensionless observable, $\overline{t_{res}}\,/\,(0.5\,H/|v_t|)$, which measures the global

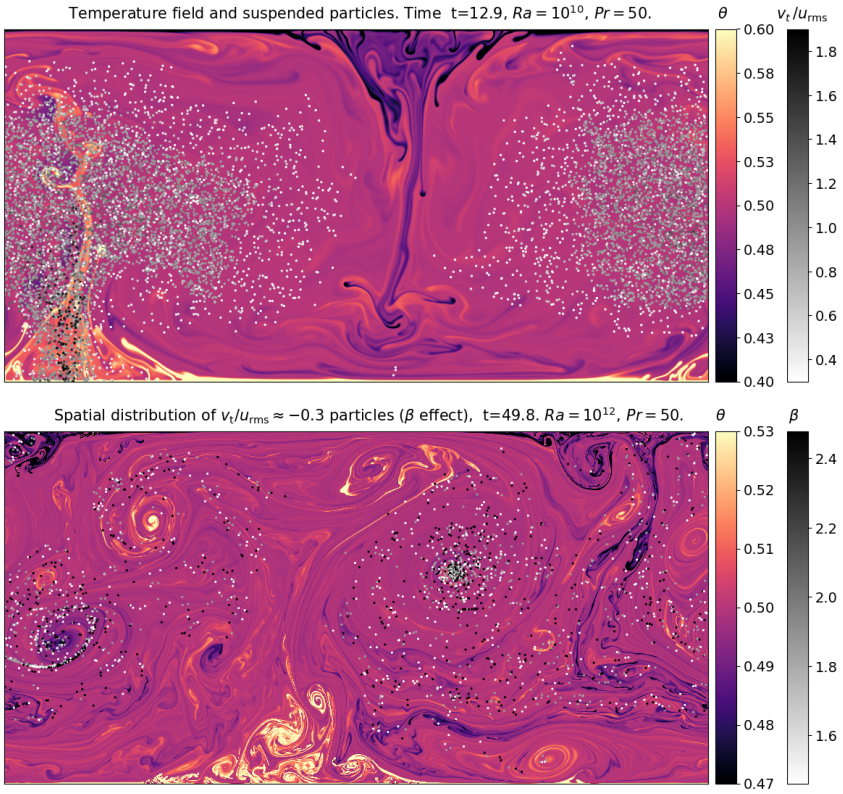


FIGURE 5.2: Visualization of suspended particles in the 2D RB system form the simulations, from (Patočka et al., 2020). (a) $Ra = 10^{10}$, $Pr = 50$, heavy particles: $\beta < 1$ and variable $v_t/u_{rms} > 0$. Noticeable asymmetry in the concentration between upwelling and downwelling plumes. (b) $Ra = 10^{12}$, $Pr = 50$ light particles: β is varied while $v_t/u_{rms} = -0.3$ is kept fixed . Time is in dimensionless large-turover-time units. We can observe strong trapping in vortices.

effect of the fluid flow on the particle settling behaviour. It depends both on the particle properties (β, St, Λ) as well on the fluid flow characteristics (Ra,Pr,Γ). Figure 5.3 illustrate the results from 3D RB simulations (Patočka et al., 2022), in which the measured normalized mean residence times are plotted against the ratio $|v_t|/u_{rms}$, with u_{rms} the global root mean square fluid velocity, which parametrize the intensity of the convective flow. The two limiting cases of $|v_t|/u_{rms} \gg 1$ and $|v_t|/u_{rms} \ll 1$ are to be understood as follows: When $|v_t|/u_{rms} \gg 1$, the particles do not effectively see the flow, because the fluid barely moves during the time it takes for these particle to reach the bottom (or top) of the container. The mean residence time $\overline{t_{res}}$ is equal to $0.5H/|v_t|$ in this limit, because the particles are initially distributed uniformly throughout the container, and their mean height is thus $0.5H$ at the time $t = 0$. We call this *stone-like* regime. When $|v_t|/u_{rms} \ll 1$, on the other hand, the particle dynamics are in the regime of a well-mixed suspension (Martin and Nokes, 1989), it corresponds to the *dust-like* regime. These particles are perfectly stirred within the convective bulk, and effectively sink only when they are randomly transported to the thin boundary layer near the bottom layer (or the top, when $\rho_p/\rho_f < 1$). In those layers their settling velocity becomes locally larger than the fluid velocity and they can sink freely as stone like particles too. The initial positions of particles do not matter in the dustl-like regime, because redistribution (mixing) within the model domain takes place in approximately one large-eddy turnover time, an interval much shorter than the typical settling time of these

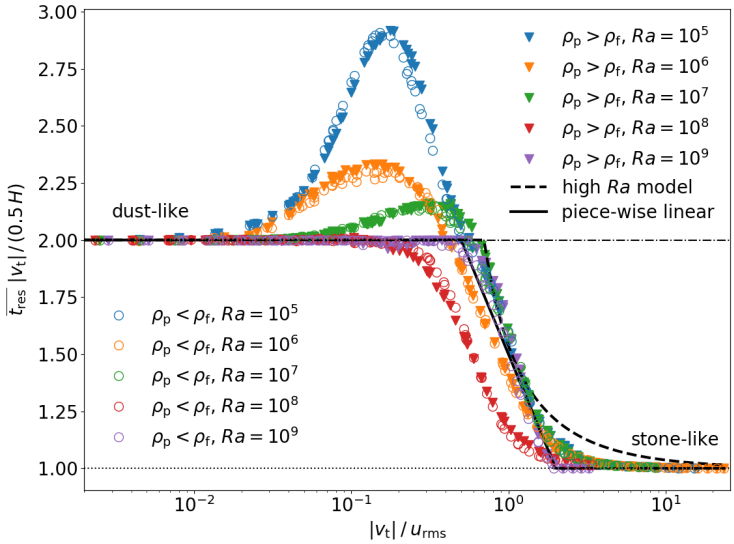


FIGURE 5.3: Mean residence time of the particles, normalized by the mean terminal time $0.5\,H/|v_t|$. Triangles represent heavy particles, i.e. the particle types with $\rho_p/\rho_f \in (1{-}2]$, while open circles stand for light particles, $\rho_p/\rho_f \in [0{-}1)$. The dashed black line represent the model proposed in (5.17) with $\gamma = 0.7$. the black solid line represents the empirical high-Ra model towards which the results appears to converge when Ra is increased. This is a piece-wise linear model that goes from 2 to 1, with $|v_t|/u_{rms} = 0.5$ and $|v_t|/u_{rms} = 2.0$ marking the transition on the x-axis.

particles. In Fig. 5.4, we show that the particle residence time over a population of particles in the dust-like regime follows an exponential distribution, with the probability density function being $\sim \exp(-t_{res}H/|v_t|)$, yielding $\overline{t_{res}} = H/|v_t|$ after averaging over the ensemble (Martin and Nokes, 1989). On the contrary in the stone-like regime the pdf is just a step-function (see the solid black line in Fig. 5.4).

It is interesting to notice that in the intermediate regime, for $0.02 \lesssim |v_t|/u_{rms} \lesssim 2.0$, the

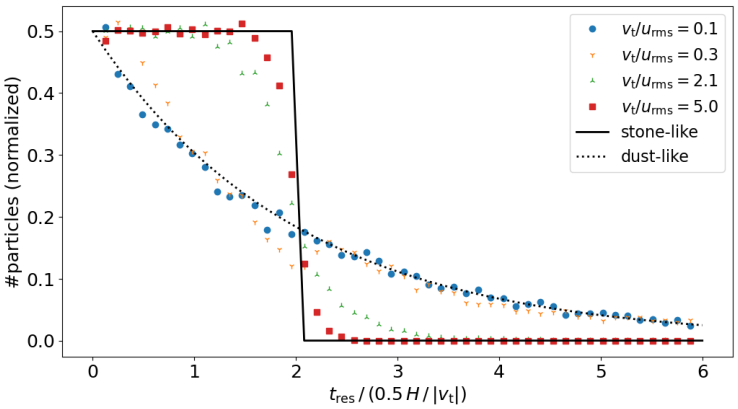


FIGURE 5.4: Probability density function of t_{res} for $Ra = 10^6$ and $Pr = 1$. The analytical distributions for the dust-like (dotted black line) and stone-like (solid black line) regimes stem from Eq. (5.14), upon considering the concentration at the settling front to be either $N(t)/H$ (dust-like regime) or N_0/H (stone-like regime). Note that the probability density distributions of t_{res} show certain deviations from the idealized end-members for values as small as $|v_t|/u_{rms} = 0.1$ and as high as $|v_t|/u_{rms} = 5.0$.

large-scale circulation of the flow may alter the obtained particle dynamics, remarkably increasing the average residence time $\overline{t_{res}}$, see gain Fig. 5.3. This increase is caused by

the trapping of particles inside relatively stable convection rolls, see figure. The second important observation connected to figure 5.3 is that $\overline{t_{res}}$ is less and less affected by the large-scale circulation when Ra increases. A very vigorous convection makes the particle trapping into fluid structures less impactful at the scale of the global population. A third remarkable aspect is that there is barely no difference in $\overline{t_{res}}$ for the heavy and light particles, not even when $Ra = 10^9$ (circles vs triangles in Fig. 5.3). The independence of $\overline{t_{res}}$ on the sign and value of $1-\beta$, cf. circles vs triangles in Fig. 5.3, points to the unimportance of the effect of preferential sampling in the explored parameter regime. Indeed, we have repeated one $Ra = 10^4$ and one $Ra = 10^8$ simulation, replacing Eq. (5.11) with even simpler particle dynamics in the form of $\boldsymbol{v} = \boldsymbol{u} - St\,\Lambda\hat{\boldsymbol{z}}$ (the so called overdamped limit, where clustering is prevented) , and the settling statistics were comparable.

With these observations an idealized model that roughly captures the observed residence times in the limit of large Ra can be proposed (which generalizes the model proposed by Martin and Nokes, 1989 for dust-like particles). The particle mass conservation imposes that the rate of particles leaving the suspension is

$$\dot{N}(t) = -|v_t|\,A\,c_{\text{wall}}, \tag{5.14}$$

where A the bottom(or top) wall surface, while $c_{\text{wall}} = \langle c(z{\to}0,t)\rangle$ is the mean particle concentration at the wall. Assuming that the particle trapping by the flow is negligible (true at high Ra), we can use the following estimation based on a homogeneous particle distribution in a progressively shrinking volume:

$$c_{\text{wall}} = \frac{N(t)}{A\,(H - t\,v_{sh})}. \tag{5.15}$$

The shrinking velocity v_{sh} describes how the particle cloud, i.e. the region that contains the $N(t)$ particles, changes in volume with time. Its value is different for each particle type, approaching 0 in the dust-like limit (particles always occupy the entire volume AH), and $|v_t|$ in the stone-like limit (the volume Av_tt at the top of the tank is particle-free). With the help of Eq. (5.15), the solution of Eq. (5.14) can be obtained:

$$N(t) = N_0\left(1 - \frac{t\,v_{sh}}{H}\right)^{\frac{|v_t|}{v_{sh}}}, \tag{5.16}$$

which gives the behaviour $N_0\exp(-v_tt/H)$ in the "dust" limit of $v_{sh} \to 0$ (in agreement with (Martin and Nokes, 1989)) and and $N_0(1-v_t\,t/H)$ in the "stone" regime for $v_{sh} \to |v_t|$. A possible approximation for the shrinking velocity is the following

$$v_{sh} = \begin{cases} |v_t| - \gamma\,u_{rms}, & \text{if } |v_t| > \gamma\,u_{rms} \\ 0, & \text{if } |v_t| \le \gamma\,u_{rms} \end{cases} \tag{5.17}$$

where γ is a constant representing the mixing of particles - it mimics the fact that some particles are transported above the settling front due to the advection by fluid eddies. The second case in Eq. (5.17) expresses the constraint $v_{sh} > 0$, because the model domain does not expand in response to mixing. The normalized residence time can then be obtained by

integrating (5.16)

$$\frac{|v_t|}{0.5\,H}\,\overline{t_{res}} = \begin{cases} \frac{2}{2-\gamma\,u_{rms}\,/\,|v_t|}, & \text{if } |v_t|/u_{rms} > \gamma \\ 2, & \text{if } |v_t|/u_{rms} \leq \gamma \end{cases} \tag{5.18}$$

Of course the parameter γ remains to be determined: based on the $Ra = 10^9$ simulations, the best-fit choice for γ is 0.7. The corresponding solution is plotted with black dashed line in Fig. 5.3. It also appears that in the large Ra limit the behaviour seems to converge to a nearly piece-wise linear model bridging between the two regimes.

Some observations are in order. First, what is not yet available is a model that describe the effect of particle retention at finite Ra numbers. A parametrisation of this regime might be possible, however the task remain challenging. We verified that there is a dependency on the dimensionality of the flow: $2D$ convection tend to trap for longer times the particles as compared to $3D$ (Patočka et al., 2022). As a consequence a reliable model shall probably call into play 3D flow effects. Beside that the Pr dependence must be taken into account as it affects the shape of coherent structures (large Prandlt number flows have thinner plumes) and this has an effect on the particle retention in the bulk. We finally note that the above model is derived for an initially uniform distribution of particles. Care must be taken when the model is applied to different settings, e.g. when all heavy particles are near the top boundary at the time $t = 0$.

5.3.2 Spatial distribution of settled particles

For the reasons discussed above, it appears evident that the question of how fluid coherent structures affect the particle settling patterns is crucial for a better understanding of the system's behaviour. We begin with a description of the phenomenon in 2D, as we did in (Patočka et al., 2020).

Figure 5.5 illustrates the average horizontal distribution of settled particles in a 2D turbulent simulation at $Ra = 10^{10}$, $Pr = 50$, $\Gamma = 2$. The top panel reports the fluid vertically- and time-averaged vertical component of the velocity field. It highlight the fact that in the RB system there are locations of upwelling and downwelling that are very persistent in time despite the long duration of the simulations over several eddy turnover times. The bottom panels display the distribution of the positions along the horizontal walls where, during the simulation, heavy (panel b) and light (panel c) have settled. The peaks of the curve correspond to the edges of large-scale convection cells, whose centres are indicated by the grey symbols in panels b),c). It is clear that heavy and light particles follow opposing patterns. Heavier particles settle preferentially in upwelling regions while lighter ones settle in downwelling areas. Interestingly, these settling regions also correspond near the walls to very low sluggish flow velocities. These regions have very little kinetic energy compared to the large-scale circulating rolls and remain quite stable in their horizontal location. In (Patočka et al., 2020), we used a geometrical characterisation of these structures. Due to their shape, we dubbed them low-velocity "piles" (see Fig. 5.6).

The observed features stay true also for stone-like particles , as depicted in fig. 5.7 which reports the same measure but for particles 10 times larger. Also these particles settle preferentially in the low-velocity pile located at the edges of the convecting rolls (at least as long

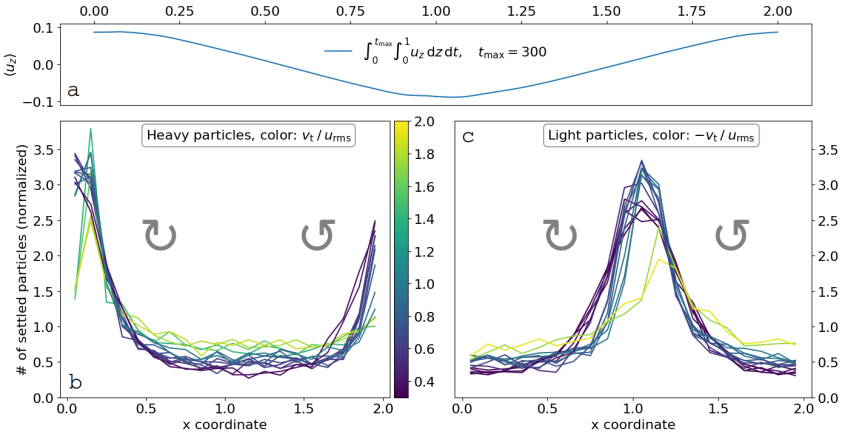


FIGURE 5.5: Horizontal distribution of settled particles in the simulation set $Ra = 10^{10}$, $Pr = 50$. The v_t/u_{rms} ratio is depicted in color, varying in the range, $0.3 < v_t/u_{rms} < 2.0$, is selected. (a) Vertically averaged vertical component of the fluid velocity, u_z. The quantity is further averaged over time, with the time window of integration covering complete sedimentation of the respective particles. (b) Heavy particles. (c) Light particles. Gray symbols indicate the flow direction of two major convection cells. The settled particles are sorted into 20 equally wide bins and the plotted value is normalized by the initial number of particles, i.e. divided by $N_0/20$.

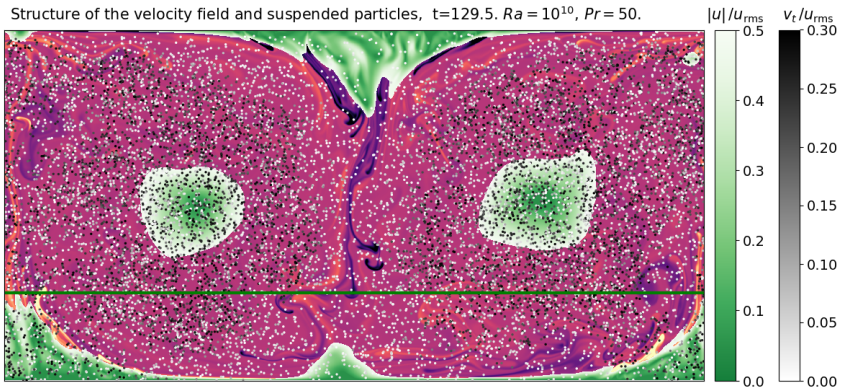


FIGURE 5.6: Same as Fig. 5.2(top), but at time $t = 129.5$ and the depicted particles have smaller terminal velocities, $v_t/u_{rms} < 0.3$. In green we show regions where thermal convection is slow, with velocities below $0.5u_{rms}$. The thick green line separates the low-velocity piles from centres of large scale convection rolls, which also show small velocities.

as the v_t/u_{rms} ratio is $\lesssim 10$ – see the dark blue lines). Due to their large sinking velocity, stone-like particles efficiently cut through the bursts of upwellings. Yet, the low-velocity pile still acts as a sink. This is because, due to the large-scale circulation rolls, the fluid velocities in the lower-half of the domain generally point towards the side edges, which sways the sinking heavy particles into that direction (and similarly for light particles on the top wall).

For the particle trajectories to be close to "ballistic", i.e. to follow the analytic solution (5.13) exactly, the v_t/u_{rms} ratios of much larger than 2 are necessary. Even when Eq. (5.13) effectively governs particle dynamics, the horizontal distribution of settled particles is not uniform. The fluid flow then enters Eq. (5.13) through the initial velocities, $\tilde{\boldsymbol{v}}(\boldsymbol{x}, t{=}0) = \boldsymbol{u}(\boldsymbol{x}, t{=}0)$. Because of large-scale circulation, ballistic particles in the upper part of model domain are generally injected in the direction of major downwellings and have sufficient

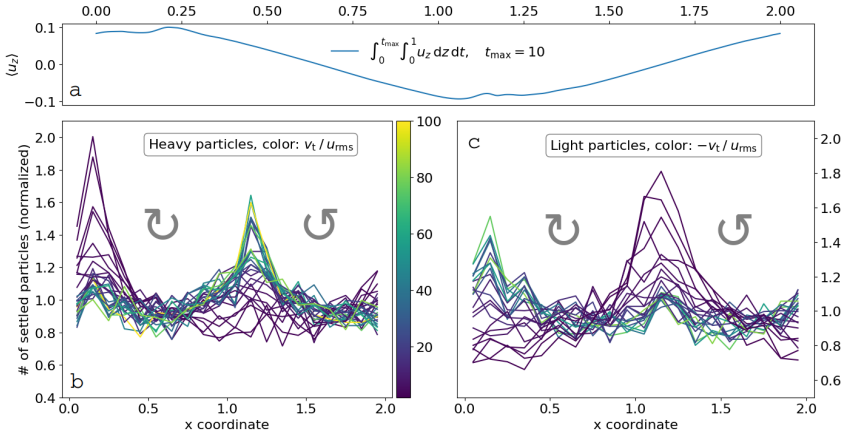


FIGURE 5.7: Spatial settling distribution of *stone-like* particles. As Fig. 5.5, but for particles a factor 10 larger in size.

time to move laterally. Particles injected into the lower half of the domain, on the other hand, do not have the time to move to the sides. As a result, the horizontal distribution reverses for $v_t/u_{rms} \gtrsim 30$, with most of the heavy particles settling below the major downwelling (light green and yellow curves in Fig. 5.7).

For small particles instead, here with $0.02 < v_t/u_{rms} < 0.3$, we plot the horizontal distribution of settling in Fig. 5.8. Particles still "see" the low velocity piles, but the settling events become horizontally uniform as $v_t \to 0.02$. We have verified that particles experience on average over twenty flow overturns between the repeated crossings of the low-velocity piles. Typically, they circulate in large convection cells, waiting to enter the slow regions through small-scale irregularities of the flow that are produced by births of new plumes. Even at $Ra = 10^{10}$ the low-velocity piles are particularly coherent and do not move horizontally, which makes it difficult to enter them. Under such conditions, the particle supply into the piles can be particularly small and the horizontal distribution of settling events can be highly non-uniform.

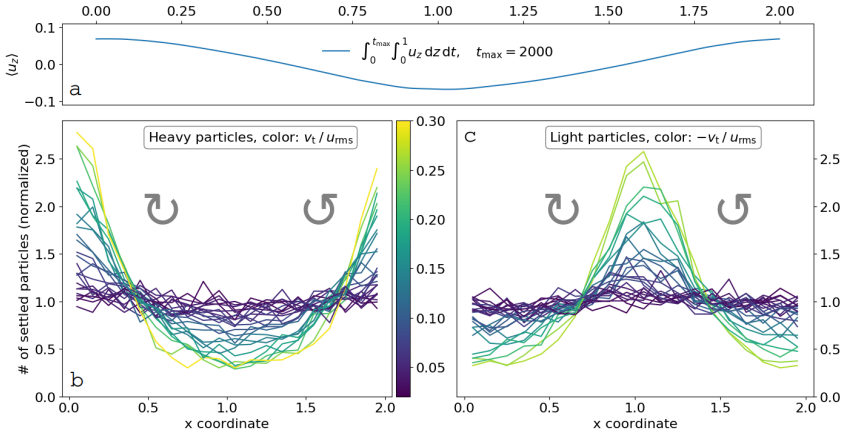


FIGURE 5.8: Spatial settling distribution of *dust-like* particles. As Fig. 5.7, but now for small inertia particles, corresponding to $0.02 < v_t/u_{rms} < 0.03$.

In the dust-like regime, the horizontal distribution of settled particles is uniform. These, almost tracer-like particles remain suspended in the fluid for very long times, repeatedly entering and leaving the low-velocity piles. Their escape probability from rolls approaches

1 as $v_t/u_{rms} \to 0$, which means that for particles with small terminal velocities the piles become transparent. Convective motions inside the piles, though relatively slow, are still fast enough to drag along the particles with a vanishing response time St (i.e. the dust-like particles). The only structure where such particles can separate from the fluid becomes the thin, laterally uniform part of the no-slip boundary layer.

This analysis has been extended to the case of 3D flow in our subsequent work (Patočka et al., 2022). Also there we observed that the concentration of settling events is increased below clusters of upwellings for heavy particles, and inversely for light particles (see Fig. 5.9). This counter-intuitive result, independently observed also in the 2D study of Xu et al., 2020, thus remains valid in 3D geometry. Although plumes themselves act against the sinking motion of particles, the region from which they originate acts as a major particle sink – the fluid flow near the floor is dominantly oriented toward the base of dominant plume clusters, and most of the solid material is thus deposited there. This is because fluctuations that encompass the birth of new plumes often cause particles to fall into the boundary layer. Only those particles that become entrained into a plume reside in the fluid anomalously long.

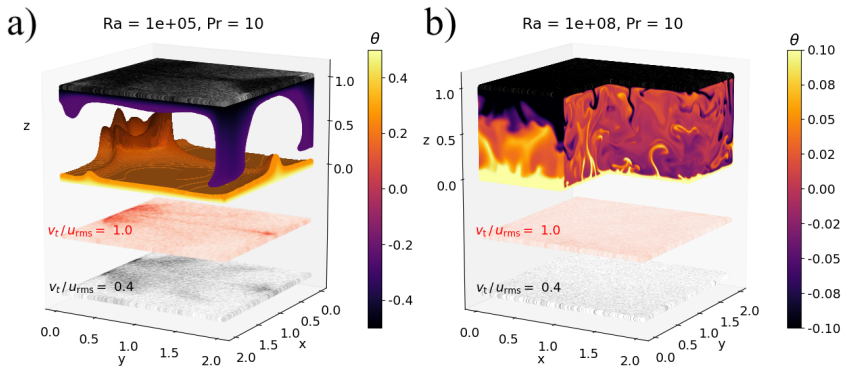


FIGURE 5.9: Temperature field and the spatial distribution of settled particles for selected v_t/u_{rms} ratios. a) Convection with $Ra = 10^5$, $Pr = 10$. The non-dimensional temperature field is thresholded at 0.4 to show the upwellings, and at -0.4 to show the downwellings. The isosurface $\theta = 0.4$ is shaded for better visibility. The 2D projections show the normalized distribution of settling events for $v_t/u_{rms} = 0.4$ (black and white, floor of the plot), $v_t/u_{rms} = -0.4$ (roof of the plot, inverse black and white), and for $v_t/u_{rms} = 1.0$ (red). Darker color corresponds to more settled particles. b) Similarly as in panel a), only the Rayleigh number is increased. For $Ra = 10^8$, we show a cut through the entire temperature field, with the colour scale being clipped for better visibility.

In summary our study showed that the existence of a stable large-scale flow structure has a clear signature on the settling of particles. First, it delays the settling on average. Second, it is responsible for the non-uniform horizontal distribution of settling events. Since the large-scale circulation and superstructures (Pandey et al., 2018) are observed even at the highest Rayleigh numbers reached so far in numerical simulations (Zhu et al., 2018) and experiments (Ahlers et al., 2009), we speculated that this can be an important feature for the extreme convecting regimes occurring in cooling magma ocean.

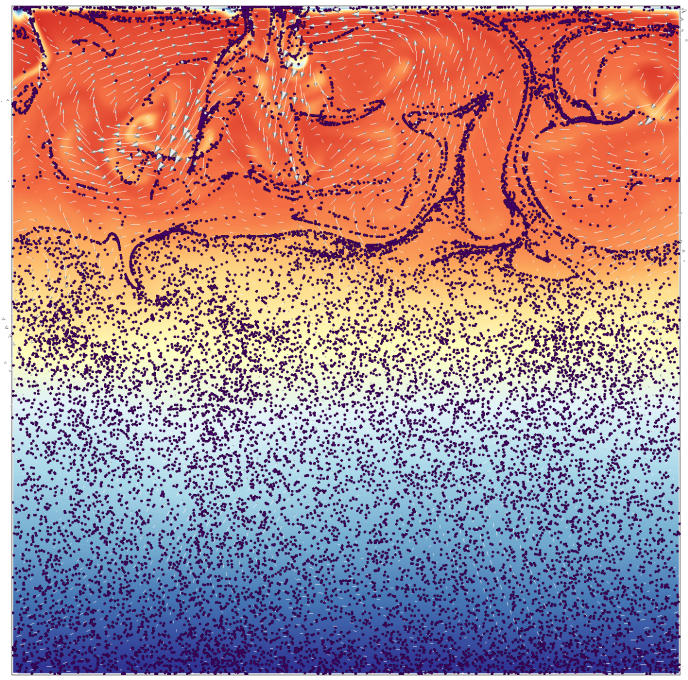


FIGURE 5.10: Visualisation of inertial particles distribution in a 2D vertical-slice model of ocean mixed layer. Particles are ejected from the top high-turbulence region and at the same time are centrifugated by vortical structures, while they are nearly uniform in the bottom strongly stratified region. The colour field represents the fluid density (lighter fluid in red, cold in blue).

5.4 Recent Developments and Future Perspectives

In recent years, my research has continued to investigate the role of gravity in particle dispersion across diverse flow conditions and transport regimes.

A first line of investigation, which is still ongoing, concerns the sedimentation of particles in a turbulent flow that is spatially inhomogeneous. When turbulence is non-homogeneous a new effect emerges, called turbophoresis (Caporaloni et al., 1975), due to their inertia particles can drift from more intense to less intense turbulence regions (see e.g. our study (Garg et al., 2018)). The combination of this phenomenon with gravitational settling leads to complex interplays. The situation becomes even more intricate when the inhomogeneity arises not only from variations in turbulence intensity but also in fluid properties, such as its density in stratified fluids. An application of current relevance is the vertical transport of microplastics in the ocean, especially across the transition from the surface mixed layer to the thermocline, where turbulence gradually decays and a density stratification is present. This problem is the focus of the PhD thesis of Luz Andrea Silva Torres (co-advised with S. Berti) (Silva Torres et al., 2026). In her study we adopt an idealized model of the marine mixed layer to investigate the vertical distribution of small particles that are nearly neutrally buoyant, see Figure 5.10 for an illustration of this model system.

A second direction of research addresses again the dynamics of inertial particles in the Rayleigh–Bénard system. In the doctoral work of Saad Raza (PhD thesis defended in december 2025), we examined how the introduction of inertial particles may alter the hydrodynamic stability of the system. This was inspired by a study by Prakhar and Prosperetti, 2021 which demonstrated that the presence of heavy particles coupled mechanically and

thermally to the fluid can strongly stabilize the system, delaying the onset of the transition from the conductive to the convective regime. Building on this, we analyzed theoretically the case of particles of arbitrary density relative to the carrier fluid (heavier and lighter) (Raza et al., 2024), with prescribed injection velocities (Raza et al., 2025), and with finite thermal inertia (Raza et al., 2026). Our results, obtained within the framework of simplified fully Eulerian models, suggest that particle sedimentation can, in principle, be exploited to regulate the stability of a thermally stratified fluid layer, either stabilizing or destabilizing it. This research is now being extended through numerical simulations moving from an Eulerian approach for the description of the particulate phase (as was necessary to conduct the stability studies) to a Lagrangian two-way coupled approach. This is currently done in the framework of the doctorate of Ousman Dauda Ali (began in October 2025), coadvised with S. Hirata.

Chapter 6

Microorganisms in turbulence as motile particles

Contents

5.1 The role of gravity in particle laden flows 49
5.2 Accelerations of settling/buoyant particles in turbulence 50
5.3 Settling of particles in turbulent convecting flows 53
5.3.1 Analysis of Particles Residence Times 55
5.3.2 Spatial distribution of settled particles 59
5.4 Recent Developments and Future Perspectives 63

The research presented in the previous chapters dealt with hydrodynamic and external forces acting on simple material objects— without internal structure, not equipped with a propulsion mechanisms, and especially not alive. For a physicist, it is very tempting to adopt the same mechanistic point of view when describing alive agents that possess active behaviors, such as motility or reorientation, in response to external environmental stimuli of hydrodynamic or other origin (see, for example, Guasto et al., 2012; Kiørboe, 2008; Wheeler et al., 2019). Although simplistic, this approach can be useful for quantifying the mechanophysical constraints acting on aquatic life in its present forms. It can also help clarify the environmental pressures that have guided natural selection, ultimately giving rise to the organisms that constitute today's plankton.

I have embraced this overtly reductionist point of view to study marine plankton. This was prompted especially by a collaboration with François G. Schmitt (CNRS) and his colleagues from the Laboratory of Oceanology and Geoscience (LOG) in Wimereux, where planktonic organisms are studied both by marine biologists and physical oceanographers.

This chapter is based on:

1. *A Lagrangian model of copepod dynamics: Clustering by escape jumps in turbulence*, Hamidreza Ardeshiri, Ibtissem Benkeddad, François G. Schmitt, Sami Souissi, Federico Toschi and Enrico Calzavarini, Phys. Rev. E 93, 043117 (2016) [PDF].
2. *Copepods encounter rates from a model of escape jump behaviour in turbulence*, Hamidreza Ardeshiri, François G. Schmitt, Sami Souissi, Federico Toschi and Enrico Calzavarini, J. Plankton Research 39, 878–890 (2017) [PDF].
3. *Copepod swimming activity and turbulence intensity: study in the Agiturb turbulence generator system*, Clotilde Le Quinou, Francois G. Schmitt, Yongxiang Huang, Enrico Calzavarini and Sami Souissi, Eur. Phys. J. Plus 137:250 (2022) [PDF].

Hydrodynamic turbulence is known to have important effects on marine ecosystems through a very efficient transport of dissolved matters, nutrients and organisms. The ecological niches of planktonic organisms, i.e., all the species that drift in oceanic currents, are certainly greatly affected by the presence of turbulent flows. This is true for phytoplankton but also for zooplankton. Among the latter, the most abundant multicellular organisms found in the aquatic ecosystems belongs to the group of *Copepods*, to which I devoted my interest. In this context, my research has focused on developing fluid-dynamical models of copepod swimming behavior—derived from observational data—to describe their responses to external mechanical cues generated by turbulence. These models are then validated against new experimental measurements. The goal of this work is to better understand how turbulent environmental conditions influence the spatial distribution and dispersion of copepods. A further objective is to bridge the gap between individual-level swimming behavior and its ecological consequences at the population level.

The rest of the chapter is structured as follows: first I provide a brief presentation of the most salient physical aspects of copepods, second I illustrate a mechanistic model for the copepods mouvements in turbulent flows. I then summarize some of the results derived from the numerical simulation of the model focussing on spatial distributions and contact rates. I will then describe the results of an experiment with real copepods on which I participated. Finally some perspectives on ongoing and future works are provided.

6.1 Planktonic Copepods: The Basics

Plankton are organisms drifting with ocean currents, spanning from microscopic viruses to krill and jellyfish. They are divided into two main groups: phytoplankton (photosynthetic) and zooplankton (animal plankton). Phytoplankton plays a major role in the global carbon cycle, accounting for nearly half of global primary production, while zooplankton—among them copepods— is a primary consumer that transfer carbon up in the food web being a prey for higher trophic levels like fishes of the marine ecosystems.

Understanding the dynamics of plankton across spatial scales is crucial to interpreting nutrients and carbon energy transfer in marine ecosystems. From a physical point of view, planktonic motion occurs at small Reynolds numbers, however both viscous and inertial effects may be relevant depending on organism size and swimming mode. This is particularly true for the highly diverse group of copepods. Copepods are small aquatic crustaceans (typical length 1–2 mm, but with variability in the range [0.2,17] mm) that inhabit nearly all water bodies, from surface layers to ocean depths down to kilometers. Figure 6.1 illustrates an estimation of their global diversity across the world oceans (Rombouts et al., 2009). A typical population density may reach $O(10^3)$ individuals per liter. Although thousands of species exist, their hydrodynamic individual behaviour is typically parametrised by a relatively small set of measurable physical parameters: their body size, mass density (approximately neutral with seawater), swimming velocity and swimming modes. Copepods possess mechanosensory hairs (setae) on their antennae and appendages that detect velocity - and possibly velocity differences- in the surrounding water (Fields and Yen, 1997; Yen and Strickler, 1996). These sensors enable them to perceive predators, prey, or turbulent events that can trigger rapid jumps. Recently a distinction has been introduced between relocation jumps and the more energetic escape jumps (Svetlichny and Uttieri, 2025).

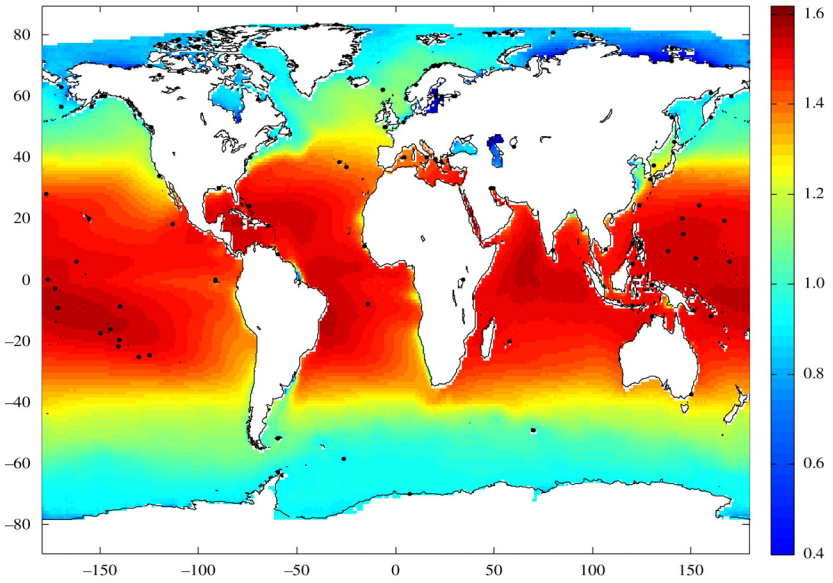


FIGURE 6.1: Estimated global ocean copepod diversity (log of taxonomic richness) reconstructed from temperature, salinity and chlorophyll A concentration (Rombouts et al., 2009).

Jumps are enabled by the movement of their four (or five) pairs of thoracic swimming legs. The hydrodynamics of these jumps differ from the regular steady motion, which they usually adopt in foraging conditions through the beating of their cephalic feeding appendages. A jump begins with a powerful stroke of the swimming legs and antennae, generating high thrust and acceleration (Fig. 6.2) (Borazjani et al., 2010; Lenz and Hartline, 1999). Peak speeds can exceed $500\,\mathrm{mm/s}$, with Reynolds numbers up to 10^3, while in comparison their normal cruising speeds is around $1\,\mathrm{mm/s}$ ($Re \sim 1$). These impul-

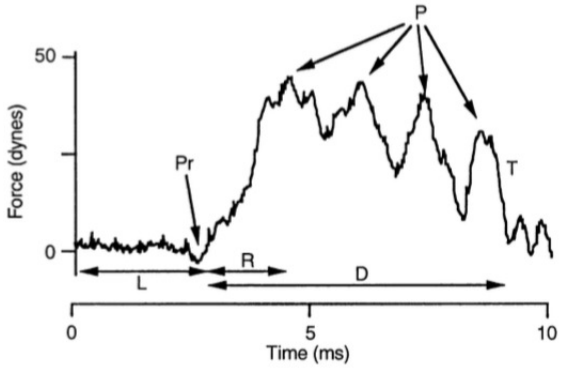


FIGURE 6.2: Force generation of *Undinula vulgaris giesbrechti* during a jump. L: latency; R: rise; D: kick duration; Pr: preparation; P: force peaks; T: termination (Lenz and Hartline, 1999).

sive events produce accelerations exceeding 10^2–$10^3\,\mathrm{mm\,s^{-2}}$. Figure 6.3 shows examples of *Acartia tonsa* responses to hydrodynamic and photic disturbances (Buskey and Hartline, 2003; Buskey et al., 2002). Sex-specific differences in escape locomotion are evident in copepods: males perform shorter jumps characterized by rapid acceleration, while females generate longer-distance jumps with reduced acceleration.

A crucial question in studying copepod behaviour is determining which fluid properties

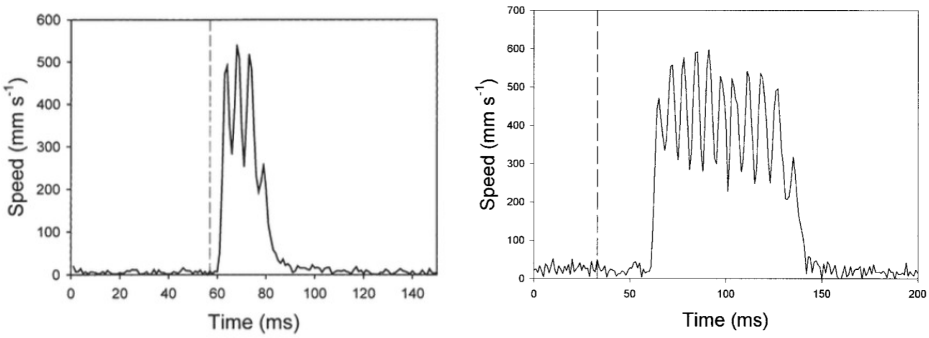


FIGURE 6.3: Escape response of *Acartia tonsa* to hydrodynamic (top) and light (bottom) stimuli (Buskey and Hartline, 2003; Buskey et al., 2002).

trigger their escape response. Experiments by Kiørboe et al. (1999) and Kiørboe and Visser (1999) investigated the effects of various fluid flow stimuli on copepods using controlled flow devices like a siphon, an oscillating chamber, a Taylor-Couette (TC) flow and a rotating cylindrical container (Fig. 6.4). These experiments exposed the copepods separately either to acceleration or shear or vorticity. It was shown that the most significant trigger is local fluid velocity shear (which include strain and vorticity) occurring in the TC with a threshold of approximately 0.4 seconds per second for a 1mm copepod. Subsequent work

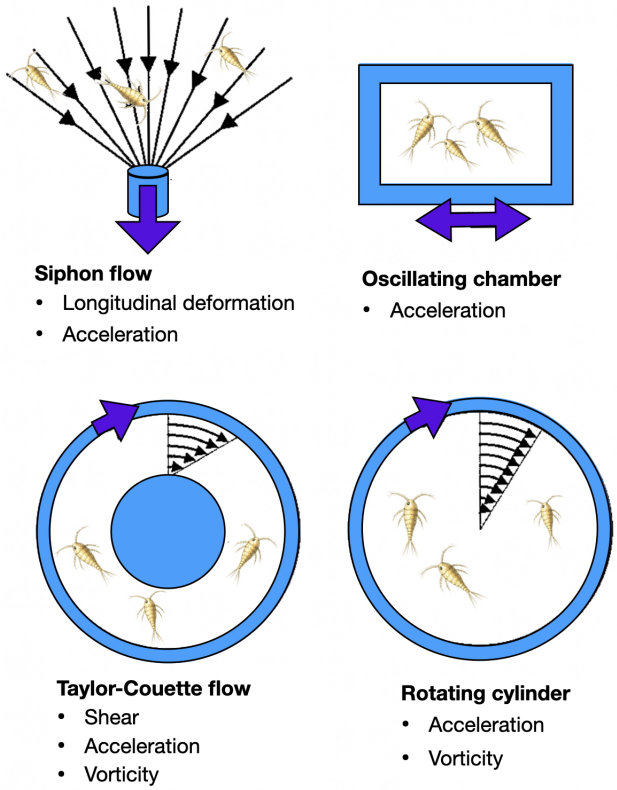


FIGURE 6.4: Hydrodynamic devices used to test copepod responses to deformation, acceleration, and vorticity, adapted from (Kiørboe, 2008).

(Woodson et al., 2005, 2007) confirmed sensitivity to strain rates as low as $0.025\,\mathrm{s}^{-1}$. Overall copepod polulations appear to inhabit a comfort zone ("dome shape" hypothesis) between low and high turbulence intensity levels: below $\sim 1\,\mathrm{s}^{-1}$ they may not detect enough motion

to locate food, while above $\sim 10\,\mathrm{s}^{-1}$ turbulence becomes energetically stressful (Fig. 6.5). However, studies of copepods in laboratory scales coherent vortical flows (Burger vortex)

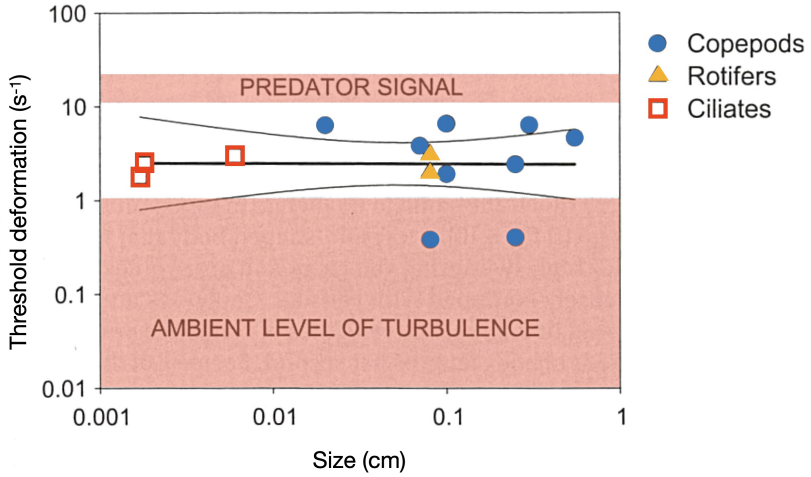


FIGURE 6.5: Threshold deformation rates for escape responses as a function of body size, adapted from (Kiørboe, 2008).

also revealed that some species, such as *Acartia tonsa*, might respond to vorticity rather than strain, indicating species-specific sensing mechanisms (Webster et al., 2015). Laboratory turbulence experiments also highlighted that copepods adjust their swimming effort to the background flow intensity: they control their motion in mild turbulence but are (or let them to be) advected passively in stronger regimes (Michalec et al., 2015; Yen et al., 2008).

Despite these uncertainties—which are common when studying living organisms—copepods are a fascinating example of small swimmers that constantly interact with turbulent water currents. From a physics point of view, they provide an intriguing model system for exploring how active organisms behave in turbulent flows. Copepods certainly sense changes in the surrounding flow and respond with their own species-dependent movements. This leads to a natural question: can we translate these biological and physical features into a simplified mechanical model that helps us understand population-level patterns, such as how copepods cluster in space or how often they encounter one another? The next section tells our developments in this direction.

6.2 The Lagrangian Copepod Model

We introduce here a Lagrangian hydromechanical model of copepod dynamics. This model was first proposed in the doctoral work of Hamidreza Ardeshiri (Ardeshiri et al., 2016). The representation is not intended to be highly realistic; rather, it provides a simplified description of copepod swimming behavior using an active-particle framework. Its primary purpose is to serve as a tool for exploring the phenomenology that emerges from different copepod swimming strategies. In particular, we focus on the distinctive jump-based mode of swimming, while neglecting continuous cruising.
The model relies both on biological and hydrodynamical assumptions. Concerning the former we assume that:

(i) Copepods respond always the same way to external flow disturbances. So to say, their jump reaction is embedded in their neural system;

(ii) The stimulus triggering the jump is only mechanical, characterized by a fixed scalar threshold (to be specified later) we ignore other possible activities induced by light, food, or chemistry such as due to the presence of pheromones trails;

(iii) Copepods have no memory of previous stimuli and jumps.

On the mechanical side we conjecture that:

(i) Copepods are small enough that their centre of mass can be considered a perfect Lagrangian fluid tracer in a flow, except for the time when a jump event takes place. In hydrodynamic terms this means that copepods are assumed to be quasi-inertialess, homogeneous, neutrally buoyant particles with a size of the order of the dissipative scale of the flow. Gravity force has no role in producing acceleration or torque. Only the drag force effect is taken into account during the jumping events;

(ii) Copepods are coupled to the fluid in a one-way fashion, they react and are carried by the fluid but they do not modify the surrounding flow. Similarly copepods-copepods interactions are also neglected.

Adding all together the above hypothesis the Lagrangian Copepod (LC) equation of motion reads as follows:

$$\dot{\mathbf{x}}_c(t) = \mathbf{u}(\mathbf{x_c}(t), t) + \boldsymbol{J}(t, t_i, t_e, \dot{\gamma}, \mathbf{p}) \tag{6.1}$$

where $\mathbf{x_c}(t)$ is the copepod position at time t, $\mathbf{u}(\mathbf{x}, t)$ is the velocity field of the carrying fluid and $\boldsymbol{J}$ is an added velocity term that describes the active behaviour (jump) of the organism. $\boldsymbol{J}(t, t_i, t_e, \dot{\gamma}, \mathbf{p})$ is not only a function of time, it depends also on an initial and a final time t_i and t_e, on flow shear rate value $\dot{\gamma} = \sqrt{2\,\mathcal{S} : \mathcal{S}}$ where $\mathcal{S} = \frac{1}{2}(\nabla\mathbf{u} + (\nabla\mathbf{u})^T)$, and on orientation vector $\mathbf{p}$. For simplicity we assume that copepods do not actively control their orientation so that the dynamics of $\mathbf{p}$ is ruled by the local fluid velocity gradients, via the previously encountered Jeffery equation:

$$\dot{\mathbf{p}}(t) = \left(\boldsymbol{\Omega} + \tfrac{\alpha^2-1}{\alpha^2+1}\left(\mathcal{S} - \mathbf{p}^{\boldsymbol{T}}(t)\cdot\mathcal{S}\cdot\mathbf{p}(t)\right)\right)\cdot\mathbf{p}(t) \tag{6.2}$$

The aspect ratio of copepod is typically around 3 for *Eurytemora affinis* species, which has been taken as a reference in our studies (although for comparison we also considered spherically-shaped organisms $\alpha = 1$).
We note that the fact that the jump term is assumed to depend on $\dot{\gamma}$ represents a generalization to three-dimension of Kiørboe's empirical findings (Kiørboe, 2008) that copepods are most sensitive to shear-rate. For the jump term we adopt the following functional form:

$$\boldsymbol{J}(t, t_i, t_e, \dot{\gamma}, \mathbf{p}) = H[\dot{\gamma}(t_i) - \dot{\gamma}_T]\, H[t_e - t] u_J\, e^{\frac{t_i - t}{\tau_J}}\, \mathbf{p}(t_i) \tag{6.3}$$

where $H[x]$ denotes the Heaviside step function, $\dot{\gamma}_T$ is a threshold value of the shear rate, u_J and τ_J are two characteristic parameters characterising the jump shape, its velocity amplitude (u_J) and decay time τ_J respectively. The first H step function models the fact that a jump can begin only when the shear rate is above the given threshold value, while the second step function accounts for the fact that the jump duration is finite. The jump direction is the one of the copepod orientation $\mathbf{p}$ at the beginning of the jump and does

not change during the jump. Figure 6.6 illustrates better the kinematics of copepods' jump when the shear rate is above the threshold value. The modelled jumps are sharp impulsive

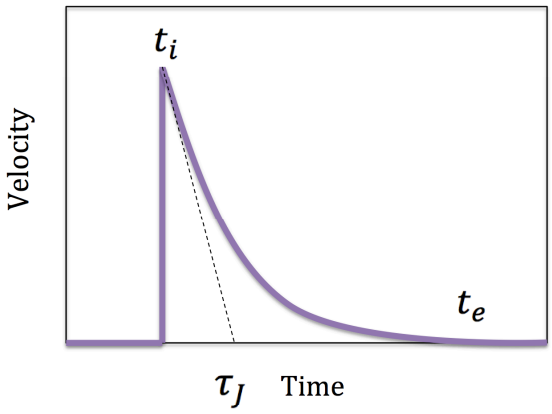


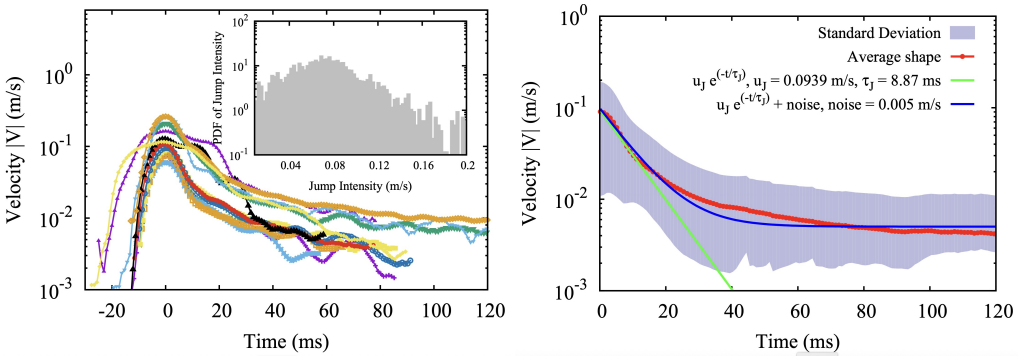
FIGURE 6.6: Kinematics of a jump of a copepod in regions where $\dot{\gamma} > \dot{\gamma}_T$. It is a function of t_i, t_e, u_J and τ_J.

at the inception and decay exponentially with latency time of τ_J. This functional form is based on the assumption that the drag is the dominant hydrodynamic force acting during the jumps. It is also supported by the data analysis of experimental measurements of alive copepods, see figure 6.7. The initial and final time of a jump are therefore defined as:

$$t_i = t \quad \text{if} \quad (\dot{\gamma}(t) > \dot{\gamma}_T) \cap (t > t_e) \tag{6.4}$$

$$t_e = t_i + c\,\tau_J = t_i + \log(10^2)\,\tau_J. \tag{6.5}$$

In other words we assume that a jump can not begin if a previous jump has not finished ($t > t_e$) and that a jump terminates when its amplitude has decreased to a negligible level, here taken as one percent of the initial amplitude, *i.e.*, $|\boldsymbol{J}(t_e)| = 10^{-2}|\boldsymbol{J}(t_i)|$.
We can associate τ_J, to the effective copepods' jump decay time that can be extracted from the experiments, see figure 6.7(a). We note that by assuming a nominal copepod radius of $0.5\,mm$ with $\rho_p \simeq \rho_f$, one can estimate the Stokes particle response time which is $\tau_p = 83.3\,ms$, but the effective particle response time may be smaller due to the non-linear effect induced by a high Reynolds number of the copepod (Re_p) which can be of the order of $\mathcal{O}(10^2)$. If we assume that a copepod can swim with a velocity of $v \simeq 2 \cdot 10^{-1} ms^{-1}$, then $Re_p \simeq 200$. By using the Shiller-Neumann relation (Schiller and Neumann, 1933) for the response time, $\tau_{p,min} = \frac{a^2}{3\beta\nu}\left(\frac{1}{1+C_{Re_p}}\right)$ where $C_{Re_p} = 0.15\,Re_p^{0.687}$, one obtains $\tau_{p,min} = 12.3\ ms$ which is closer to our estimation from the experiments ($\tau_J \simeq 9ms$), Fig. 6.7(b).



(a) (b)

FIGURE 6.7: (a) Experimental measures of copepod velocity evolution during several jump events, for copepods in still water stimulated by visible lights (Ardeshiri et al., 2016). The jump records are superposed by a temporal shift, taking as reference time the peak velocity position. The exponential decay is evident. (Inset) The probability density function (PDF) of the jump intensity. (b) Average shape of copepod velocity over about 730 jumps: mean value (red line) and standard deviation (shaded area). Green line: fitted exponential function $u_J e^{-t/\tau_J}$, where u_J is the jump intensity and τ_J is the decay time of the jump. Blue line: same fit with the addition of a noise velocity offset.

Model tuning for turbulent flows

How to tune this model with respect to the typical properties of oceanic turbulence? The properties of oceanic turbulence relevant to our study have been examined extensively. For instance MacKenzie and Leggett (1993) and Jiménez (1997) report that the mean turbulent kinetic energy dissipation rate (ε) varies from about $10^{-8}\,\mathrm{m^2 s^{-3}}$ in the open ocean to $10^{-4}\,\mathrm{m^2 s^{-3}}$ in coastal regions, with additional dependence on wind conditions and depth. From the values of ε and the kinematic viscosity of seawater, one can estimate the associated Kolmogorov length, time, and velocity scales. According to the same authors, the Taylor-scale Reynolds number in the ocean has typical values of order $\mathcal{O}(10^2)$. This variability is illustrated in figure 6.8, which shows the smallest and largest turbulent scales present in the ocean as functions of ε and of the buoyancy (Brunt–Väisälä) frequency N. The smallest scale, the Kolmogorov length, is indicated by L_K in the figure. Since copepods are typically only a few millimetres in size, the flow scales most relevant to their dynamics lie near the Kolmogorov scale (Yen, 2000) and the turbulence that they live in can be considered 3D homogeneous and isotropic.

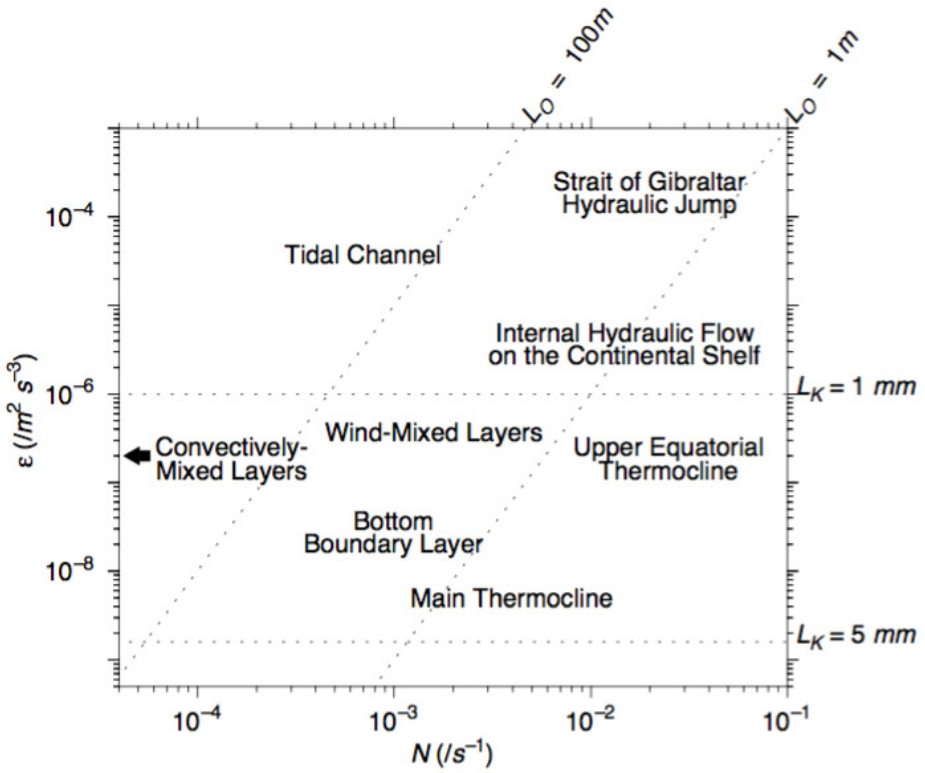


FIGURE 6.8: Chart of the regimes of ocean turbulence with respect to the density stratification (expressed in terms of the buoyancy frequency N) and energy dissipation rate (ε). Horizontal dotted lines indicate Kolmogorov $L_O = (\nu^3/\varepsilon)^{1/4}$ length, diagonal ones the Ozmidov scale $L_O = (\varepsilon/N^3)^{1/2}$. Below the Ozmidov scale turbulence is less affected by density stratification. (Smyth and Moum, 2000).

When the LC model is recast in a dimensionless form in terms of the dissipative scales of turbulence we get three dimensionless groups of parameters: τ_J/τ_η, u_J/u_η and $\tau_\eta\dot{\gamma}_T$. These parameters, together with the flow Reynolds number Re_λ, fully specify the operating conditions of the copepods–in–turbulence model.

In our simulations we took $\varepsilon = 10^{-6}\,\mathrm{m^2 s^{-3}}$ as a reference value for the energy dissipation rate. Using the measured jump intensity u_J and jump decay time τ_J, the corresponding similarity ratios for *E. affinis* and *A. tonsa* are of the order $u_J/u_\eta \simeq \mathcal{O}(10^2)$ and $\tau_J/\tau_\eta \simeq \mathcal{O}(10^{-2})$. These values indicate that, under typical turbulent conditions, copepods react almost instantaneously as compared to fluid flow changes. In contrast, the jump velocity they reach is comparable to, and most often larger than, the characteristic turbulent velocity fluctuations (in fact in turbulence $u_{rms}/u_\eta \simeq Re_\lambda^{1/2}$). Finally, we note that at the time we began this study experimental estimates on the threshold values $\dot{\gamma}_T$ were affected by large uncertainties, so the quantity $\tau_\eta\dot{\gamma}_T$ was taken as a free adjustable parameter in the model.

In summary the LC model is defined by three dimensionless parameters: jump intensity u_J/u_η, decay time τ_J/τ_η, and shear rate threshold $\dot{\gamma}_T\tau_\eta$, and is one-way coupled to the fluid. These means that in practice multiple copepod families, each with triplet $[u_J/u_\eta, \tau_J/\tau_\eta, \dot{\gamma}_T\tau_\eta]$, can be numerically simulated simultaneously. In the simulations we

fixed the decay time at $\tau_J/\tau_\eta = 10^{-2}$, while $u_J/u_\eta \in [1, 400]$ and $\tau_\eta\dot{\gamma}_T \in [0, 4]$ vary. Simulations involve typically $\sim 10^5$ particles per family, evolved over few ($\simeq 2$) eddy turnover times. Passive tracers are always included for comparison. In the following I will briefly overview our results on two aspects: clustering and patchiness of a copepod population and secondly their encounter rates.

6.3 Clustering and Patchiness

We first we analyzed how LC particle dynamics in a turbulent flow differ from fluid tracers by examining their single-component velocity statistics. While the latter follow a Gaussian distribution, copepods exhibit slower-decaying tails, increasingly pronounced with higher jump intensity u_J (see Fig. 6.9a) or lower shear threshold $\dot{\gamma}_T$ (see Fig. 6.9b) which corresponds to more frequent jumps. On the opposite, when $u_J < 10\,u_\eta$ or $\dot{\gamma}_T > 3\tau_\eta^{-1}$ the copepod velocity statistics become effectively indistinguishable from tracers.

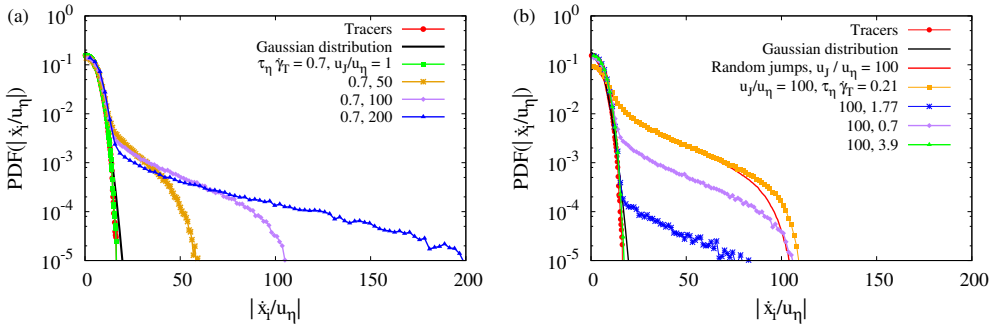


FIGURE 6.9: Probability density function of the absolute value of a single velocity component, $|\dot{x}_i/u_\eta|$, for copepods. (a) Results at a constant threshold value, $\tau_\eta\dot{\gamma}_T = 0.7$, and for different jump intensities. The Gaussian distribution has a standard deviation equal to the root-mean-square velocity of the Eulerian fluid velocity field. (b) Results at a constant jump intensity, $u_J/u\eta = 100$, and for different shear-rate threshold values. Random jumps represent the expected velocity distribution when randomly oriented jumps occur uniformly in time, superimposed on the turbulent fluid velocity field.

Furthermore, we showed that a probabilistic model can describe this single-point velocity statistics as the sum of three independent random variables: a Gaussian component - mimicking turbulent fluctuations-, a uniform in time jump frequency and an isotropic jump orientation. This model qualitatively reproduces observed PDFs, with slight deviations in the tails probably probably due to residual flow-correlated jump orientations (see figure 6.10 for a comparison). Fitting the measured PDF with the probabilistic model allows to indirectly estimate the instantaneous fraction of jumping particles. This fraction turns out to decreases sharply, exponentially in fact, with increasing $\dot{\gamma}_T$, see figure 6.10(inset). This is a consequence of the highly intermittent distribution of the energy dissipation rate and so of $\dot{\gamma}$ of the turbulent flow. The velocity PDFs from the LC model also qualitatively agree with the functional forms observed in experiments at $Re_\lambda \sim 30$ (Michalec et al., 2015).

Additionally the LC model simulations provides informations on the three-dimensional spatial distribution of copepods (we note that such informations were not experimentally available at the time we started this study, but have been later quantified in Michalec et al., 2022). The spatial distribution of LC particles is highly non-homogeneous, as illustrated in

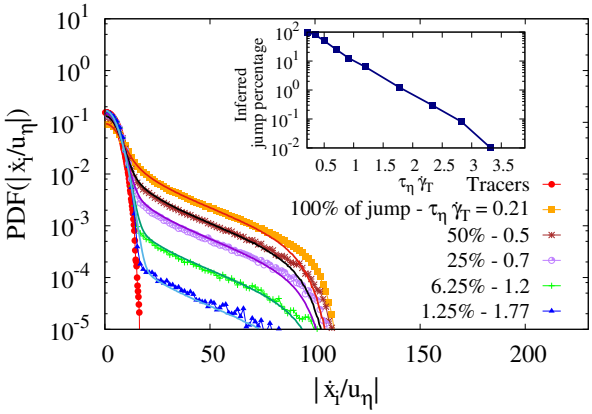
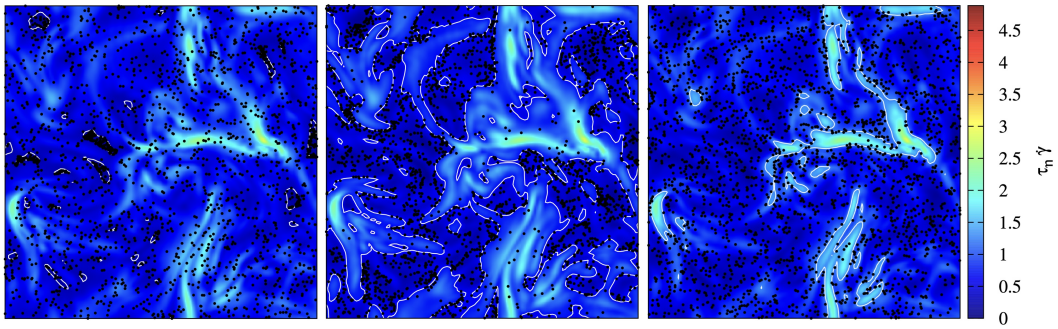


FIGURE 6.10: Probability density function of the absolute value of a single velocity component, $|\dot{x}_i/u_\eta|$, for copepods at a constant jump intensity, $u_J/u_\eta = 100$, and for different shear-rate threshold values $\dot{\gamma}_T$. The PDF from the probabilistic model are fitted by adjusting the jumping frequency. (Inset) Deduced fraction of jumps as a function of the shear-rate threshold value, $\tau_\eta \dot{\gamma}_T$.



(a) $\tau_\eta \dot{\gamma}_T = 0.35$ (b) $\tau_\eta \dot{\gamma}_T = 0.92$ (c) $\tau_\eta \dot{\gamma}_T = 1.77$

FIGURE 6.11: Patchiness of copepods obtained from the simulations. The color field represents the instantaneous local fluid shear rate $\dot{\gamma}$ in dimensionless units. The jump intensity value $u_J/u\eta = 250$ is kept fixed for all cases. (a) Copepod distribution for $\tau_\eta \dot{\gamma} T = 0.35$. (b) Same for $\tau_\eta \dot{\gamma} T = 0.92$. (c) Same for $\tau_\eta \dot{\gamma}_T = 1.77$. The contour lines identify the set where $\dot{\gamma} = \dot{\gamma}_T$, marking the boundary between comfort (dark colours) and alert regions (in lighter shades of colour).

Fig. 6.11, and is characterised by a patchiness with peculiar features. Particles clearly tend to avoid regions where the shear rate exceeds the threshold $\dot{\gamma}_T$. When this threshold is low, corresponding to comfort regions relatively rare, the numerical copepods manage only in part to reach such areas where they form dense isolated colonies (panel a). The opposite occurs for very large shear-rate threshold, comfort regions are wide and LC particles manage to escape easily from the rare energetically dangerous events. In this situation particles spatial distribution appears nearly homogeneously (panel c). In the intermediate threshold regions, where $\dot{\gamma}_T \simeq \tau_\eta^{-1}$, we observe clusters concentrated near the comfort-alert interfaces (panel b). This latter fact can be rationalized by taking an Eulerian point of view on the particle description. In fact if we associate a velcoity field to the lagrangian particles $\boldsymbol{v} = \dot{\boldsymbol{x}}_c$, we can observe that its divergence can be different form zero only at the crossing between comfort and alert regions. This is because in comfort regions ($\nabla \cdot v = \nabla \cdot u = 0$) and in alert regions ($\nabla \cdot v = \nabla \cdot u + \nabla \cdot J = 0$, as we can safely assume the jump term to be there on average spatially constant). At the interface however, the change from the

fluid velocity intensity u to $u + u_J$ has a spatial transition scale roughly proportional to $u_J \cdot \log(10^2)\tau_J$ which leads to a non-null divergence. This explains qualitatively the LC accumulation that we observe in correspondence of the surfaces delimiting alert/comfort sub-volumes, which effectively acts as sink or source term of the LC velocity field.

The small-scale geometrical properties of particle accumulations (clusters) can be quantified by means of the correlation dimension D_2 (Grassberger and Procaccia, 1983), see figure 6.12. The maximal clustering ($D_2 \simeq 2.3$) occurs again at intermediate threshold values, $\dot{\gamma}_T \sim 0.5\,\tau_\eta^{-1}$, Fig. 6.12(b), this is where the volumetric extent of comfort and alert regions are comparable and their bounding surface is maximal hence also the velocity copepods divergence. We recall that for weakly inertial particles a relation connects the correlation dimension to the mean flow divergence, i.e. $3 - D_2 \propto \langle \nabla \cdot \boldsymbol{v} \rangle^2$. The fact that $D_2 \simeq 2$ means that particles accumulates in sheet like regions, likely the frontiers between the two regions. The observed saturation of D_2 for large jump intensities u_J , Fig. 6.12(c) is instead less obvious and still awaits for a clear qualitative explanation (Ardeshiri et al., 2016).

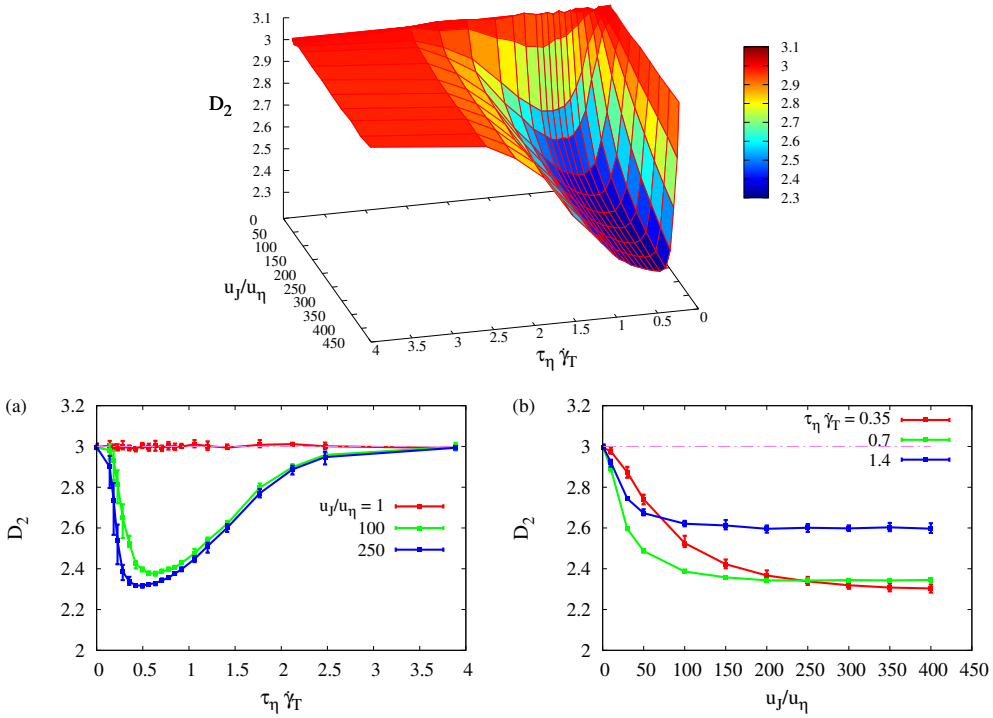


FIGURE 6.12: Correlation dimension D_2 of copepods as a function of jump intensity u_J/u_η and threshold value $\tau_\eta \dot{\gamma}_T$. (a)-(b) Lateral sections of D_2 as a function of the jump intensity u_J/u_η and threshold value $\tau_\eta \dot{\gamma}_T$. Error bars indicate the range of variability of the measurements from 10 independent particle snapshots.

In summary, we have shown that the proposed LC model for escape jumps from high shear-rate regions leads to non-homogeneous spatial distributions in the population, with maximal clustering occurring when the shear threshold $\dot{\gamma}_T \sim \tau_\eta^{-1}$ roughly divides the flow into roughly comparable comfort and alert volumes. The correlation dimension analysis indicates the formation of quasi-bidimensional ($D_2 \sim 2$) structures around alert regions, with a tendency to a saturation for jump intensities $u_J \gg u_\eta$.

While other marine microorganisms, such as phytoplankton, exhibit preferential concentration due to gyrotactic or gravitactic mechanisms (Durham et al., 2013; Lillo et al., 2014),

copepod patchiness may instead result from their reactive behaviour in turbulence, a phenomenon we refer to as escape-induced clustering. This hypothesis might have also measurable effects on the encounter rates of copepods. It is an aspect that we have addressed in a second work and that will be briefly detailed in the next section.

6.4 Encounter Rates

The clustering mechanism induced by an escape reaction involving jumps can lead to an increase in the encounter rate among organisms. This effect may be significant when - as in the case of our model - other behavioural factors are absent. We aimed to quantify this phenomenon using the LC model (Ardeshiri et al., 2017). More specifically we looked at the copepod-copepod encounter rate $E(r)$, defined as the number of encounters per unit time for a copepod in a population of N individuals within volume V (and number density $n = N/V$). For statistically homogeneous and isotropic motion, it can be expressed as (Saffman and Turner, 1956; Sundaram and Collins, 1977):

$$E(r) = n\, 2\pi r^2\, g(r)\, \langle \delta v_{\mathrm{rad}}(r) \rangle, \tag{6.6}$$

where r is twice the organism's perceptive radius. The so called collision kernel is composed by the product of two functions: the pair distribution function $g(r)$ and the first-order radial velocity structure function $\langle \delta v_{\mathrm{rad}}(r) \rangle$. The pair distribution function $g(r)$ accounts for local accumulation, with $g(r) > 1$ indicating preferential concentration. For small r, $g(r)$ is related to the correlation dimension D_2, through $g(r) \sim r^{D_2 - 3}$. It is computed as

$$g(r) = \frac{1}{4\pi r^2 n N} \sum_{i=1}^{N} \sum_{j \neq i}^{N} \delta\left(r - |\boldsymbol{r}_{ij}|\right), \quad \boldsymbol{r}_{ij} = \boldsymbol{x}_{c,j} - \boldsymbol{x}_{c,i}, \tag{6.7}$$

where the index i and j indicate distinct copepods. The mean radial velocity between two organisms separated by r is instead:

$$\langle \delta v_{\mathrm{rad}}(r) \rangle = \frac{\sum_{i=1}^{N} \sum_{j \neq i}^{N} |\dot{\boldsymbol{r}}_{ij} \cdot \boldsymbol{r}_{ij} / |\boldsymbol{r}_{ij}|\, \delta(r - |\boldsymbol{r}_{ij}|)}{\sum_{i=1}^{N} \sum_{j \neq i}^{N} \delta(r - |\boldsymbol{r}_{ij}|)}, \quad \dot{\boldsymbol{r}}_{ij} = \dot{\boldsymbol{x}}_{c,j} - \dot{\boldsymbol{x}}_{c,i}. \tag{6.8}$$

We first look separately at the trends in these two important factors, $g(r)$ and $\langle \delta v_{\mathrm{rad}}(r) \rangle$.

The pair correlation function $g(r)$, shows strong local accumulation of copepods at small distances, peaking at $\tau_\eta \dot{\gamma}_T \simeq 0.5$, in correspondence of the minimum of the correlation dimension $D_2 \sim 2.3$, see Fig. 6.13(a). Such preferential concentration occurs in a narrow range $\tau_\eta \dot{\gamma}_T \in [0.125, 2]$. Furthermore it is strong for short perception radii $\simeq \eta$ and tend to vanish for $r > 10\eta$.

The mean radial velocity $\langle \delta v_{\mathrm{rad}}(r) \rangle$ increases monotonically with copepod reactivity (Fig. 6.14). Unlike $g(r)$, it does not exhibit an optimal reactivity. For low reactivity (high $\tau_\eta \dot{\gamma}_T$), copepods behave as passive tracers, while for very low $\tau_\eta \dot{\gamma}_T$ (high reactivity), their motion approaches a Brownian-like behavior with an effective diffusivity $\sim u_J^2 \tau_J$. In this

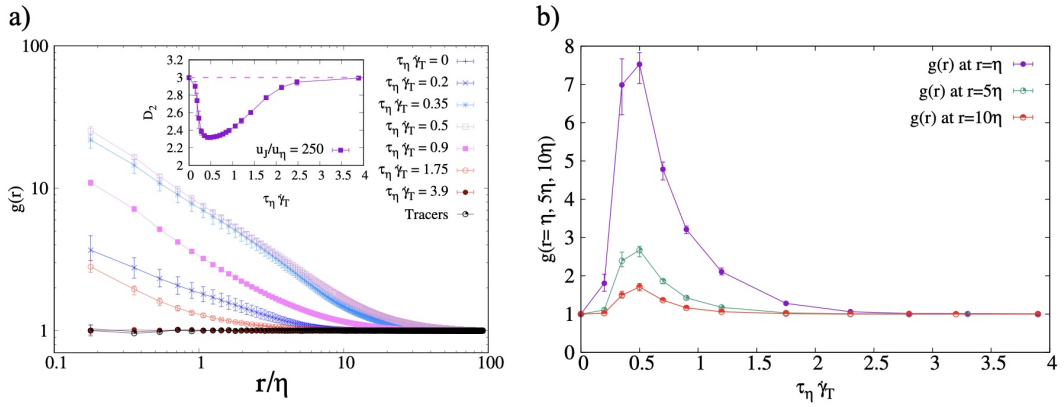


FIGURE 6.13: (a) Pair-radial-distribution function, $g(r)$, for different Lagrangian copepod families with different threshold values of the dimensionless shear rate $\tau_\eta \dot{\gamma}_T$. In the inset the behaviour of the corresponding correlation dimension D_2. (b) Variation of $g(r)$ at different perception radius distances as a function of the threshold $\tau_\eta \dot{\gamma}_T$.

regime, $\langle \delta v_{\rm rad}(r) \rangle$ remains non-zero even as $r \to 0$. This can be interpreted as a consequence of the formation of caustics (i.e., discontinuities) in the associated Eulerian velocity field of the copepods.

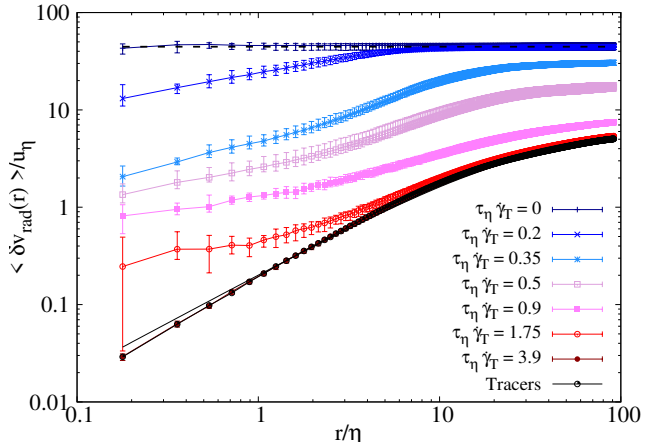


FIGURE 6.14: Dimensionless mean radial velocity, $\langle \delta v_{rad}(r) \rangle / u_\eta$ between couples of Lagrangian copepods separated by a distance r/η for different values of the dimensionless threshold strain rate intensity $\tau_\eta \dot{\gamma}_T$. The continuous line is the prediction for fluid tracers based on the empirical approximation on the second-order longitudinal Eulerian structure function by Borgas and Yeung, 2004. The dashed line plateau is derived from random fields of spatially and temporally uncorrelated jumps.

The resulting encounter rate $E(r)$ is shown in Figure 6.15, where it is normalized by the corresponding value for fluid tracers with the same perception radius. The main observation is that the enhancement of the encounter rate for LC agents, compared to fluid tracers, can be substantial. Encounter rate enhancements by factors of 10 to 100 are obtained for $\tau_\eta \dot{\gamma} T \simeq 0.5$ and perception radii $r \in [1, 5]\eta$. Conversely, for $\tau \eta \dot{\gamma} T > 2.75$, the encounter rates between LC agents become comparable to those of fluid tracers with the same finite perception radius. The observed monotonic decrease with $\tau \eta \dot{\gamma}_T$ suggests that $E(r)$ is primarily dominated by the corresponding radial approaching velocity component.

Up to now we assumed that a copepod's jump was terminated after a prescribed time interval, τ_w, from the jump inception, defined as when the jump velocity amplitude reaches

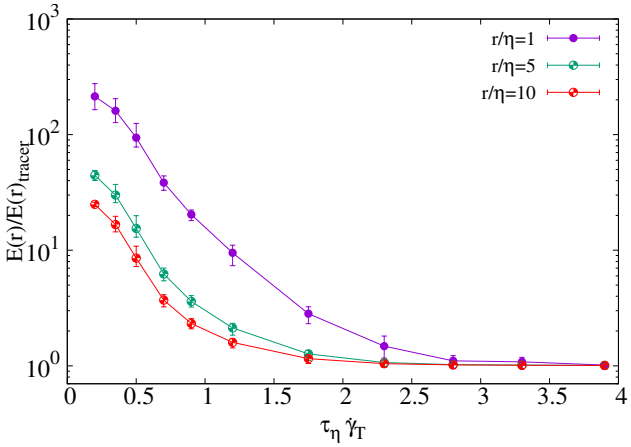


FIGURE 6.15: Ratio between encounter rates experienced by Lagrangian copepods and the one experienced by fluid tracer particles with the same perception radius.

one percent of the copepods' initial jump intensity. However, copepods could behave differently. For instance they could be less reactive of what has been modelled so far since physically they have certainly a finite energy amount available for swimming and after repeated jumps they may need some time in order to recover their lost energy (Visser and Thygesen, 2003). The probability density function of time between successive jumps for *E. Affinis* and *A.Tonsa* indicates the presence of memory on the previous jumps of copepods (see e.g (Dur et al., 2010)) but there is a lack of quantitative elements in order to have enough information to model this feature in the LC model.
In order to explore this we varied the duration of the waiting time, taking as a reference the family for which optimal clustering happened: $\tau_w/\tau_J = c$ with $c = 4.6$ (a family with $u_J/u_\eta = 250$, $\tau_J/\tau_\eta = 10^{-2}$ and $\tau_\eta\dot{\gamma}_T = 0.5$ where a complete jump lasts for $46\,ms$) as shown in blue in Fig.6.16. We now have Lagrangian copepod families with $u_J/u_\eta = 250$, $\tau_J/\tau_\eta = 10^{-2}$, $\tau_\eta\dot{\gamma}_T = 0.5$ and τ_w/τ_J which varies in range $[0.5c, 200c]$.
Figure 6.16 interestingly shows that by making copepods progressively less reactive, the small scale clustering, characterised by D_2, fades away and only a prompt copepod reactions may lead to non-homogenous spatial distribution. Moreover, when the waiting time, τ_w, is larger than the Kolmogorov time scale of the flow, τ_η, copepods' spatial distribution becomes nearly homogenous. It is now interesting to see how these changes in spatial distribution can affect the encounter rate.

The encounter rate experienced by different copepod families normalized by the one of tracers at the same perception radius is shown in Fig. 6.17. It is seen that the increase of the waiting time decreases the copepods' encounter rates. For $\tau_w \simeq 2\tau_\eta$ the encounter rate enhancement as compared to tracers is already reduced to a factor ~ 8 for $r = \eta$ and and becomes as low as a factor ~ 2 for $r = 5\eta$.

In summary our parametric analysis shows that the escape-jump dynamics can enhance encounter rates by up to two orders of magnitude compared with passive tracers. Lower shear rate thresholds $\tau_\eta\dot{\gamma}_T$ and shorter inter-jump times τ_w increase encounter rates (with $\delta v_{\rm rad}(r)$ being the dominating factor in this enhancement). This reflects the intuitive idea that more reactive organisms explore space more efficiently. The dissipative scale τ_η sets the relevant reference for both $\dot{\gamma}_T$ and τ_w: encounter enhancement is effective only if copepods sense shear rates finer than τ_η^{-1} and jump at frequencies exceeding this scale. On the other

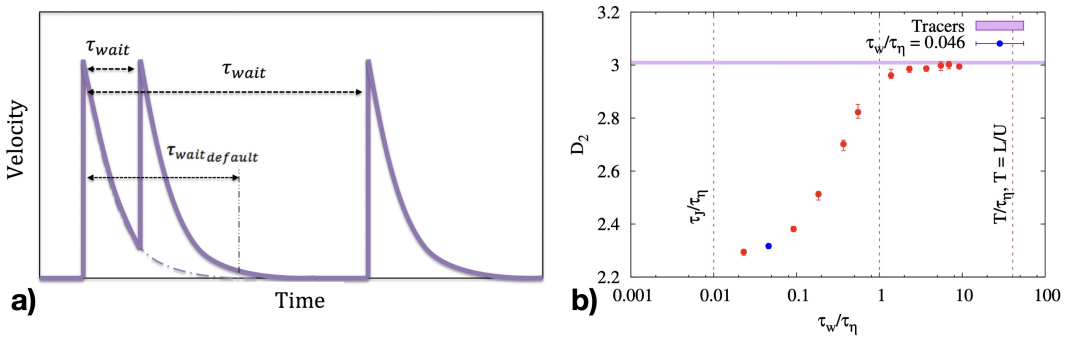


FIGURE 6.16: (a) Sketch of successive jumps of a copepod at varying inter-jump time latency. (b) Effect of the waiting time between successive jumps on the correlation dimension. Blue dot corresponds to copepods of the optimal clustering family with $u_J/u_\eta = 250$, $\tau_J/\tau_\eta = 10^{-2}$, $\dot{\gamma}_T = 0.5\tau_\eta^{-1}$ and $\tau_w/\tau_\eta = 0.046$. The vertical dashed lines show the τ_J/τ_η, $\tau_w = \tau_\eta$ and the ratio between the large eddy turnover time of the flow, T, and Kolmogorov time scale,τ_η, from left to right. Note that in this test $\dot{\gamma}_T$ is kept fixed at the maximal clustering value $0.5\tau_\eta^{-1}$.

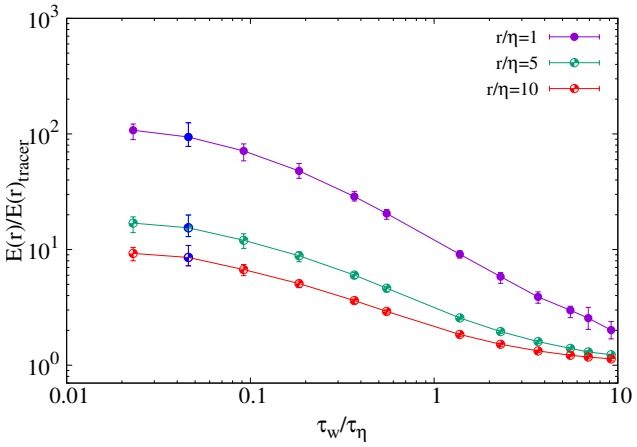


FIGURE 6.17: Ratio between encounter rates experienced by Lagrangian copepod particles and the one experienced by fluid tracer particles with the same perception radius as a function of waiting time between successive jumps. The filled symbols correspond to the copepods family with $\tau_w/\tau_J = c$ at different perception radius.

hand large perception radii ($r \gtrsim 10\eta$) do not produce any advantage in enhancing the encounter rates.

These findings are in qualitative agreement with observations on real copepods, which estimates sensitivities of the order of τ_η^{-1} (Kiørboe et al., 1999; Woodson et al., 2005) and perception scales in the mm-range (Bagoien and Kiørboe, 2005; Doall et al., 1998; Lenz and Yen, 1993). However, the model has also clear limitations: it neglects energetic constraints and post-encounter dynamics. Copepods likely exhibit periods of activity followed by rest, and real encounters may alter trajectories. Experimental studies (Michalec et al., 2015) indicate that copepods modulate jumping with turbulence intensity, suggesting species-specific threshold values that deserve further investigation. More recently, Michalec et al., 2022 has demonstrated that Voronoi cluster analysis of spatial distributions of copepods in high to moderate turbulence does not reveal traces of preferential accumulations, thus weakening part of the encounter rate mechanism discussed here.

Despite all these caveats regarding the limitations of the LC model, our analysis has made

it possible to apply established frameworks for analyzing particle collision rates to the case of active organisms. Ultimately, only repeatable experimental validation will determine whether these results accurately reflect reality, which naturally leads us to the next section.

6.5 Experimental Investigations

Numerical studies like those discussed above build up on observational knowledge of plankton. It is only on the basis of such observations that the level of realism and accuracy of mechanistic models like the LC model can be improved. Observations of these organisms can be carried out either in their natural environment, the ocean, or in smaller and more manageable laboratory systems, where the external conditions are directly controllable by the researcher (see for recent works Michalec et al., 2026; Michalec et al., 2022; Michalec et al., 2020; Svetlichny and Uttieri, 2025). It is this second option that we have sought to pursue in recent years.

In particular, together with collaborators from the LOG laboratory, we have conceived a simple experimental apparatus (dubbed *Agiturb*) capable of generating turbulence in a fluid with a tunable intensity (Le Quiniou et al., 2022). This system, consisting of four magnetic stirrers arranged in a square at the bottom of a container, is inspired by the four-rotor mill studied by J. Taylor (Taylor, 1934) used to characterize the rheological properties of complex fluids. At difference from the classical apparatus that uses rotating cylinders, here we use magnetic stirrers that are capable to generate a vigorous turbulent flow. The device is shown in Fig. 6.18.

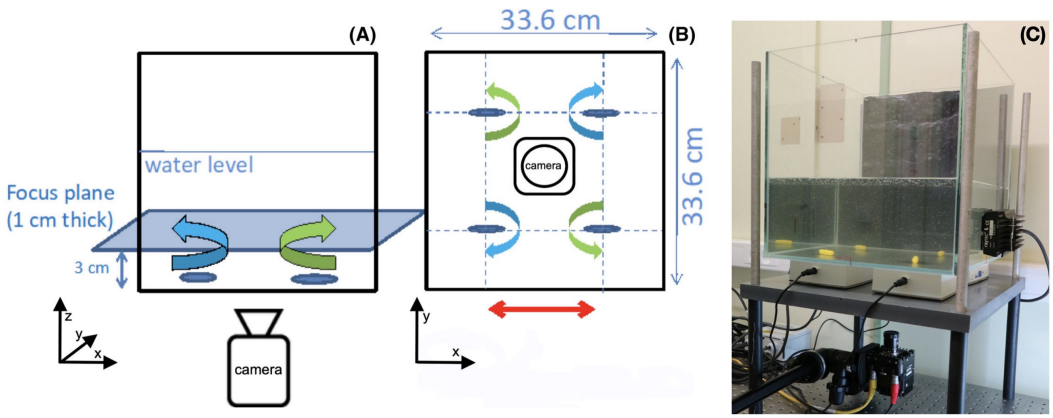


FIGURE 6.18: Sketch of the experimental setup showing the position of the camera, the corresponding focus plane and the position of the stirrers, side view (A), top view (B). The red arrow indicates the scale roughly corresponding to the maximal energy injection scale. Note the rotation direction stirrers maximising strain. (C) Photo of the Agiturb device, note one of the two IR-lamps on the lateral opposite sides of the tank.

We studied Copepods of the species *Acartia tonsa* at estimated Taylor-scale Reynolds numbers in the range 130–360. Trajectories of alive and dead copepod individuals, together with those of neutrally buoyant polystyrene spherical particles of similar size (600 μm diameter), were recorded using a high-speed camera operating at 1200 frames per second. Records were performed in darkness, with the use of an infrared illumination ($850nm$ wavelength).

This is necessary in order to prevent the phototactic movement of copepods, that are attracted by the visible light. After signal processing (Le Quiniou et al., 2022), 2D horizontal velocity and acceleration statistics were extracted.

In figure 6.19(a) we report the velocity probability density functions (PDFs) of alive and dead copepods in a 100 rpm flow (corresponding to Taylor Reynolds number ~ 130), we observe that they are markedly different. The long tail present for alive copepods is the signature of jumping motile behaviour. This tail has similar features to the case of the same copeods in still water, as if the resulting PDF for alive copepods is the sum of the two components: turbulence and jumps. A feature shared also by the LC model discussed before. In panel (b) of the same figure, the velocity PDF is relative to larger levels of turbulence. In that case the curve for dead and alive copepods as well as for the polystyrene particles are not distinguishable. Therefore swimming activity in A. tonsa is apparent under moderate turbulence levels but is suppressed under high-intensity turbulence. This behavior provides insight into the existence of an optimal upper bound on the level of turbulence for A. tonsa, beyond which elevated turbulent forcing overwhelms active behavioral responses and copepods reduce their jumping escape strategy behaving effectively as passive particles.
Panel (c) and (d) of the same figure 6.19 report similar measurements for the accelerations, which are obtained by differentiating in time the measured velocity signals. In such a case differences between alive and dead copepods seem to persist even at largest turbulence intensity (300 rpm). This is because acceleration is an observable that is particularly sensitive to discontinuities in particle trajectories. At the same time, however, it is more prone to systematic errors, requiring special care in data processing. Although the experiments are conducted using high-speed imaging, reliable tracking of copepods remains a challenging task: standard protocols routinely adopted for inertial particles cannot be directly transferred to copepod trajectories without careful validation. This is undoubtedly an aspect where further experimental improvements can be achieved.

In summary, the results of these first in-house experiments on copepods in turbulence, described in detail in Le Quiniou et al., 2022, have been encouraging. They have confirmed some of the hypotheses underlying our mechanistic model: in particular, the copepod's sensitivity to turbulence intensity, and the fact that a superposition of jumps and fluid velocity can account for the velocity statistics. They certainly provide strong motivation for future investigations.

6.6 Conclusions and Perspectives

In this chapter, I described how a fluid-dynamical perspective and a reductionist mechanistic approach can be adopted to investigate the behavior of motile planktonic organisms in turbulent environments. The focus has been on the zooplankton, specifically copepods. By extending Lagrangian particle descriptions to include simplified escape-jump dynamics, the Lagrangian Copepod model provided an elementary system to relate individual responses to flow fluctuations with emergent population-level properties.

The results suggest that the coupling between turbulence and intermittent escape behaviour can lead to non-homogeneous spatial distributions, with clustering emerging near interfaces between low- and high-shear regions. This "escape-induced clustering" offers

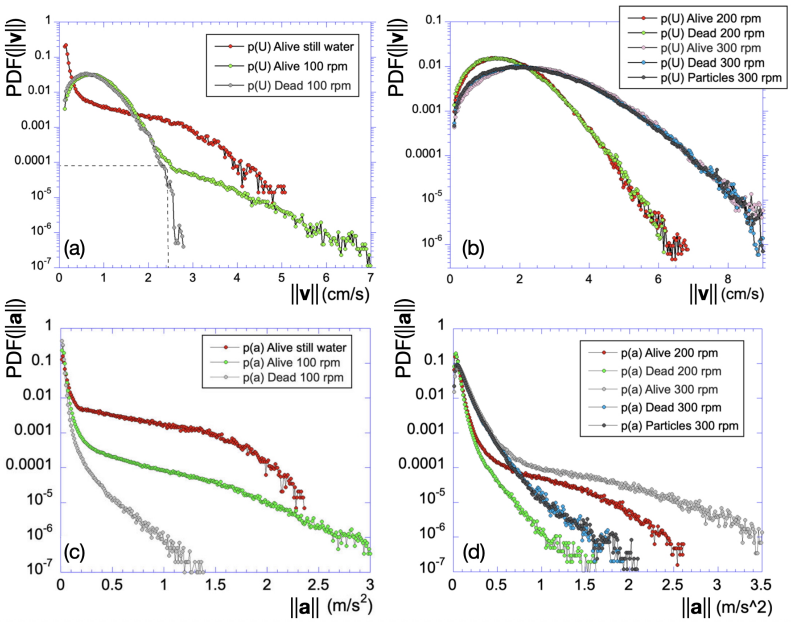


FIGURE 6.19: (a) Probability density functions (PDFs) of the horizontal velocity magnitude $||\boldsymbol{v}|| = \sqrt{v_x^2 + v_y^2}$. In still water with normally swimming copepods (red) and in turbulence at forcing rotation rate $\Omega = 100$ rpm, PDFs are shown for dead (gray) and alive copepods (green). (b) Same PDFs for rotation rates $\Omega = 200$ and 300 rpm, for alive and dead copepods, and additionally (for $\Omega = 300$ rpm only) for spherical polystyrene particles. (c) PDFs of the Lagrangian horizontal acceleration magnitude $||\boldsymbol{a}|| = \sqrt{a_x^2 + a_y^2}$ in still water (no turbulence) and for a rotation rate $\Omega = 100$ rpm. (d) PDFs of the Lagrangian horizontal acceleration magnitude for a rotation rate $\Omega = 200$ rpm (alive and dead copepods), and for $\Omega = 300$ rpm (alive and dead copepods, and spherical polystyrene particles).

a possible physical mechanism contributing to patchiness in plankton distributions. The analysis also indicates that such behaviour may affect encounter rates, with potential implications for ecological processes such as mating and predation. However, these effects depend sensitively on model parameters, particularly the shear-rate threshold and the characteristic timescales of the jumps relative to those of the flow. At the same time, the simplicity of the LC model imposes clear limitations. Several biological aspects—such as energy constraints, memory effects, sensory variability/diversity, and interactions between individuals—are not included and may significantly influence real copepod dynamics.

Laboratory experiments, such as those performed with the introduced *Agiturb* device, provide useful insights into copepod behaviour under controlled turbulence. Notably we highlighted the transition toward a more passive dynamics at high turbulence intensities. These observations underline the need for further experimental investigations, both in the laboratory and in situ, to better constrain model assumptions and parameters. I am currently exploring this area thanks to funding from the INSU institute of CNRS (project TRACKPOD). The project aims to delve deeper into plankton's affinity for turbulence, with a key idea to be able to measure copepods' concentrations fields in a non-spatially homogeneous turbulent flow. The idea is that if copepods have some affinity for a specific level of turbulence, they should position themselves preferentially in the specific regions of the flow where such an intensity is attained. It is an hypothesis that we are currently testing by means of imaging copepods in a planar jet flow device.

Overall, the LC model should be viewed as a first step toward a more quantitative description of motile organisms in turbulence. Future work will require closer integration between experiments, observations, and modeling in order to refine these approaches and assess their ecological relevance more robustly. We also note a recent fascinating development in these approaches: the integration of purely mechanical models with machine learning algorithms like reinforcement learning (see Colabrese et al., 2017 for one of the first studies along these lines). We shall mention also the works by Mousavi et al., 2024, directly applied to the case of copepods which constitute a natural extension of the LC model. This novel and fast evolving approach could validate or even discover optimal swimming strategies not pre-programmed (hard wired) into the mechanistic models.

Chapter 7

Introduction to freezing and melting in the presence of flows

This chapter introduces the second broad research topic that has been at the center of my work in recent years. Unlike the subjects discussed previously, which were concerned with the dynamics of discrete entities—particles or living organisms— naturally described from a Lagrangian perspective, this research area focuses on continuous media and is approached entirely through an Eulerian filed description. The central question is that of the dynamics of phase-change processes, namely melting and solidification, in systems where convective transport plays a crucial role. This topic encompasses a variety of transport processes, including turbulent heat transfer, solute advection and diffusion in porous media, and fluid–boundaries interactions, whose coupling leads to a rich phenomenology.

7.1 Motivation

There are many motivations for undertaking a research in this direction. They may be technology driven: for example related to the development of latent heat energy storage systems (Agyenim et al., 2010) or additive manufacturing through fused deposition and laser melting (Zhao et al., 2022), or even related to cryopreservation (Haan and Rabelink, 2023). They may be environmental, such as the study of the *Cryosphere*, all processes involving ice in the natural context. Because it is this second motivation that led me to my research, in the following I will provide a brief overview on the importance of environmental ice and its many links with fluid-dynamics problems.

The role of ice in the environment

Ice covers nearly one-tenth of the Earth's surface and is a component of many geophysical processes on timescales ranging from hours to seasons, years and even geological ages (Bintanja and Wal, 2008; Hanna et al., 2013; Notz, 2009; Shepherd et al., 2009; Tietsche et al., 2011). Its evolution plays a key role in the global water cycle and global climate, influencing the sea level (Alley et al., 2005; Jacob et al., 2012; Lambeck et al., 2014), ocean circulation (Alley et al., 2005; Clark et al., 1999; Golledge et al., 2019), ocean surface temperature (Clark et al., 1999; Golledge et al., 2019) and land-surface albedo (Clark et al., 1999; Curry et al., 1995;

This chapter is based on:

1. *The physics of freezing and melting in the presence of flows*, Yihong Du, Enrico Calzavarini, Chao Sun, Nature Reviews Physics, 2024, ⟨10.1038/s42254-024-00766-5⟩ [PDF].

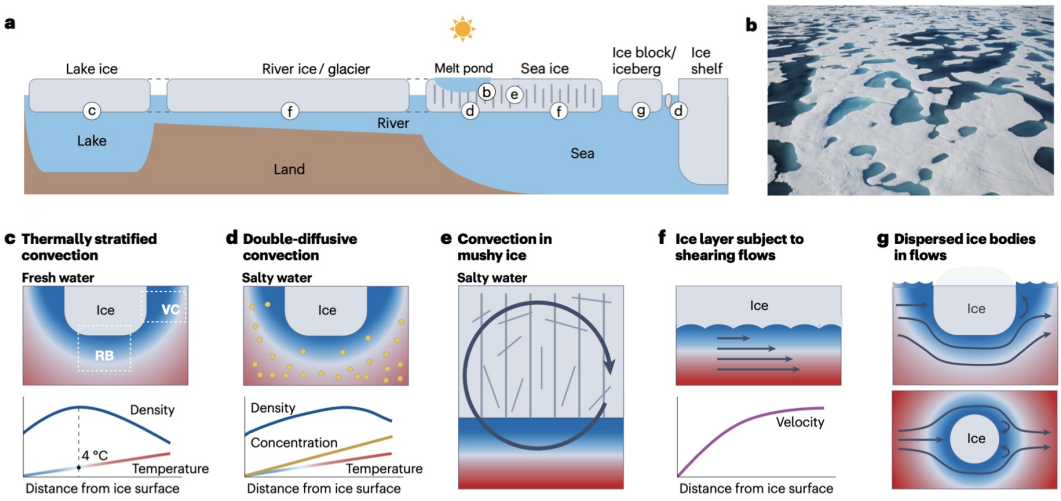


FIGURE 7.1: Sketch of different situations in which environmental ice interacts with fluid flows (a). These include: (b) radiative convection of freshwater in melt ponds; (c) stratified (or penetrative) convection in Rayleigh–Bénard (RB) and vertical convection (VC) configurations in lakes; (d) double-diffusive convection beneath ice in sea-water; (e) convection within porous, mushy sea ice; (f) forced convection and shear-dominated flows beneath ice blocks in rivers, glaciers, and the ocean surface mixed layer; and (g) dispersed ice, icebergs, and debris.

Perovich et al., 2002a). In addition, landforms and other geological patterns are shaped by the growth and melting of ice (Gardner, 2020).

The current global decline of ice in relation to climate change (Stroeve and Notz, 2018) is already having sensible effects. Examples include alterations in ecological niches (Post et al., 2013), biodiversity (Boetius et al., 2015) and ocean productivity (Duprat et al., 2016; Horvat et al., 2017), impact on the global carbon cycle (Wadham et al., 2019), and release of pathogens and pollutants (e.g. microplastics) into the oceans (Obbard et al., 2014; Peeken et al., 2018; Smith et al., 2004). Ice is also a precious freshwater resource (Weeks and Campbell, 1973), and in high-latitude and polar regions it affects considerably human activities such as navigation and the fishery industry (Andrés et al., 2018; Ho, 2010).

Environmental ice and fluid flows

The physics of freezing and melting has been extensively studied since Josef Stefan's work around 1890 on the diffusive advance of a freezing front (see also Davis, 2001; Gupta, 2017; Huppert, 1990). In most natural cases, however, ice interacts with fluid flows in the surrounding environment (Bell, 2008; Joughin et al., 2012; Rafat et al., 2023; Straneo and Heimbach, 2013). Figure 7.1 attempts to sketch the variety of such interactions. It depicts radiatively driven convection of freshwater in Arctic melt ponds; penetrative (*i.e.* stratified) convection beneath ice in lakes and freshwaters; thermo-solutal convection under ice in sea-water; convection within porous mushy sea ice; forced convection and shear-dominated flows surrounding ice blocks in rivers, glaciers, and the ocean mixed layer; and finally advection by currents and waves of dispersed ice from giant icebergs to small debris.

In natural sciences the couplings between fluid mechanics and ice phase change processes are typically explored in field campaigns, or modelled through very large-scale (regional or

global) numerical simulations. Both these essential methodologies have their drawbacks, while field measurements are lengthy, costly and sometime even risky, the numerical models are required to approximate and underrepresent small scale physical processes due to their spatiail and tempral resolution limitations.

A complementary role is taken nowadays by small scale studies performed either in the laboratory or through fully resolved simulations. These approaches are particularly interesting as they can allow to understand so called microscopic physics (in geophysical sense) and help in providing parametrizations needed for the predictions of regional and planetary scale ice processes. Laboratory studies benefit from the well controlled environment, system setting and boundary conditions, and by the possibility to use accurate measurement tools (that are sometime prevented in field campaigns). Furthermore, the adoption of simplified configurations makes it possible to define *model systems* that can be studied analytically or simulated numerically with high accuracy. The connection between the lab-scale studies and the geophysical-scale processes is a challenging problem in itself. This upscaling is typically made by means of dimensional analysis which brings to scaling laws, but it can be done also with reduced models elaborated through data-driven approaches.

As we observed in Fig.7.1, freezing and melting involve spatial temperature variations, which typically cause a gravity-induced buoyancy force and set the liquid into motion. This makes buoyancy-driven thermal convection (i.e. natural convection) one of the most common types of flow coupled with phase change. As we mentioned earlier in this thesis, the prototypical model system for this process is the Rayleigh–Bénard (RB) system (Ahlers et al., 2009; Chillà and Schumacher, 2012). As a consequence it was quite natural to address the melting/freezing problem in such a device (Davis et al., 1984). Some other typical configurations are realized when the RB system is tilted, notably by 90^o (so called vertical convection, VC) (Ng et al., 2015; Shishkina, 2016), or even flipped upside down. The detailed knowledge of fluid dynamic processes in these systems makes them perfect candidates for studying phase-change processes and their coupling with fluid flows. Another appealing feature of the system is its reproducibility in both numerical and experimental research. It's likely this is why, in recent years, a large number of studies have adopted the RB system (and its VC variation) as a framework for investigating melting phenomena. We could dub this the"ice in a box" framework (see (Du et al., 2024) for a more thorough review on these approaches).

In the following section I describe my path over this topic. It is intended as guide to the next chapters where some of the studied problem will be exposed in greater detail.

7.2 My path through Phase-change coupled to Natural Convection

Around 2014, I became fascinated by the geophysical processes of Arctic melt ponds (Fetterer and Untersteiner, 1998). Arctic melt ponds form on floating sea ice during the summer, when meltwater (mostly from melted snow) accumulates on the surface. These puddles play a significant role in the overall melting process of sea-ice because they absorb more solar radiation than the surrounding ice (they absorb 80% as compared to $\sim 30\%$ for bare

ice). This is due to their lower albedo (reflectivity), which also creates a positive feedback mechanism: increased absorption of sunlight leads to faster melting, which in turn deepens and expands the ponds leading to even more radiation absorption. In addition, as these ponds grow, they can become thermally unstable. They are unstable because their bottom temperature is close to 0^oC, the melting temperature of pure water of which they are composed, while their surfacial temperature is typically around 2^oC. In this regime (due to the water density anomaly) warmer water is heavier than colder one and due to buoyancy it tends to sink in the pond. This instability may trigger convective motions within the liquid water, which are further coupled with ongoing melting of the surrounding ice. The role of melt-ponds is considered to be relevant for the planetary climatological scale, responsible for an acceleration of sea-ice melting that cannot yet be well predicted by global sea-ice models (where the process is difficult to parametrize due to its sub-grid character).

From a physicist's perspective, this quite naturally led me to study such configurations within the simplified framework of RB convection, that is, the classical fluid layer subjected to a temperature difference between its lower and upper boundaries. The key question I addressed was therefore how the classical RB dynamics is modified when one of the boundaries is not fixed but can evolve due to melting.

To tackle this problem, I first considered idealized configurations in which a solid at its melting temperature is heated from below. (Note that his is in fact an upside-down version of the configuration of melt ponds, but it is dynamically equivalent to it provided that the buoyancy is reverted too, i.e. the hot fluid is lighter than the cold one). In this setting, the system can be described within the Oberbeck-Boussinesq approximation, with equations supplemented with boundary conditions accounting for the phase change at the moving interface. The relevant control parameters are ones for the classical RB system (namely Rayleigh, Prandlt, and the domain spect ratio) plus a new one the Stefan number which compares sensible heat to latent heat. In particular, the above mentioned ice melt ponds correspond to small Stefan numbers (i.e. dominated by the large latent heat of water, $\sim 334\ KJ/Kg$) , whereas other systems such as cooling of magmatic chambers may involve much larger Stefan values. Because the thickness of the melted layer evolves in time, the response parameter of the system, such as the Nusselt (Nu) and Reynolds (Re) numbers are based on the effective height o the system, which evolve over time.

Within this framework, I investigated the relationship between heat transport and interface dynamics. In the purely conductive regime, the interface advances diffusively, scaling as the square root of time, and the heat flux remains constant. In contrast, in the convective regime, different scaling laws for the dimensionless heat flux (Nusselt) lead to qualitatively different interface dynamics: a $Nu \sim Ra^{1/3}$ scaling corresponds to a constant melt-front velocity, while a $Ra^{1/2}$ scaling, expected at high Rayleigh numbers, leads to an accelerated propagation of the liquid-solid interface. Numerical simulations allowed me to explore these regimes in detail and to characterize the transition from conduction to convection, as well as the subsequent evolution of the system (Rabbanipour Esfahani et al., 2018).

These simulations, in both two and three dimensions, showed that many features of classical RB convection are recovered, albeit with a shifted convective onset transition depending on the Stefan number. As the Rayleigh number increases, the influence of phase change becomes less pronounced, and the system approaches the standard RB behavior.

At the same time, the coupling with a moving boundary introduces new phenomena, particularly in the morphogenesis and morphodynamics of the interface. For instance, multiple dome-like structures emerge at locations where hot plumes impinge on the interface, whereas downward-pointing cusps form at the detachment sites of cold plumes. Over time, these domes progressively merge. Statistical analyses further reveal that the interface roughness remains relatively small and even decreases slightly with increasing Ra, suggesting that the interface largely reflects the structure of the underlying turbulent convective flow.

In collaboration with Andrea Scagliarini (CNR Rome) and colleagues, we investigated the modeling of melt ponds at larger spatial scales, with particular emphasis on the mutual interactions between melt ponds and the evolution of their resulting network. Our contribution was to quantify the impact of scaling laws for convective heat transfer within melt ponds on their seasonal evolution during the summer melt season (Scagliarini et al., 2020).

Another important part of my research program involved comparing numerical simulations findings with laboratory experiments. In practice, experimental studies often focus on freezing rather than melting, as melting experiments are more difficult to control, especially due to the challenge of producing defect-free ice. Modeling (numericaly and theoretically) such experiments required going beyond the simplest Boussinesq assumptions, in particular by accounting for the nonlinear dependence of buoyancy on temperature for water (and the water density anomaly) and for the differences in thermal properties between ice and liquid water phases, leading to a conjugate heat transfer problem. Within this framework, I studied the evolution toward equilibrium states of the RB systems with an upper freezing boundary, combining numerical simulations, experimental data, and reduced order one-dimensional models (Wang et al., 2021b).

These investigations showed that convection significantly affects the equilibrium thickness of the liquid and solid layers. In particular, the thickness of the ice layer decreases with the temperature of the warm boundary, initially linearly and then much more rapidly once convection sets in. Together with my collaborators, we showed that reduced one-dimensional models can recover the observed behavior for the mean ice thickness, when nonlinear buoyancy effects are properly included. This analysis also revealed that, when the warm wall temperature is above 4°C, the system can organize into three distinct layers: a solid ice layer, a stably stratified liquid layer, and an upper unstable layer that can be either diffusive or convective. This stratification leads to multiple possible regimes, and even to situations where the initially present convective motion shuts down when the unstable liquid layer becomes too thin.

These results further highlighted that freezing and melting are not equivalent processes: they do not necessarily lead to the same equilibrium states, and multiple stable configurations may coexist. Building on this, I explored more complex geometries, including variations of the cell aspect ratio and of their horizontal inclination. In systems rotated horizontally by 90° relative to the RB case (i.e., vertical convection), the density anomaly of water plays a crucial role in shaping the dynamics. It drives competition between counterrotating convective rolls and leads to the formation of interfaces with inflection points, whose position depends on the relative strength of the two rolls (Wang et al., 2021a,c).

Finally, I extended this work to the case of saline water, where an additional control parameter, salinity, modifies both the density (through the equation of state now depending both on temperature and salinity) and the phase diagram. In this context, several nontrivial effects arise: the growth of ice can be faster than purely diffusive, and the dependence of ice thickness on the salt content in the cell can be non-monotonic. These behaviors cannot be explained by simple 1D models, even when effects like the change of the equation-of-state in saline water are included. The key ingredient is the formation of a porous, spatially inhomogeneous, partially solidified region known as a mushy layer, within which fluid flow and convection can also occur. Accounting for this additional physics introduces significant modeling complexity and requires often ad-hoc parametrizations (Du et al., 2023b).

At longer timescales, of the order of several weeks as compared to the duration in days of the previous studies, the freezing systems with salty water exhibit a slow evolution toward a final state characterized by thinner, nearly salt-free, and non-porous ice. This process, referred to as ice aging, is controlled by the diffusion of salt and can be described, at least qualitatively, by reduced models under appropriate assumptions (Du et al., 2025; Wang et al., 2026)

Altogether, this body of work highlighted the richness of convection coupled with phase change: even in relatively simple geometries, the interplay between fluid flow, thermodynamics, and additional effects such as salinity leads to a wide range of dynamical behaviors.
In the following chapters, I will present a selection of these results in more detail. In Chapter 8, I explore numerically the basal melting in a pure fluid in a RB-like configuration and discuss its application to modelling Arctic melt ponds. Chapter 9 delves into freshwater ice dynamics under convective flows. Here, the anomalous temperature dependence of water density becomes relevant. The chapter proposes both numerical and experimental insights. Chapter 10 explores freezing modes in salty water, the equilibria states that forms in convective cells and the phenomenon of ice aging.

Chapter 8

Convection with a melting boundary

The problem and the particular setting studied in this chapter is relevant for all situations where a substance melt from below. In the context of natural phenomena, for instance in the case of glaciers and ice sheets, this is referred to as *basal melting*. The configuration is also relevant for the case of ice melt ponds where the fusion rather occurs from above, but the buoyancy force is also reverted due to the thermal density anomaly in the water equation-of-state. This chapter briefly reviews the main results achieved during the PhD thesis of Babak Rabbanipour Esfahani and discuss later applications more specifically focused on melting dynamics multiple ice melt ponds.

8.1 Basal melting driven by thermal convection

The so-called convective-melting (CM) model is probably the simplest extension of the Rayleigh–Bénard system that incorporates the occurrence of a melting process. It consists of a layer of a pure substance initially at its melting temperature, T_m, that is heated from below (see Fig. 8.1). Due to this special initial condition, the phase-change process begins immediately (at time $t = 0$) without any heat conductive transfer occurring in the solid phase. A fluid layer forms at the heated bottom of the system and gradually grows until it reaches an unstable state, leading to the onset of convection. As the convective layer continues to increase in thickness, the flow becomes progressively more structured, transitioning from a quasi-steady state to a time-dependent regime, then to a chaotic state, and eventually to fully developed turbulence (see Fig. 8.2).

In this relatively idealized setting the dynamic of the system is governed by the same Boussinesq equations that describe the evolution of the RB system. However in the present case these equations applies to a spatially evolving domain, where the boundary condition

This chapter is based on:

1. *Basal melting driven by turbulent thermal convection*, B. Rabbanipour Esfahani, S. C. Hirata, S. Berti and E. Calzavarini, Phys. Rev. Fluids 3, 053501 (2018) [PDF].
2. *Modelling the evolution of sea ice and melt ponds: sensitivity to microscale heat transfer mechanisms*, A. Scagliarini, E. Calzavarini, D. Mansutti and F. Toschi, In: Cannarsa P., Mansutti D., Provenzale A. (eds) Mathematical Approach to Climate Change and its Impacts. Springer INdAM Series, vol 38. Springer, Cham (2020) [PDF].

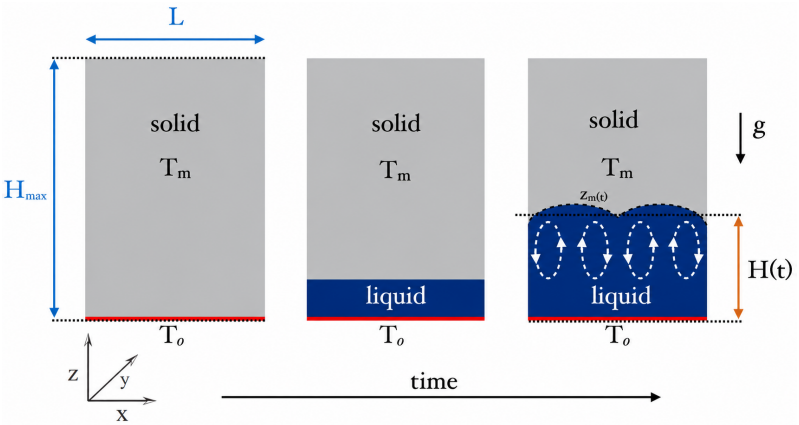


FIGURE 8.1: Schematic view (two-dimensional cut) of the melting system. This initially consists of a pure solid at the melting temperature (T_m). The bottom temperature is kept fixed at a value $T_0 > T_\mathrm{m}$, allowing the formation of a liquid phase. As time progresses, the bottom fluid layer becomes thicker and convection can develop in it. The local height of the liquid-solid interface, measured from the bottom, is denoted $z_\mathrm{m}(x, y, t)$; its average value is $H(t)$.

at the fluid–solid interface, ($\boldsymbol{x}_m$), evolves according to

$$c_p\, \kappa\, \boldsymbol{\nabla} T|_{\boldsymbol{x}=\boldsymbol{x}_m(t)} = \mathcal{L}\, \dot{\boldsymbol{x}}_m(t), \tag{8.1}$$

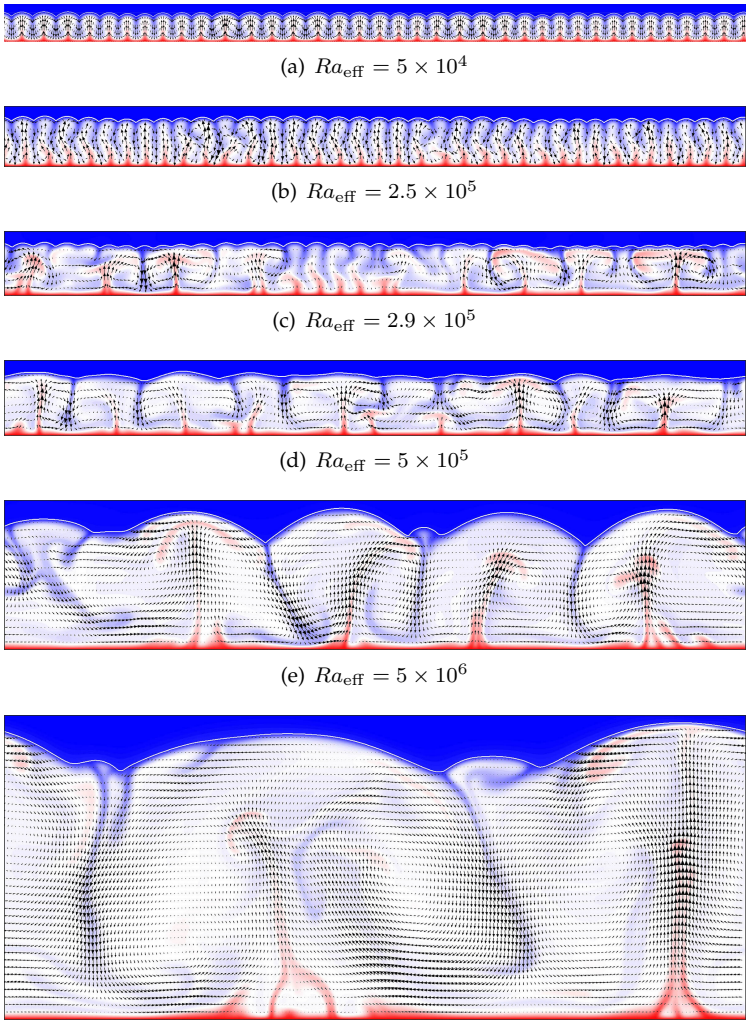
where c_p the specific heat capacity, k is the thermal diffusivity and $\mathcal{L}$ the latent heat of melting of the considered material. This is a simplified form of the so-called Stefan condition (Gupta, 2017). The simplification arises because the solid is assumed to remain at the melting temperature, so that conductive heat flux within the solid domain is absent and the melt front progress proportionally to the heat flux from the fluid to the solid wall.
When the Boussinesq equations, together with the above boundary condition, are nondimensionalized, an additional control parameter appears alongside the Rayleigh number, Prandtl number, and aspect ratio (Ra, Pr, and Γ): the Stefan number,

$$St = \frac{c_p \Delta T}{\mathcal{L}}.$$

The Stefan number represents the ratio of sensible heat to latent heat for the material under consideration. The limit, $St \to 0$, corresponds to the singular case of a material that requires an infinite amount of heat to melt.

We do not discuss here the available numerical methods for the solution of the resulting differential problem, i.e. the Boussinesq equations coupled with the Stefan and the other boundary conditions for the velocity and temperature fields (i.e. no-slip on solid boundaries and isothermal on the bottom plane). Two main approaches are commonly employed. The first consists in solving the moving-boundary problem directly. The second introduces a scalar phase field, ϕ_l, representing the local liquid fraction, together with an additional evolution equation. In this approach, the fluid–solid interface is diffuse rather than sharp, but the numerical algorithm results considerably simplified. The evolution of the phase field can be described by an Allen–Cahn-type equation Hester et al., 2020 or computed iteratively using an enthalpy-based formulation (Chatterjee and Chakraborty, 2005). The latter approach is the one adopted in our numerical studies, implemented in our code

(Calzavarini, 2019).



(a) $Ra_{\text{eff}} = 5 \times 10^4$

(b) $Ra_{\text{eff}} = 2.5 \times 10^5$

(c) $Ra_{\text{eff}} = 2.9 \times 10^5$

(d) $Ra_{\text{eff}} = 5 \times 10^5$

(e) $Ra_{\text{eff}} = 5 \times 10^6$

(f) $Ra_{\text{eff}} = 5 \times 10^7$

FIGURE 8.2: Visualization of the 2D CM system in different stages at increasing effective Rayleigh numbers (from top to bottom). The lateral size of the system is $2H_{max}$, while the vertical size has been cut at $\sim 1.1\ H(t)$. Color codes the normalized temperature deviation from the mean $(T_0 + T_m)/2$ (red is for -0.5, blue for 0.5 and white for zero). Arrows represent the velocity field normalized by the instantaneous maximum velocity magnitude. The thin white line in the top part of each temperature field marks the liquid-solid interface. The other global parameters are $St = 1$ and $Pr = 10$.

Because the melting dynamics spans a finite amount of time (till when the melting front reaches the height H_{max}) it is more convenient to adopt as a representative length-scale a dynamic scale given by the instantaneous (spatially) averaged height of the fluid layer, which is defined as

$$H(t) = H_{max}\langle\phi_l\rangle, \tag{8.2}$$

where $\langle\ldots\rangle \equiv V^{-1}\int_V \ldots d^3x$ indicates a volume average over the entire domain (i.e. fluid and solid); hence $\langle\phi_l\rangle$ denotes the global liquid fraction in the system. This is particularly useful in view of contrasting the behaviour of the CM system with the one of a RB system of

equivalent height. Such a choice allows to introduce the effective Rayleigh number:

$$Ra_{\text{eff}} = \frac{\beta g \Delta T H(t)^3}{\nu\kappa} = Ra\, \langle\phi_l\rangle^3, \tag{8.3}$$

where Ra was the usual Rayleigh based on $H_{\max}$ and $\Delta T = T_0 - T_m$, and similarly an effective (width over height) aspect ratio:

$$\Gamma_{\text{eff}} = L/H(t) = \Gamma_{min}/\langle\phi_l\rangle. \tag{8.4}$$

Note that during its dynamics the convective melting system always explores a range of increasing effective Rayleigh numbers and decreasing effective aspect ratios, the latter starting from $\Gamma_{\text{eff}} = +\infty$ and reaching a value than cannot be smaller than $\Gamma_{min} \equiv L/H_{max}$. Similarly to these effective input parameter one can define effective global output parameters. The two most evident ones are the Nusselt number and the Reynolds number, i.e. respectively the dimensionless thermal heat flux and kinetic energy across the system. The first read:

$$Nu^{in}_{\text{eff}} = -\frac{\langle\partial_z T|_{z=0}\rangle_A}{\Delta T/H_{max}} \langle\phi_l\rangle\,, \tag{8.5}$$

where $\langle\ldots\rangle_A$ denotes horizontal plane (area) average and the index "*in*" the inlet heat flux in the system. Note in fact that the inlet flux in the system can be different from the outlet one as the global temperature of the system can in fact rise with time. The link between the two Nusselt numbers is $Nu^{in}_{\text{eff}} - Nu^{out}_{\text{eff}} = \langle\phi_l\rangle^2 \langle\partial_{\tilde{t}}\tilde{T}\rangle_{V_l} > 0$ (where $\tilde{t} = tH^2_{max}/\kappa$ and $\tilde{T} = T\Delta T$). We note that the Nu^{out}_{eff} is directly linked to the advancement of the melting front through the relation $Nu^{out}_{\text{eff}} = \frac{1}{2St}\frac{d\langle\phi_l\rangle^2}{d\tilde{t}}$. The effective Reynolds number is instead:

$$Re_{\text{eff}} = \frac{u_{rms,V_l}\, H(t)}{\nu} = \frac{u_{rms} H_{max}}{\nu}\langle\phi_l\rangle^{1/2}, \tag{8.6}$$

where u_{rms,V_l} is the fluid root-mean-square velocity computed over the liquid phase only and u_{rms} its counterpart obtained from averaging over the whole volume.

8.1.1 Scaling of global quantities

The first question one can ask about this system is in which respect its global dynamics - quantified in terms of the effective parameters - differs from the one of the RB system. Specifically, we compare the scaling relations $Nu_{\text{eff}}(Ra_{\text{eff}})$ and $Re_{\text{eff}}(Ra_{\text{eff}})$ with the corresponding scalings established for the RB system (Ahlers et al., 2009).

Figure 8.3 show the effective Nusselt number ($Nu^{\text{in}}_{\text{eff}}$) and the effective Reynolds number (Re_{eff}) as functions of the Ra_{eff}, for the CM and RB systems in 2D and 3D acorss several order of magnitudes in Rayleigh. Here the choice was made to fix Prandtl number, $Pr = 10$, close to that of fresh water just above the freezing point (Skyllingstad et al., 2009), and keeping, $St = 1$. The latter choice is not so representative of ice-water problems, where the Stefan number tend to be small (due to the large latent heat), it is rather motivated by the need to keep computational time reasonably small. The figure clearly shows that CM and RB systems exhibit similar behaviours.

Noticeable differences are in the critical onset of convection, in the CM system it happens at higher Rayleigh number ($Ra_{\text{eff}} \simeq 5 \times 10^3$) than in the RB one ($Ra \simeq 1708$). Furthermore,

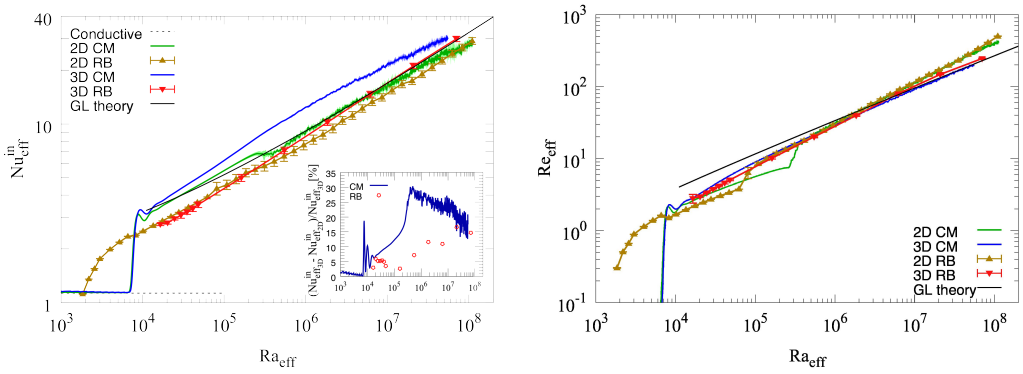


FIGURE 8.3: (left) Effective Nusselt number *vs* the effective Rayleigh number for 2D and 3D systems. The global parameters are $St = 1$ and $Pr = 10$. The Nu vs Ra data for the RB 2D and 3D cases are also shown. The horizontal dashed line is the conductive value for the effective Nusselt number, $Nu^{\text{in}}_{\text{eff}} = 2\lambda^2 e^{\lambda^2}/St$, where λ is a constant depending on St Alexiades, 1992, while the solid black line is the prediction from Grossmann-Lohse (GL) theory, calculated as in Refs. (Stevens et al., 2013). The inset shows the relative difference (in percentage) between the 2D and 3D global heat fluxes for the CM and RB systems, for different Rayleigh numbers in the same range as in the main panel. (right) Effective Reynolds number vs the effective Rayleigh number for 2D and 3D systems with the same melting process' configuration. The global parameters are $St = 1$ and $Pr = 10$. The Re vs Ra data for the RB 2D and 3D cases are also shown. Solid black line is again GL theory.

a sudden jump in $Nu^{\text{in}}_{\text{eff}}$ is observed when convection is triggered in the CM system. This behavior resembles the transient response of the Nusselt number in the classical RB system following an impulsive increase of the Rayleigh number beyond the convection threshold. In that case, the heat flux undergoes an initial overshoot, which is gradually absorbed as the flow evolves toward its statistically steady state.
The 3D effective Nusselt number is always above its 2D counterpart at corresponding Ra_{eff} values. This is also a known feature of the classical RB (Van Der Poel et al., 2013). In amplitude, the difference between CM and RB appears to be more important than in the corresponding RB situation, except beyond Ra_{eff}, $Ra > 10^7$ where it reaches similar values for the two systems (see inset of Fig. 8.3). This suggests that the differences between the two systems may vanish asymptotically with increasing Rayleigh number.

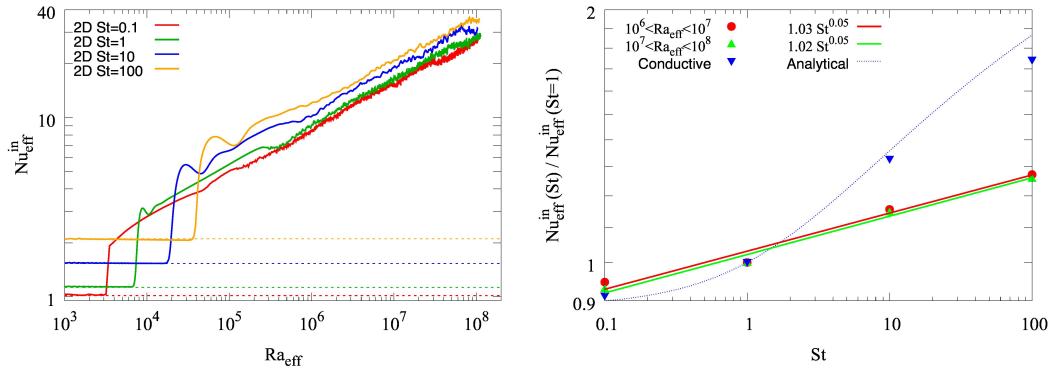
The Reynolds number, Fig. 8.3, dysplays a nearly perfect agreement between CM and RB. Furthermore 3D CM simulations match asymptotically very well the prediction from the Grossman-Lohse (GL) theory for the RB system. It can be observed that, Ra_{eff} in 3D does not show abrupt changes associated with pattern transitions, while these jumps are present in 2D. With respect to what is found for the Nusselt number, for which $Nu^{\text{3D}}_{\text{eff}} > Nu^{\text{2D}}_{\text{eff}}$, at high Ra_{eff} we find that the effect of dimensionality is opposite for the Reynolds number, namely $Ra^{\text{2D}}_{\text{eff}} > Ra^{\text{3D}}_{\text{eff}}$, in qualitative agreement with previous observations in 2D and 3D bounded RB systems (Van Der Poel et al., 2013).

In summary, we showed that the CM system in the range of Ra parameter studied here (and with $Pr = 10$, $St = 1$) behaves in a qualitatively similar manner as the RB system. The role of dimensionality (2D, 3D) is also alike in the CM and RB cases. However, while the Reynolds number is nearly identical with or without melting, the Nusselt number displays a distinct behavior characterized by $Nu^{\text{CM}}_{\text{eff}} > Nu^{\text{RB}}_{\text{eff}}$ for $10^4 \leq Ra_{\text{eff}} \leq 10^7$. However

it is difficult to extrapolate such tendencies beyond the maximal Ra_{eff} that we have simulated. Overall, these findings suggest that in turbulent conditions, RB phenomenology can provide quantitative predictions for CM dynamics and this is particularly true for the more intense turbulent conditions.

8.1.2 Effect of Stefan number

It makes sense to ask what is the effect of the extra control parameter in the CM system as compared to RB, namely the Stefan number. To this end we performed simulations (in 2D) varying it in the wide range $0.1 \leq St \leq 100$. Although Fig. 8.4(a) illustrates that increasing St significantly delays the onset of convection, only quite small differences were observed in the dimensionless global heat flux (see Fig. 8.4(b)), notably at high Rayleigh numbers. Fig. 8.4(b) further shows that heat flux scaling with St according to a power law with a small exponent (0.05) over a broad range of Ra_{eff} values, with reasonably good accuracy. This result has relevant consequences for numerical approaches, because it means that it is possible to extrapolate results of high-St fast simulations to small-St conditions that would be otherwise unattainable in direct numerical simulations. Because for asymptotically small St the CM system approaches the RB one, an extrapolation procedure for the estimation of the heat flux at any small St can be devised too.



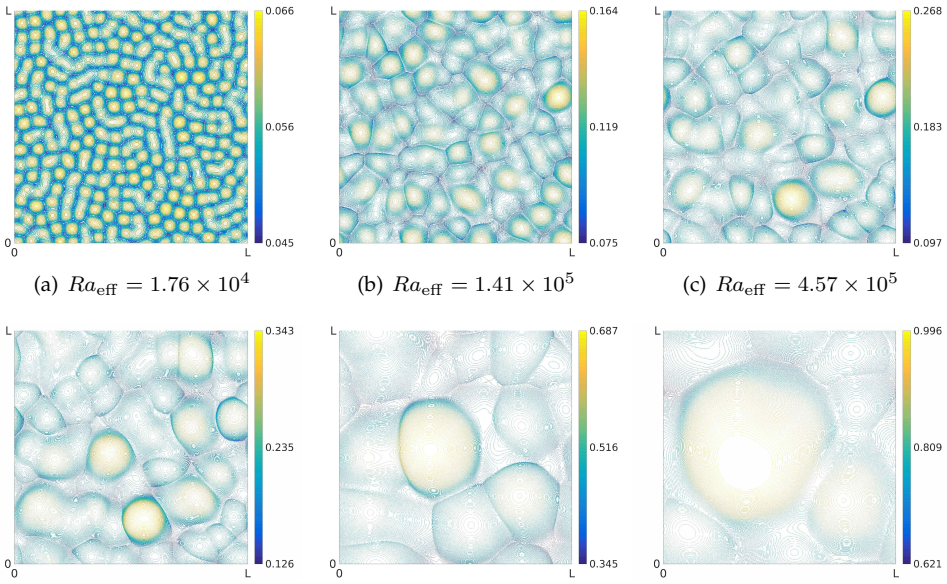
(a) (b)

FIGURE 8.4: (a) Nusselt number *vs.* the effective Rayleigh at $St = 0.1,1,10,100$ in 2D. The horizontal dashed lines correspond to the heat-flux conductive values, that can be computed analytically. (b) Behavior of the 2D $Nu^{\text{in}}_{\text{eff}}$, rescaled with its value at $St = 1$, for the same values of St as in panel (a), for the conductive regime as well as for the convective regime ranges $Ra_{\text{eff}} \in [10^6, 10^7]$ and $Ra_{\text{eff}} \in [10^7, 10^8]$. In the conductive regime the trend is described by the analytical Stefan solution. In the highly convective regime a surprisingly weak scaling, $St^{0.05}$, could be identified.

We also addressed the difference between the instantaneous incoming and outgoing heat fluxes, which is connected to the mean temporal variation of the fluid temperature. The results showed that such heat-flux imbalance is essentially controlled by conductive processes and that it is more pronounced in systems where the melting process is faster, i.e. at larger Stefan numbers. This leads to a consequence for the case of Arctic ice-melt ponds. With the Stefan number in this case being $St \approx 10^{-2}$, an extrapolation from our results would then indicate that $Nu^{\text{in}}_{\text{eff}} \approx Nu^{\text{out}}_{\text{eff}}$ in them. This means that, at least for heat-transfer features, basic classical RB modeling is appropriate in that case.

8.1.3 Morphology of the phase-change interface

Another interesting aspect of the CM system concerns the characterisation of the evolving shape of the melting front. Already from the 2D numerical results in Fig. 8.2 we see that such front is uneven, it is characterized by a succession dome shaped profiles that undergoes a coarsening process as time proceeds.



(a) $Ra_{\mathrm{eff}} = 1.76 \times 10^4$ (b) $Ra_{\mathrm{eff}} = 1.41 \times 10^5$ (c) $Ra_{\mathrm{eff}} = 4.57 \times 10^5$

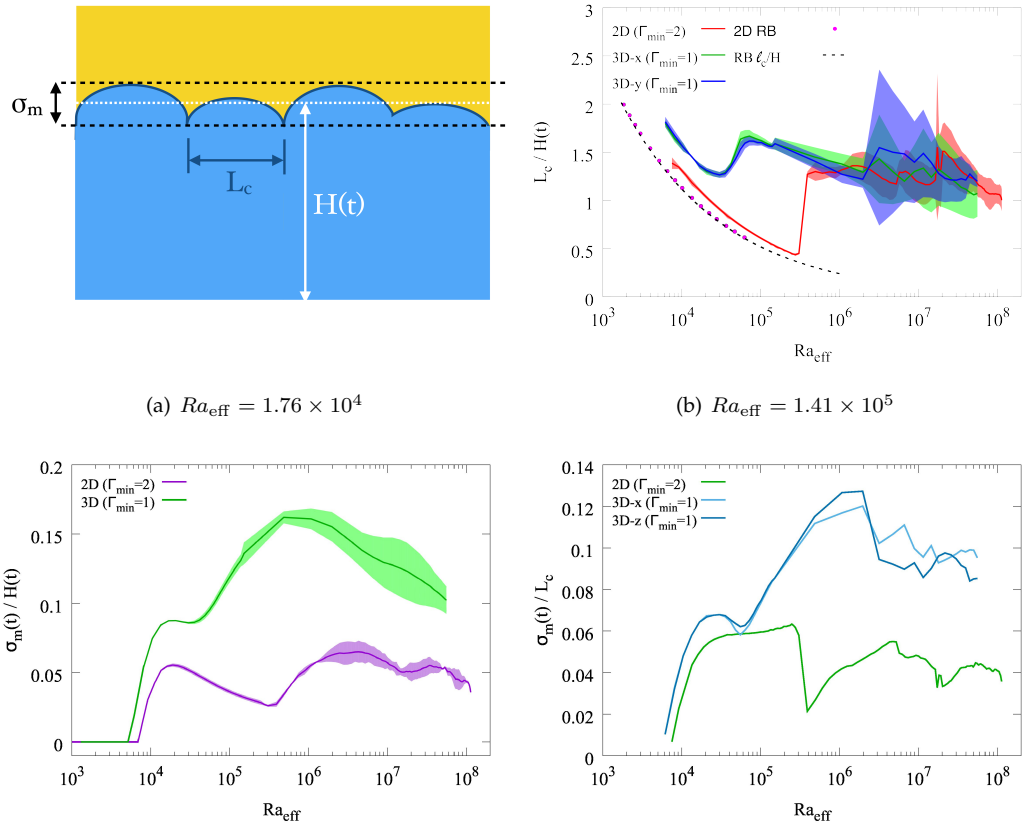
(d) $Ra_{\mathrm{eff}} = 1.04 \times 10^6$ (e) $Ra_{\mathrm{eff}} = 1.15 \times 10^7$ (f) $Ra_{\mathrm{eff}} = 5.54 \times 10^7$

FIGURE 8.5: Isolines of the phase-change interface from 3D simulations at different Rayleigh numbers. The color codes $z_{\mathrm{m}}(x, y, z, t)/H_{\max}$. Panel (a) corresponds to a stage close to the convective onset where horizontally steady patterns are observed. The shape of these convective cells is found to be approximately hexagonal. As can be seen, few cells have already merged, creating elongated patterns. The merging process further intensifies at higher Rayleigh numbers [panels (b)–(e)]. In panel (f), where the aspect ratio is $\Gamma_{\mathrm{eff}} \simeq \Gamma_{\min} = 1$, a single pattern has become dominant.

The same is true in 3D, as shown in Fig. 8.5. This case shows the appearance of convective patterns with irregular polygonal cross section. As Ra_{eff} increases, i.e., as the fluid layer grows, such cells merge in larger and deeper ones. These results qualitatively agree with previous observations in experimental investigations with differntent melting materials (Davis et al., 1984; Hill, 1996; Sugawara et al., 2006).

Both in 2D and in 3D visualizations, the interface shape at a given time appears to be fairly well characterized by two length scales: a single wavelength corresponding to the typical lateral size of convective patterns L_{c} (note that in 3D these are essentially isotropic on the horizontal) and a typical roughness associated with the interface modulation along the vertical σ_{m} (see Fig. 8.6(a) for a schematic view). These two quantities can be used to characterize - in a statistical sense - how the front shape evolves over time.

L_{c}, can be measured by means of the autocorrelation functions of the local interface height. The computed $L_{\mathrm{c}}(t)$, normalized by $H(t)$, as a function of Ra_{eff} is shown in Fig. 8.6(b). We observe that initially, the interface is flat since convection is absent; in this case the correlation length is not really defined ($L_{\mathrm{c}} \to \infty$). Later on, a finite L_{c} emerges due to the onset of convection, which triggers the formation of recirculating patterns (cells) with an aspect ratio ≈ 1.5. In the stationary regime of convection, the identification of the width



(a) $Ra_{\mathrm{eff}} = 1.76 \times 10^4$ (b) $Ra_{\mathrm{eff}} = 1.41 \times 10^5$

(c) $Ra_{\mathrm{eff}} = 4.57 \times 10^5$ (d) $Ra_{\mathrm{eff}} = 1.04 \times 10^6$

FIGURE 8.6: (a) Schematic view of the melt layer with relevant interface length scales: horizontal correlation length $L_c(t)$, roughness $\sigma_m(t)$, and mean height $H(t)$; (b) Correlation length vs Ra_{eff}. For comparison, we also show the normalized theoretical prediction for the RB system $\ell_c/H = (2\pi/k_c)\,(Ra_c/Ra_{\mathrm{eff}})^{1/3}$; (c) Roughness vs Ra_{eff}; (d) Ratio of the roughness to the correlation length, σ_m/L_c.

of convection patterns is unambiguous. In such a stage of RB system, one has $Ra_c \simeq 1708$ and horizontal wave vector $k_c \simeq 3.117$, so that ℓ_c/H closely matches the corresponding measurements. This proves that the characteristic correlation length of the interface in the CM system shows clear fingerprints of the convective patterns associated to the first supercritical instability of the RB system. Asymptotically in Ra, convective rolls of typical aspect ratio 1 tend to prevail, independent of dimensionality. This feature is also common to RB convection between flat walls (Van Der Poel et al., 2013).

The roughness of the liquid-solid interface σ_m can be defined as $\sigma_m(t) = \sqrt{\langle [z_m(t) - H(t)]^2 \rangle_A}$, where z_m is the local height of the interface. Fig. 8.6(c) shows that in 3D, the roughness is typically larger than in 2D, but, regardless of spatial dimensionality, the difference decreases when Ra_{eff} is sufficiently large. Such low values of the melting front roughness again point to strong similarities between the CM and the flat or weakly rough-walls RB systems (Brichet et al., 2025). Finally, Fig. 8.6(d) demonstrates that the shape of interface, as characterized by the ratio of the two discussed global scales, σ_m and L_c, appears to remain similar and essentially flat in the highly convective regime. Similar results, confirming these trends at even larger Rayleigh numbers, have been recently obtained by Yang et al., 2023b.

8.2 A glimpse into the evolution of multiple ice melt ponds

As discussed in the previous chapter, the formation and growth of Arctic melt ponds sparked my interest and provided the intial motivation for studying the CM model system. While this model captures some of the fundamental physical processes that take place within an individual melt pond, it is, of course, only a simplified representation of a much more complex reality.
This naturally leads to a number of broader questions. How can we describe the long-term evolution of an ensemble of melt ponds developing over a specific ice topography? To what extent is this evolution controlled by the natural convection that arises within the ponds? Motivated by these questions, I investigated a large-scale model for melt ponds evolution. The model and the main results of this study are presented in the reminder of this chapter.

8.2.1 A model of melt pond topography evolution

The physical processes that occur within the ice pack and lead to variation of the sea ice thickness, can be grouped essentially into two categories: thermodynamic and mechanical. Thermodynamic processes are those related to the radiative budget: the fraction of incoming radiation that is absorbed by the ice pack is spent to increase the surface temperature and to melt ice. Mechanical processes are related to deformations of sea ice are induced by ocean and wind stresses. These can drive sea ice transport, as well as elasto-plastic deformations in the pack, giving rise to events such as ridging and rafting (Hopkins et al., 1999). Since we are interested in simulating processes involving ice melting and meltwater dynamics, we will neglect sea ice transport and mechanical deformation terms (despite they can act on time scales comparable to melting in summer). As ice melts, meltwater is formed and transported, by sliding over the ice topography and seepage through its porous structure. It will eventually concentrate in local minima of the ice topography, forming melt ponds.

The system we adopted to describe this phenomenon is composed by two coupled partial differential equations for the fields representing the ice thickness, $h(\boldsymbol{x}, t)$, and pond depth, $w(\boldsymbol{x}, t)$ (Lüthje et al., 2006). They read:

$$\begin{aligned} \partial_t h &= -f \\ \partial_t w &= -\nabla \cdot (\boldsymbol{u} w) + \frac{\rho_i}{\rho_w} f - s, \end{aligned} \tag{8.7}$$

where f, $\boldsymbol{u}w$ and s represent, respectively, the melting rate, the meltwater flux (per unit cross-sectional area) and the seepage rate, which are, in general, functions of h and w. The model accounts for the volume change of water at freezing through the distinct densities, ρ_i, ρ_w for ice and water. The transport of meltwater is realised essentially with two mechanisms: sliding of water over slopes of the ice surface $\boldsymbol{u}_{\text{sliding}}$ and lateral drainage through the porous structure of ice $\boldsymbol{u}_{\text{lateral}}$ whose details are provided in (Scagliarini et al., 2020). The expression for the seepage rate is $s = (Kg/\nu)(w/h)$, where K and η are the permeability of ice and water kinematic viscosity, and it is based on Darcy law (Scott and Feltham, 2010). The presence of salt (which is quite low in ponds) is here neglected.

A key part of the model is the total melting rate f appearing in (8.7). It can be expressed as the sum of two terms:

$$f = (1-\chi)\phi_1(w) + \chi\phi_2(w, \nabla w, \nabla h). \tag{8.8}$$

The first term, ϕ_1, is *local*, in fact it depends only on the pond depth $w(\boldsymbol{x}, t)$, whereas the second term, ϕ_2, includes also *lateral melting* mechanisms and may, thus, in principle depend also on gradients of the pond depth and ice thickness fields. The binary variable $\chi \in \{0, 1\}$ is introduced to switch on ($\chi = 1$) or off ($\chi = 0$) or weight such lateral melting contribution. We focus here on the parametrization of the local melt rate. Based on the fact that $Ra \propto w^3$ and $Nu \sim Ra^c$, we can model it as:

$$\phi_1(w) = m_i + m_{\mathrm{p}}(w), \quad \text{with } m_{\mathrm{p}}(w) = \begin{cases} m_{\mathrm{p,rad}}\, w & \text{if } w \in [0, w_{\max}] \\ m_{\mathrm{p,conv}}\, w^{3c-1} & \text{if } w > w_{\max}, \end{cases} \tag{8.9}$$

This expression indicates that, when ponded water is present ($w > 0$), the melt rate is enhanced relative to that of bare ice (m_i). For shallow ponds ($w < w_{max}$), this enhancement increases linearly with water depth and is proportional to $m_{\mathrm{p,rad}}$. This behavior arises from the volumetric absorption of radiative heating, which is assumed to remain approximately effective up to a depth of $w = w_{max} = 0.1\mathrm{m}$ (Lüthje et al., 2006). Once convection sets in, the heat flux is substantially enhanced ($m_{\mathrm{p,conv}} > m_{\mathrm{p,rad}}$), but its dependence on water depth is weaker because convection provides a highly efficient heat transfer mechanism. The corresponding scaling law depends on the exponent c in the Nusselt–Rayleigh relationship. This exponent is often taken to be $1/3$, this value denotes the classical Malkus scaling. However, precise studies of RB convection show that it is generally smaller, typically closer to $2/7$, which leads to a depth exponent of $\alpha = 3c - 1 = -1/7$. This physical argument and the resulting parameterization of the pond heat flux formed the basis of our sensitivity study on melt-pond-induced melting and represent the main original contribution of our work. We tested its influence through numerical simulations.

To this end the system of equations (8.7) can be discretized on a bidimensional grid (1024×1024) with periodic boundary conditions corresponding to a physical surface of $L^2 \approx 1\,\mathrm{km}^2$. The equations are integrated numerically using an Runge-Kutta 4th order time marching scheme with time step $\Delta t = 60\,\mathrm{s}$ for a duration of ≈ 30 days. We aim to simulate the summer time evolution of sea ice, so the initail simulation time, t_0, is to be considered indicatively June 1st and, in view of this, refreezing of meltwater is not accounted for. The initial values of the sea ice topography $h^0_{ij} \equiv h(x_i, y_j, t_0)$ are random Gaussian numbers with given mean and variance. The initial topography is spatially correlated over a characteristic length $\delta \approx 8\,\mathrm{m}$. Two types of ice are used as initial conditions, namely thin (and more porous) first-year ice (FYI) and the ticker multi-year ice (MYI). The statistical parameters (mean $\langle h \rangle$ and variance σ_{h} of the thickness distribution) employed are $\langle h \rangle = 0.92\,\mathrm{m}$, $\sigma_{\mathrm{h}} = 0.18\,\mathrm{m}$, for FYI, and $\langle h \rangle = 3.67\,\mathrm{m}$, $\sigma_{\mathrm{h}} = 1.5\,\mathrm{m}$, for MYI (Hvidegaard and Forsberg, 2002; Lüthje et al., 2006). Snow cover is absent and no melt water is assumed at the initial time (i.e. $w(\boldsymbol{x}, t_0) = 0\ \forall \boldsymbol{x}$). A visualization of the distribution of ponds corresponding to day 20 from the beginning of the simulation is shown in figure 8.7.

In order to extract quantitative statistical informations on the melt pond coverage of the sea ice, one need to be able to identify individual ponds. To do this, for each time t we define a pond as any connected subset of points on the lattice such that $w(\mathbf{x}, t) > 0$. The

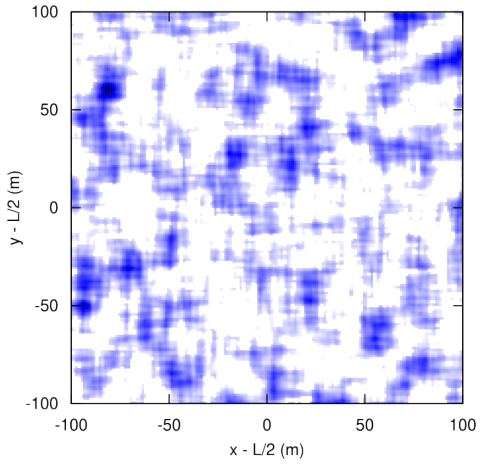
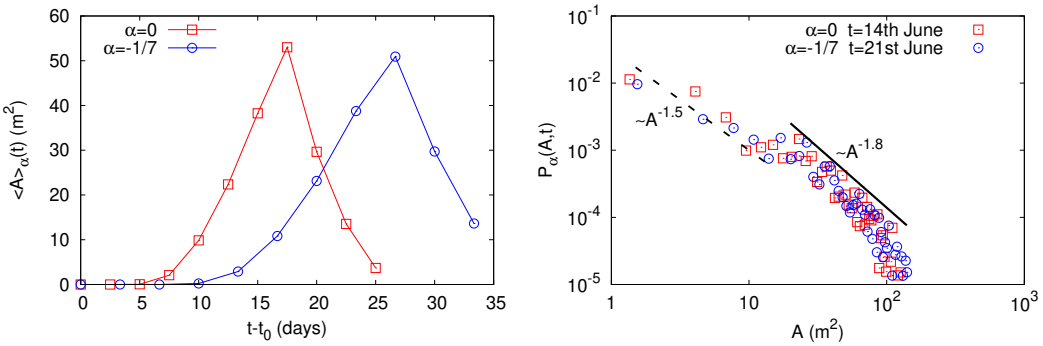


FIGURE 8.7: Configuration of the depth field $w(\mathbf{x}, t)$ showing the melt ponds distribution over the sea ice surface, for FYI after 20 simulated days (a $200 \times 200\ m^2$ region at the centre of the simulated domain is taken). White color corresponds to bare ice and blue color indicates the presence of a pond, the darker the blue the deeper the pond (deepest ponds have $w \simeq 2\ m$).

full pond configuration is determined by a cluster analysis (for which we employ the so called Hoshen-Kopelman algorithm Hoshen and Kopelman, 1976) over the whole system. The area of the i-th pond is then $A_i = n_i \Delta_x \Delta_y$, n_i being the number of points in the i-th cluster.

8.2.2 Sensitivity to turbulent heat flux scaling



(a) (b)

FIGURE 8.8: (a) Mean pond area vs time for the $1/3$ (red squares) and $2/7$ (blue circles) laws. (b) PDFs of pond areas after 13 days, for $\alpha = 0$, and 20 days, for $\alpha = -1/7$. Notice that the two sets of points basically overlap. The dashed and solid lines correspond to the power law $A^{1.5}$ and $A^{1.8}$, respectively.

In Figure 8.8(a) we show the time evolution of the mean pond area:

$$\langle A \rangle_\alpha(t) = \frac{1}{N(t)} \sum_{i=1}^{N(t)} A_i(t) \tag{8.10}$$

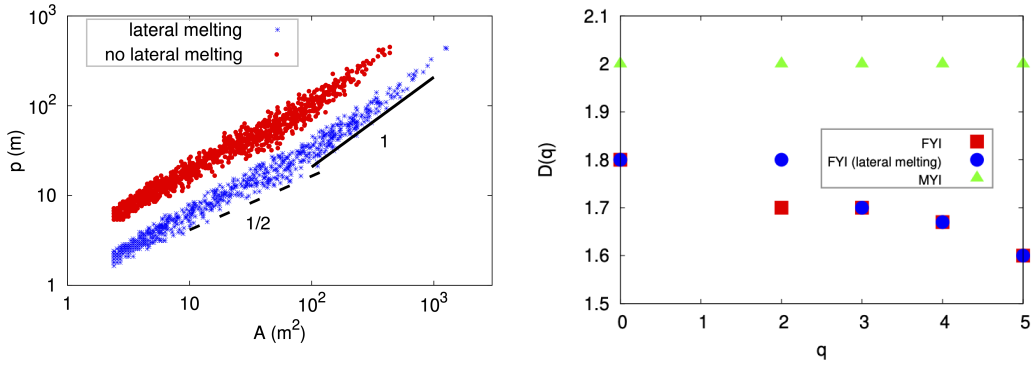
(where $N(t)$ is the total of ponds detected at time t) for FYI and assuming Malkus ($1/3$) and anomalous ($2/7$) scaling for the turbulent heat flux, respectively, that is, with reference to Eq. 8.9, with $\alpha = 3c - 1 = 0$ (red squares, equivalent to the study in Lüthje et al., 2006) and $\alpha = -1/7$ (blue circles). We observe that the pond area grows and reaches a maximum faster when $\alpha = 0$: after 13 days, e.g., the $2/7$-model gives a prediction for the mean pond area approximately seven times smaller than it is for the constant flux case. If we consider PDFs with *equal mean*, instead of *equal time* PDFs, interestingly, the two sets of points (for $\alpha = 0$ and $\alpha = -1/7$) collapse onto each other, as shown in Fig. 8.8(b). There we plot $P_{\alpha=0}(A, t_1)$ and $P_{\alpha=-1/7}(A, t_2)$, where t_1 and t_2 are such that $\langle A\rangle_{\alpha=0}(t_1) = \langle A\rangle_{\alpha=-1/7}(t_2)$; with reference to Fig. 8.8(a), this occurs, for instance, if we pick $t_1 - t_0 = 13$ days and $t_2 - t_0 = 20$ days, i.e. on June 14th for $\alpha = 0$ and June 21st for $\alpha = -1/7$. The two PDFs nicely follow the scaling $P_\alpha(A) \sim A^{1.5}$ for relatively small areas ($A < 20\,\mathrm{m}^2$), with a steeper fall-off for larger values, $P_\alpha(A) \sim A^{1.8}$. Such functional forms agreed with available observational data, as those collected by means of aerial photography during the SHEBA and HOTRAX campaigns (Perovich et al., 2002b).

In summary our simulations of the pond network model system showed that a minimal variation of the scaling exponent of the turbulent heat flux within the pond impacts the time evolution of the mean pond size (shifting the maximum by approximately a week), hence of the average melting rate. We emphasize that our assumption—namely, that the melt rate in ponds deeper than w_{max} decreases weakly with water layer depth, rather than remaining constant as is commonly assumed in the geophysical literature—is supported by an extensive body of work on turbulent heat transfer in RB-like systems. Therefore, our study suggested that a thorough knowledge and parametrization of melt pond hydrodynamics is needed in order to not get wrong estimates of observables of climatological relevance.
We also highlight a second striking aspect of this system: the area distribution of melt ponds is remarkably insensitive to variations in physical parameters governing their dynamics (such as the heat flux across the pond). This robustness is so pronounced that even simple models lacking an explicit representation of melt pond formation and evolution can reproduce these statistical fingerprints (see Ma et al., 2019; Popović et al., 2018). We will focus, then, on an aspect of melt pond configuration that one might expect to be affected by details of the evolution, namely their morphology.

8.2.3 Robustness of pond geometry

Characterizing the morphology of the global ponds configuration and understanding how it emerges can be of great relevance also for large (global) scale models of sea ice. In fact, the perimeter p and area A of a multi-pond configuration are related by $p \sim A^{d_\mathrm{p}/2}$, where d_p is the so called perimeter fractal dimension: for a smooth curve $d_\mathrm{p} = 1$, while for a fractal, in the strict sense, $d_\mathrm{p} > 1$. It was observed that surfaces of small ponds tend to be of roundish shape, while large ones, that typically stem from aggregation of several small ponds, display features of clusters in percolating systems and appear fractal-like (Hohenger et al., 2012). This transition to a fractal geometry is supposedly connected with the way melt ponds grow over the sea ice surface. It is natural to ask, then, whether the explicit modelling of the physical mechanisms leading to such in-plane growth has any impact on the final global morphology. To this aim, we ran the same simulation, for the FYI, with

and without the lateral melting term ϕ_2 (see Scagliarini et al., 2020 for a description of this term). Switching on the lateral melting, that was previously kept disabled, has the potential to increase the pond area, but what is more important is that being non-local (it depends on the gradients of w and w), it has the potential to affect the pond shapes.



(a) (b)

FIGURE 8.9: (a) Scatter plot of perimeter (p) and area (A) for all melt ponds on 21st June. The dashed and solid lines indicate the power law $A^{1/2}$ and A, corresponding to perimeter fractal dimensions $d_{\mathrm{p}} = 1$ (smooth shapes) and $d_{\mathrm{p}} = 2$ (fractal), respectively; the transition between the two regimes occur at $A \approx 100\,\mathrm{m}^2$. Symbols relative to the two data sets are shifted from each other by a factor 3 for the sake of clarity, otherwise they would overlap. (b) Generalized fractal (or Renyi's) dimensions for the melt pond distribution after 70 days from three simulations. FYI without lateral melting (red squares), FYI without lateral melting (blue dots) and MYI without lateral melting (green triangles).

Figure 8.9(a) illustrates that the two power laws, $p \sim A^{1/2}$, for $A < A_{\mathrm{c}}$, and $p \sim A$, for $A > A_{\mathrm{c}}$, are reasonably well followed in both cases (note that the symbols of the two data sets are shifted from each other by a factor 3 for the sake of clarity, otherwise they would overlap). The only minor effect of the presence of lateral melting seems to be a slightly clearer scaling behaviour, especially for large A (in the fractal regime). The transition to the fractal geometry occurs at $A_{\mathrm{c}} \approx 100\,\mathrm{m}^2$, in agreement with the observations (Hohengger et al., 2012). Lateral melting ($\chi = 1$) enhances the fractal characteristics of the large pool without altering the scaling law.

To get a deeper insight on the geometrical configuration of melt ponds in our model, we also performed an analysis of the *generalized fractal dimensions* (GFD), $D(q)$ (Grassberger, 1993), which provide a more detailed description of the geometry of the fractal manifold. Let us call $\mu_i(\varepsilon)$ the measure of ponds within the i-th element of a regular tessellation of the domain in squares of side ε (i.e. the fractional area of the ε-square occupied by meltwater), and $N(\varepsilon)$ the total number of squares into which the domain is partitioned; we can then define the following quantity:

$$I(q,\varepsilon) = \frac{1}{1-q} \log \left(\sum_{i=1}^{N(\varepsilon)} \mu_i(\varepsilon)^q \right), \tag{8.11}$$

for any positive $q \neq 1$. The GFD are then computed as:

$$D(q) = \lim_{\varepsilon \to 0} \frac{I(q,\varepsilon)}{\log(1/\varepsilon)}; \tag{8.12}$$

for $q = 0$, $I(0, \varepsilon)$ equals the number of non-void elements of the tessellation, therefore $D(q = 0) \equiv D_0$ coincides with the Haussdorf, or box-counting, dimension, which is an estimate of the fractal dimension of the set. It is clear, then, in which sense the $D(q)$ are generalized fractal dimensions. In Fig. 8.9(b) we show the $D(q)$ computed from numerical data from three simulations, namely: FYI without lateral melting, FYI with lateral melting and MYI. The plot tells us that melt ponds on FYI lay on a fractal manifold, as suggested also by the perimeter-area relation, since $D_0 < 2$, whereas those on MYI do not $D(q) = 2 \; \forall q$; however, we observe a modest decrease of $D(q)$ with q, indicating a weak multifractality, with very minor (if any) differences between the run with lateral melting and the one without.

In summary, statistical and geometrical properties of the melt pond system, such as the probability distribution function of pond surface areas and fractal dimensions, appeared to be robust against heat flux scaling variations as well as against the inclusion or not of an explicit modelling of lateral melting inside the pond. In particular, our results agreed well with observation for what concerns the power law decay of the PDFs and the perimeter-area relation, and the corresponding perimeter fractal dimension, for ponds.

Finally, extending the analysis of melt pond geometry to generalized fractal dimensions revealed that melt ponds on first-year ice exhibit weak multifractality, whereas those on multi-year ice are essentially smooth. This also implies a sensitivity to the initial ice topography, as the first-year ice (FYI) and multi-year ice (MYI) simulations are initialized differently. These findings suggest that it would be of considerable interest to initialize the numerical model with more realistic conditions, for example using topographies derived from field measurements.

This concludes my brief exploration of large-scale geophysical modelling. In the following chapters, our focus will shift back to small-scale processes that have so far been neglected. In particular, the next chapter examines the effects associated with the density anomaly of freshwater.

Chapter 9

Convective Freezing & Melting in Water

In the previous chapter, although we discussed about ice, we deliberately omitted a peculiar property of the equation of state of water that can become important whenever the temperature range involved extends beyond the interval between 0 and $4\,^{\circ}\mathrm{C}$. Indeed, for water the relationship between mass density and temperature is non-linear (see Figure 9.1). As a consequence, the thermal expansion coefficient of liquid water (defined as $\beta_T = -\rho^{-1}\,(\partial\rho/\partial T)$) changes sign at a temperature of approximately $4\,^{\circ}\mathrm{C}$, where the density is maximal. This, in turn, affects the buoyancy force, which also reverses sign at this temperature.

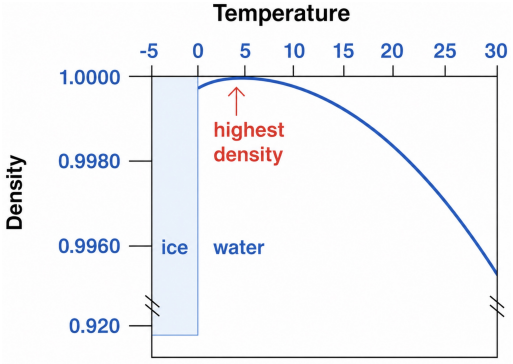


FIGURE 9.1: Density vs. temperature in pure water at atmospheric pressure.

The studies presented in this chapter focus on the dynamical consequences of this physical property. As we shall see, these implications are far from being trivial, primarily because of the interplay among the various nonlinearities involved.

Unlike the previous chapter, however, this one presents work that combines experimental investigations with numerical studies. These experiments were motivated by the need to validate the numerical modelizations against measurable phenomena under controlled laboratory conditions. They were carried out within the research group of Chao Sun at Tsinghua University in Beijing, with whom I had the pleasure of collaborating. This offered me the opportunity to closely follow the work of few PhD students, including Ziqi Wang and Yihong Du, which gave major contributions to the studies here presented.

This chapter is based on:

1. *How the growth of ice depends on the fluid dynamics underneath*, Z. Wang, E. Calzavarini, C. Sun, F. Toschi, PNAS March 9, 2021 118 (10) e2012870118 [PDF]
2. *Ice front shaping by upward convective current*, Z. Wang, L. Jiang, Y. Du, Chao Sun, E. Calzavarini Phys. Rev. Fluids 6, L091501(2021) [PDF]
3. *Equilibrium states of the ice-water front in a differentially heated rectangular cell*, Ziqi Wang, Enrico Calzavarini and Chao Sun, Europhys. Lett. (EPL), 135 (2021) 54001 [PDF]

Our investigations focussed primarily on the freezing process because, from an experimental perspective, a freezing system is considerably more reproducible and easier to control than a melting one. This is mainly due to the difficulty of producing homogeneous ice samples free from inclusions such as trapped air bubbles. Nevertheless, throughout this chapter I will also tackle the differences between the processes of freezing and melting, particularly in what concerns the equilibrium states reached in convection cells.

9.1 Convective freezing in freshwater

As in the previous study, our objective is to investigate an idealized system that provides a high degree of control over both the material properties of the fluid and its boundary conditions. To this end, we again consider the classical Rayleigh–Bénard (RB) convection cell, this time with an upper boundary maintained at the freezing temperature. This configuration can be realized experimentally as well as studied numerically by means of fully resolved simulations.

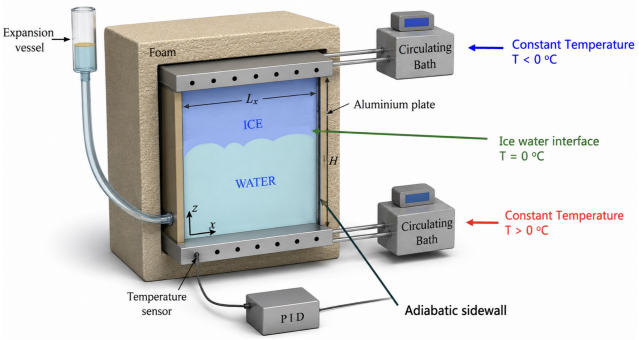


FIGURE 9.2: Sketch of the experiment.

Experiments

In the study here presented, we consider a cuboidal cell with a reduced lateral dimension, characterized by aspect ratios ($\Gamma_x = L_x/H = 1$) and ($\Gamma_y = L_y/H = 1/4$), where (L_x, H, L_y) denote the cell width, height and lateral depth, respectively. The large square vertical sides are transparent to allow optical inspection as shown in the sketch in Figure 9.2. The cell is filled with water, that has been filtered, deionized and degassed. The system is heated from below and cooled from above and thermally insulated on the sides thorough an active control system. The top plate temperature, T_t, and bottom plate temperature, T_b, are imposed by two water-circulating baths, with $T_\mathrm{t} < T_M$ and $T_\mathrm{b} > T_M$ ($T_M = 0°\mathrm{C}$ is the water freezing point). In such a configuration, ice starts forming from the top plate, and it grows till a saturation thickness that defines the ice equilibrium state for the given control conditions. Below the ice layer, thermal convection can occur or not, depending on the thermal forcing conditions imposed at the bottom. The phase change from liquid to ice is accompanied by a change in density, in order to compensate for the overpressure that this would create in the system an expansion vessel is added in the experiment (to avoid evaporation from the vessel a thin silicone oil layer is deposed on water surface). The level of liquid in the expansion vessel can be used to estimate the total amount of ice present in the system. A more precise and also local measurement is possible through images taken from a camera monitoring the system and positioned on its front side (see Fig. 9.3(A) for a typical view).

Simulations

In addition to the experiments, the numerical simulations are carried out using an adapted

version of the code developed for convective melting (based on the lattice Boltzmann (LB) method both for the liquid and the temperature and on an iterative enthalpy formulation for the phase-change processes (Rabbanipour Esfahani et al., 2018)). The specific adaptations concerned the following aspects.
First, we considered the effect of the density anomaly on the buoyancy force. The water density near to its maximum at temperature, $T_c = 4^o\ C$, is well approximated by the expression $\rho = \rho_0(1 - \beta_T^*|T - T_c|^q)$, where β_T^* is not the usual thermal expansion coefficient but has units of K^{-q} with $q = 1.895$ and $\beta_T^* = 9.30 \times 10^{-6}(K^{-q})$. This equation gives the maximum density of water $\rho_0 = 999.972\ \mathrm{kg/m^3}$ at $T = T_c$ (Gebhart and Mollendorf, 1977).
Second, we consider that water and ice have different thermal conductivities (the one of ice being ~ 4 times bigger) and specific heat capacities (for ice being half of the one of water). This implies that we need to properly account for the conjugate heat transfer between the two phases. This is done with careful modifications of the LB method according to (Chen et al., 2017; Faden et al., 2019) (Full details on the methods are available in (Wang et al., 2021b) supplementary materials). For simplicity we neglect the volume expansion of ice as compared to water. This assumption is consistent with the experimental setup which is open through the tiny tube connecting the cell to the expansion vessel so that the variations in its volume are not supposed to affect the global circulation dynamics inside the system. We also do not account for the Gibbs-Thomson effect, assuming that the curvature of the ice front is weak so the impact of this term is negligible. Both two-dimensional ($\Gamma_x = L_x/H = 1$, $\Gamma_y = 0$) and three-dimensional simulations (of the same dimensions as the experimental cell) were conducted, with boundary conditions: no-slip for the velocity, adiabatic at the sidewalls, and constant temperatures at the top and bottom plates. A visualization of the temperature field and ice interface shape obtained from the simulations is reported in Fig. 9.3(B).

Both in the experiments and the simulations the initial condition were set to be still fluid at a uniform temperature equal to the one of the bottom wall, $T_b > T_M$. The top temperature was fixed at $T_t = -10°C$. Considering the thermal gap in the ice, $\Delta T = T_b - T_M = 10°C$, this leads to a Stefan number $St = c_{p,ice}\Delta T/\mathcal{L} \simeq 0.063$ meaning that the latent heat released upon solidification is about 16 times larger than the sensible heat required to cool the newly formed ice from $0 \circ C$ to $-10°C$. The bottom plate temperature, T_b, was varied through separate experimental runs in the range $3.8°C \leq T_b \leq 8°C$ in experiments and $0.5°C \leq T_b \leq 15°C$ in simulations. The temperature T_b is clearly linked to the thermal forcing of the system, the gap across the liquid is in fact connected to the effective Rayleigh number of the process (although with some complexities that we will mention later).

9.1.1 Equilibrium ice thickness

We first focused on the asymptotic state reached by the system, and in particular on the equilibrium mean ice-thickness. The measurements obtained from both the experiments and the numerical simulations are reported in Fig. 9.3(C). The figure shows the final liquid layer height as a function of the (hot) bottom temperature T_b. There is a good agreement between the experiments and the simulations, both in three and two dimensions, indicating that, with respect to this global observable, the experimental system behaves essentially as a quasi-two-dimensional system.

The same figure also reports theoretical predictions obtained from a reduced one-dimensional (or integral) model. This model represents the system as a sequence of layers, each characterized by a specific heat-transfer mechanism (conduction or convection) and a corresponding heat-transfer intensity. The equilibrium state is determined by requiring that the heat flux be constant across all layers.

The model assumes that heat transfer through the ice occurs exclusively by conduction, consistent with a compact solid ice layer, whereas heat transfer within the liquid can occur either by conduction or by convection depending on whether the thermal stratification is stable or unstable. A key ingredient of the model is an accurate parameterization of the buoyancy force, which is directly linked to the density anomaly of water. As shown in the figure, for the temperature range considered here it is not possible to assume a linear dependence of buoyancy on temperature, as is commonly done under the Boussinesq approximation. The model is robust because it relies on well-established parameterizations of heat transport in Rayleigh–Bénard convection, namely the scaling relationship between the Nusselt and Rayleigh numbers (Ahlers et al., 2009).

Four dynamical regimes

Looking again at Figure 9.3(C), one observes that a pronounced change in the equilibrium state occurs for a bottom temperature of approximately $5°$C. This transition is associated with the onset of convection in the liquid layer, replacing the purely conductive heat-transfer regime. Because convective heat transport is much more efficient than conduction, the transition results in a substantial reduction of the equilibrium ice thickness.

However, the liquid layer in this configuration does not exhibit only two possible states. Instead, our numerical simulations reveal the existence of up to four distinct flow regimes, as illustrated in Fig. 9.4 (see in particular panels III). Beneath the growing ice layer, the liquid in the temperature interval between $0°$C at the ice–water interface and $4°$C, corresponding to the temperature of maximum density of water, is stably stratified, thereby suppressing convection. In contrast, the liquid below the $4°$C isotherm, extending down to the heated bottom boundary, is unstably stratified and behaves as in a classical RB system.

When the below unstable liquid layer becomes convective while the upper stable layer is continuously perturbed by turbulent entrainment from below, the resulting flow configuration is known as *penetrative convection*. As the convective intensity in the lower layer increases, the upper stable layer becomes progressively thinner and may nearly disappear. This behavior is clearly visible from the $T = 4°$C isotherm, which marks the boundary between the stable and unstable layers. The convective motions beneath the ice also affect the morphology of the ice–water interface, which departs from planarity only once convection becomes sufficiently vigorous. Figure 9.5 shows the relation between the 4 different heat transfer regimes and the equilibrium state of the system.

This phenomenology may also be relevant to environmental systems such as ice-covered lakes. In fact, the convection beneath the ice can produce spatial variations in freezing and melting rates, leading to local variations in ice thickness. Such thinner regions may provide preferential locations for the onset of ice breakup.

Temporal dynamics

We have described the variety of heat transfer regimes that can arise in the system at equilibrium. It is then natural to ask how the system evolves dynamically. How fast does the

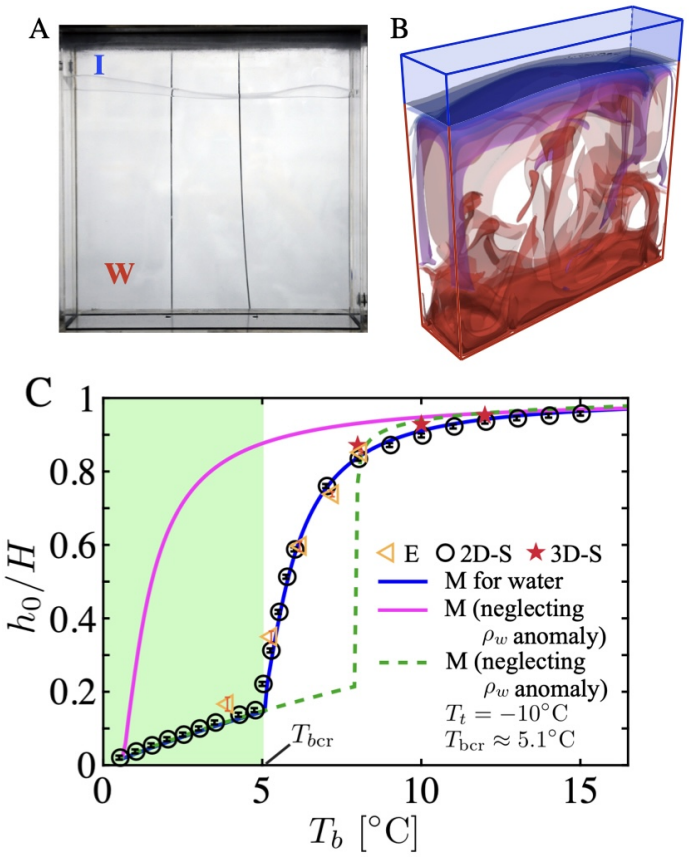


FIGURE 9.3: (a) Picture of the experiment with the visible corrugated ice (I) - water (W) interface. (b) Visualization of the temperature field across the numerical domain at the statistical equilibrium state (3D simulation for $T_{\rm b} = 8\,^{\circ}$C and $T_{\rm t} = -10\,^{\circ}$C). The blue-colored domain is in the ice region. The ice-water interface is drawn in dark blue. (c) Spatially-averaged water-layer height (h_0) from the experiments "E" (triangles), the "2D-S" (circles) and '3D-S" (stars) simulations, as well as the 1D theoretical model (lines). Model predictions for water (blue line) with considering water density anomaly at $T_{\rm c}$; (violet line) without considering water density anomaly at $T_{\rm c}$; (green dashed line) without considering water density anomaly at $T_{\rm c}$, and the thermal expansion coefficient α is a function of temperature, which is evaluated at the mean temperature $T_{\rm mean}$ of the water region for each bottom plate temperature $T_{\rm b}$, which is $T_{\rm mean} = (T_{\rm b} + T_{\phi})/2$. The green-shaded area shows the temperature range corresponding to the diffusive regime of the system (i.e. no detectable fluid motion in the liquid layer). $T_{\rm bcr}$ is the critical bottom plate temperature ($T_{\rm bcr} \approx 5.1\,^{\circ}$C from the 1D model) above which the system ends up in a convective state.

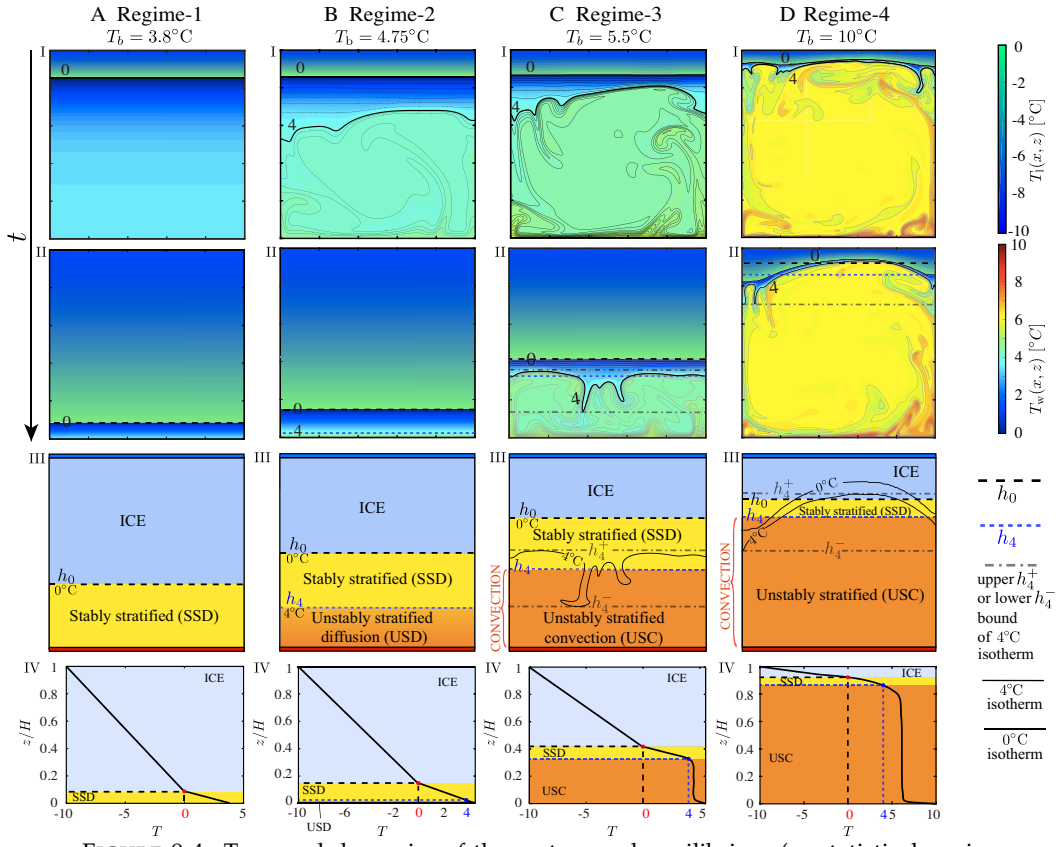


FIGURE 9.4: Temporal dynamics of the system and equilibrium (or statistical equilibrium) states for selected values of the bottom temperature. Four possible different regimes are identified. Regime 1: Stably Stratified Diffusion (SSD) with flat ice ($T_b \leq T_c$); Regime 2: SSD + Unstably Stratified Diffusion (USD) with flat ice ($T_c < T_b \leq 5.1°C$); Regime 3: SSD + Unstably Stratified Convection (USC) with flat ice ($5.1°C < T_b \leq 6.9°C$); Regime 4: SSD + USC with a deformed ice front ($T_b > 6.9°C$). The isolines of temperature at $T_M = 0°C$ and $T_c = 4°C$ are also shown. In the bottom panels (IV) the measured equilibrium mean temperature profiles are traced.

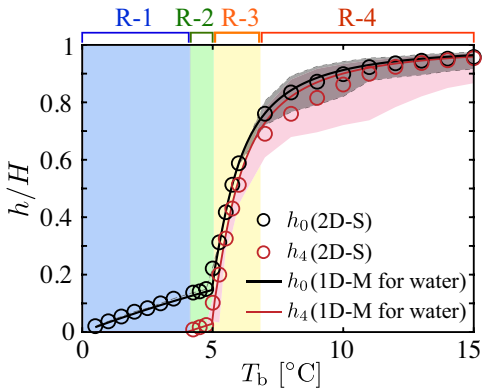


FIGURE 9.5: Mean water-layer height h_0 (black) and mean maximal fluid density height h_4 (red) from simulations (symbols) and 1D model (lines); shaded areas (gray and red) indicating their spatial fluctuations in the simulations.Depending on the bottom temperature value different system regimes (R-1 to R-4) occur, they are indicated with different shaded area colors.

ice front advance? Does it come to a halt abruptly or gradually? And how does convection evolve during this process? These questions can be addressed through numerical simulations and experiments.

As can already be seen from the flow visualizations in Figure 9.4(I, II), the character of the heat transfer regime may change over time. For example, the system may initially be in a convective state and subsequently transition to a purely conductive regime as the water layer becomes thinner and the corresponding Rayleigh number decreases below the critical threshold for the onset of convection (this specifically occurs in the case denoted as Regime 2).

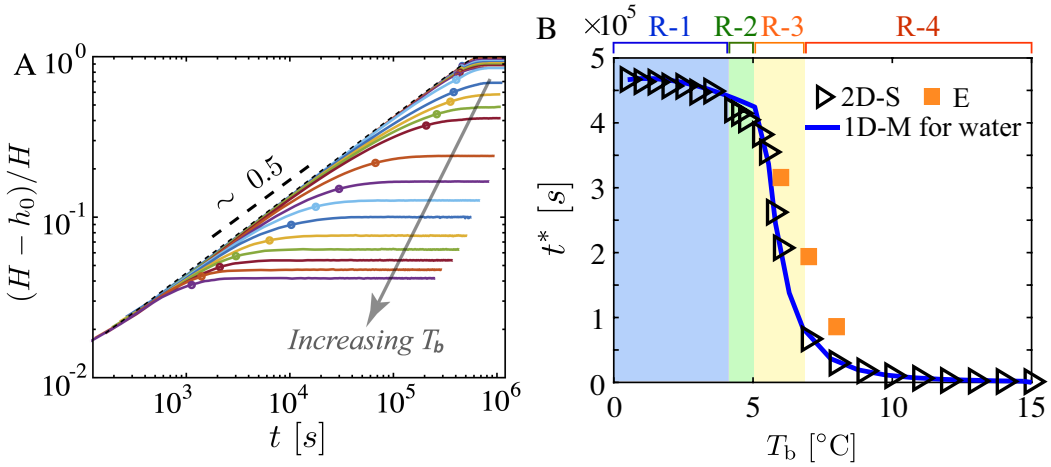


FIGURE 9.6: (A) Time evolution of the normalized mean ice thickness $(H - h_0/H)$ (where h_0 is the ice of the water layer) for different bottom temperatures, T_b. The top-plate temperature is fixed at ($T_t = -10°C$), while ($0.5°C \leq T_b \leq 15°C$). The circles denote the saturation time,t^*, defined as the time at which the ice thickness reaches 90% of its equilibrium value. (B) Saturation time as a function of T_b. The blue-, green-, and yellow-shaded regions correspond to equilibrium regimes R-1 to R-4 as in Fig. 9.4.

The simulations show that, during the early stages, the mean ice-layer height growth is diffusion-controlled, following the scaling $\propto t^{0.5}$. At later times, however, the growth rate progressively decreases until the ice thickness eventually saturates (see Fig. 9.6A) .

Because it is difficult to precisely identify the saturation time, we define a proxy of it, t^*, as the time required for the ice thickness to reach 90% of its equilibrium value. The measured t^* (our nominal saturation time) as a function of the bottom-plate temperature, is fully consitent between simulations and experiments, providing further validation of the assumptions and modelling approach adopted in the DNS (see Fig. 9.6*B*). Moreover, the same figure shows that a transient in time extension of the 1D multilayer theoretical model accurately predicts the evolution of the system (see Wang et al., 2021b for more details). Overall, these results indicate that, in the present configuration, the detailed shape of the ice front has little influence on the global behaviour of the system. A properly parametrized 1D (i.e. integral) model can describe both the evolution of the system and its equilibrium.

On the other hand if one is interested to the precise ice front topography, the 1D model is not enough and DNS reveals essential. Our simulations as well as the experiment clearly show that at best one single dome structure form in the system. This is interpreted as the imprint of the large circulation motion in the cell. This is clearly related to the fact that

the cell we considered has an aspect ratio $\Gamma = 1$, and in this condition, just one large-scale circulating motion is expected (Sugiyama et al., 2009).

9.2 Effects of inclination and container aspect ratio

We have seen that the density anomaly does not appear to have a significant effect on the shape of the ice–liquid interface in the Rayleigh–Bénard (RB) cell. Here too, weakly curved, dome-shaped structures emerge as a consequence of the imprint of the large-scale circulation roll, in close analogy with what is observed in the CM system with linear buoyancy. This situation changes, however, when considering a slightly different but closely related system, namely the so-called vertical convection (VC) configuration. This consists of the same RB cell rotated by 90°, so that the hot and cold isothermal walls are oriented vertically.

The VC system is always dynamically unstable because the temperature gradient is horizontal. Under ordinary conditions, in a fluid without a density anomaly, or in water at temperatures close to ambient ($\simeq 20°\mathrm{C}$), the flow is dominated by a large-scale circulation: warm, lighter fluid rises along the heated wall, while cooler fluid descends along the cold wall. In contrast, for a fluid exhibiting a density anomaly (such as water) with wall temperatures straddling the temperature of maximum density, two competing convective rolls develop. One is the “normal" circulation, in which warm, lighter water rises, while the other is the “anomalous" circulation, in which cold, lighter water also rises.

This remains true even when the cold wall is maintained below the freezing temperature, causing an ice layer to form on its surface. What shape should we then expect for the ice–liquid interface under these conditions?

To answer this question, we carried out both experimental and numerical investigations under conditions very similar to those considered previously. The cold temperature wall was maintained as before fixed at $T_b = -10°C$, while the hot one was set at different values $T_t = 6, 10, 12°C$ in different experimental and numerical runs. Our main findings are summarized in Figure 9.7.

9.2.1 Ice front shaping by upward convective current

First we observe that numerics show good agreement with the experimental measurements in Fig. 9.7. Second we remark that the ice front morphology displays an intriguing change as T_b increases. The system transits from a situation where the ice is thicker at the top due to the anomalous circulation roll (we called this mechanism ice front shaping by upward convective current (Wang et al., 2021c)), to a situation where two rolls compete. In the latter case, the ice thickness is non-monotonous with height. On the opposite for very large driving temperatures, the ice layer profile thickness is expected to revert, and maximal ice thickness will occur at the bottom (as in the case of a fluid without density anomaly). This phenomenology is also expected to occur in nature in freshwater systems or weakly salty waters (as in salty water, the anomaly vanishes), particularly in ice shelves or in floating blocks of ice.

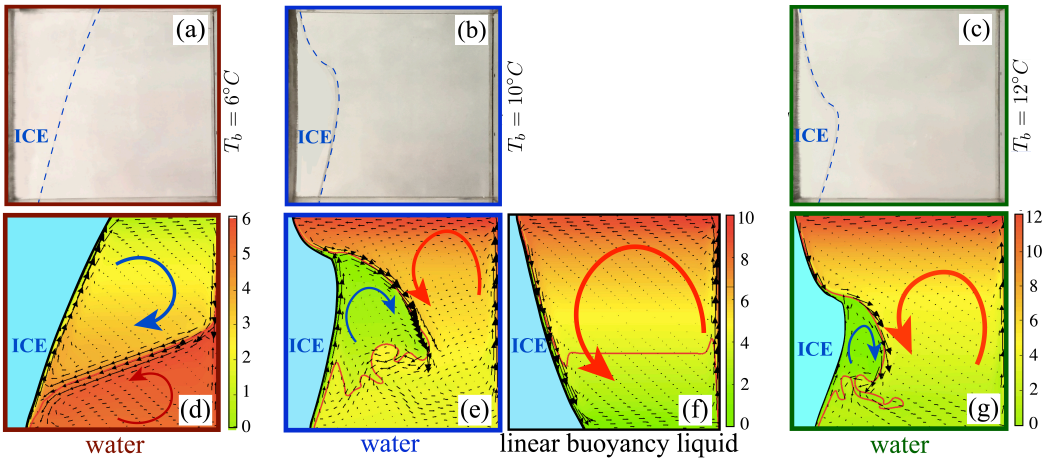


FIGURE 9.7: Equilibrium state in VC system from experiments (a-c), and simulations (d-g) for different heating conditions: $T_\mathrm{b} = 6°\mathrm{C}$ (a, d), $10°\mathrm{C}$ (b, e, f), $12°\mathrm{C}$ (c, g). Panel (f) is from simulations but does not consider the density anomaly. (d-g) Temperature fields are represented in color, $0°\mathrm{C}$ (black line) and $4°\mathrm{C}$ (red line) isotherms, and velocity vectors (black arrows). The colored arrows in blue/red show the orientation of large scale convective rolls, denoting respectively the ascending cold/warm water.

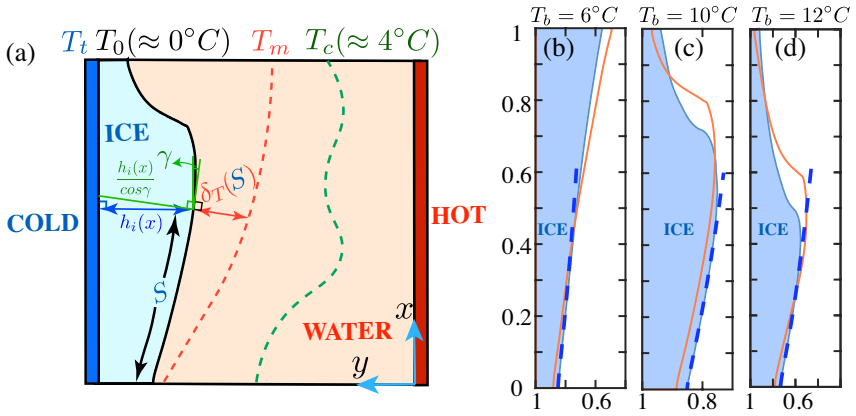


FIGURE 9.8: (a) Sketch of the boundary-layer model for ice front morphology in VC: The ice front at $T_0 = 0°\mathrm{C}$ (black line), the T_m isotherm which is the outer edge of the thermal boundary (red dashed line), and the T_c maximal density isotherm (green dashed line). The angle between the tangent to the ice front and the x direction is γ; the thickness normal to the ice front (green thick line in the ice) is $h_i(x)/\cos\gamma$ (with $\cos\gamma = dS/dx$). (b-d) Comparison of ice front shapes from experiments (light blue shaded area), simulations (orange line), and the model (dashed line) for different T_b.

A theoretical prediction of the shape of the ice–water interface in the VC system proves to be complex. It is necessary, in fact, to take into account the effects of the flow two-dimensionality and the presence of thermal boundary layers on the ice surface. A phenomenological model based on these minimal features allows to predict only some of the observed characteristics. The conceptual sketch of the model (proposed in (Wang et al., 2021c)) is shown in Fig. 9.8(a). We introduced a curvilinear coordinate, S, measuring the length of the ice front starting from its boundary point at the $x = 0$ position, which is linked to the local ice thickness by the arclength formula $S(x) = \int_0^x \sqrt{1 + [\frac{d(h_i(\xi))}{d\xi}]^2}\, d\xi$. We then expressed heat flux balance in the direction normal to the ice surface as:

$$k_i \frac{(T_0 - T_\mathrm{t})}{h_i(x)\frac{dS(x)}{dx}} = k_w \frac{(T_\mathrm{m} - T_0)}{\delta_T[S(x)]}, \tag{9.1}$$

where k_w and k_i are the thermal conductivity of water and ice, $(T_0 - T_\mathrm{t})$ is the temperature difference in the ice, and $h_i(x)\frac{dS(x)}{dx}$ is the ice thickness in the direction normal to the ice front. Here $T_\mathrm{m} = (T_0 + T_\mathrm{c})/2$ and the boundary layer thickness $\delta_T(S)$ is assumed to vary along the ice front, as in a developing vertical thermal boundary layer, with a dependence that we take to be $\delta_T(S) = C_1(S + C_2)^{1/4}$ (Bejan, 2013; Shishkina, 2016; White and Corfield, 2006).

Fig. 9.8(b-d) shows the comparison of the model prediction with experiments and simulations. A qualitative agreement is reached in the region where the upward convective current takes place. The disagreement in the upper part of the ice front is expected as the boundary layer no longer develops in that region due to the downward warmer convective current. Although the exact spatial dependence of δ_T along the ice interface is not known, the model pinpoints to the physical mechanism leading to the observed phenomenon.

We also explored systems intermediate between RB and VC and even upside-down RB cells (see figure 9.9), but here I will not enter in the detail of the phenomenology of these configurations (Wang et al., 2021c).

9.2.2 Effects of aspect ratio

We have seen that, in the case of vertical convection, the effects associated with the anomalous buoyancy force can have a significant impact on the morphology of the ice. So far, however, all these results have been obtained in a cell with unit aspect ratio. How does the situation change when the aspect ratio of the container is varied?

This question was investigated in (Wang et al., 2021a) and our main results are summarized in Figure 9.10. There, side-by-side experiments and numerical simulations reveal that, in the RB configuration, the large-scale convective structures—which have an approximate aspect ratio of unity—govern the shape of the ice–water interface. This is particularly evident in the "vertical" cells with aspect ratio $\Gamma = L_x/H < 1$, where two or more such convection rolls are stacked one above the other, and the curvature of the ice interface is directly connected to the upper cell. An analogous behavior is observed in the more horizontally extended cells ($\Gamma > 1$), where the curvature of the dome-shaped ice structures remains essentially unchanged even when the aspect ratio is doubled or quadrupled. We note that the position of the thinner ice depends on whether a hot plume is impacting it. In the DNS,

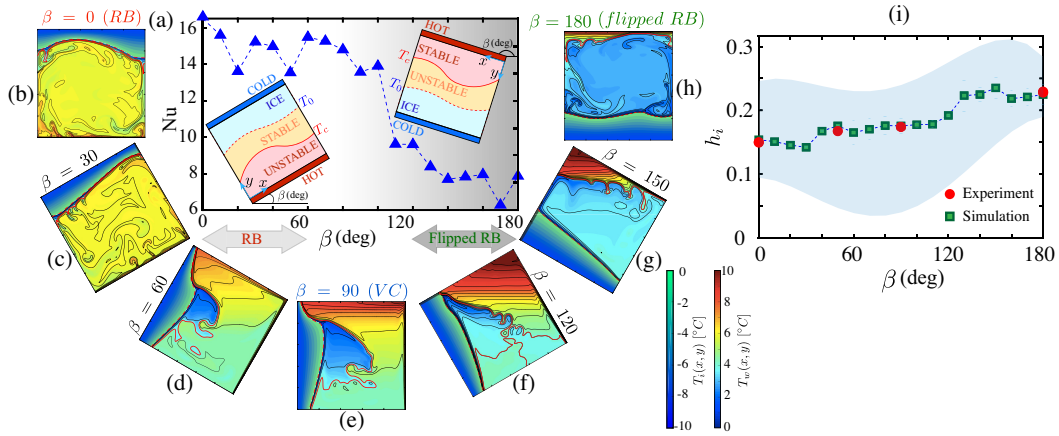


FIGURE 9.9: (a) Nusselt number Nu as a function of the inclination angle β, from RB to VC to flipped RB. The error bars (estimated based on the temporal time series of Nu in one simulation) are smaller than the symbols. (b-h) Instantaneous temperature field in ice, $T_i(x, y)$, and water, $T_w(x, y)$, and isotherms (black thin lines) at the equilibrium state for different angles $\beta = [0, 180]$. The red dashed line and red thick line in panels (b-h) are 0 and 4°C isotherms, respectively. (i) Global ice thickness h_i as a function of β. The shaded area shows the spatial variation of $h_i(x)$ in the simulations. For all caes $T_\mathrm{b} = 10°\mathrm{C}$ and $T_\mathrm{t} = -10°\mathrm{C}$.

we observe two equally possible (i.e. degenerate) configurations depending on the rotation direction of the main circulation rolls, so that the maximal ice local thickness can be shift horizontally of half a wave-length. This does not occur in the experiments, probably due to weak non-adiabatic effects of the lateral walls (i.e. heat leakage). Furthermore for $\Gamma > 1$ we observe a perfect saturation of the relative global ice content (H_i).

In the case of vertical convection, under conditions where the two counter-rotating rolls compete, the change of shape towards vertically elongate cells appears to promote ice growth. There H_i more than double passing from 1/4 to 2 aspect ratio cells (note that for the definition of Γ we keep the same convention as for RB). However, this quickly saturates for aspect ratios 2. (Fig. 9.10(c)).

Overall, despite the significant changes in the flow patterns induced by varying the aspect ratio over the range $\Gamma = [1/4, 4]$, the total ice content at equilibrium remains largely unchanged.

9.2.3 Bistability

This brief section addresses a question that has so far been left aside. Throughout this chapter, we have focused on the freezing process, whereas in the previous chapter we investigated melting (albeit under simpler conditions, without the density inversion). A natural question is whether these two processes lead to the same final state in the convective cell. Specifically, does starting from an initially isothermal liquid at the lower-wall temperature in the Rayleigh–Bénard system, or from a block of ice at the temperature of the upper wall, result in the same final equilibrium state?

Bistability phenomena in phase-change Rayleigh–Bénard-type convective systems have already been reported in the literature. Purseed et al., 2020 investigated the case of a fluid with positive buoyancy in RB with a top melting boundary, while Yang et al., 2023a studied

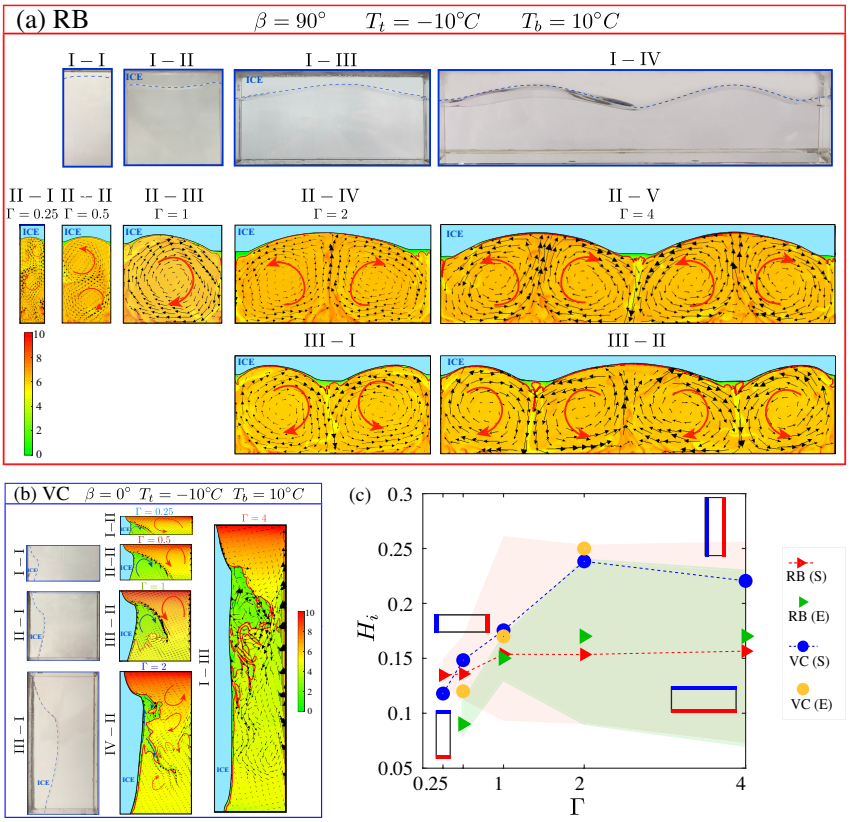


FIGURE 9.10: Aspect ratio dependence of the equilibrium state in freezing RB (a) and freezing VC (b) systems, from experiments and simulations. For simulations: visualizations of the temperature field in (a), (b) display T_0 (black line) and T_c (red line) isotherms. (c) Normalized average ice height H_i as a function of Γ for RB and VC cases from simulations (S) and experiments (E). The shaded area shows the spatial variation of the ice front (from minima to maxima of $h_i(x, t \to \infty)/h$) in the RB case for experiments (green) and simulations (red).

a melt-pond model with volumetric radiative heating. Our contribution has been to explore the freezing RB system in the presence of the anomalous thermal properties of water.

For this we choose four typical cases of the thermal driving condition from each of the existing four different regimes described above (Wang et al., 2021b), i.e., $T_\mathrm{b} = 3,\ 4.5,\ 5.5,\ 10°\mathrm{C}$, and perform long numerical simulations for melting (initial condition is $H_i = 1$) and freezing (initial condition is $H_i = 0$). Note that the duration of the simulations is of the order of 10 days in physical units.

It is observed that melting and freezing processes in general reach asymptotically the same state that can be steady in the case of a conductive equilibrium or statistically steady when there convection in the fluid persists. However, there are also special conditions - close to $T_\mathrm{b} = 5.5°\mathrm{C}$ (corresponding to regime 3) - where the outcome of the two processes is different (see Fig. 9.11(a)). In that case freezing process does not manage to turn off the convective motion of the fluid, while the melting one does not manage to switch it on. As a result in the freezing experiments the global amount of ice at the equilibrium result to be smaller (because convection is more efficient in transferring heat), see Fig. 9.11(d).

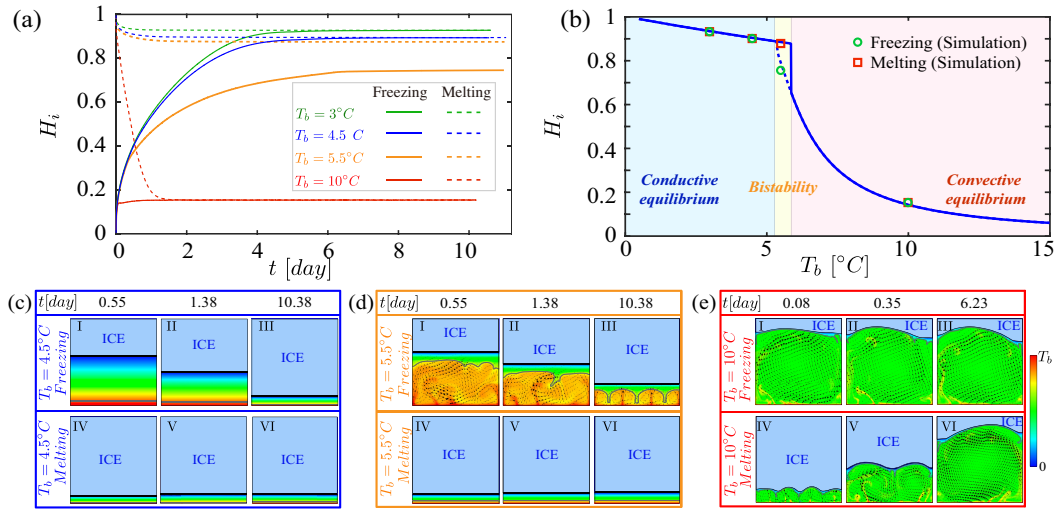


FIGURE 9.11: Phenomenon of bistability. (a) Temporal evolution of dimensionless ice thickness, H_i, during freezing (thick line) and melting (dashed line) processes. (b) Comparison of the simulation (symbols) and the theoretical model (dashed and solid lines): H_i as a function of T_b. (c), (d) and (e): panels I-III display the evolution of the instantaneous temperature field of the freezing process, with the bottom plate temperature $T_\mathrm{b} = 4.5,\ 5.5,\ 10°\mathrm{C}$, respectively; panels IV-VI display the evolution of the instantaneous temperature field of the melting process, for the same bottom plate temperatures.

The observed bistability can be quantitatively predicted by means of a 1D heat flux balance model. Depending on the value of T_b, the equilibrium condition is the result of the balance between 2 (ice , stable stratified fluid) or 3 layers (ice, stably stratified fluid, and unstably stratified one). In the first case $T_\mathrm{b} \leq T_\mathrm{c}$ the heat flux balance reads $q_i = k_i \frac{T_0 - T_\mathrm{t}}{h_i} = k_w \frac{T_\mathrm{b} - T_0}{h_s}$. In the second case, $T_\mathrm{b} > T_\mathrm{c}$, the heat flux balance reads $q_i = q_s = Nu_\mathrm{eff} k_w \frac{T_\mathrm{b} - T_0}{h_u}$, where the effective Nusselt number Nu_eff as a function of the Ra_eff is assumed to go as in the classical RB convection. From the two equations above, the ice thickness h_i can be calculated. It is easy to see that in this second case two possible solutions exist. Which one is chosen depends on the system initial condition either leading to melting or to freezing, see Fig.

9.12 The theoretical prediction (dashed and thick lines) agrees well with the numerical simulation results (symbols), see Fig. 9.11(b).

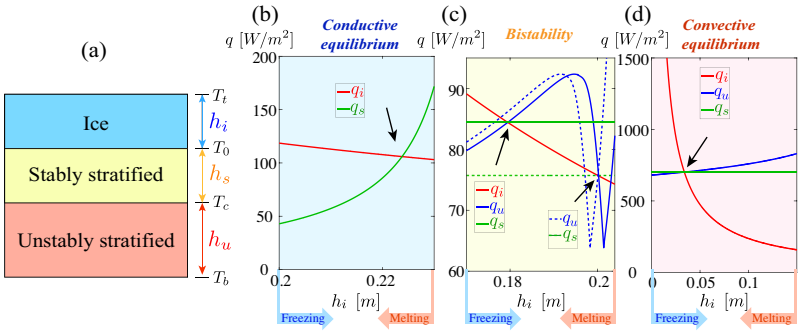


FIGURE 9.12: Mechanism of bistability: (a) sketch of the 1D model: three plane layers are connected in series. Note that if $T_b < T_c$ the unstably stratified layer is absent; the computed heat fluxes across the cell as a function of the ice thickness, h_i, in the purely conductive regime (b), the bistable regime (c), and the convective one (d).

Finally, let's note that such multiple equilibrium behaviour is unique to RB dynamics. It's absent in the VC configuration where the flow is always unstable; we could also verify this also through numerical simulations.

We conclude by noting that these studies of the melting and solidification dynamics in a closed cell are relevant to latent heat thermal energy storage applications. In such devices, it is essential to accurately characterize the charging and discharging times of thermal energy. Beyond reducing these times, achieving a regular and predictable thermal response is also of considerable interest. To this end, several studies have investigated modifications to the internal geometry of the storage cell, for example by using heterogeneous heating sources or by introducing internal fins to enhance heat transfer and improve control of the phase-change process, see e.g. (Proia et al., 2024, 2026).

Chapter 10

Freezing Modes and Ice Aging in Salty Water

Drawing once again on the natural environment for inspiration and motivation, it can be observed that all sea ice found in polar regions forms from salty waters. The thermodynamic properties of seawater, and more generally of all water–salt solutions, exhibit peculiar characteristics that differ from those of pure water. First, the amount of dissolved salt determines the strength of the density anomaly, which gradually weakens till disappearing at salinities above approximately 25 g of salt per kg of water (see Fig. 10.1). Consequently, seawater, with an average salinity of about 35 g/kg, does not exhibit a density anomaly and therefore does not display the phenomenon of inverted buoyancy. Second, the melting (or freezing) point depends on salinity and, under typical environmental conditions, decreases approximately linearly with increasing salt concentration. Third, and most importantly, seawater is a solution that contains less salt than the eutectic concentration (hypoeutectic). As a consequence during cooling water freezes first, while salt forms solid crystals only at much lower temperatures (below $-21°C$). As a result, sea ice forms as a *mushy* material, accompanied during freezing by the rejection of concentrated salty water (*brine*) and by the continuous evolution of the porous ice matrix as solidification proceeds.

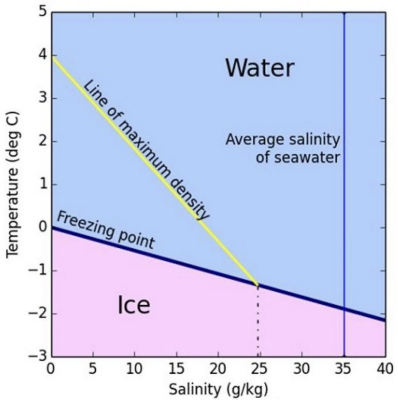


FIGURE 10.1: Saline water equation of state at atmospheric pressure.

In natural environments, these processes control the microstructure of sea ice, its mechanical properties, and the vertical salinity profile within the ice. They also strongly influence ice–ocean interactions, as well as the seasonal evolution and persistence of sea ice. Sea-ice

This chapter is based on:

1. *Sea Water Freezing Modes in a Natural Convection System*, Yihong Du, Ziqi Wang, Linfeng Jiang, Enrico Calzavarini and Chao Sun, J. Fluid Mech. (2023), vol. 960, A35 [PDF].
2. *Sea ice aging by diffusion-driven desalination*, Yihong Du, Feng Wang, Enrico Calzavarini, and Chao Sun, Phys. Rev. Lett. 135, 104201 (2025) [PDF].
3. *Freezing and ice aging dynamics in saline water under natural convection*, Feng Wang, Yihong Du, Xueyi Xie, Enrico Calzavarini and Chao Sun, Phys. Rev. Fluids 11, 013504 (2026) [PDF].

scientists distinguish between different types of sea ice according to their age. Indeed, earlier in this thesis, when discussing melt pond modelling, we introduced the terms first-year ice (FYI) and multi-year ice (MYI). These two ice types differ in several respects, including their colour, salinity, thickness, and mechanical strength. These characteristics are fundamental to understanding the physical behaviour of sea ice and play a key role in polar climate studies.

This chapter addresses only a subset of these important topics. It focuses on well-controlled small-scale experiments on the freezing of salt water interacting with a convective fluid layer and their interpretation. The research presented here is my most recent work and is, in part, still ongoing. I provide a brief overview of the studies to which I have contributed so far, followed by concluding remarks and suggestions for future research directions.

10.1 Convective freezing in salty water

Similarly to the previous case of pure water, we focus here on the freezing dynamics of saline water in a Rayleigh–Bénard (RB) convection cell (Wang et al., 2021b). The experimental setup is essentially the same as the one described in the previous chapter, with the only difference being the cell aspect ratio. For these experiments, a container of height $H = 0.12\mathrm{m}$ was used, with an aspect ratio $\Gamma = L_x/H = 2$ and a width-to-height ratio $L_y/H = 0.5$.

In separate experimental runs, the salinity of the water was varied over the range $[0, 3.5]\%$ in mass, with the upper limit corresponding to the typical salinity of seawater. The temperature of the cold top plate (T_t) was maintained at $10°C$ below the freezing temperature, denoted here by $T_{0,i}$. Since the freezing temperature decreases with increasing salinity, T_t was adjusted accordingly for each salinity level. The temperature of the heated bottom plate (T_b) was varied between experiments. These temperatures can be combined to define the dimensionless number, dubbed bottom superheat parameter, $\Theta_i = \frac{T_\mathrm{b} - T_{0,i}}{T_\mathrm{b} - T_\mathrm{t}}$, which roughly quantifies the level of the effective thermal driving of the system. A visualization of the temperature–salinity parameter space explored in the experiments is provided in Fig. 10.2.

The ice mushy phase thickness $h(t)$ and its porosity $\phi(t)$ (i.e. the volume fraction of residual liquid in the ice matrix) can be obtained, respectively by identifying the ice–liquid interface in the camera images of the system, and by using the expansion vessel readings (together with the assumption of total mass conservation in the system, similar to Wettlaufer et al., 1997). In this study we assumed that the equilibrium state is attained when the mean ice thickness $h(t)$ changes less than 1% in eight hours, with the maximum experiment duration being three days.

10.1.1 Mushy ice and its growth dynamics

The types of ice that form in water with and without salt are quite different. This can be promptly appreciated by depositing a drop of dye over a tiny (5 mm) hemispherical cavity made on the top horizontal surface of the ice matrices formed in the experiments. Specifically we consider here ice made in two salinity conditions: $S_i = 0\%$ and 3.5% (and $\Theta_i = 3/8$ in both cases). When $S_i = 0$ (Fig. 10.3 a,b), the ice is transparent and the dye does

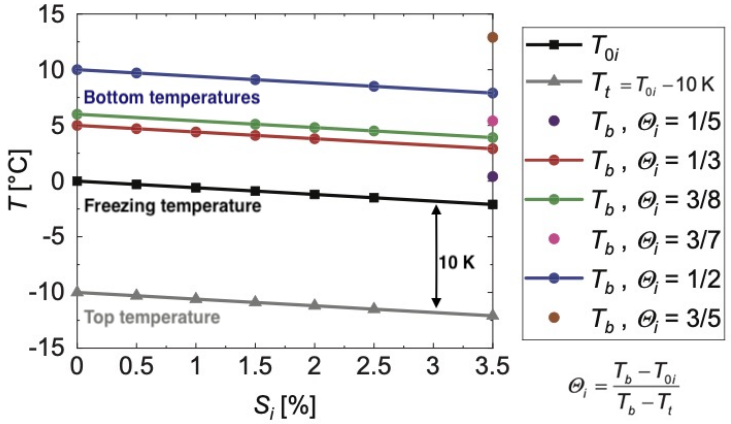


FIGURE 10.2: Sketch of the experimental system and temperature–salinity parameter space. Temperature–salinity parameter space explored in the experiments. The bottom plate temperature is kept at T_b, and the top plate temperature T_t is maintained at 10 K below the freezing point T_{0i} at the initial salinity S_i. The dimensionless bottom superheat parameter is defined as $\Theta_i = (T_\mathrm{b} - T_{0i})/(T_\mathrm{b} - T_\mathrm{t})$.

not spread into it, indicating the dense structure of the matrix. In contrast, at $S_i = 3.5\%$ (Fig. 10.3c,d), the ice phase appears opaque, and the dye spreads anisotropically, revealing the presence of a structured porous medium with predominantly vertical liquid-filled channels, characteristic of a mushy phase.

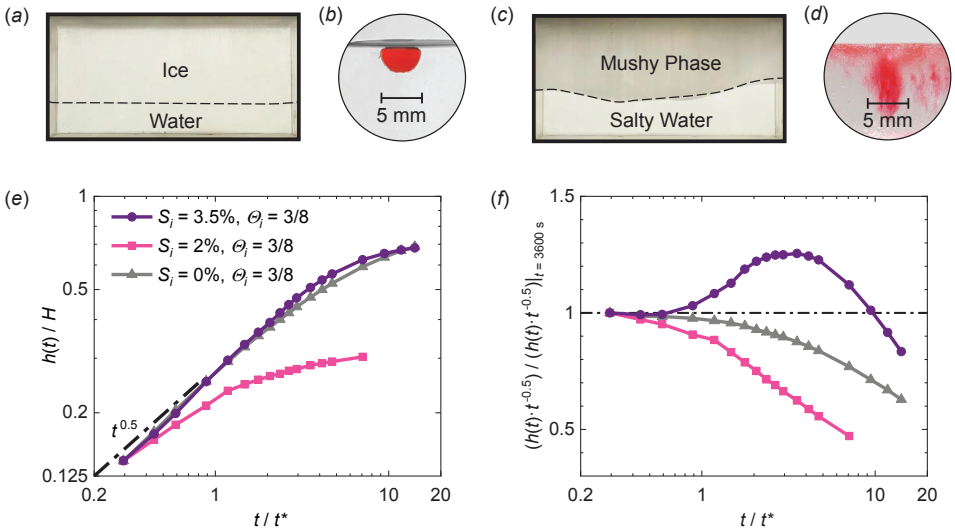


FIGURE 10.3: Images of the iced layer together with its internal structure, and evolution of the freezing front. (a–d) Photos of ice/mushy phases without (a,b) and with (c,d) porosity. (e) Dynamics of the freezing front. The mushy phase thicknesses $h(t)$ non-dimensionalized by H, are plotted as functions of time non-dimensionalized by the diffusive time scale $t^* = H^2/\kappa_\mathrm{ice} = 1.22 \times 10^4$ s (where κ_ice is ice thermal diffusivity) for three experiments. (f) Same data as that in (e) compensated by the diffusive behaviour, $h(t)/\sqrt{t}$ (and normalized by the first data point for better comparison).

Furthermore, the different ice types results to have different freezing kinetics, as can be seen in Fig. 10.3(e,f). Though all three different cases shown in the figure display a diffusion-dominated initial growth, i.e. $h \propto \sqrt{t}$, at later times the growth rate for the cases $S_i = 0,\ 2\%$ decreases, while the high-salinity case, $S_i = 3.5\%$, has a transient acceleration that exceeds

the diffusive growth rate before slowing down towards the equilibrium. We will see that this non-monotonic trend in the solidification front is related to the fluid dynamics inside the mushy-ice layer.

10.1.2 Global properties of the equilibrium state

Figure 10.4 displays some global properties of the mushy ice at the equilibrium (from now on denoted with a subscript e): they are the dimensionless thickness h_e/H, the porosity ϕ_e and the time to reach the equilibrium. The dependence of the thickness h_e as a function of the initial salinity S_i is rather different for distinct values of the control parameter Θ_i (see Fig. 10.4a). h_e monotonically decreases with S_i when $\Theta_i = 1/2$. Note that this is the largest Θ_i value we consider, for it one should expect stronger convection and consequently the thinnest ice, which is what we observe. On the other hand for $\Theta_i = 1/3, 3/8$ the thicker ice thickness h_e varies non-monotonically with S_i (see the decrease–increase–decrease pattern). Further we observe that the trends for the time to reach the equilibrium $t_e^{90\%}$ are consistent with those of h_e (Fig. 10.4(d)), an apparent linear correlation can be seen between the two quantities (Fig. 10.4(e)). This correspondence can provide a way to estimate the time to equilibrium just by focusing on the magnitude of h_e. Finally these trends are accompained by an overall increase of ϕ_e, meaning that more saline water implies a more porous ice (see Fig. 10.4(b)), however, the experimental results suggest that there is no trivial correlation between the equilibrium thickness and the final porosity.

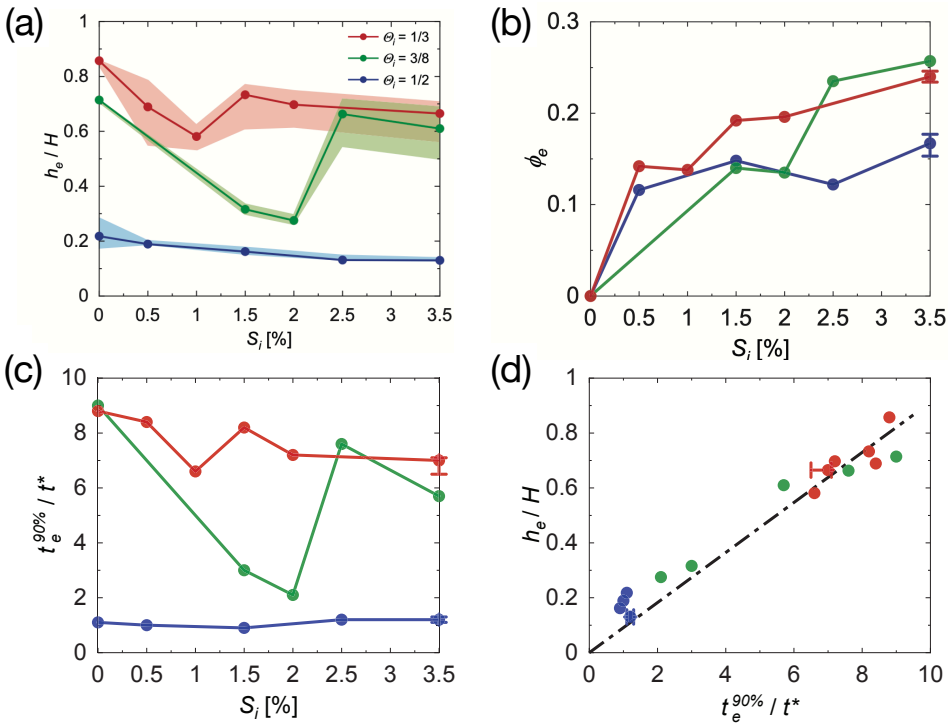


FIGURE 10.4: Global properties of the equilibrium state. a) The mean ice layer thickness h_e as a function of initial salinity S_i, for $\Theta_i = 1/3$ (red), $3/8$ (green), and $1/2$ (blue). Shaded areas indicate the minimal and maximal thickness of ice layer. (b) The mean ice porosity ϕ_e. (c) The saturation time $t_e^{90\%}$ idefined as the time to reach 90% of the equilibrium mushy phase thickness h_e. It is non-dimensionalized by the diffusive time scale $t^* = 1.22 \times 10^4$ s. (e) Thickness h_e versus $t_e^{90\%}$, a linear fit gives $h_e/H = 0.0912 \cdot t_e^{90\%}/t^*$ (dash-dot line), with correlation coefficient $R^2 = 0.9846$.

In our study, we focused on the relationship $h_e(S_i, \Theta_i)$. At first glance, one might expect that, for a fixed thermal forcing (parameterized by (Θ_i)), increasing the salinity would simply reduce the amount of ice formed (h_e). In other words, a more saline solution should produce progressively less ice. However, our results show that this intuitive expectation is not always valid. What physical mechanisms govern this relationship? How can we explain the emergence of a non-monotonic dependence with S_i under certain conditions?

10.1.3 Multi-layer 1D heat flux model

Clearly one would like to have a theoretical model, similar to the 1D heat flux balance model adopted for freshwater, that predicts the height of the mushy ice at the equilibrium. This is what we attempted in (Du et al., 2023a). The approach poses in this case more challenges, first of all because heat across the mushy phase can be transferred not only by conduction but also by convection of the brine in the pores. One may model the convective heat flux by means of the $Nu(Ra)$ relations known for porous media. It is known for instance that convective onset in a Darcy porous medium occurs for $Ra > 4\pi^2$ and follow a linear scaling law, i.e. $Nu \propto Ra$. However, the difficult stems from the proper estimation of the Rayleigh number, which requires the value of porosity and permeability. There are large uncertainties on the parametrization of permeability Π in ice (notoriously Kozeny-Carman-type of relations do not provide reliable estimates). A phenomenological but more accurate parametrization of this quantity for sea-ice is (Wells et al., 2019):

$$\Pi = \begin{cases} 0, & \phi_e < 0.054, \\ 7 \times 10^{-8} \, (\phi_e - 0.054)^{\alpha}, & \phi_e \geq 0.054. \end{cases} \tag{10.1}$$

A second source of difficulties is that the heat fluxes also depends on the amount of salt present in each layer (in the mushy ice and in the liquid). A simplifying assumption is that the salt concentration is approximately homogeneous in the liquid layer (where convection rapidly mix it) and that it is a the thermodynamic equilibrium in the mushy layer (meaning the local brine salinity is determined by the local temperature through the liquidus relation, Wells et al., 2019). A scheme of the resulting model is given in figure 10.5, this is made to stress its complexity, and the fact that it relies not only on the relations of material properties as a function of the local temperature and salinity, but also on several paramterizations ($Nu \; vs. Ra$) in the liquid and in the porous ice.

The main results of the model are illustrated in figure 10.6(a). It is shown that the non-monotonic behaviour of h_e vs. S_i, for $\Theta_i = 1/3$ and $3/8$ can be reproduced by the model (solid lines). Its physical origin is the onset of convection in the mushy layer (denoted with the letters). The agreement with the experiment is qualitative as the source of uncertainties in the model parametrizations are many.

Fig. 10.6(b) try to organize the dynamic regimes realized in the experiments through the Rayleigh numbers respectively in the liquid and in the mushy layers. We can have in fact 3 regimes in the liquid: conduction, convection and penetrative-convection (denoted LD, LC, LPC) and 2 in the mushy layer (conduction MD and convection MC). It is worth noticing that whenever convection appears in the mushy layer its thickness results greatly increased.

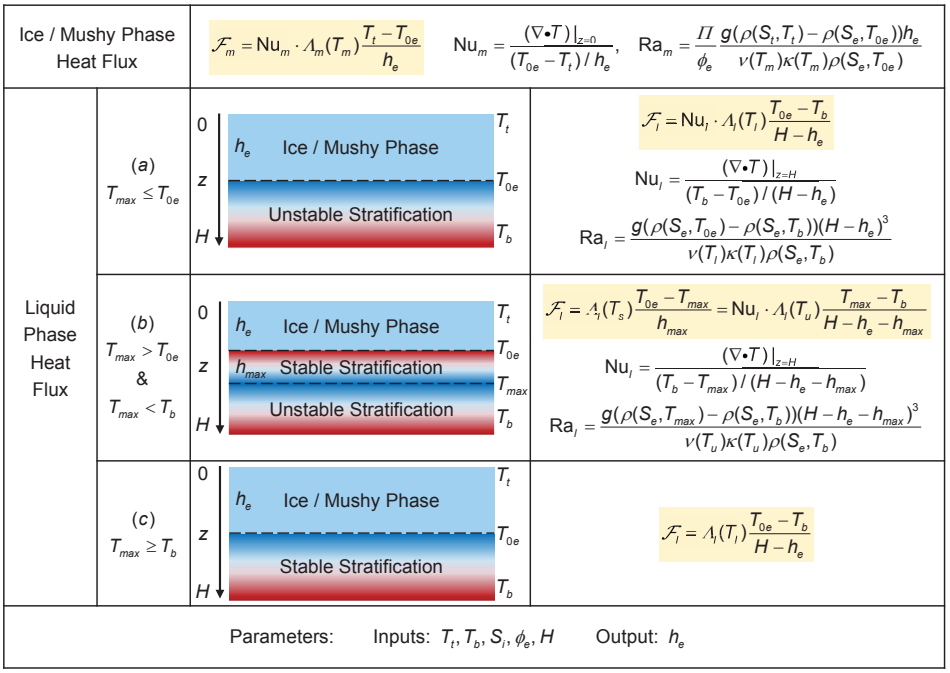


FIGURE 10.5: Scheme of the 1D multi-layer heat-flux balance model. The first row provides the adopted parametrization for the global heat flux expression in the mushy phase, $\mathcal{F}_m$, together with the definitions of Nu_m and Ra_m. Rows 2–4 report the expression for the global heat flux in the liquid phase, $\mathcal{F}_l$, together with the Nu_l and Ra_l definitions. Three different combinations of stratifications may exist: (a) unstable, (b) mixed, (c) unstable. The discriminating criterion for their occurrence is the monotonicity of liquid density within the temperature range $[T_{0e}, T_b]$, i.e. the relative magnitude of T_{0e}, T_b and the maximum-density temperature T_{max} (column 2), which depends on the salinity S_e. The model is supplemented with five input parameters, T_t, T_b, S_i, ϕ_e and H, and leads to an estimation of h_e (row 5) through the assumption of a statistically steady heat flux balance among layers (taken from (Du et al., 2023a)).

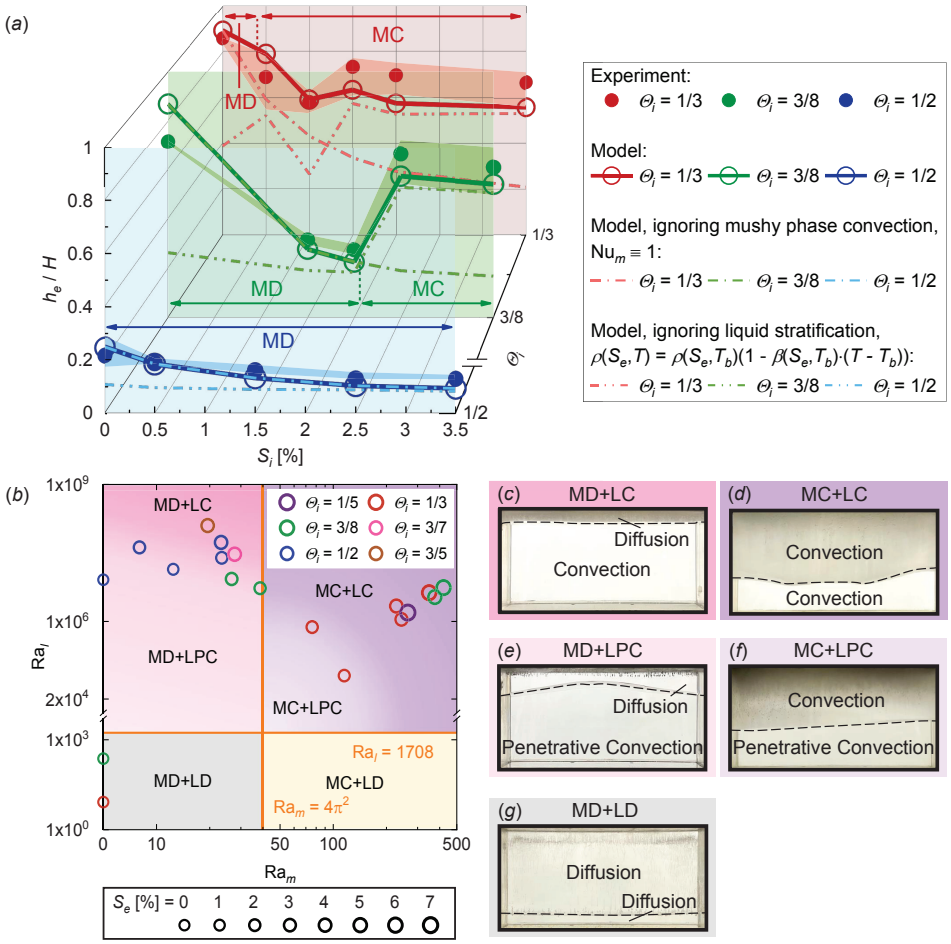


FIGURE 10.6: (a) Model results for ice/mushy phase thickness compared with the experiments; (b) Identification of heat transport modes. MD/MC stands for diffusive/convective heat transfer in the mushy phase; similarly, LD/LC stand for diffusive/convective heat transport in the liquid phase, while LPC stands for penetrative convection in the liquid phase, i.e. a combination of diffusive and convective heat transport, as a stable stratification lies above an unstable one. The third effective control parameter S_e in panel (b) is not presented as an axis for readability. Instead, different circle sizes are used to distinguish the different S_e. There are in total six heat transport modes of the system. Our experiments fall within five cases (see panels (c)-(g)). The highest salinity ($S_e \gtrsim 2.7\%$ is expected to suppress the LPC regime as it removes the density anomaly of the solution.

One may ask whether it is possible to achieve a more detailed understanding of the phenomenon, including the transient evolution of the system. In particular, can the problem be addressed through direct numerical simulations?

A significant step in this direction has recently been taken by (Guo and Yang, 2026), who proposed a unified numerical framework that monolithically couples the Navier–Stokes and Darcy equations. The model simultaneously solves the advection–diffusion equations for temperature and salinity, incorporates buoyancy forces arising from both scalar fields, and represents phase change through a phase-field formulation. This framework successfully reproduces the temporal evolution of ice growth up to its equilibrium state and demonstrates the spontaneous formation of vertically oriented brine channels within the mushy layer. However, despite these advances, the approach still relies on several empirical parameterizations. These stem from the fact that the mushy layer cannot be regarded as a conventional porous medium: rather, it is a heterogeneous porous structure whose morphology continuously evolves during solidification. One critical aspect of the model is that the numerical phase-field does not directly correspond to the local porosity of the mushy layer; instead, the two quantities are related through an empirical, nonlinear algebraic relationship. Another delicate issue concerns the effective thermal conductivity of the mushy layer. This quantity cannot be represented simply as the conductivity of the solid–liquid mixture, i.e., the weighted average of the conductivities of the two phases, but also depends on the flow velocity within the pore space (which must be empirically parametrized). Overall, although this numerical framework provides valuable insight into the transient dynamics of sea-ice growth and brine drainage, it also highlights the intrinsic difficulties of representing, within a continuum framework at the scale of a representative elementary volume, the complex multiphase processes occurring inside the mushy layer.

10.2 Sea ice aging by diffusion-driven desalination

As mentioned at the beginning of this chapter, the phenomenon of ice aging is well known in the geophysical literature. It is accompanied by progressive desalination of the ice matrix, changes in its transparency, and an increase in its mechanical strength. Under natural environmental conditions, desalination may result from several mechanisms, including brine expulsion during cooling, gravity-driven brine drainage, flushing by freshwater generated through surface melting, and repeated seasonal cycles of melting and refreezing.

We investigated instead how the desalination process develops in laboratory conditions in the convective cell employed in our experiments. To this end, we monitored the freezing process over much longer timescales than those considered previously, extending the duration of the experiments from a maximum of three days to approximately three weeks. Both vertical convection configurations and Rayleigh–Bénard convection cells were used. In addition, the experimental apparatus was equipped with a local salinity probe, enabling time-resolved measurements of the salt concentration in the liquid phase.

On these timescales, which are of the same order of magnitude as the diffusive timescale of salt transport across the cell, the ice was found to evolve toward a fully compact state with vanishing porosity. At equilibrium, the ice layer exhibited in general a smaller average

thickness than at earlier stages of growth, while essentially all of the salt had been rejected into the remaining liquid phase. Although many previous studies have focused on the characterization of the mushy layer and on the convective processes occurring within it (Du et al., 2023a; Middleton et al., 2016; Peppin et al., 2007, 2008; Wells et al., 2019; Wettlaufer et al., 1997; Worster, 1997), our work was among the firsts to investigate the coupling between the internal dynamics of the mushy layer and the external convective flow (and particularly in a closed system) (Du et al., 2025; Wang et al., 2026).

Our results for the VC system are illustrated in figure 10.7. We display the ice layer evolution in a typical case with initial salinity $S_i = S_{\text{bulk}}|_{t=0} = 3.44\%$ and $\Theta_i \approx 1/2$. The system first experiences a fast icing process at the cold plate (purple regime in Fig. 10.7b). The ice layer grows in about 1.5 days to a maximal thickness (Fig. 10.7(b1), (b2), (c). The rapid growth of mushy ice is driven by heat transfer across the ice and is controlled by the strength of the convection in the liquid region (Wang et al., 2021b). Note that the ice layer is thicker at the bottom because this liquid does not exhibit a density anomaly. As a result, the warm, saline water is less dense than the surrounding fluid and rises, preferentially melting the ice from above and leading to the observed asymmetry.

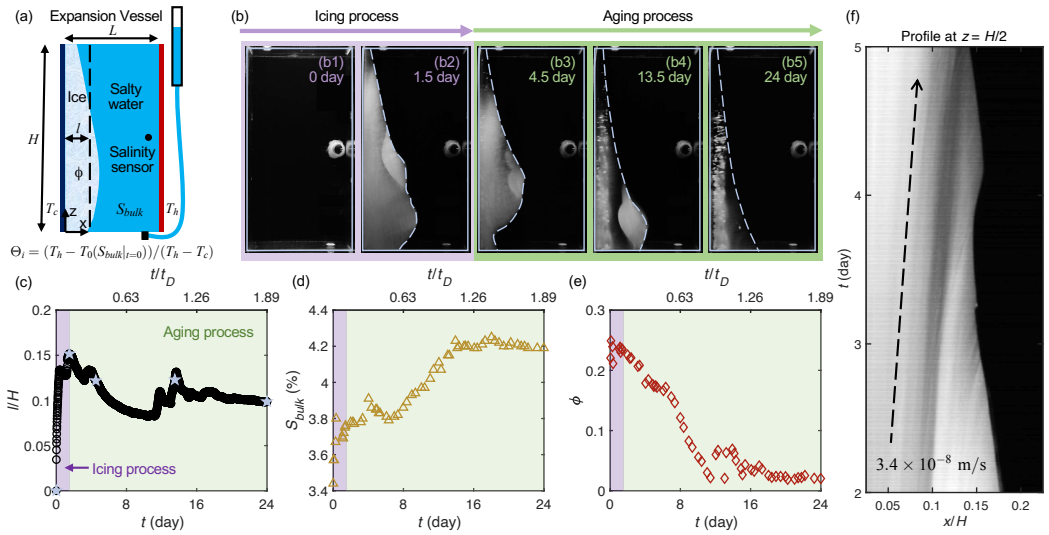


FIGURE 10.7: Experiment on mushy ice evolution. (a) Sketch of the experimental setup. (b-f) Mushy ice evolution with $S_{\text{bulk}}|_{t=0} = 3.44\%$, $T_{\text{c}} = -12.1^\circ$ C and $T_{\text{h}} = 7.9^\circ$ C ($\Theta_i \approx 1/2$). (b) Snapshots of the ice layer correspond to the blue stars in (c). (c-e) Temporal evolution of the spatially-averaged ice layer thickness l made dimensionless by the system height H (black circles in (c)), bulk salinity S_{bulk} (yellow triangles in (d)) and the spatially-averaged ice layer porosity ϕ (red diamonds in (e)). (f) Space-time diagram for the ice layer profile along $z = 0.5H$ from Day 2 to Day 5.

Unlike in the freezing of fresh water or other pure liquids, the evolution of ice does not end here. After about 3 days - without any change in the experimental conditions - the ice layer spontaneously enters a slow aging process (green regime in Fig.10.7), which lasts until the system converges to a new and final equilibrium state (this takes about 2 weeks in the present case). Transient and local advancements and retreats of the ice front occur (Fig. 10.7(b3)-(b5), however, the average ice thickness varies with time only gradually and with an overall decreasing trend (Fig. 10.7(c)). In contrast, the salinity of the liquid in the convecting region (i.e. the bulk) increases (Fig. 10.7(d)). The average ice porosity exhibits a small yet noticeable decline (Fig. 10.7(e)) and the ice layer becomes gradually

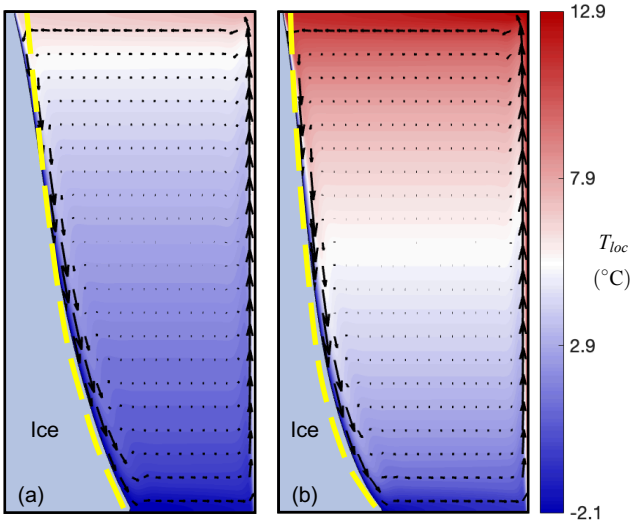


FIGURE 10.8: The final - after aging - ice front morphologies from the experiment (yellow dashed line) compared with those from direct numerical simulation of a positively buoyant pure liquid freezing under the same conditions (thin black line). From the simulations we also show in color the temperature field in the liquid phase, and with arrows the velocity field. The "ad hoc" positively buoyant liquid on which the simulations are based possess the same thermal properties as salty water with the bulk salinity measured at the end of the experiments. (a) $\Theta_i \approx 1/2$. (b) $\Theta_i \approx 3/5$.

transparent, as for solid ice formed in freshwater. The space–time diagram constructed from experimental images of the ice (Fig. 10.7(f)) reveals that the porous structures within the ice gradually migrate toward the outer edge of the ice layer, i.e., toward the bulk liquid region. The estimated migration velocity - between day 2 and 5 of the experiment - is on the order of $3\ \mathrm{mm/day}$.

The numerical simulations provide valuable insight into the final equilibrium state of the ice. Notably, the final shape of the ice front (yellow dashed line in Fig. 10.8) closely matches that obtained from direct numerical simulations of the solidification of a pure liquid governed by the same equation of state as saline water at the end of the experiment (thin black line in Fig. 10.8). This remarkable agreement suggests that, by the end of the experiment, the ice layer has effectively evolved into a layer of pure ice.

We later conducted analogous experiments in the RB configuration (Wang et al., 2026). These experiments exhibited similar behaviour over time scales of two to three weeks, namely a rapid growth of a thick porous ice layer, followed by a slow thinning process accompanied by a marked desalination.

10.2.1 Dynamics of ice aging

The experiments we have described highlight the large separation of time scales between the ice growth process (1–2 days) and the so-called aging process which involves desalination, a reduction in porosity, and often a decrease in ice thickness (which instead occurs over a period of 10–20 days). This is because the latter process is controlled by salt mass diffusion, which is quite slow. Comparing the diffusion coefficient of salt (D) and heat leads to the Lewis number, $Le = \kappa/D \simeq 200$ (where κ is the brine thermal diffusivity). For the VC experiment in the case $\Theta_i \approx 1/2$, the solute diffusion time scale $t_{\mathrm{D}} = l^{*2}/D$ is about

1.1×10^6, ≈ 12.7 days, where l^* is the mean ice thickness during the aging process and D is the salt diffusivity in the brine.

As heat diffusion is much faster than mass diffusion in salty water, mushy ice is in local thermal equilibrium (Feltham et al., 2006) during the aging process. Fig. 10.9(a)-10.9(b) show the conceptual schematics of this process. The local temperature always equals the local freezing/melting point. The increase in temperature in horizontal (increasing x) direction (gray line) leads to a decrease in local salinity (yellow line). With such a salinity gradient, the salt is expelled from the mushy ice. The salinity of the bulk salty water increases. Simultaneously, the excess water freezes inside the mushy ice, resulting in the shrinkage of porosity and maintaining pockets of very concentrated brine.

The apparent velocity scale for brine pockets migration toward the outside of the ice can be estimated by dividing the diffusive salt flux $D(S_c - S_{\rm bulk})/l$ with the reference (average) salinity of the mushy layer $(S_c + S_{\rm bulk})/2$, which leads to:

$$v_{\rm D} \simeq \frac{2D}{l}\frac{S_c - S_{\rm bulk}}{S_c + S_{\rm bulk}} \tag{10.2}$$

(Notz and Worster, 2009; Rempel et al., 2001), where S_c is the salinity at the cold plate determined by its temperature T_c, and the bulk salinity $S_{\rm bulk}$ is approximately the salinity at the ice front, assuming sufficiently strong convective mixing in the bulk. For the case in Fig.10.7(f), it is about 1.8 to 2.3 mm/day, close to the observed migration velocity ($3.4 \times 10^{-8} m/s = 2.94\ mm/day$).

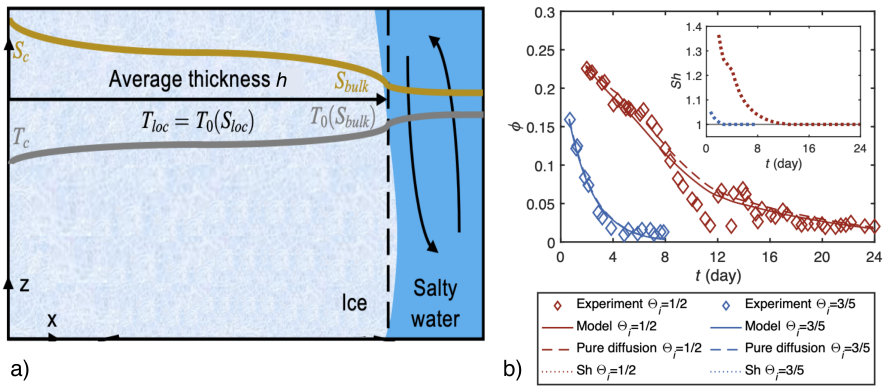


FIGURE 10.9: (a) Sketch of the desalination of the whole ice layer. The reduction of salt in the mushy ice equals salt removed through diffusion and advection. The grey line sketches the variation of local temperature in x direction, while the yellow line represents local salinity. The local temperature and salinity are related by the local thermal equilibrium in the mushy ice. (b) Integral desalination model (solid lines) and experiment (diamonds) results for the evolution of spatially-averaged ice layer porosity ϕ, with initial superheat parameters $\Theta_i \approx 1/2$ (red) and $3/5$ (blue). The model predictions when advective transport is neglected by imposing $Sh \equiv 1$ (dashed lines) are also attached for comparing the relative role of diffusion and advection. The inset of panel (b) shows the corresponding time evolution of Sh from the model (dotted lines).

The temporal evolution of this process can be roughly captured by an integral desalination model of the form:

$$\frac{d}{dt}\left(l\phi\frac{S_c + S_{\rm bulk}}{2}\right) = -C \cdot Sh\ v_{\rm D} \cdot \phi\frac{S_c + S_{\rm bulk}}{2}, \tag{10.3}$$

where the left-hand-side represent the rate of variation of the salt content in the mushy-layer and the right hand side the desalination flux due to a possibly combined effect of salt mass diffusion and convection. The latter being parametrized by Sh, the Sherwood number (the adjustable parameter C compensates for influences of non-uniform ice thickness and porosity). Therefore, providing the temporal series of $S_{\mathrm{bulk}}(t)$ measured in the experiment, assuming l constant and providing the initial value of porosity ϕ, the temporal evolution of ϕ can be explicitly solved by the model. We choose $C = 1.1$ for $\Theta_i \approx 1/2$ (red) and $C = 2.2$ for $\Theta_i \approx 3/5$ (blue) to best fit the experimental data. Fig. 10.9(c) shows that the model agrees reasonably with the experimental results. The convective salt transport inside the ice appears necessary only at the beginning of the process and plays a limited role in the desalination and ice aging within the parameter regime of the current system.

In (Wang et al., 2026), we proposed a more elaborate version of the integral model. By enforcing total salt conservation within the system and assuming quasi-equilibrium heat transfer between the mushy layer and the bulk liquid, the model is able to reproduce the observed trends using only the initial conditions as experimental input. However, it still relies on the presence of ad hoc adjustable parameters. This limitation clearly underscores the need for further studies on the underlying physical mechanisms.

10.3 Conclusions and Future perspectives

We have seen that the freezing of saline solutions coupled with convective transport phenomena is more complex than any of the processes discussed in the previous chapters. This is mainly due to two reasons. First, one is no longer dealing with a pure substance, but rather with a solidification process that gives rise to a mushy layer. Second, a new dynamical time scale, associated with mass diffusion, comes into play, leading to a much slower asymptotic equilibration process.

These physical phenomena pose significant challenges both from the perspective of their macroscopic modelling and from that of numerical simulations. As already mentioned, only empirical parameterizations are currently available for the permeability of an ice mushy layer, as well as for its effective thermal properties and mass diffusivity.

From the numerical perspective, an additional difficulty should also be mentioned. It is related to the large differences between the diffusivities of momentum (i.e. the kinematic viscosity), heat, and salt. These quantities differ by approximately one order of magnitude, with ($Pr = \nu/\kappa \simeq 10$) and ($Le = \kappa/D \simeq 200$). In numerical simulations, this requires appropriate discretization strategies, for example significantly finer grids to accurately resolve the dynamics of the salt concentration. Moreover, because salt dynamics are associated with very long diffusive time scales, the duration of the simulations also becomes a critical issue. Accurately resolving the ice aging process in either a Rayleigh–Bénard (RB) or a vertical convection (VC) configuration requires extremely computationally intensive simulations which, to the best of my knowledge, have not yet been performed. It is also for this reason that the present chapter did not include direct side-by-side comparisons between simulations and experiments (except for the simplified case shown in Fig. 10.8). This therefore represents a challenging but promising direction for future research.

Other aspects that remain largely unexplored concern freezing in the presence of different types of flows, such as horizontal currents that generate persistent shear. It would also be interesting to investigate time-modulated phenomena, for example freezing–melting cycles (representative of diurnal or seasonal cycles), and to analyze the resulting ice structure.

Another research direction that could be pursued in the future is to understand the effect of volume changes (and, consequently, density changes) during the solidification process, an aspect that has so far been largely neglected.

Finally, I would like to mention that natural ice very often contains air trapped within it in the form of bubbles, which are sometimes compressed. It has been hypothesized that these bubbles may accelerate the melting of ice (Josberger, 1980; Wengrove et al., 2023). It would therefore be interesting to pursue studies in this direction, which would consequently involve not only multicomponent but also multiphase systems. Beyond their relevance to natural processes, such studies would also be of practical interest for energy storage applications and for the optimization of heat transfer processes.

Bibliography

Agyenim, F., N. Hewitt, P. Eames, and M. Smyth (2010). "A review of materials, heat transfer and phase change problem formulation for latent heat thermal energy storage systems (LHTESS)". *Renewable and Sustainable Energy Reviews* 14.2, pp. 615–628.

Ahlers, G., S. Grossmann, and D. Lohse (2009). "Heat transfer and large scale dynamics in turbulent Rayleigh-Bénard convection". *Rev. Mod. Phys.* 81 (2), pp. 503–537.

Alexakis, A. and L. Biferale (2018). "Cascades and transitions in turbulent flows". *Physics Reports* 767-769. Cascades and transitions in turbulent flows, pp. 1–101. ISSN: 0370-1573.

Alexiades, V. (1992). *Mathematical Modeling of Melting and Freezing Processes*. CRC Press.

Alley, R. B., P. U. Clark, P. Huybrechts, and I. Joughin (2005). "Ice-Sheet and Sea-Level Changes". *Science* 310.5747, pp. 456–460.

Andrés, C. R. A. de, S. Saarinen, and A. Uuskallio (2018). "Review of ice challenges and ice management in port areas". *Coast. Eng. Proc.* 36, pp. 79–79.

Ardekani, M. N., P. Costa, W. P. Breugem, and L. Brandt (2016). "Numerical study of the sedimentation of spheroidal particles". *Int. J. Multiph. Flow* 87, pp. 16–34.

Ardeshiri, H., I. Benkeddad, F. G. Schmitt, S. Souissi, F. Toschi, and E. Calzavarini (2016). "Lagrangian model of copepod dynamics: Clustering by escape jumps in turbulence". *Physical Review E* 93, p. 043117.

Ardeshiri, H., F. Schmitt, S. Souissi, F. Toschi, and E. Calzavarini (2017). "Copepods encounter rates from a model of escape jump behaviour in turbulence". *J. Plankton Research* 39.6, pp. 878–890.

Auton, T. (1987). "The lift force on a spherical body in a rotational flow". *J. Fluid Mech.* 183, 199–218.

Bagoien, E. and T. Kiørboe (2005). "Blind dating-mate finding in planktonic copepods. I. Tracking the pheromone trail of Centropages typicus". *Marine Ecology Progress Series* 300, pp. 105–115.

Balachandar, S and J. K. Eaton (2010). "Turbulent dispersed multiphase flow". *Annu. Rev. Fluid Mech.* 42, pp. 111–133.

Ballmer, M. D., D. L. Lourenço, K. Hirose, R. Caracas, and R. Nomura (2017). "Reconciling magma-ocean crystallization models with the present-day structure of the Earth's mantle". *Geochem. Geophys. Geosyst.* 18.7, pp. 2785–2806.

Bec, J., L. Biferale, G. Boffetta, A. Celani, M. Cencini, A. Lanotte, S. Musacchio, and F. Toschi (2006). "Acceleration statistics of heavy particles in turbulence". *J. Fluid Mech.* 550, pp. 349–358.

Bec, J., H. Homann, and S. S. Ray (2014). "Gravity-Driven Enhancement of Heavy Particle Clustering in Turbulent Flow". *Phys. Rev. Lett.* 112 (18), p. 184501.

Bec, J., K. Gustavsson, and B. Mehlig (2024). "Statistical models for the dynamics of heavy particles in turbulence". *Ann. Rev. Fluid Mech.* 56, pp. 189–214.

Bejan, A. (2013). *Convection Heat Transfer*. Wiley.

Bell, R. E. (2008). "The role of subglacial water in ice-sheet mass balance". *Nat. Geosci.* 1.5, pp. 297–304.

Beron-Vera, F. J. (2021). "Nonlinear dynamics of inertial particles in the ocean: From drifters and floats to marine debris and Sargassum". *Nonlinear Dynamics* 103.1, pp. 1–26.

Biferale, L., G. Boffetta, A. Celani, A. Lanotte, and F. Toschi (Dec. 2004a). "Particle trapping in three-dimensional fully developed turbulence". *Phys Fluids* 17.2, p. 021701.

Biferale, L, E Calzavarini, A. Lanotte, F Toschi, and R Tripiccione (2004b). "Universality of anisotropic turbulence". *Physica A* 338.1, pp. 194–200.

Bintanja, R. and R. S. W. Van de Wal (2008). "North American ice-sheet dynamics and the onset of 100,000-year glacial cycles". *Nature* 454.7206, pp. 869–872.

Boetius, A., A. M. Anesio, J. W. Deming, J. A. Mikucki, and J. Z. Rapp (2015). "Microbial ecology of the cryosphere: sea ice and glacial habitats". *Nat. Rev. Microbiol.* 13.11, pp. 677–690.

Borazjani, I., F. Sotiropoulos, E. Malkiel, and J. Katz (2010). "On the role of copepod antennae in the production of hydrodynamic force during hopping". *Journal of Experimental Biology* 213, pp. 3019–3035.

Bordoloi, A. D. and E. Variano (2017). "Rotational kinematics of large cylindrical particles in turbulence". *J. Fluid Mech.* 815, pp. 199–222.

Borgas, M. S. and P. K. Yeung (2004). "Relative dispersion in isotropic turbulence. Part 2. A new stochastic model with Reynolds-number dependence". *J. Fluid Mech.* 503, pp. 125–160.

Borgnino, M., K. Gustavsson, F. De Lillo, G. Boffetta, M. Cencini, and B. Mehlig (2019). "Alignment of Nonspherical Active Particles in Chaotic Flows". *Phys. Rev. Lett.* 123.13, p. 138003.

Bounoua, S., G. Bouchet, and G. Verhille (2018). "Tumbling of Inertial Fibers in Turbulence". *Phys. Rev. Lett.* 121 (12), p. 124502.

Brandt, L. and F. Coletti (2022). "Particle-laden turbulence: Progress and perspectives". *Ann. Rev. Fluid Mech.* 54, pp. 159–189.

Brenner, H. (1961). "The slow motion of a sphere through a viscous fluid towards a plane surface". *Chem. Eng. Sci.* 16.3, pp. 242–251.

Breuer, D., T. Rueckriemen, and T. Spohn (2015). "Iron snow, crystal floats, and inner-core growth: modes of core solidification and implications for dynamos in terrestrial planets and moons". *Prog. Earth Planet. Sci.* 2, 39, p. 39.

Brichet, L., N. Carbonneau, E. Bernard, R. Braun, L. Méthivier, Y. Fraigneau, D. Lucor, F. Chillà, A. Sergent, and J. Salort (2025). "Universal scaling law in turbulent Rayleigh–Bénard convection with and without roughness". *J. Fluid Mech.* 1025, A10.

Brown, R. D., Z. Warhaft, and G. A. Voth (2009). "Acceleration Statistics of Neutrally Buoyant Spherical Particles in Intense Turbulence". *Phys. Rev. Lett.* 103 (19), p. 194501.

Buskey, E. J. and D. K. Hartline (2003). "High-Speed Video Analysis of the Escape Responses of the Copepod Acartia tonsa to Shadows". *The Biological Bulletin* 204, pp. 28–37.

Buskey, E. J., P. H. Lenz, and D. K. Hartline (2002). "Escape behavior of planktonic copepods in response to hydrodynamic disturbances: high speed video analysis". *Marine Ecology Progress Series* 235, pp. 135–146.

Byron, M., J. Einarsson, K. Gustavsson, G. A. Voth, B. Mehlig, and E. Variano (2015). "Shape-dependence of particle rotation in isotropic turbulence". *Phys. Fluids* 27.3, p. 035101.

Calzavarini, E., L.-F. Jiang, and C Sun (2020a). "Anisotropic particles in two-dimensional convective turbulence". *Phys. Fluids* 32.2, p. 023305.

Calzavarini, E., R. Volk, M. Bourgoin, E. Leveque, J. F. Pinton, and F. Toschi (2009). "Acceleration statistics of finite-sized particles in turbulent flow: the role of Faxén forces". *J. Fluid Mech.* 630, pp. 179–189.

Calzavarini, E. (Sept. 2019). "Eulerian–Lagrangian fluid dynamics platform: The ch4-project". *Software Impacts* 1, p. 100002.

Calzavarini, E., M. Cencini, D. Lohse, and F. Toschi (2008a). "Quantifying turbulence-induced segregation of inertial particles". *Phys. Rev. Lett.* 101.8, p. 084504.

Calzavarini, E., L. Jiang, and C. A. Sun (Feb. 2020b). "Anisotropic particles in two-dimensional convective turbulence". *Phys. Fluids* 32.2, p. 023305.

Calzavarini, E., M. Kerscher, D. Lohse, and F. Toschi (2008b). "Dimensionality and morphology of particle and bubble clusters in turbulent flow". *J. Fluid Mech.* 607, pp. 13–24.

Calzavarini, E., R. Volk, E. Leveque, J. F Pinton, and F. Toschi (2012). "Impact of trailing wake drag on the statistical properties and dynamics of finite-sized particle in turbulence". *Physica D* 241.3, pp. 237–244.

Caporaloni, M., F. Tampieri, F. Trombetti, and O. Vittori (1975). "Transfer of particles in nonisotropic air turbulence". *J. Atmospheric Sciences* 32, pp. 565–568.

Challabotla, N. R., L. Zhao, and H. I. Andersson (2015). "Orientation and rotation of inertial disk particles in wall turbulence". *J. Fluid Mech.* 766, R2.

Chatterjee, D. and S. Chakraborty (2005). "An enthalpy-based lattice Boltzmann model for diffusion dominated solid-liquid phase transformation". *Phys. Letters A* 341, pp. 320–330.

Chen, S., Y. Yan, and W. Gong (2017). "A simple Lattice-Boltzmann model for conjugate heat transfer research". *Int. J. Heat Mass Tran.* 107, pp. 862–870.

Chiarini, A. and M. E. Rosti (2024). "Finite-size inertial spherical particles in turbulence". *J. Fluid Mech.* 988, A17.

Chillà, F. and J. Schumacher (2012). "New perspectives in turbulent Rayleigh-Bénard convection". *Eur. Phys. J. E* 35, pp. 1–25.

Cisse, M., H. Homann, and J. Bec (2013). "Slipping motion of large neutrally buoyant particles in turbulence". *J. Fluid Mech.* 735, R1.

Clark, P. U., R. B. Alley, and D. Pollard (1999). "Northern Hemisphere ice-sheet influences on global climate change". *Science* 286.5442, pp. 1104–1111.

Colabrese, S., K. Gustavsson, A. Celani, and L. Biferale (2017). "Flow Navigation by Smart Microswimmers via Reinforcement Learning". *Phys. Rev. Lett.* 118 (15), p. 158004.

Cooley, M. D. A. and M. E. O'Neill (1969). "On the slow motion generated in a viscous fluid by the approach of a sphere to a plane wall or stationary sphere". *Mathematika* 16.1, pp. 37–49.

Costa, P., B. J. Boersma, J. Westerweel, and W.-P. Breugem (2015). "Collision model for fully resolved simulations of flows laden with finite-size particles". *Phys. Rev. E* 92 (5), p. 053012.

Curry, J. A., J. L. Schramm, and E. E. Ebert (1995). "Sea ice-albedo climate feedback mechanism". *J. Climate* 8.2, pp. 240–247.

Davis, S. H. (2001). *Theory of solidification*. Cambridge University Press.

Davis, S. H., U. Müller, and C. Dietsche (1984). "Pattern selection in single-component systems coupling Bénard convection and solidification". *J. Fluid Mech.* 144, pp. 133–151.

Devenish, B. J., P. Bartello, J.-L. Brenguier, L. R. Collins, W. W. Grabowski, R. H. A. IJzermans, S. P. Malinowski, M. W. Reeks, J. C. Vassilicos, L.-P. Wang, and Z. Warhaft (2012). "Droplet growth in warm turbulent clouds". *Quarterly J. Royal Meteorological Society* 138.667, pp. 1401–1429.

Doall, M. H., S. P. Colin, J. R. Strickler, and J. Yen (1998). "Locating a mate in 3D: the case of Temora longicornis". *Philosophical transactions of the Royal Society of London, Series B* 353, pp. 681–689.

Du, Y., Z. Wang, L. Jiang, E. Calzavarini, and C. Sun (2023a). "Sea water freezing modes in a natural convection system". *J. Fluid Mech.* 960, A35.

Du, Y., E. Calzavarini, and C. Sun (2024). "The physics of freezing and melting in the presence of flows". *Nat. Reviews Physics* 6.11, pp. 676–690.

Du, Y., F. Wang, E. Calzavarini, and C. Sun (Sept. 2025). "Sea Ice Aging by Diffusion-Driven Desalination". *Phys. Rev. Lett.* 135.10.

Du, Y., Z. Wang, L. Jiang, E. Calzavarini, and C. Sun (Apr. 2023b). "Sea water freezing modes in a natural convection system". *J. Fluid Mech.* 960.

Duprat, L. P. A. M., G. R. Bigg, and D. J. Wilton (2016). "Enhanced Southern Ocean marine productivity due to fertilization by giant icebergs". *Nat. Geosci.* 9.3, pp. 219–221.

Dur, G., S. Souissi, F. G. Schmitt, S. Cheng, and J. S. Hwang (2010). "The different aspects in motion of the three reproductive stages of Pseudodiaptomus annandalei (Copepoda, Calanoida)". *Journal of Plankton Research* 32, pp. 423–440.

Durham, W. M., E. Climent, M. Barry, F. D. Lillo, G. Boffetta, M. Cencini, and R. Stocker (2013). "Turbulence drives microscale patches of motile phytoplankton". *Nature Communication* 4, pp. 1–7.

Eckert, M. (2019). *The Turbulence Problem: A Persistent Riddle in Historical Perspective*. 1st ed. SpringerBriefs in History of Science and Technology. Cham, Switzerland: Springer Cham, pp. XII + 107. ISBN: 978-3-030-31862-8 (softcover), 978-3-030-31863-5 (ebook).

Elghobashi, S. (1994). "On predicting particle-laden turbulent flows". *Appl. Sci. Res.* 52.4, pp. 309–329.

Elkins-Tanton, L. T. (2012). "Magma Oceans in the Inner Solar System". *Ann. Rev. Earth and Planetary Sci.* 40, pp. 113–139.

Faden, M., A. König-Haagen, and D. Brüggemann (2019). "An optimum enthalpy approach for melting and solidification with volume change". *Energies* 12, p. 868.

Falkovich, G., A. Fouxon, and M. G. Stepanov (2002). "Acceleration of rain initiation by cloud turbulence". *Nature* 419.6903, pp. 151–154.

Fan, Y., C. Wang, L. Jiang, C. Sun, and E. Calzavarini (Feb. 2024). "Accelerations of large inertial particles in turbulence". *EPL - Europhys. Lett.* 145.4, p. 43001.

Feltham, D. L., N. Untersteiner, J. S. Wettlaufer, and M. G. Worster (2006). "Sea ice is a mushy layer". *Geophys. Res. Lett.* 33.14, p. L14501.

Fessler, J. R., J. D. Kulick, and J. K. Eaton (1994). "Preferential concentration of heavy particles in a turbulent channel flow". *Phys. Fluids* 6.11, pp. 3742–3749.

Fetterer, F. and N. Untersteiner (1998). "Observations of melt ponds on Arctic sea ice". *J. Geophysical Research: Oceans* 103.C11, pp. 24821–24835.

Fiabane, L., R. Zimmermann, R. Volk, J. F. Pinton, and M. Bourgoin (2012). "Clustering of finite-size particles in turbulence". *Phys. Rev. E* 86, p. 035301.

Fields, D. A. and J. Yen (1997). "The escape behavior of marine copepods in response to a quantifiable fluid mechanical disturbance". *Journal of Plankton Research* 19, pp. 1289–1304.

Frisch, U. (1995). *Turbulence: The Legacy of A. N. Kolmogorov*. Cambridge: Cambridge University Press. ISBN: 9780521457132.

Gan, H, J Chang, J. J. Feng, and H. H. HU (2003). "Direct numerical simulation of the sedimentation of solid particles with thermal convection". *J. Fluid Mech* 481, 385–411.

Gardner, J. (2020). "How water, wind, waves and ice shape landscapes and landforms: historical contributions to geomorphic science". *Geomorphology* 366, p. 106687.

Garg, H., E. Calzavarini, and S. Berti (Sept. 2021). "Statistical properties of two-dimensional elastic turbulence". *Phys. Rev. E* 104.3.

Garg, H., E. Calzavarini, G. Mompean, and S. Berti (2018). "Particle-laden two-dimensional elastic turbulence". *European physical journal. E, Soft matter* 41.10, p. 115.

Gatignol, R (1983). "The Faxen formulas for a rigid particle in an unsteady non-uniform Stokes-flow". *J. Mecan. Theor. Appl.* 2.2, 143–160.

Gebhart, B. and J. C. Mollendorf (1977). "A new density relation for pure and saline water". *Deep Sea Res. Part II Top. Stud. Oceanogr.* 24, pp. 831–848.

Giurgiu, V., G. C. A. Caridi, M. De Paoli, and A. Soldati (2024). "Full Rotational Dynamics of Plastic Microfibers in Turbulence". *Phys. Rev. Lett.* 133 (5), p. 054101.

Golledge, N. R., E. D. Keller, N. Gomez, K. A. Naughten, J. Bernales, L. D. Trusel, and T. L. Edwards (2019). "Global environmental consequences of twenty-first-century ice-sheet melt". *Nature* 566.7742, pp. 65–72.

Grassberger, P. (1993). "Generalized dimensions of strange attractors". *Phys. Lett.* 97A, pp. 227–230.

Grassberger, P. and I. Procaccia (1983). "Measuring the Strangeness of Strange Attractors". *Physica D: Nonlinear Phenomena* 9, pp. 189–208.

Grossmann, S. and D. Lohse (2000). "Scaling in thermal convection: a unifying theory". *J. Fluid Mech.* 407, pp. 27–56.

Guasto, J. S., R. Rusconi, and R. Stocker (2012). "Fluid Mechanics of Planktonic Microorganisms". *Ann. Rev. Fluid Mech.* 44, pp. 373–400.

Guo, R. and Y. Yang (2026). "A Unified Numerical Framework for Turbulent Convection and Phase-Change Dynamics in Coupled Fluid-Porous Systems". *arXiv preprint arXiv:2510.22730v2*. arXiv: 2510.22730v2 [physics.flu-dyn].

Gupta, A., D. Vincenzi, and R. Pandit (2014). "Elliptical tracers in two-dimensional, homogeneous, isotropic fluid turbulence: The statistics of alignment, rotation, and nematic order". *Phys. Rev. E* 89.2, p. 021001.

Gupta, S. C. (2017). *The Classical Stefan Problem Basic Concepts, Modelling and Analysis with Quasi-Analytical Solutions and Methods*. Elsevier.

Gustavsson, K., J. Einarsson, and B. Mehlig (2014a). "Tumbling of Small Axisymmetric Particles in Random and Turbulent Flows". *Phys. Rev. Lett.* 112 (1), p. 014501.

Gustavsson, K., S. Vajedi, and B. Mehlig (2014b). "Clustering of Particles Falling in a Turbulent Flow". *Phys. Rev. Lett.* 112 (21), p. 214501.

Haan, M. J. A. de and T. J. Rabelink (2023). "Cryopreservation breaks the organ transplant time barrier". *Nature Reviews Nephrology* 19, pp. 623–624.

Hanna, E., F. J. Navarro, F. Pattyn, C. M. Domingues, X. Fettweis, E. R. Ivins, R. J. Nicholls, C. Ritz, B. Smith, S. Tulaczyk, P. L. Whitehouse, and H. J. Zwally (2013). "Ice-sheet mass balance and climate change". *Nature* 498.7452, pp. 51–59.

Hester, E. W., L. A. Couston, B. Favier, K. J. Burns, and G. M. Vasil (2020). "Improved phase-field models of melting and dissolution in multi-component flows". *Proc. Roy. Soc. A: Mathematical, Physical and Engineering Sciences* 476.2242, p. 20200508.

Heymsfield, A. J. (1977). "Precipitation development in stratiform ice clouds: A microphysical and dynamical study". *J. Atoms. Sci.* 34.2, pp. 367–381.

Hill, X. (1996). "La convection sous un solide. Applications aux planètes". Thèse de doctorat, Institut de Physique du Globe de Paris. PhD thesis. Université Paris 7.

Ho, J. (2010). "The implications of Arctic sea ice decline on shipping". *Mar. Policy* 34.3, pp. 713–715.

Hohengger, C., B. Alali, K. Steffen, D. Perovich, and K. Golden (2012). "Transition in the fractal geometry of Arctic melt ponds". *The Cryosphere* 6, pp. 1157–1162.

Homann, H. and J. Bec (2010). "Finite-size effects in the dynamics of neutrally buoyant particles in turbulent flow". *J. Fluid Mech.* 651, pp. 81–91.

Hopkins, M. A., J. Tuhkuri, and M. Lensu (1999). "Rafting and ridging of thin ice sheets". *J. Geophysical Research: Oceans* 104.C6, pp. 13605–13613.

Horvat, C., D. R. Jones, S. Iams, D. Schroeder, D. Flocco, and D. Feltham (2017). "The frequency and extent of sub-ice phytoplankton blooms in the Arctic Ocean". *Sci. Adv.* 3.3, e1601191.

Hoshen, J. and R. Kopelman (1976). "Percolation and Cluster Distribution. I. Cluster Multiple Labeling Technique and Critical Concentration Algorithm". *Phys. Rev. B* 14.8, pp. 3438–3445.

Huppert, H. E. (1990). "The fluid mechanics of solidification". *J. Fluid Mech.* 212, pp. 209–240.

Huseby, E., J. Gissinger, F. Candelier, N. Pujara, G. Verhille, B. Mehlig, and G. Voth (2025). "Helical ribbons: Simple chiral sedimentation". *Phys. Rev. Fluids* 10 (2), p. 024101.

Hvidegaard, S. and R. Forsberg (2002). "Sea–ice thickness from airborne laser altimetry over the Arctic Ocean north of Greenland". *Geophys. Res. Lett.* 29, p. 1952.

Ishihara, T., Y. Kaneda, M. Yokokawa, K. Itakura, and A. Uno (2007). "Small-scale statistics in high-resolution direct numerical simulation of turbulence: Reynolds number dependence of one-point velocity gradient statistics". *J. Fluid Mech.* 592, 335–366.

Jaccod, A., S. Berti, E. Calzavarini, and S. Chibbaro (Oct. 2021). "Predator-prey plankton dynamics in turbulent flow past an obstacle". *Phys. Rev. Fluids* 6.10.

— (Jan. 2022). "Three-dimensional turbulence effects on plankton dynamics behind an obstacle". *European Physical J. Plus* 137.2.

Jacob, T., J. Wahr, W. T. Pfeffer, and S. Swenson (2012). "Recent contributions of glaciers and ice caps to sea level rise". *Nature* 482.7386, pp. 514–518.

Jaganathan, D., S. G. Prasath, R. Govindarajan, and V. Vasan (2023). "The Basset–Boussinesq history force: its neglect, validity, and recent numerical developments". *Frontiers in Physics* Volume 11 - 2023.

Jeffery, G. B. (1922). "The motion of ellipsoidal particles immersed in a viscous fluid". *Proc. R. Soc. Lond. A* 102.715, pp. 161–179.

Jiang, L., C. Wang, S. Liu, C. Sun, and E. Calzavarini (Mar. 2022). "Dynamics of finite-size spheroids in turbulent flow: the roles of flow structures and particle boundary layers". *J. Fluid Mech.* 939.

Jiménez, J. (1997). "Oceanic turbulence at millimeter scales". *Scientia Marina* 61, pp. 47–56.

Jones, C. A. (2015). "Thermal and Compositional Convection in the Outer Core". *Treatise on Geophysics (Second Edition)*. Ed. by G. Schubert. Second Edition. Oxford: Elsevier. Chap. 8.05, pp. 115 –159.

Josberger, E. G. (1980). "The Effect of Bubbles Released from a Melting Ice Wall on the Melt-Driven Convection in Salt Water". *J. Physical Oceanography* 10.3, pp. 474–477.

Joughin, I., R. B. Alley, and D. M. Holland (2012). "Ice-sheet response to oceanic forcing". *Science* 338.6111, pp. 1172–1176.

Jucha, J., A. Naso, E. Lévêque, and A. Pumir (2018). "Settling and collision between small ice crystals in turbulent flows". *Phys. Rev. Fluids* 3 (1), p. 014604.

Kiørboe, T. (2008). *A Mechanistic Approch to Plankon Ecology*. Princeton University Press.

Kiørboe, T., E. Saiz, and A. Visser (1999). "Hydrodynamic signal perception in the copepod Acartia tonsa". *Marine Ecology Progress Series* 179, pp. 97–111.

Kiørboe, T. and A. Visser (1999). "Predator and prey perception in copepods due to hydromechanical signals". *Marine Ecology Progress Series* 179, pp. 81–95.

Kolmogorov, A. N. (1962). "A refinement of previous hypotheses concerning the local structure of turbulence in a viscous incompressible fluid at high Reynolds number". *J. Fluid Mech.* 13.1, pp. 82–85.

Koyaguchi, T., M. A. Hallworth, H. E. Huppert, and R. Stephen J. Sparks (1990). "Sedimentation of particles from a convecting fluid". *Nature* 343.6257, pp. 447–450.

Kramel, S., G. A. Voth, S. Tympel, and F. Toschi (2016). "Preferential rotation of chiral dipoles in isotropic turbulence". *Phys. Rev. Lett.* 117.15, p. 154501.

La Porta, A., G. A. Voth, A. M. Crawford, J. Alexander, and E. Bodenschatz (2001). "Fluid particle accelerations in fully developed turbulence". *Nature* 409.6823, pp. 1017–1019.

Lambeck, K., H. Rouby, A. Purcell, Y. Sun, and M. Sambridge (2014). "Sea level and global ice volumes from the Last Glacial Maximum to the Holocene". *Proc. Natl. Acad. Sci. USA* 111.43, pp. 15296–15303.

Le Quiniou, C., F. Schmitt, E. Calzavarini, S. Souissi, and Y. Huang (Feb. 2022). "Copepod swimming activity and turbulence intensity: study in the Agiturb turbulence generator system". *European Physical Journal Plus* 137.2, p. 250.

Lenz, P. H. and D. K. Hartline (1999). "Reaction times and force production during escape behavior of a calanoid copepod, Undinula vulgaris". *Marine Biology* 133, pp. 249–258.

Lenz, P. H. and J. Yen (1993). "Distal setal mechanoreceptors of the first antennae of marine copepods". *Bulletin of Marine Science* 53, pp. 170–179.

Leppin, L. A. and M. Wilczek (2020). "Capturing Velocity Gradients and Particle Rotation Rates in Turbulence". *Phys. Rev. Lett.* 125 (22), p. 224501.

Lillo, F. D., M. Cencini, W. M. Durham, M. Barry, R. Stocker, E. Climent, and G. Boffetta (2014). "Turbulent Fluid Acceleration Generates Clusters of Gyrotactic Microorganisms". *Physical Review Letters* 112, p. 044502.

Lundell, F., L. D. Soderberg, and P. H. Alfredsson (2011). "Fluid Mechanics of Papermaking". *Annu. Rev. Fluid Mech.*

Luo, K., Z. Wang, J. Fan, and K. Cen (2007). "Full-scale solutions to particle-laden flows: Multidirect forcing and immersed boundary method". *Phys. Rev. E* 76 (6), p. 066709.

Lüthje, M., D. Feltham, P. Taylor, and M. Worster (2006). "Modeling the summertime evolution of sea–ice melt ponds". *J. Geophys. Res.* 111, p. C02001.

Ma, Y.-P., I. Sudakov, C. Strong, and K. M. Golden (2019). "Ising Model for Melt Ponds on Arctic Sea Ice". *New J. Physics* 21.6, p. 063029.

MacKenzie, B. R. and W. C. Leggett (1993). "Wind-based models for estimating the dissipation rates of turbulent energy in aquatic environments: empirical comparisons". *Marine Ecology Progress Series* 94, pp. 207–216.

Marchioli, C., M. Fantoni, and A. Soldati (2010). "Orientation, distribution, and deposition of elongated, inertial fibers in turbulent channel flow". *Phys. Fluids* 22.3, p. 033301.

Marchioli, C. and A. Soldati (2013). "Rotation statistics of fibers in wall shear turbulence". *Acta Mech.* 224.10, pp. 2311–2329.

Marcus, G. G., S. Parsa, S. Kramel, R. Ni, and G. A. Voth (2014). "Measurements of the solid-body rotation of anisotropic particles in 3D turbulence". *New J. Phys.* 16.10, p. 102001.

Marsh, B. and M. Maxey (1985). "On the distribution and separation of crystals in convecting magma". *J. Vol. Geo. Res.* 24.1-2, 95–150.

Martin, D and R Nokes (1988). "Crystal settling in a vigorously convecting magma chamber". *Nature* 332.6164, 534–536.

Martin, D. and R. Nokes (Dec. 1989). "A Fluid-Dynamical Study of Crystal Settling in Convecting Magmas". *J. Petrology* 30.6, pp. 1471–1500.

Mathai, V., M. W. M. Neut, E. P. V. D. Poel, and C. Sun (2016). "Translational and rotational dynamics of a large buoyant sphere in turbulence". *Exp. Fluids* 57, p. 51.

Mathai, V., E. Calzavarini, J. Brons, C. Sun, and D. Lohse (2016). "Microbubbles and Microparticles are Not Faithful Tracers of Turbulent Acceleration". *Phys. Rev. Letters* 117.2.

Maurice, M., N. Tosi, H. Samuel, A.-C. Plesa, C. Hüttig, and D. Breuer (2017). "Onset of solid-state mantle convection and mixing during magma ocean solidification". *J. Geophys. Res. Planets* 122.3, pp. 577–598.

Maxey, M. R. (1987). "The gravitational settling of aerosol particles in homogeneous turbulence and random flow fields". *J. Fluid Mech.* 174, pp. 441–465.

Maxey, M. and J. Riley (1983). "Equation of motion for a small rigid sphere in a nonuniform flow". *Phys. Fluids* 26.4, 883–889.

Mazzitelli, I. M. and D. Lohse (2004). "Lagrangian statistics for fluid particles and bubbles in turbulence". *New J. Physics* 6, p. 203.

Meiburg, E. and B. Kneller (2010). "Turbidity Currents and Their Deposits". *Annu. Rev. Fluid Mech.* 42.1, pp. 135–156.

Meyer, C. and D. Deglon (2011). "Particle collision modeling – A review". *Miner. Eng.* 24.8, pp. 719–730.

Michalec, F.-G., O. Praud, M. Lorite-Diez, S. Cazin, S. Souissi, and E. Climent (May 27, 2026). "Cruising and jumping: the effect of microplastics on the swimming behavior of copepods measured by 3D Lagrangian particle tracking velocimetry". *European Physical Journal E* 49, p. 43.

Michalec, F. G., S. Souissi, and M. Holzner (2015). "Turbulence triggers vigorous swimming but hinders motion strategy in planktonic copepods". *Journal of The Royal Society Interface* 12, p. 20150158.

Michalec, F.-G., O. Praud, S. Cazin, and E. Climent (2022). "Experimental Investigation of Preferential Concentration in Zooplankton Swimming in Turbulence". *European Physical Journal E* 45.2, p. 12.

Michalec, F.-G., I. Fouxon, S. Souissi, and M. Holzner (2020). "Efficient mate finding in planktonic copepods swimming in turbulence". *eLife* 9. Ed. by A. Seminara and A. M. Walczak, e62014.

Middleton, C. A., C. Thomas, A. De Wit, and J. L. Tison (2016). "Visualizing brine channel development and convective processes during artificial sea-ice growth using Schlieren optical methods". *J. Glaciol.* 62.231, pp. 1–17.

Mittal, R. and G. Iaccarino (2005). "Immersed boundary methods". *Annu. Rev. Fluid Mech.* 37, pp. 239–261.

Mousavi, N., J. Qiu, B. Mehlig, L. Zhao, and K. Gustavsson (2024). "Efficient survival strategy for zooplankton in turbulence". *Phys. Rev. Res.* 6 (2), p. L022034.

Ng, C. S., A. Ooi, D. Lohse, and D. Chung (2015). "Vertical natural convection: application of the unifying theory of thermal convection". *J. Fluid Mech.* 764, pp. 349–361.

Ni, R., S. Kramel, N. T. Ouellette, and G. A. Voth (2015). "Measurements of the coupling between the tumbling of rods and the velocity gradient tensor in turbulence". *J. Fluid Mech.* 766, pp. 202–225.

Notz, D. (2009). "The future of ice sheets and sea ice: between reversible retreat and unstoppable loss". *Proc. Natl. Acad. Sci. USA* 106.49, pp. 20590–20595.

Notz, D. and M. G. Worster (2009). "Desalination processes of sea ice revisited". *J. Geophys. Res. Oceans* 114.C5, p. C05006.

Obbard, R. W., S. Sadri, Y. Q. Wong, A. A. Khitun, I. Baker, and R. C. Thompson (2014). "Global warming releases microplastic legacy frozen in Arctic Sea ice". *Earth's Future* 2.6, pp. 315–320.

Oehmke, T. B., A. D. Bordoloi, E. Variano, and G. Verhille (2021). "Spinning and tumbling of long fibers in isotropic turbulence". *Phys. Rev. Fluids* 6, p. 044610.

Pandey, A., J. D. Scheel, and J. Schumacher (2018). "Turbulent superstructures in Rayleigh-Bénard convection". *Nature Communications* 9.1, p. 2118.

Parsa, S., E. Calzavarini, F. Toschi, and G. A. Voth (2012). "Rotation rate of rods in turbulent fluid flow". *Phys. Rev. Lett.* 109.13, p. 134501.

Parsa, S. and G. A. Voth (2014). "Inertial Range Scaling in Rotations of Long Rods in Turbulence". *Phys. Rev. Lett.* 112 (2), p. 024501.

Patočka, V., N. Tosi, and E. Calzavarini (2022). "Residence time of inertial particles in 3D thermal convection: Implications for magma reservoirs". *Earth and Planetary Science Letters* 591, p. 117622.

Patočka, V., E. Calzavarini, and N. Tosi (2020). "Settling of inertial particles in turbulent Rayleigh-Bénard convection". *Phys. Rev. Fluids* 5 (11), p. 114304.

Peeken, I., S. Primpke, B. Beyer, J. Gütermann, C. Katlein, T. Krumpen, M. Bergmann, L. Hehemann, and G. Gerdts (2018). "Arctic sea ice is an important temporal sink and means of transport for microplastic". *Nat. Commun.* 9.1, pp. 1–12.

Peppin, S. S. L., P. Aussillous, H. E. Huppert, and M. G. Worster (2007). "Steady-state mushy layers: experiments and theory". *J. Fluid Mech.* 570, pp. 69–77.

Peppin, S. S. L., H. E. Huppert, and M. G. Worster (2008). "Steady-state solidification of aqueous ammonium chloride". *J. Fluid Mech.* 599, pp. 465–476.

Perovich, D. K., T. C. Grenfell, B. Light, and P. V. Hobbs (2002a). "Seasonal evolution of the albedo of multiyear Arctic sea ice". *J. Geophys. Res.* 107.C10, SHE–20.

Perovich, D., W. Tucker III, and K. Ligett (2002b). "Aerial observations of the evolution of ice surface conditions during summer". *J. Geophys. Res.* 107, p. 8048.

Peskin, C. S. (2002). "The immersed boundary method". *Acta Numer.* 11, pp. 479–517.

Petersen, A. J., L. Baker, and F. Coletti (2019). "Experimental study of inertial particles clustering and settling in homogeneous turbulence". *J. Fluid Mech.* 864, 925–970.

Plesa, A.-C., N. Tosi, and D. Breuer (2014). "Can a fractionally crystallized magma ocean explain the thermo-chemical evolution of Mars?" *Earth Planet. Sci. Lett.* 403, pp. 225–235.

Pope, S. B. (2000). *Turbulent Flows*. Cambridge; New York: Cambridge University Press, p. 771. ISBN: 9780521598866.

Popović, P., M. Cael B.B.a nd Silber, and D. Abbot (2018). "Simple Rules Govern the Patterns of Arctic Sea Ice Melt Ponds". *Phys. Rev. Lett.* 120 (14), p. 148701.

Post, E., U. S. Bhatt, C. M. Bitz, J. F. Brodie, T. L. Fulton, M. Hebblewhite, J. Kerby, S. J. Kutz, I. Stirling, and D. A. Walker (2013). "Ecological consequences of sea-ice decline". *Science* 341.6145, pp. 519–524.

Prakash, V. N., Y. Tagawa, E. Calzavarini, J. M. Mercado, F. Toschi, D. Lohse, and C. Sun (2012). "How gravity and size affect the acceleration statistics of bubbles in turbulence". *New J. Phys.* 14.10, p. 105017.

Prakhar, S. and A. Prosperetti (2021). "Linear theory of particulate Rayleigh-Bénard instability". *Phys. Rev. Fluids* 6 (8), p. 083901.

Proia, P., M. Sbragaglia, and G. Falcucci (2024). "Melting with natural convection with heterogeneous heating sources". *Applied Thermal Engineering* 257, p. 124089. ISSN: 1359-4311.

— (2026). "Heat transfer in phase change materials with multiple fin insertion". *EPL - Europhys. Lett.*

Pujara, N., M. A. R. Koehl, and E. A. Variano (2018). "Rotations and accumulation of ellipsoidal microswimmers in isotropic turbulence". *J. Fluid Mech.* 838, pp. 356–368.

Pumir, A. and M. Wilkinson (2011). "Orientation statistics of small particles in turbulence". *New J. Phys.* 13.9, p. 093030.

Pumir, A., M. Z. Sheikh, K. Gustavsson, E. Lévêque, B. Mehlig, and A. Naso (2026). "Statistical orientation and distribution of columnar ice crystals in turbulent flows". *Phys. Rev. Fluids* 11 (6), p. 064608.

Purseed, J., B. Favier, L. Duchemin, and E. W. Hester (2020). "Bistability in Rayleigh-Bénard convection with a melting boundary". *Phys. Rev. Fluids* 5.2, p. 023501.

Qureshi, N. M., M. Bourgoin, C. Baudet, A. Cartellier, and Y. Gagne (2007). "Turbulent transport of material particles: an experimental study of finite size effects". *Phys. Rev. Lett.* 99.18, p. 184502.

Rabbanipour Esfahani, B., S. Hirata, S. Berti, and E. Calzavarini (2018). "Basal melting driven by turbulent thermal convection". *Phys. Rev. Fluids* 3.5.

Rafat, A., H. K. Pour, C. Spence, M. J. Palmer, and A. MacLean (2023). "An analysis of ice growth and temperature dynamics in two Canadian subarctic lakes". *Cold Reg. Sci. Technol.* 210, p. 103808.

Raza, S., R. B. Freitas, L. S. Alves, E. Calzavarini, and S. C. Hirata (July 2025). "Impact of particle injection velocity on the stability of the particulate Rayleigh–Bénard system". *J. Fluid Mech.* 1015.

Raza, S., S. C. Hirata, and E. Calzavarini (Dec. 2024). "Stabilization of the Rayleigh–Bénard system by injection of thermal inertial particles and bubbles". *Phys. Fluids* 36.12.

Raza, S., A. Lemoine, Y. Zhang, E. Calzavarini, R. B. Freitas, L. S. Alves, and S. C. Hirata (Apr. 2026). "Particle thermal inertia delays the onset of convection in particulate Rayleigh–Bénard system". *Int. J. Multiphase Flow* 198, p. 105660.

Reartes, C. and P. D. Mininni (2021). "Settling and clustering of particles of moderate mass density in turbulence". *Phys. Rev. Fluids* 6 (11), p. 114304.

Rempel, A. W., E. D. Waddington, J. S. Wettlaufer, and M. G. Worster (2001). "Possible displacement of the climate signal in ancient ice by premelting and anomalous diffusion". *Nature* 411.6837, pp. 568–571.

Rombouts, I, G. Beaugrand, F. Ibanez, S. Gasparini, S. Chiba, and L. Legendre (2009). "Global latitudinal variations in marine copepod diversity and environmental factors". *Proceedings of the Royal Society of London B* 276, pp. 3053–3062.

Rosén, T., J Einarsson, A. Nordmark, C. Aidun, F. Lundell, and B Mehlig (2015). "Numerical analysis of the angular motion of a neutrally buoyant spheroid in shear flow at small Reynolds numbers". *Phys. Rev. E* 92.6, p. 063022.

Ruiz, J, D Macias, and F Peters (2004). "Turbulence increases the average settling velocity of phytoplankton cells". *Proc. Natl. Acad. Sci. USA* 101.51, 17720–17724.

Sabban, L. and R. van Hout (2011). "Measurements of pollen grain dispersal in still air and stationary, near homogeneous, isotropic turbulence". *J. Aerosol. Sci.* 42.12, pp. 867–882.

Saffman, P. G. and J. S. Turner (1956). "On the collision of drops in turbulent clouds". *J. Fluid Mech.* 1, pp. 16–30.

Safronov, V. S. (1969). *Evolution of the Protoplanetary Cloud and Formation of the Earth and the Planets*. Israel program for scientific translations. NASA.

Scagliarini, A., E. Calzavarini, D. Mansutti, and F. Toschi (Mar. 2020). "Modelling Sea Ice and Melt Ponds Evolution: Sensitivity to Microscale Heat Transfer Mechanisms". *Mathematical Approach to Climate Change and its Impacts, Cannarsa P., Mansutti D., Provenzale A. (eds), Springer INdAM Series, vol 38. Springer, Cham (2020)*, pp. 179–198.

Schiller, L. and A. Naumann (1935). "A Drag Coefficient Correlation". *Zeitschrift des Vereins Deutscher Ingenieure* 77, pp. 318–320.

Schiller, L. and A. Neumann (1933). "Über die grundlegenden Berechnungen bei der Schwerkraft-aufbereitung". *Z. Ver. Dtsch. Ing.* 77, pp. 318–320.

Schwaiger, H. F., R. P. Denlinger, and L. G. Mastin (2012). "Ash3d: A finite-volume, conservative numerical model for ash transport and tephra deposition". *J. Geophys. Res.* 117.B4.

Scott, F. and D. L. Feltham (2010). "A model of the three-dimensional evolution of Arctic melt ponds on first-year and multiyear sea ice". *J. Geophysical Research: Oceans* 115.C12, p. C12064.

She, Z.-S. and E. Leveque (1994). "Universal Scaling Laws in Fully Developed Turbulence". *Phys. Rev. Lett.* 72.3, pp. 336–339.

Shepherd, A., A. Hubbard, P. Nienow, M. King, M. McMillan, and I. Joughin (2009). "Greenland ice sheet motion coupled with daily melting in late summer". *Geophys. Res. Lett.* 36.1, p. L01501.

Shishkina, O. (2016). "Momentum and heat transport scalings in laminar vertical convection". *Phys. Rev. E* 93.5, p. 051102.

Shraiman, B. I. and E. D. Siggia (1990). "Heat transport in high-Rayleigh-number convection". *Phys. Rev. A* 42 (6), pp. 3650–3653.

Silva Torres, L. A., S. Berti, and E. Calzavarini (2026). "Vertical distribution of weakly inertial, quasi-neutrally buoyant particles in a convective ocean mixed layer". *EGU General Assembly 2026*. EGU26-4256. Vienna, Austria.

Skyllingstad, E. D., C. A. Paulson, and D. K. Perovich (2009). "Simulation of melt pond evolution on level ice". *J. Geophys. Res.: Oceans* 114, p. C12019.

Smith, A. W., D. E. Skilling, J. D. Castello, and S. O. Rogers (2004). "Ice as a reservoir for pathogenic human viruses: specifically, caliciviruses, influenza viruses, and enteroviruses". *Med. Hypotheses* 63.4, pp. 560–566.

Smyth, W. D. and J. N. Moum (2000). *Ocean Turbulence*. Lecture notes / educational manuscript. URL: https://www.chem.pmf.hr/_download/repository/OceanTurbulence-Smyth.pdf.

Squires, K. and H Yamazaki (1995). "Preferential concentration of marine particles in isotropic turbulence". *Deep Sea Res. Oceanogr. Res. Pap.* 42.11-12, 1989–2004.

Sreenivasan, K. R. and J. Schumacher (2025). "What Is the Turbulence Problem, and When May We Regard It as Solved?" *Ann. Rev. Cond. Matt. Phys.* 16.Volume 16, 2025, pp. 121–143.

Stevens, R. J. A. M., E. P. Van Der Poel, S. Grossmann, and D. Lohse (2013). "The unifying theory of scaling in thermal convection: the updated prefactors". *J. Fluid Mech.* 730, pp. 295–308.

Straneo, F. and P. Heimbach (2013). "North Atlantic warming and the retreat of Greenland's outlet glaciers". *Nature* 504.7478, pp. 36–43.

Stroeve, J. and D. Notz (2018). "Changing state of Arctic sea ice across all seasons". *Environ. Res. Lett.* 13.10, p. 103001.

Sugawara, M., E. Tamura, Y. Satoh, Y. Komatsu, M. Tago, and H. Beer (2006). "Visual observations of flow structure and melting front morphology in horizontal ice plate melting from above into a mixture". *Heat and Mass Transfer* 43, p. 1009.

Sugiyama, K., E. Calzavarini, S. Grossmann, and D. Lohse (2009). "Flow organization in two-dimensional non-Oberbeck–Boussinesq Rayleigh–Bénard convection in water". *J. Fluid Mech.* 637, pp. 105–135.

Sundaram, S. and L. R. Collins (1977). "Collision statistics in an isotropic particle-laden turbulent suspension. Part 1. Direct numerical simulations". *J. Fluid Mech.* 335, pp. 75–109.

Svetlichny, L. and M. Uttieri (Mar. 2025). "Kinematic characteristics of calanoid copepod appendage motion". *J. Plankton Research* 47.2, fbae030.

Szeri, A. J. (1993). "Pattern formation in recirculating flows of suspensions of orientable particles". *Philos. Trans. R. Soc. A-Math. Phys. Eng. Sci.* 345.1677, pp. 477–506.

Tagawa, Y., J. M. Mercado, V. N. Prakash, E. Calzavarini, C. Sun, and D. Lohse (2012). "Three-dimensional Lagrangian Voronoï analysis for clustering of particles and bubbles in turbulence". *J. Fluid Mech.* 693, pp. 201–215.

Tavoulareas, E. S. (1991). "Fluidized-Bed Combustion Technology". *Annu. Rev. Energ. Environ.* 16.1, pp. 25–57.

Taylor, G. I. (1934). "The Formation of Emulsions in Definable Fields of Flow". *Proc. Royal Soc. A* 146, pp. 501–523.

Ten Cate, A., J. J. Derksen, L. M. Portela, and H. E. Van Den Akker (2004). "Fully resolved simulations of colliding monodisperse spheres in forced isotropic turbulence". *J. Fluid Mech.* 519, pp. 233–271.

Tergolina, V. B., E. Calzavarini, G. Mompean, and S. Berti (Dec. 2021). "Effects of large-scale advection and small-scale turbulent diffusion on vertical phytoplankton dynamics". *Phys. Rev. E* 104.6.

— (Dec. 2022). "Surface light modulation by sea ice and phytoplankton survival in a convective flow model". *The European Physical Journal Plus* 137.12.

Tietsche, S., D. Notz, J. H. Jungclaus, and J. Marotzke (2011). "Recovery mechanisms of Arctic summer sea ice". *Geophys. Res. Lett.* 38.2, p. L02707.

Tonks, W. B. and H. J. Melosh (1992). "Core formation by giant impacts". *Icarus* 100.2, pp. 326–346.

— (1993). "Magma ocean formation due to giant impacts". *J. Geophys. Res.: Planets* 98.E3, pp. 5319–5333.

Toschi, F. and E. Bodenschatz (2009). "Lagrangian Properties of Particles in Turbulence". *Annu. Rev. Fluid Mech.* 41, p. 375.

Tosi, N. and S. Padovan (2020). "Mercury, Moon, Mars: Surface expressions of mantle convection and interior evolution of stagnant-lid bodies". *Mantle convection and surface expressions*. Ed. by H. Marquardt, M. Ballmer, S. Cottar, and K. Jasper. AGU Monograph Series. arXiv:1912.05207. In press. Wiley, pp. 1 –45.

Tosi, N., A. C. Plesa, and D. Breuer (2013). "Overturn and evolution of a crystallized magma ocean: A numerical parameter study for Mars". *J. Geophys. Res. Planets* 118.7, pp. 1512–1528.

Uhlmann, M. (2005). "An immersed boundary method with direct forcing for the simulation of particulate flows". *J. Comput. Phys.* 209.2, pp. 448–476.

Uhlmann, M. and A. Chouippe (2017). "Clustering and preferential concentration of finite-size particles in forced homogeneous-isotropic turbulence". *J. Fluid Mech.* 812, 991–1023.

Van Der Poel, E. P., R. J. A. M. Stevens, and D. Lohse (2013). "Comparison between two- and three-dimensional Rayleigh–Bénard convection". *J. Fluid Mech.* 736, pp. 177–194.

Visser, A. W. and U. H. Thygesen (2003). "Random motility of plankton: diffusive and aggregative contributions". *Journal of Plankton Research* 25, pp. 1157–1168.

Volk, R, E Calzavarini, G Verhille, D Lohse, N Mordant, J.-F. Pinton, and F Toschi (2008). "Acceleration of heavy and light particles in turbulence: comparison between experiments and direct numerical simulations". *Physica D* 237.14, pp. 2084–2089.

Volk, R., E. Calzavarini, E. Leveque, and J. F. Pinton (2011). "Dynamics of inertial particles in a turbulent von Kármán flow". *J. Fluid Mech.* 668, pp. 223–235.

Voth, G. A. and A. Soldati (2017). "Anisotropic particles in turbulence". *Annu. Rev. Fluid Mech.* 49, pp. 249–276.

Wadham, J. L., J. R. Hawkings, L. Tarasov, L. J. Gregoire, R. G. M. Spencer, M. Gutjahr, A. Ridgwell, and K. E. Kohfeld (2019). "Ice sheets matter for the global carbon cycle". *Nat. Commun.* 10.1, p. 3567.

Wang, F., Y. Du, X. Xie, E. Calzavarini, and C. Sun (Jan. 2026). "Freezing and ice aging dynamics in saline water under natural convection". *Phys. Rev. Fluids* 11.1.

Wang, L.-P. and M. R. Maxey (1993). "Settling velocity and concentration distribution of heavy particles in homogeneous isotropic turbulence". *J. Fluid Mech.* 256, pp. 27–68.

Wang, Z., E. Calzavarini, and C. Sun (Nov. 2021a). "Equilibrium states of the ice-water front in a differentially heated rectangular cell (a)". *EPL - Europhys. Lett.* 135.5, p. 54001.

Wang, Z., E. Calzavarini, C. Sun, and F. Toschi (2021b). "How the growth of ice depends on the fluid dynamics underneath". *Proc. Natl. Acad. Sci. U.S.A.* 118.10, e2012870118.

Wang, Z., L. Jiang, Y. Du, C. Sun, and E. Calzavarini (Sept. 2021c). "Ice front shaping by upward convective current". *Phys. Rev. Fluids* 6.9.

Webster, D. R., D. L. Young, and J. Yen (2015). "Copepods' Response to Burgers' Vortex: Deconstructing Interactions of Copepods with Turbulence". *Integrative and Comparative Biology* 55, pp. 706–718.

Weeks, W. F. and W. J. Campbell (1973). "Icebergs as a fresh-water source: an appraisal". *J. Glaciol.* 12.65, pp. 207–233.

Wells, A. J., J. R. Hitchen, and J. R. G. Parkinson (2019). "Mushy-layer growth and convection, with application to sea ice". *Phil. Trans. R. Soc. A.* 377.2146, p. 20180165.

Wengrove, M. E., E. C. Pettit, J. D. Nash, R. H. Jackson, and E. D. Skyllingstad (2023). "Melting of Glacier Ice Enhanced by Bursting Air Bubbles". *Nature Geoscience* 16.10, pp. 871–876.

Wettlaufer, J. S., M. G. Worster, and H. E. Huppert (1997). "Natural convection during solidification of an alloy from above with application to the evolution of sea ice". *J. Fluid Mech.* 344, pp. 291–316.

Wheeler, J. D., E. Secchi, R. Rusconi, and R. Stocker (2019). "Not just going with the flow: the effects of fluid flow on bacteria and plankton". *Ann. Rev. Cell Develop. Biology* 35, pp. 213–237.

White, F. and I. Corfield (2006). *Viscous Fluid Flow*. McGraw-Hill.

Woodson, C. B., D. R. Webster, M. J. Weissburg, and J. Yen (2005). "Response of copepods to physical gradients associated with structure in the ocean". *Limnology and Oceanography* 50(5), pp. 1552–1564.

— (2007). "Cue hierarchy and foraging in calanoid copepods: ecological implications of oceanographic structure". *Marine Ecology Progress Series* 330, pp. 163–177.

Worster, M. G. (1997). "Convection in mushy layers". *Annu. Rev. Fluid Mech.* 29.1, pp. 91–122.

Wu, W., E. Calzavarini, F. G. Schmitt, and L. Wang (2020). "Fluctuations and correlations of reactive scalars near chemical equilibrium in incompressible turbulence". *Phys. Rev. Fluids* 5.8.

Wu, W., F. G. Schmitt, E. Calzavarini, and L. Wang (Dec. 2021). "A quadratic Reynolds stress development for the turbulent Kolmogorov flow". *Phys. Fluids* 33.12.

Wu, W., L. Wang, E. Calzavarini, and F. G. Schmitt (Mar. 2022). "Reactive scalars in incompressible turbulence with strongly out of equilibrium chemistry". *J. Fluid Mech.* 938.

Xu, A., S. Tao, L. Shi, and H.-D. Xi (2020). "Transport and deposition of dilute microparticles in turbulent thermal convection". *Physics of Fluids* 32.8, p. 083301.

Xu, H. and E. Bodenschatz (2008). "Motion of inertial particles with size larger than Kolmogorov scale in turbulent flows". *Physica D* 237.14. Euler Equations: 250 Years On, pp. 2095–2100.

Xu, H., N. T. Ouellette, D. Vincenzi, and E. Bodenschatz (2007). "Acceleration Correlations and Pressure Structure Functions in High-Reynolds Number Turbulence". *Phys. Rev. Lett.* 99 (20), p. 204501.

Yang, R., C. J. Howland, H.-R. Liu, R. Verzicco, and D. Lohse (2023a). "Bistability in Radiatively Heated Melt Ponds". *Phys. Rev. Lett.* 131 (23), p. 234002.

— (2023b). "Morphology evolution of a melting solid layer above its melt heated from below". *J. Fluid Mech.* 956, A23.

Yen, J. (2000). "Life in transition: balancing inertial and viscous forces by planktonic copepods". *The Biological Bulletin* 198, pp. 213–244.

Yen, J., K. D. Rasberry, and D. R. Webster (2008). "Quantifying copepod kinematics in a laboratory turbulence apparatus". *Journal of Marine systems* 69, pp. 283–294.

Yen, J. and J. R. Strickler (1996). "Advertisement and concealment in the plankton: what makes a copepod hydrodynamically conspicuous?" *Invertebrate Biology* 115, pp. 191–205.

Yeung, P. K. and S. B. Pope (1989). "Lagrangian statistics from direct numerical simulations of isotropic turbulence". *J. Fluid Mech.* 207, 531–586.

Zhao, C., B. Shi, S. Chen, D. Du, T. Sun, B. J. Simonds, K. Fezzaa, and A. D. Rollett (2022). "Laser melting modes in metal powder bed fusion additive manufacturing". *Rev. Mod. Phys.* 94 (4), p. 045002.

Zhao, L., N. R. Challabotla, H. I. Andersson, and E. A. Variano (2015). "Rotation of Nonspherical Particles in Turbulent Channel Flow". *Phys. Rev. Lett.* 115 (24), p. 244501.

Zhu, X., V. Mathai, R. J. A. M. Stevens, R. Verzicco, and D. Lohse (2018). "Transition to the Ultimate Regime in Two-Dimensional Rayleigh-Benard Convection". *Phys. Rev. Letters* 120.14.

Zimmermann, R., Y. Gasteuil, M. Bourgoin, R. Volk, A. Pumir, and J.-F. m. c. Pinton (2011). "Rotational Intermittency and Turbulence Induced Lift Experienced by Large Particles in a Turbulent Flow". *Phys. Rev. Lett.* 106 (15), p. 154501.

Appendix A

Code Infrastructure the CH4-PROJECT

The `ch4-project` is a modular, parallelized computational fluid dynamics code developed for the high-fidelity simulation of multiphysics problems in turbulent flows. It is based on the lattice Boltzmann method (LBM) for solving the incompressible Navier-Stokes equations both on uniform and non-uniforms grids (through a finite volume formulation), and is implemented in `C` with `MPI` for distributed-memory parallelization and `HDF5` for scalable I/O. The code is designed to accommodate a wide range of physical scenarios, with the following major features:

- **Flow configurations:** Support for several canonical turbulent flow types in two (2D) and three dimensions (3D), including homogeneous isotropic turbulence in a spatially periodic domain, Kolmogorov flow, channel flows, Rayleigh–Bénard convection, double-diffusive convection, flows in porous media. External forcing can be applied in customizable forms.
- **Thermal and scalar transport:** Implementation of passive and active scalar fields governed by advection–diffusion equations, with options for source/sink terms and reaction terms. Thermal coupling is available via the Boussinesq approximation.
- **Phase change modeling:** A thermal enthalpy formulation enables the simulation of solid/liquid phase transitions, allowing study of melting and solidification processes in turbulent flows. Specific options to treat conjugate-heat transfer problems for phase-change simulations in freshwater.
- **Lagrangian particle tracking:** Advanced Eulerian–Lagrangian modules support:
  - Tracer and inertial particle tracking (including heavy/light particles with Stokes drag, added-mass,Lift force),
  - Anisotropic particle dynamics (e.g., spheroidal particles under Jeffery orbits),
  - Motile particles (e.g., swimming gyrotactic cells, jumping plankton),
  - Bidirectional two-way coupling between particles and fluid (both mechanical and thermal coupling).
- **Turbulence modeling:** Large-Eddy Simulation (LES) capabilities are included via Smagorinsky and shear-improved Smagorinsky models.

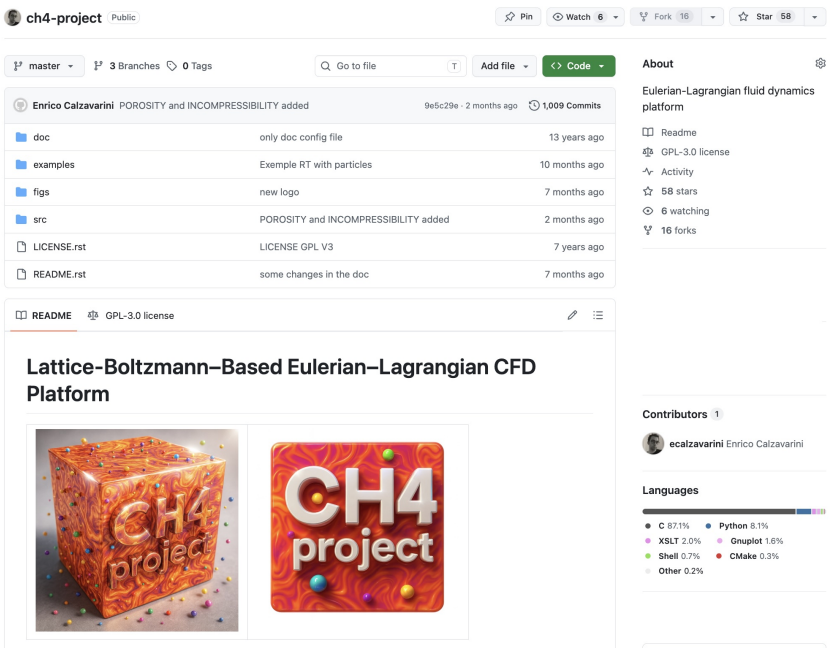


FIGURE A.1: The CH4-PROJECT code as it appears on github repository, july 2026.

The framework is designed for high extensibility and has been used extensively in studies of turbulent convection, scalar transport, and particle-laden flows. The project is openly available under the GNU GPL-3.0 license at: `https://github.com/ecalzavarini/ch4-project`, see Fig. A.1. It has been downloaded and modified by other users to conduct independent research. To date, the code has been used in 16 published works.

Appendix B

Complete publications list

The full texts of my publications - in pdf format - are accessible at this link:
https://www.ecalzavarini.info/research/production/publications-by-year

In journals

64. Particle Thermal Inertia Delays the Onset of Convection in Particulate Rayleigh-Bénard System, Saad Raza, Apolline Lemoine, Yan Zhang, Enrico Calzavarini, Romulo B. Freitas, Leonardo S. de B. Alves, Silvia C. Hirata, Int. J. Multiphase Flow, 2026, 198, pp.105660

63. Freezing and ice aging dynamics in saline water under natural convection, Feng Wang, Yihong Du, Xueyi Xie, Enrico Calzavarini and Chao Sun1, Phys. Rev. Fluids 11, 013504 (2026)

62. Sea ice aging by diffusion-driven desalination, Yihong Du, Feng Wang, Enrico Calzavarini, and Chao Sun, Phys. Rev. Lett. 135, 104201 (2025)

61. Impact of Particle Injection Velocity on the Stability of the Particulate Rayleigh-Bénard System Saad Raza, Romulo B. Freitas, Leonardo S. B. Alves, Enrico Calzavarini, Silvia C. Hirata , J.Fluid Mech. vol. 1015, R2, (2025)

60. Stabilization of the Rayleigh-Bénard system by injection of thermal inertial particles and bubbles, Saad Raza, Silvia C. Hirata, Enrico Calzavarini Phys. Fluids 36, 124141 (2024)

59. The physics of freezing and melting in the presence of flows, Yihong Du, Enrico Calzavarini, Chao Sun, Nature Reviews Physics, 2024, ⟨10.1038/s42254-024-00766-5⟩.

58. Accelerations of large particles in turbulence, Yaning Fan, Cheng Wang, Linfeng Jiang, Chao Sun and Enrico Calzavarini, EPL – Europhys. Lett., 2024, 145 (4), pp.43001.

57. Dispersion and deformation of molecular patterns written in turbulent air, Willem van de Water, Nico Dam and Enrico Calzavarini Phys. Rev. Fluids 9, 014502 (2024).

56. Convective heat transfer in the Burgers-Rayleigh-Bénard system, Enrico Calzavarini and Silvia C. Hirata Phys. Rev. Fluids 8, 063502 (2023)

55. Sea Water Freezing Modes in a Natural Convection System, Yihong Du, Ziqi Wang, Linfeng Jiang, Enrico Calzavarini and Chao Sun, J. Fluid Mech. (2023), vol. 960, A35,

54. Surface light modulation by sea ice and phytoplankton survival in a convective flow model, Vinicius Beltram Tergolina, Enrico Calzavarini, Gilmar Mompean, Stefano Berti, Eur. Phys. J. Plus (2022) 137:1387

53. Dispersion of molecular patterns written in turbulent air, Willem van de Water, Nico Dam, and Enrico Calzavarini, Phys. Rev. Lett. 129, 254501 (2022)

52. Residence time of inertial particles in 3D thermal convection: implications for magma reservoirs, Vojtěch Patočka, Nicola Tosi, Enrico Calzavarini, Earth and Planetary Science Letters 591 (2022) 117622

51. Dynamics of finite-size spheroids in turbulent flow: the roles of flow structures and particle boundary layers, Lin-Feng Jiang, Cheng Wang, Shuang Liu, Chao Sun, Enrico Calzavarini, J. Fluid Mech 939 , A22 (2022)

50. Reactive scalars in incompressible turbulence with strongly out of equilibrium chemistry, Wenwei Wu, Lipo Wang, Enrico Calzavarini, Francois Schmitt, J. Fluid Mech 938, A19 (2022)

49. Copepod swimming activity and turbulence intensity: study in the Agiturb turbulence generator system, Clotilde Le Quinou, Francois G. Schmitt, Yongxiang Huang, Enrico Calzavarini and Sami Souissi, European Physical Journal Plus (EPJ Plus) (2022) 137:250

48. Three-dimensional turbulence effects on plankton dynamics behind an obstacle, Alice Jaccod, Stefano Berti, Enrico Calzavarini, Sergio Chibbaro, European Physical Journal Plus (EPJ Plus)(2022) 137:184

47. A quadratic Reynolds stress development for the turbulent Kolmogorov flow, Wenwei Wu, Francois G. Schmitt, Enrico Calzavarini, Lipo Wang, Phys. Fluids 33, 125129 (2021)

46. Effects of large-scale advection and small-scale turbulent diffusion on vertical phytoplankton dynamics, Vinicius Beltram Tergolina, Enrico Calzavarini, Gilmar Mompean, and Stefano Berti, Phys. Rev. E, 104, 065106 (2021)

45. Equilibrium states of the ice-water front in a differentially heated rectangular cell, Ziqi Wang, Enrico Calzavarini and Chao Sun, Europhys. Lett. (EPL), 135 (2021) 54001

44. Predator-prey plankton dynamics in turbulent wakes behind islands, Alice Jaccod, Stefano Berti, Enrico Calzavarini and Sergio Chibbaro Phys. Rev. Fluids 6,103802(2021)

43. Ice front shaping by upward convective current, Z. Wang, L. Jiang, Y. Du, Chao Sun, E. Calzavarini, Phys. Rev. Fluids 6, L091501(2021)

42. Statistical properties of two-dimensional elastic turbulence, Himani Garg, Enrico Calzavarini and Stefano Berti, Phys. Rev. E 104, 035103 (2021)

41. How the growth of ice depends on the fluid dynamics underneath, Z. Wang, E. Calzavarini, C. Sun, F. Toschi, Proceedings of the National Academy of Sciences of the United States of America (PNAS) 118, e2012870118 (2021)

40. Rotational dynamics of bottom-heavy rods in turbulence from experiments and numerical simulations, L. Jiang, C. Wang, S. Liu, C. Sun, E. Calzavarini, Theor. Appl. Mech. Lett. 11 (2021) 100227

39. Settling of inertial particles in turbulent Rayleigh-Bénard convection, V. Patocka, E. Calzavarini, and N. Tosi, Phys. Rev. Fluids 5, 114304 (2020)

38. Fluctuations and correlations of reactive scalars near chemical equilibrium in incompressible turbulence, W. Wu, E. Calzavarini, F. G. Schmitt, and L. Wang, Phys. Rev. Fluids 5, 084608 (2020)

37. Rotation of anisotropic particles in Rayleigh-Bénard turbulence, L. Jiang, E. Calzavarini, and C.Sun, J. Fluid Mech. vol. 901, A8 (2020)

36. Anisotropic particles in two-dimensional convective turbulence, E. Calzavarini, L. Jiang, and C. Sun, Phys. Fluids 32, 023305 (2020)

35. Eulerian-Lagrangian fluid dynamics platform: the ch4-project, E.Calzavarini, Software Impacts 1, 100002 (2019)

34. Robustness of heat-transfer in confined inclined convection at high-Prandtl number, L.Jiang,C. Sun, E. Calzavarini, Phys. Rev. E 99, 013108 (2019)

33. Particle-laden two-dimensional elastic turbulence, H. Garg , E. Calzavarini, G. Mompean, and S. Berti, Eur. Phys. J. E 41: 115 (2018)

32. Basal melting driven by turbulent thermal convection, B. Rabbanipour Esfahani, S. C. Hirata, S. Berti and E. Calzavarini, Phys. Rev. Fluids 3, 053501 (2018)

31. Propelled microprobes in turbulence, E. Calzavarini, Y. X. Huang, F. G. Schmitt and L. Wang, Phys. Rev. Fluids 3, 054604 (2018)

30. Copepods encounter rates from a model of escape jump behaviour in turbulence, Hamidreza Ardeshiri, François G. Schmitt, Sami Souissi, Federico Toschi and Enrico Calzavarini, J. Plankton Research 39, 878–890 (2017)

29. Micro-bubbles and micro-particles are not faithful tracers of turbulent acceleration, Varghese Mathai, Enrico Calzavarini, Jon Brons, Chao Sun and Detlef Lohse, Phys. Rev. Lett. 117, 024501 (2016)

28. A Lagrangian model of copepod dynamics: Clustering by escape jumps in turbulence, Hamidreza Ardeshiri, Ibtissem Benkeddad, François G. Schmitt, Sami Souissi, Federico Toschi and Enrico Calzavarini, Phys. Rev. E 93, 043117 (2016)

27. Finite volume versus streaming-based lattice Boltzmann algorithm for fluid-dynamics simulations: A one-to-one accuracy and performance study, K.Shrestha, G.Mompean and E.Calzavarini, Phys. Rev. E 93, 023306 (2016)

26. Lagrangian single particle statistics through the lens of Hilbert-Huang Transform, Y. Huang, L. Biferale, E. Calzavarini, C. Sun and F. Toschi, Phys. Rev. E 87, 041003(R) (2013)

25. How size and gravity affect bubble acceleration in turbulence, V.Prakash, Y.Tagawa, E.Calzavarini, J. Martinez Mercado, F. Toschi, C Sun and D. Lohse, New J. Phys. 14, 105017(2012)

24. Rotation rate of rods in turbulent fluid flow, S.Parsa, E.Calzavarini, F.Toschi, G.A.Voth, Phys. Rev. Lett. 109, 134501 (2012)

23. Three dimensional Lagrangian Voronoi analysis for clustering of particles and bubbles in turbulence, Y. Tagawa, J. Martínez Mercado, V. Prakash, E. Calzavarini, C Sun and D. Lohse, J. Fluid. Mech. 693, 201-215 (2012)

22. Axially-homogeneous Rayleigh-Benard convection in a cylindrical cell, L.E.Schmidt, E.Calzavarini, D. Lohse, F. Toschi, R. Verzicco, J. Fluid Mech. 691, 52-68 (2012)

21. Impact of trailing wake drag on the statistical properties and dynamics of finite size particles in turbulence, E. Calzavarini, R. Volk, E. Leveque and J.-F. Pinton and F. Toschi, Physica D 241, 237-244 (2012)

20. Multi-Time Multi-Scale Correlation Functions in Hydrodynamic Turbulence, L. Biferale, E. Calzavarini and F. Toschi, Phys. Fluids 23, 085107 (2011)

19. Dynamics of inertial particles in a turbulent von Karman flow, R. Volk , E. Calzavarini,, E. Leveque and J.-F. Pinton, J. Fluid Mech. 668, 223-235 (2011)

18. Flow organization in non-Oberbeck-Boussinesq Rayleigh-Benard convection in water, K. Sugiyama, E. Calzavarini, S. Grossmann and D. Lohse, J. Fluid Mech. 637, 105 - 135 (2009)

17. Velocity gradients along particles trajectories in turbulent flows: the refined similarity hypothesis in the Lagrangian frame, R. Benzi, L. Biferale, E. Calzavarini, D. Lohse and F. Toschi, Phys. Rev. E 80, 066318 (2009)

16. Exploring the limits of granular hydrodynamics: a horizontal array of inelastic particles, P. Eshuis, K. van der Weele, E. Calzavarini, D. van der Meer and D. Lohse, Phys. Rev. E 80, 011302 (2009)

15. Acceleration statistics of finite-sized particles in turbulent flow: the role of Faxen forces, E. Calzavarini, R. Volk, M. Bourgoin, E. Leveque, J.-F. Pinton and F. Toschi, J.Fluid Mech., 630, 179-189 (2009)

14. Universal statistical properties of particle trajectories in highly turbulent flows, A. Arneodo, R. Benzi, J. Berg, L. Biferale, E. Bodenschatz, A. Busse, E. Calzavarini, B. Castaing, M. Cencini, L. Chevillard, R. Fisher, R. Grauer, H. Homann, D. Lamb, A.S. Lanotte, E. Leveque, B. Luthi, J. Mann, N. Mordant, W.-C. Muller, S. Ott, N. T. Ouellette, J.-F. Pinton, S.B. Pope, S.G. Roux, F. Toschi, H. Xu and P.K. Yeung, Phys. Rev. Lett. 100, 254504 (2008)

13. Quantifying microbubble clustering in turbulent flow from single-point measurements, E.Calzavarini, T. H. van den Berg, F. Toschi and D. Lohse, Phys. Fluids 20, 040702 (2008)

12. Dimensionality and morphology of particle and bubble clusters in turbulent flow, E.Calzavarini, M. Kerscher, D. Lohse and F. Toschi, J. Fluid Mech. 607,13 - 24 (2008)

11. Micro-bubbly drag reduction in Taylor-Couette flow in the wavy vortex regime, K. Sugiyama, E. Calzavarini, and D. Lohse, J. Fluid Mech. 608, 21 - 41 (2008)

10. Acceleration of heavy and light particles in turbulence: comparison between experiments and direct numerical simulations, R. Volk , E. Calzavarini, G. Verhille, D. Lohse, N. Mordant, J.-F. Pinton and F. Toschi, Physica D 237, 2084 - 2089 (2008)
9. Quantifying turbulence induced segregation of inertial particles, E. Calzavarini, M. Cencini, D. Lohse and F. Toschi, Phys. Rev. Lett. 101, 084504 (2008)
8. Non-Oberbeck-Boussinesq effects in turbulent thermal convection in ethane close to the critical point, G. Ahlers, E. Calzavarini, F. Fontenele Araujo, D. Funfschilling, S. Grossmann, D. Lohse and K. Sugiyama, Phys. Rev. E 77, 046302 (2008)
7. Non-Oberbeck-Boussinesq effects in two-dimensional Rayleigh-Benard convection in glycerol, K. Sugiyama, E. Calzavarini, S. Grossmann and D. Lohse, Europhys. Lett. 80, 34002 (2007)
6. Exponentially growing solutions of homogeneous Rayleigh-Benard flow, E. Calzavarini, C. R. Doering, J. D. Gibbon, D. Lohse, A. Tanabe, and F. Toschi, Phys. Rev. E 73, 035301(R) (2006).
5. Rayleigh and Prandtl number scaling in the bulk of Rayleigh-Benard turbulence, E. Calzavarini, D. Lohse, F. Toschi and R. Tripiccione, Phys. Fluids 17, 5, 055107 (2005).
4. Universality of anisotropic turbulence, L. Biferale, E. Calzavarini, A. S. Lanotte, F. Toschi and R.Tripiccione, Physica A, 338, 194-200, (2004).
3. Matched filters for coalescing binaries detection on massively parallel computers, E.Calzavarini, L. Sartori, F. Schifano, R. Tripiccione and A. Vicere, Comp. Phys. Comm. 152, 3, 295-306 (2003)
2. Universality of anisotropic fluctuations from numerical simulations of turbulent flows, L.Biferale, E. Calzavarini, F. Toschi and R. Tripiccione, Europhys. Lett. 64, 461-467 (2003)
1. Evidences of Bolgiano-Obhukhov scaling in three-dimensional Rayleigh-Benard convection, E. Calzavarini, F. Toschi and R. Tripiccione, Phys. Rev. E 66, 016304 (2002)

Book chapters

1. Modelling the evolution of sea ice and melt ponds: sensitivity to microscale heat transfer mechanisms, A. Scagliarini, E. Calzavarini, D. Mansutti and F. Toschi, Mathematical Approach to Climate Change and its Impacts. Springer INdAM Series, vol 38. Springer, Cham (2020)

Conference proceedings

10. Mechanical modelling of marine planktonic copepod dynamics in fluid flows, H. Ardeshiri, F. G. Schmitt, S. Souissi, F. Toschi and E. Calzavarini, Proceedings 23ème Congrès Français de Mécanique (CFM) Lille, 28/08 -1/09 2017, (2017).
9. On the error estimate in sub-grid models for particles in turbulent flows, E. Calzavarini, A. Donini,V. Lavezzo, C. Marchioli, E. Pitton, A. Soldati, F. Toschi, Direct and Large-Eddy Simulation VIII (ERCOFTAC Workshop, Eindhoven, the Netherlands, July 6-9, 2010), (2010).

8. Lagrangian modelling and properties of particles with inertia, F.Toschi, L.Biferale, E.Calzavarini, A. Scagliarini and E. Leveque, Advances in Turbulence XII, Proceedings of the 12th European Turbulence Conference (ETC-12), Marburg (D), 7 - 10 September 2009, Springer Proceedings in Physics (2009).

7. Effect of Faxen forces on acceleration statistics of material particles in turbulent flow, E.Calzavarini, R. Volk, M. Bourgoin, E. Leveque, J.-F. Pinton and F. Toschi, Advances in Turbulence XII, Proceedings of the 12th European Turbulence Conference (ETC-12), Marburg (D), 7 - 10 September 2009, Springer Proceedings in Physics (2009)

6. Various flow amplitudes in 2D non-Oberbeck-Boussinesq Rayleigh-Benard convection in water, E. Calzavarini, S. Grossmann, D. Lohse and K. Sugiyama, Advances in Turbulence XII, Proceedings of the 12th European Turbulence Conference (ETC-12), Marburg (D), 7 - 10 September 2009, Springer Proceedings in Physics (2009).

5. Homogeneous Rayleigh-Benard convection, E. Calzavarini, D. Lohse, and F. Toschi, Progress in Turbulence II, Proceedings of the iTi Conference in Turbulence, Bad Zwischenhahn (D), September 2005, Springer Proceedings in Physics 109, 181-184, (2007).

4. Concentration and segregation of particles and bubbles by turbulence, E.Calzavarini, M.Cencini, D.Lohse and F. Toschi, Advances in Turbulence XI, Proceedings of the 11th European Turbulence Conference (ETC-11), Porto (PT), 25 -28 June 2007, Springer Proceedings in Physics 117, 418-420, (2007).

3. Numerical study of Non-Oberbeck Boussinesq effects on the heat transport in turbulent Rayleigh- Benard convection in liquids, K. Sugiyama, E. Calzavarini and D. Lohse, Advances in Turbulence XI, Proceedings of the 11th European Turbulence Conference (ETC-11), Porto (PT), 25 -28 June 2007, Springer Proceedings in Physics 117, 642-644, (2007).

2. Prandtl number scaling laws in the Homogeneous Rayleigh-Benard system, E. Calzavarini, F. Toschi and R. Tripiccione, on Advances in Turbulence X, Proceedings of the 10th European Turbulence Conference (ETC-10), Trondheim (NO), 29 June-2 July 2004, H.I. Andersson and P.-A. Krogstad (eds.), CIMNE, (2004).

1. Bolgiano scaling in a 3D convective cell, E.Calzavarini, F.Toschi and R. Tripiccione, Advances in Turbulence IX, Proceedings of the 9th European Turbulence Conference (ETC-9), Southampton (UK), July 2-5 2002, I.P. Castro, P.E. Hancock and T.G. Thomas (eds), CIMNE, (2002).